UNIVERSITY OF HULL

WETTABILITY OF ANISOTROPIC AND POROUS PARTICLES ADSORBED TO FLUID INTERFACES

being a Thesis submitted for the Degree of doctor of philosophy

in the University of Hull

by

Hamza Saeed A. Al–Shehri B Sc., M. Sc.

(June 2015)

ACKNOWLEDGMENTS

I would like to express my sincere appreciation and gratitude of my supervisors Prof. V. N. Paunov, Dr T. S. Horozov for not only their invaluable scientific guidance and suggestions but also for their constructive discussion and devoting plenty of time to help me in many ways throughout these years of my work.

I am indebted to my many colleagues Paunov Research Group who supported me through this PhD especially: Marius Rutkevičius, Anupam Das, Mohammed Alawady, Emmanuel E Ubuo, Osama Alswafy, Saba Al-Obaidy, Khaled Althubeiti, Jevan Medlock, and Benjamin Thomson.

I would like to thank all members of the Surfactant & Colloid group at the University of Hull for their support and friendship during my PhD. I especially thanks Andrew Johnson, Saeed Mashinchi, Luke Sovary, Ioannis Marinopoulos.

Also, I am grateful to all my Saudi colleagues especially Jari Algethami, Ahmed Fallatah, Amin Khattab, Zeid Oiaidha, Mohammed Alotaibi, Ali Alorabi, and Seraj Alzahrani

I greatly appreciate the support of Mr Tony Sinclair for SEM images

I am also indebted to the contribution of the Emma Sharp in Chapter 3.

I would like to show my gratitude to my Saudi friends. I especially thanks Ziead Alzaidy, Abdulrahman Alqarni, Ahmed Aldaffaa, Fahad Alkhaleefa , Jari Algethami, Faleh Alqahtany, Rami Albasha, Khalid Alogaili, Othman Alfahad, Yaser Alnaam, Mohammed Algamdi, Thamer Almahbob Saeed Alqarni, Ibrahim Alharthi, Mohammed Alshumrani, Ali Alqahtany, Faisal Al Hudithi, Adel Althagafy and Abdulrahman Bajaber, all of those who I cannot remember their names.

I owe immense gratitude to the Ministry of Education in Saudi Arabia and the Royal Embassy of Saudi Arabia Cultural Bureau in London for the generous scholarship they provided to me.

Finally, I would like to thank my family for their support and encouragement throughout this time. I especially thank my father (Saeed Al-Shehri), my mother

(Sarra'a Al-Shehri), my brothers (Ali, Dhyab, Raad and Mohammed) and my sisters (Aziza, Dokhna and Najah), my wife (Asma Alshehri) for their patience and unconditional support. I truly feel failure is not possible with you all by my side.

PRESENTATIONS

Some of the results obtained in this project have been published and presented at conferences as follows:

Publications:

- ***Adsorption of shape–anisotropic and porous particles at the air–water and the decane–water interface studied by the Gel Trapping Technique.***
  Emma L. Sharp, Hamza Al–Shehri, Tommy S. Horozov, Simeon D. Stoyanov and Vesselin N. Paunov, *RSC Adv.*, **2014**, 4, 2205–2213.

- ***Adsorption of carboxylic modified latex particles at liquid interfaces studied by the Gel Trapping Technique.***
  Hamza Al–Shehri, Tommy S. Horozov and Vesselin N. Paunov , *Soft Matter*, **2014**,10,6433–6441.

Poster presentations:

- ***Wettability of porous particles at liquid interface*,** Hybrid Materials 2015, 9th 13th March. Meliá Sitges Hotel Congress Centre, Sitges (near Barcelona). Presented poster

- ***Porous particles attachment at fluid–fluid interfaces*,** SSC8, 31st Jan–1st Feb. 2015 QEII Conference Centre, United Kingdom.

- ***Preparation and wettability of porous supra–particles at fluid interfaces***, Science Showcase, 26th Apr. 2013 Hull City Hall,

- ***Wettability of latex particles determined by the Gel Trapping Technique*** SSC7, London, Brunel University, llth – 14th Oct. 2012,

- ***Wettability of latex particles determined by the Gel Trapping Technique***, Chemistry Colloquia 2012, University of Hull, United Kingdom

Oral presentations:

- ***Attachment of porous particles at liquid interfaces***,
  Chemistry Colloquia 2014, University of Hull, United Kingdom.

- ***Preparation and wettability of porous supra–particles at fluid interfaces***, Surfactant and Colloid Group Seminar 2012 Faculty of Science and Engineering, Department of Chemistry.

ABSTRACT

The wettability of particles and the way they attach to liquid interfaces is important for many technologies where powders are mixed with liquids or used as emulsifiers. Most such powders are highly agglomerated into larger aggregates that are highly porous. The attachment of such porous particles to liquid–fluid interfaces has not been studied in detail, especially in cases where the porous particles are impregnated with another fluid phase. The overall aim of the thesis is to study the behaviour of particles at the liquid–fluid interface with an emphasis on non–spherical and porous solid particles.

We study the orientation of anisotropic microparticles and measure the contact angle of smooth and porous microparticles with the gel–trapping technique (GTT) to find the wettability of microparticles adsorbed in fluid interfaces. This technique allows us to obtain micrographs by scanning electron microscopy (SEM) for particles resting on polydimethylsiloxane (PDMS), which replicates the non–polar phase and allows for measuring the particle contact angle. We show the results of the typical attachment and orientation of needle–like (aragonite), rhombohedra–like (calcite) microcrystals and ethyl cellulose micro–rods, as well as highly porous hydrophilic and hydrophobic silica microparticles at these liquid interfaces. The importance of these results is in gaining an understanding of the adsorption behaviour and demonstrating actual information on anisotropic particles which have potential applications in industrial formulations and products.

We also investigate how carboxylate modified latex (CML) microparticles adsorb at liquid surfaces and the preferred type of emulsion they can stabilise depending on the particle size and the surface density of carboxylic groups. We also study, both theoretically and experimentally, the effect of salt in the aqueous phase on the contact angle of such microparticles. The main finding is that the wettability of CML microparticles is governed by the carboxylic group density on the particle surface rather than their ionisation. We demonstrate that the type of Pickering emulsions is governed by the wettability of microparticles at the oil–water interface.

We study the effect of the initial impregnation of porous particles with polar or non–polar phases on their attachment at liquid interfaces both theoretically and experimentally. Model supra–particles have been prepared by using building blocks of smaller colloid particles packed in a spherical aggregate. The particles were produced by drying latex particle suspensions of various particle volume fractions and

concentrations, followed by partial fusion of the particles achieved by thermal annealing. We have studied the particle surface morphology and porosity and showed how the annealing temperature, the initial particle volume fraction of sulphate latex suspension and the evaporation temperature can be used to control the supra–particle final structure and porosity. Furthermore, we have investigated the link between the wettability of the porous supra–particle building blocks, i.e. sulphate latex particles, and the macroscopic (apparent) contact angle of the porous supra–particle when attached to liquid surfaces. The contact angles of porous supra–particles infused with water at the oil–water interface were found to be much bigger than those at the air–water interface as expected. We also show how the type of liquid filling the pores of the supra–particle affects its macroscopic contact angle at the oil–water interface.

Table of Contents

Chapter 1: Introduction 1

1.1 Research objectives and thesis presentation 1

1.2 Basic concepts in solid wetting 2

1.3 Spreading coefficient and works of adhesion and cohesion 3

1.4 Wetting of ideal solid surfaces and the Young equation 5

1.5 Wetting of rough surfaces 6

1.5.1 The Wenzel model 6

1.5.2 The Cassie and Baxter model for heterogeneous wetting 7

1.6 Contact angle hysteresis 8

1.7 Particle contact angles and energies at liquid interfaces 10

1.8 Methods for measuring particle contact angles 13

1.8.1 Methods using multiple particles (integral methods) 13

1.8.2 Methods for measuring contact angles of individual particles 15

1.9 Porous particles 21

1.9.1 Properties and characterisation of porous particles 21

1.9.2 Preparation of porous supra–particles 24

1.10 Emulsions 27

Chapter 2: Materials and methods 30

2.1 Materials 30

2.1.1 Water 30

2.1.2 Organic solvents and other chemicals 30

2.1.3 Other materials 30

2.1.4 Spherical latex particles 31

2.1.5 Non–spherical and porous microparticles 32

2.1.6 Fluorescent dyes 34

2.2 Methods 35

2.2.1 Cleaning procedures for glassware 35

2.2.2 Measuring the surface and interfacial tensions 35

2.2.3 Zeta potential 35

2.2.4 Measuring particle contact angles with the Gel Trapping Technique 36

2.2.5 Fabrication of model of porous supra–particles 40

2.2.6 Supra–particle attachments and contact angle measurements at fluid interfaces using drop shape analysis (DSA) 47

Chapter 3: Adsorption of shape–anisotropic and porous particles at the air–water and the decane–water interfaces studied by the Gel Trapping Technique 56

3.1 Introduction 56

3.2 Results and Discussion 58

3.2.1 Anisotropic particles 58

3.2.2 Ethyl cellulose microfibres 63

3.2.3 Hydrophilic porous silica microparticles 64

3.2.4 Hydrophobic porous silica microparticles 65

3.3 Conclusions 67

Chapter 4: Adsorption of carboxylic–modified latex at a liquid–liquid interface studied by the gel trapping technique 69

4.1 Introduction 69

4.2 Results and discussion 71

4.2.1 Wettability of CML particles at liquid surfaces 71

4.2.2 Effect of syneresis on contact angle measurements 76

4.2.3 Effect of salt concentration on the contact angle of CML particles at liquid surfaces 78

4.2.4 Emulsions stabilised by CML particles 85

4.3 Conclusions 87

Chapter 5: Fabrication of porous supra–particles 89

5.1 Introduction 89

5.2 Results and discussion. 91

5.2.1 Porous supra–particles fabrication 91

5.2.2 Model supra–particles made by rolling latex particle suspension on hot superhydrophobic surface 93

5.2.3 Characterisation of the supra–particles morphology 98

5.2.4 Thermal annealing of the porous supra–particles 103

5.2.5 Characterisation of the supra–particles' density and porosity 105

5.2.6 Observation of impregnation of the supra–particles with fluid 109

5.3 Conclusions 111

Chapter 6: Theory of the adsorption of porous particles and colloidosomes to a liquid–fluid interface 113

6.1 Introduction 113

6.2 Theoretical background 114

6.2.1 Attachment of a single colloid particle at the liquid–fluid interface 114

6.3 Theoretical model for the adsorption of a porous spherical supra–particle (or a spherical colloidosome) at the oil–water interface 118

6.3.1 Adsorption of a porous supra–particle or a colloidosome from the aqueous phase to the oil–water interface. 120

6.3.2 Adsorption of a porous supra–particle or a colloidosome from the oil phase to the oil–water interface 123

6.4 Results and discussions 126

6.4.1 Contact angle of a porous supra–particle (or colloidosome) adsorbed from the aqueous phase to the oil–water interface. 126

6.4.2 Contact angle of a porous supra–particle (or colloidosome) adsorbed from the oil phase to the oil–water interface. 133

6.5 Conclusions 141

Chapter 1: Measurement of the three-phase contact angle of porous composite supra-particles at the air-water and oil-water interfaces 143

1.1 Introduction 143

1.2 Contact angle of sulphate latex particles at the air-water interface studied using the gel-trapping technique 145

1.3 Measurement of the supra-particle contact angles at liquid-fluid interfaces using a Drop Shape Analysis (DSA) 148

1.4 Pendant drop method to determine the contact angle of porous particles . 149

1.4.1 Contact angles of dry porous supra-particles at the a/w interface. 151

1.4.2 Contact angles of dry porous supra-particles at the air-NaCl(aq) solution interface. 157

1.4.3 Contact angles of water-infused porous supra-particles at the a/w surface 161

1.4.4 Contact angles of water-infused porous supra-particles at the air-NaCl(aq) solution surface. 164

1.4.5 Contact angles of water-infused porous supra-particles at the hexadecane-water interface 167

1.4.6 Contact angles of porous supra-particles infused with a NaCl(aq) solution at the hexadecane-NaCl(aq) solution interface. 169

1.4.7 Contact angle of hexadecane-infused porous supra-particles attached at the hexadecane-water interface. 172

1.4.8 Contact angles of hexadecane-infused porous supra-particles at the hexadecane-NaCl(aq) solution interface. 174

1.5 Sonication method for determining the contact angle of porous supra-particles at the air-water and oil-water interfaces. 179

1.5.1 Contact angle of dry porous supra-particles sonicated at the air-water interface. 179

1.5.2 Contact angle of water-infused particles sonicated at the air-water interface. 181

1.5.3 Contact angle of porous supra-particles impregnated with water at the hexadecane-water interface. 185

1.5.4 Contact angle of porous supra-particles impregnated with hexadecane at the hexadecane-water interface. 187

1.6 Magnetic resonance imaging for porous supra-particles at fluid-liquid interfaces. 190

1.6.1 Magnetic resonance imaging for dry and wet composite porous supra-particles at the air-water interface. 190

1.6.2 Magnetic resonance imaging for water wet porous supra-particles attached at an oil-water interface 191

1.6.3 Magnetic resonance imaging for oil-wet porous supra-particles at air-oil and oil-water interfaces. 192

1.7 Conclusions 193

Chapter 1: Summary of conclusions, main results and future work 195

1.1 Conclusions 195

1.2 Future work 202

1.3 Appendix 203

References 219

List of figures

Figure 1.1. Liquid drop behaviour on a solid surface. (A) partial wetting, (B) complete wetting, and (C) complete dewetting.[1] 3
Figure 1.2. A diagram illustrating (A) the work of cohesion, which is the energy required to reversibly split a column of a pure liquid (water), W, thus forming two water–air, WA, interfaces with surface tension and unit areas; and (B) the work of adhesion, which is the energy required to separate reversibly a liquid in contact with solid, S, by forming solid–air, SA, and liquid–vapour surfaces with unit areas and the respective interfacial tensions. 4
Figure 1.3. Schematic of a water droplet (cross–section) resting at equilibrium on an ideal smooth solid surface in air. 6
Figure 1.4. A diagram illustrating the Wenzel model for the apparent contact angle of a water droplet on a rough surface. The surface roughness is exaggerated. 7
Figure 1.5. Cassie–Baxter model for apparent contact angle of a droplet on a rough surface of hydrophobic material. 8
Figure 1.6. (a) Illustration of the advancing and receding contact angles of a droplet on a tilted solid surface[21] and (b) adding an amount of liquid results in advancing and reducing an amount of liquid results in receding of the contact angle.[22] 9
Figure 1.7. (a) Diagrams showing the position of spherical particles with different contact angles, θ, at the oil–water interface. (b) The energy required to remove a spherical particle with radius 10 nm from a liquid interfaces with interfacial tension 27 mN/m at 298 K into a bulk liquid as a function of the particle contact angle (adapted from[26] and[27]) 11
Figure 1.8. A diagram showing a large dense spherical particle attached to a liquid interface.[37] 12
Figure 1.9. Individual cylindrical particle adsorbed at planar air–water interface. (a) Simulated shape with contact angle θ = 80 ± 2° and (b) SEM image of SU–8 cylinder at air–water interface [38, 40]. 13
Figure 1.10. Illustrative view of the capillary rise wetting method.[47, 49] 14
Figure 1.11. Schematic diagram of sample preparation for measuring the contact angle of particles at (A) air–water and (B) oil–water interfaces. The equatorial particle diameter, d, can be determined directly (C) or after profiling the particle with a circle (D). The GTT method is used with SEM or AFM.[4, 55, 59] 17

Figure 1.12. Illustration of the contact angle measurements using the film calliper method. The image on the left shows interference fringes of a water film in air with 2 μm bridging particles in the film meniscus.[19] 18
Figure 1.13. A sketch of the bridging particles in the air–water interface for particle movements in thicker or thinner liquid interfaces. [19] 19
Figure 1.14. Illustration of particle adsorption at the frozen liquid after coating with metal: (a) hydrophilic particles and (b) hydrophobic particles. (c) Demonstration sample preparation for cryo–SEM Fresca imaging. 20
Figure 1.15. (a) Illustration of X–ray imaging technique to visualise particle adsorption at the oil–water interface. (b) In–situ X–ray image of polystyrene latex particles at the decalin–water interface.[54] 21
Figure 1.16. Porous solid physical properties.[73] 22
Figure 1.17. A diagram showing a monolith where L is the cylindrical length, and R is the radius 23
Figure 1.18. Packing density for colloidal particle arrangements: (a) and (b) diagram and SEM micrograph of hcp packing, (c) and (d) diagram and SEM micrograph of fcc packing, (e) and (f) diagram and SEM micrograph of bcc packing.[76]. 24
Figure 1.19. A diagram showing a supra–particle and a colloidosome 25
Figure 1.20. SEM micrographs for colloidosomes made by emulsion assembly (oil droplet dispersed in water): (a) dry colloidosome composed (10 μm) of 0.9 μm polystyrene particles and (b, c) close–ups of a, b, respectively. 0.15 μm holes, denoted by an arrow, express the penetrability.[76, 103] 26
Figure 1.21. (A) Schematic diagram for the preparation of porous particles. (B) Optical micrograph of supra–particles made from 320 nm latex particles.[79] 27
Figure 1.22. Schematic representation of the different mechanisms involved in the breakdown of an unstable emulsion.[105] 28
Figure 1.23. Schematic representation of water–in–oil (left) and oil–in–water (right) emulsions stabilised by hydrophobic and hydrophilic particles, respectively. 29
Figure 2.1. SEM images of (a) aragonite microcrystals, (b) hydrophilic porous silica microparticles (VP Aeroperl® 300/30), and (c) calcite microcrystals. (d) Optical microscopy images of ethyl cellulose microrods in aqueous solution. 34
Figure 2.2. Chemical structure of (A) Rhodamine 6G, (B) Fluorescein 5(6)–isothiocyanate (FITC). 34

Figure 2.3. Gellan gum structure.....36
Figure 2.4. Illustrations showing how the particles adsorbed and spread on the surface of the gellan solution. (A) Injecting the particles through the water phase and (B) injecting the particles through the air–oil phase. 39
Figure 2.5. Schematic diagram illustrating supra–particles prepared using the PDMS template. (a) The PDMS with the curing agent was poured onto the stainless steel balls. (b) The cured PDMS elastomer was peeled off at 50°C in the oven. (c) The steel balls were removed, creating a well cavity, and holes were made towards the wells. (d) The PDMS on top of the 0.02 µm Anotop filter, a 3 µm filter paper, and a Petri dish with holes were clamped to allow the injection of the particle suspension into the wells. (f) The particle suspension was allowed to fuse and the suspension was evaporated at 106°C. 41
Figure 2.6. Methods used to insert the sulphate latex suspensions into the ball cavities in the PDMS template: (A) by hand, (B) calliper, and (C) syringe pump. (D) The image on the right shows steel balls in the PDMS template. 42
Figure 2.7. Representation of the formation of a dry porous supra–particle from a drop of concentrated polystyrene latex suspension which was evaporated at 90°C. The dry porous particles (2 mm) were partially fused at 106°C to form a stable porous supra–particle for our studies on porous particle adsorption at liquid surfaces. The scale bar is 10 mm. 44
Figure 2.8. Illustration of impregnation of pores with liquids. (A) Particles filled with water need an intermediate solution (i.e. ethanol) to get fully impregnated with an aqueous solution. (B) Particles impregnated with hexadecane. Air bubbles were observed when ethanol and hexadecane were used to impregnate the particles. The particles were placed in water and hexadecane overnight to make sure they were fully impregnated. 48
Figure 2.9. Schematic for dry (left) and wet (right) porous supra–particle attachment to air–water interfaces. 49
Figure 2.10. Illustration showing how the water penetrates into the pores and how the particle was attached to the water pendant droplet or air bubble. 50
Figure 2.11. Photograph of dry porous supra–particles (1.7 ± 0.2 mm) at the air–water interface using an ultrasonic probe ranging from 0% amplitude to 100% amplitude. 51

Figure 2.12. Attachment of wet porous particles at air–water interface after (a) vibrating the particles at thin film and (B) injecting water to make the particles float. 52
Figure 2.13. Side image obtained from DSA 10 for a porous supra–particle (1.7 0.2 mm) filled with water attached to an air bubble. D is the particle diameter, b is the particle protrusion through water, and θ_{Flat} and θ_{Curve} are the contact angles for flat liquid surface contact angle (FCA) and curved liquid surface contact angle (CCA), respectively. 53
Figure 2.14. Pictures of the probe used for the MRI experiment to visualise the penetration of liquid into the porous particles. Photographs (side and top) of the 2 mm solenoid coil attached to the Bruker microimaging probe. 55
Figure 3.1. Scheme of a solid porous microparticle adsorbed at (A) the air–water and (B) the oil–water interface. The position of the porous particle (or a particle aggregate) when adsorbed at the liquid interface depends on the effective contact angle, θ_{eff}, which is different from the contact angle of the individual particles in the aggregate. Needle–like (C) and rhombohedra–like microcrystals (D) may have several possible orientations at the liquid interface. (E–F) The orientation of microfiber particles when adsorbed at liquid surfaces may also depend on the packing conditions and their surface concentration at the air–water and the oil–water interface. 57
Figure 3.2. (a)–(c) SEM images of aragonite microcrystals adsorbed at the air–water interface followed by its replication with PDMS by using the Gel Trapping Technique (GTT). The parts of the aragonite microcrystals immersed in the PDMS have been exposed to the air phase when adsorbed at the air–water interface. Sample area of low (a) and high (b–c) surface concentration of aragonite microcrystals; (d)–(f) SEM images of aragonite microcrystals adsorbed at the decane–water interface followed by its replication with PDMS by the GTT. The exposed parts of the microcrystals were originally immersed in the aqueous phase. Sample areas of low (d) and high (e), (f) surface concentration of aragonite microcrystals. 60
Figure 3.3. (a)–(c) SEM images of calcite microcrystals adsorbed at the air–water interface followed by its replication with PDMS using the GTT. The parts of the calcite microcrystals immersed in the PDMS have been exposed to the air phase when adsorbed at the air–water interface. (d)–(f) SEM images of calcite microcrystals adsorbed at the decane–water interface followed by its replication with PDMS using the GTT. Images viewed at angle of 65°. 61

Figure 3.4. Percentages of the occurrence of particle surface orientations for three most typical configurations of adsorbed calcite microcrystals at the air–water and decane–water interfaces. 62
Figure 3.5. (a)–(c) SEM images of ethyl cellulose microfibres adsorbed at the air–water interface followed by replication with PDMS using the GTT. The parts of the microfibres immersed in the PDMS were exposed to the air phase when adsorbed at the air–water interface. (d)–(f) SEM images of aragonite microcrystals adsorbed at the decane–water interface followed by replication with PDMS using the GTT. The parts of the aragonite microcrystals immersed in the PDMS were originally immersed in the decane phase when adsorbed at the decane–water interface. The exposed surface of the microfibres was originally immersed in the aqueous phase.....63
Figure 3.6. SEM images of hydrophilic porous silica particles (VP Aeroperl® 300/30) adsorbed at the air–water interface (a)–(c) and the decane–water interface (d)–(f) followed by the surface replication with PDMS using the GTT. The samples were imaged at a viewing angle of 65° between the electron beam and the detector. The exposed part of the particle surface was exposed to the aqueous phase when adsorbed at the air–water surface (a)–(c) and the decane–water interface (d)–(f). 65
Figure 3.7. SEM images of hydrophobic porous silica particles (VP Aeroperl® R806/30) adsorbed at the decane–water interface followed by the liquid surface replication with PDMS using the GTT. The samples are imaged at a viewing angle of 65° between the electron beam and the detector. The exposed parts of the particle surface were immersed in the aqueous phase when adsorbed at the decane–water interface (a) and (b) correspond to different resolutions.....66
Figure 4.1. Schematic representation of the effect of carboxylic (–COOH) surface groups on particle adsorption and the three–phase contact angle at the oil–water interface: (A) high surface density of carboxylic groups on the particle surface makes them hydrophilic ($\theta < 90°$), while (B) low surface density of carboxylic groups on the latex particle surface makes them hydrophobic ($\theta > 90°$).....70
Figure 4.2. Scanning electron microscopy images of the CML particles of various diameters examined in this paper: (A1, A2, A3) 0.9 μm, (B1, B2, B3) 1.2 μm, (C1, C2, C3) 2 μm, and (D1, D2, D3) 3 μm. High–resolution SEM images (A2–D2) and (A3–D3) showing the local surface morphology of the CML particles. The scale bars are 3 μm for images (A1–D1) and 500 nm for images (A2–D2) and (A3–D3).....71

Figure 4.3. SEM micrographs of CML particles of different diameters and their contact angles at the air–water, dodecane–water, and hexadecane–water interfaces. The samples were prepared by injecting a particle dispersion in a spreading solvent into water or a non–polar phase near the liquid interface. The detector tilt angle used for imaging the particles was 85°. The scale bar is 500 nm for all images. 74
Figure 4.4. CML particle three–phase contact angle as a function of the area per carboxylic group on the particle surface. A Large area per –COOH group corresponds to hydrophobic particles, while a low area per –COOH group corresponds to hydrophilic particles. The lines between the data points are only guides to the eye. 75
Figure 4.5. SEM micrographs of CML particles of different diameters and their contact angles at the air–water and dodecane–water interfaces. The samples were prepared by injection of a particle dispersion in a spreading solvent into the water near the liquid interface and put in the fridge at 4°C for 10–20 min before PDMS curing. The detector tilt angle used for imaging the particles was 85°. The scale bar is 500 nm for all images. 76
Figure 4.6. Schematic representation for syneresis effect on particles at oil–water interface after cooling for 10–20 min at 4 ºC.....77
Figure 4.7. SEM images of 3 μm CML particles templated with PDMS at different liquid interfaces, where the particles are injected through the water phase. The contact angle does not change upon adding a known amount of NaCl (1 mM) to the aqueous phase (A and B). Typical SEM images of the CML particles at the air–water surface; (C and D) at the dodecane–water interface and (E and F) at the hexadecane–water interface. The scale bar is 500 nm for all images. Note that the three–phase contact angle of 3 μm CML particles at both the air–water and the oil–water interface does not change significantly upon the addition of salt to the aqueous phase. 79
Figure 4.8. Zeta potential of the 1.2 μm and 3 μm CML particles as a function of pH at 1 mM NaCl in the aqueous solution. The zeta potential gradually changes with the pH. The lines between the data points are only guides to the eye. 82
Figure 4.9. The estimated effect of the salt concentration on the CML particle contact angle based on the change of the electric double layer free energy. The calculations are based on the parameters of 1.2 μm CML particles. The value of the zeta potential is used here as a proxy for the respective surface electric potentials. The particle surface charge density is estimated from the value of the zeta potential, which is −36 mv for the particle at pH 5 and salt concentration of 1 mM (see Figure 4.8). 84

Figure 4.10. Optical photographs of emulsion made from 50 : 50 dodecane : water stabilised by 5 wt% CML particles in 1 mM NaCl immediately after emulsification. The emulsification was done by the hand–shaking method. Florescence and optical microscopy images of the particle–stabilised emulsions, where the aqueous phase was doped with fluorescein. The type of the emulsion changed from (w/o) water–in–oil emulsion to oil–in–water (o/w) emulsion not because of the different sizes of the particles but because of the decreasing area per COOH group on the particle surface which switches the nature of the particles from hydrophobic to hydrophilic. The scale bar is 200 μm for all images. 86
Figure 4.11. Schematic representation of the particles stabilise emulsion. the unsaturated surfaces of (A) two oil droplet with hydrophilic particles in water approaches to each other and form (B) a bridge particles stabilises the emulsion droplet. In the case of hydrophobic particles on surface of oil droplet the distance between the two droplets are close enough to rupture the file and cause coalescence. 87
Figure 5.1. Representation of the formation of a dry porous supra–particle from a drop of concentrated polystyrene latex suspension (15μl, 40 wt%) which was evaporated at 90 ^{o}C. The dry porous particles (2 mm) were partially fused at 106 ^{o}C to form stable porous supra–particles for our studies of porous particle adsorption at liquid surfaces. 90
Figure 5.2. Optical photograph showing supra–particles made from partially fused latex particles (2.6 μm in diameter) using a PDMS mould. The irregularity of the shape is due to loose packing and incomplete removal of the ethylene glycol. A and B were made by the injection of particles via calliper, while C and D were produced via syringe pump and E, via hand. 92
Figure 5.3. R 202 silica particle size in particle suspension, after using ultrasonic probe at 50% amplitude for 20 min, with pulse every 5 seconds for 2 seconds, for 5 % wt silica in ethanol. This suspension of hydrophobic silica particles (mean diameter 256 nm) was used in preparation of superhydrophobic surfaces for the drop evaporation technique. 94
Figure 5.4. Optical microscopy images for (A) plate–like (B) dimple. The scale bar is 1 mm. Particles have different structures due to the effect of the viscosity of the sulphate latex after evaporation at room temperature and the fact that they stick to the

hydrophobic surface. The structure is formed because of the high speed, at around 1000 rpm (A), and the low speed of 200 rpm (B). 95
Figure 5.5. Optical images of supra–particles formed by evaporation of sulphate latex suspension of various particle concentrations 8–70 wt% on a superhydrophobic surface at 90 ^{o}C. The latex suspension drop was rolled over the hot superhydrophobic surface until complete evaporation occurred. The scale bars for these particles are 0.50 mm in all images. 97
Figure 5.6. SEM images of the surface of supra–particles made from much smaller sulphate latex particles (2.6 μm in diameter) define the outer surface morphology of supra–particles at (A) 8.1 wt%, and (C) 40 wt%, and also show the inner structure at the edge of sectioned supra–particles for (B) 8 wt%, and (D) 40 wt% latex suspension, respectively. The supra–particles in (B) and (D) were sectioned to reveal the internal structure of the latex particle assembly near the supra–particle surface. The scale bar is 100 μm in all images. 98
Figure 5.7. SEM images of the surface of supra–particles made from (2.6 μm) sulphate latex particles. The SEM images show the outer surface morphology of the supra–particles prepared from (A) 50 wt%, and (C) 70 wt% latex suspension; and shows the inner structure at the edge of supra–particles for (B) 50 wt%, and (D) 70 wt% initial latex particle concentrations, respectively. The supra–particles in (B) and (D) were sectioned to reveal the internal structure of the latex particle assembly near the supra–particle surface. The scale bar is 100 μm in all images. 100
Figure 5.8. SEM images of the core of fragmented supra–particles made from 2.6 μm sulphate latex particles (A) 50 wt% and (B) 70 wt% initial latex concentration. These cavities appear only at the supra–particle core for particles formed from latex suspension above 50 wt%. The scale bar is 100 μm in all images. 101
Figure 5.9. SEM images of porous supra–particles made by evaporating drops of 50 wt% latex suspension on a hot superhydrophobic surface, heated at 60 °C (A and B), 80 °C (C and D) and 105 °C (E and F). Surface morphology (A, C and E), and the inner structure at the edge of fragmented supra–particles (B, D, and F) can also be seen. The scale bar in all images is 10 μm. 103
Figure 5.10. Illustration of the effect of temperature on the fusion of individual polystyrene latex particles inside a composite supra–particle: (A) schematics of the fusion of latex particles annealed at $T > T_{g;}$ (B) SEM image of supra–particle made from 40 wt% latex particle suspension annealed at 120 ^{o}C; (C) schematics of a supra–

particle annealed at the glass transition temperature (T_g) of polystyrene (106 ^oC); (D) SEM image of a fractured porous supra–particle made from 50 wt% particle suspension after annealing at T_g.....104
Figure 5.11. Optical microscopy images for melted (T>120 ^oC) particles prepared by injecting the building block particles into a PDMS mould. The scale bar is 500 µm. 105
Figure 5.12. Relation between the latex particles' initial concentration in w/w % and the volume fraction of sulphate latex particles in the supra–particle. The volume fraction of these particles increased with the increase in the particles' initial concentration and reduced the pores' fraction of the total particles. Above 50 wt%, the particles' volume fraction levelled off. 107
Figure 5.13. Supra–particles' packing density versus the initial volume of the latex suspension used for their prepration. This graph shows the importance of maintaining the same condtions for annealing all particles at the same time and the same set–up. 108
Figure 5.14. Fluorescence microscopy images of: (A) a porous supra–particle impregnated with 10^{-5} M Rhodamine 6G solution after 1 hour; (B) porous supra–particle impregnated with 10^{-5} M Rhodamine 6G overnight. The particles were fragmented after infusion with the liquid before being observed and imaged with a fluorescence microscope, with TRITC filter set. 109
Figure 5.15. Confocal fluorescence microscope image for a supra–particle immersed in water. The water interface was 10^{-5} M solution of Rhodamine 6G. The scales X, Y and Z are in mm, while the depth of the imaged aqueous layer within the supra–particle is about 0.1 mm, which shows that the laser has only reached this depth and cannot enable the complete mapping of the liquid in–situ in such large supra–particles....110
Figure 5.16. SEM images represent the infusion of an aqueous solution of silver nitrate inside the pores of a supra–particle; (A) is a SEM image of the supra–particle's outer surface, while (B) is a SEM image of the inner structure at the edge of a fractured supra–particle. The scale bar in both images is 10 µm. The particles have been removed from the solution and dried up before imaging. 111
Figure 6.1. Schematics illustrating a smooth spherical colloidal particle (a) approaching the oil–water interface from the oil phase; (b) attached at the oil–water interface; and (c) approaching the oil–water interface from the water phase.[175] 114

Figure 6.2. Variation of energy of attachment (ΔE_{attach}) of a colloidal particle of radius a = 10 nm from the water phase to a planar oil–water interface of interfacial tension γ_{ow} = 27 mN/m, at 298 K with contact angle θ.[134, 176] 116
Figure 6.3. Schematic representation of the process of adsorption of a colloidosome capsule whose shell is made of smaller colloid particles: adsorption of colloidosome from the water phase (a) to the oil–water interface (b); adsorption from the oil phase (c) to the oil–water interface (d). Note that the contact angle of a water–infused colloidosome adsorbed at the oil–water interface (a)–(b) is different from the contact angle of the same colloidosome infused initially with oil (c)–(d). The theoretical model assumes that the oil–water interface is attached only on the surface layer of colloid particles of the adsorbed colloidosome and does not penetrate through its membrane. 117
Figure 6.4. Schematic representation of the process of adsorption of a spherical composite supra–particle made of smaller colloid particles: adsorption of a supra–particle from the water phase (a) to the oil–water interface (b); adsorption from the oil phase (c) to the oil–water interface (d). Note that the contact angle of a water–infused supra–particle adsorbed at the oil–water interface (a)–(b) is different from the contact angle of the same supra–particle infused initially with oil (c)–(d). The theoretical model assumes that the oil–water interface is attached only on the surface layer of colloid particles of the adsorbed supra–particle. 119
Figure 6.5. Schematic of the attachment energy of porous supraparticles to an oil–water interface (A) from water phase to (B) oil–water interfaces and from (C) oil interface to (D) oil–water interface. 120
Figure 6.6. Theoretical dependence of the three–phase contact angle, θ, of a water–filled porous supra–particle (or a colloidosome) adsorbed at the oil–water interface and the three–phase contact angle of their "building block" colloid particles, θ_o. ..128
Figure 6.7. Dimensionless free energy of adsorption for a supra–particle impregnated by water from the water phase to the oil–water interface as a function of its macroscopic contact angle, θ (see Eq. (6.15)). The colloid particles on the supra–particle surface are arranged in hexagonal packing. The different lines correspond to selected values of the contact angle of building block colloid particles. The circular dots (•) represent the global minimum of the adsorption free surface energy of the porous supra–particle, with respect to its contact angle for a fixed value of the contact angle of the building block particles, θ_o. In this case, the macroscopic contact angle of

the supra–particle (or colloidosome), θ, is determined from Eq. (6.20) for the respective value of θ_o, which corresponds to the minimum of the free energy curve presented on this graph.....130
Figure 6.8. Dimensionless free energy of adsorption for a supra–particle impregnated with water from the water phase to the oil–water interface as a function of its macroscopic contact angle, θ (see Eq. (6.16)). The colloid particles on the supra–particle surface are arranged in square packing. The different lines correspond to selected values of the contact angle of building block colloid particles. The circular dots (•) represent the global minimum of the adsorption free surface energy of the porous supra–particle with respect to its contact angle for a fixed value of the contact angle of the building block particles, θ_o.....131
Figure 6.9. Dimensionless free energy of adsorption for a supra–particle impregnated with oil from the oil phase to the oil–water interface as a function of its macroscopic contact angle, θ (see Eq. (6.26)). The colloid particles on the supra–particle surface are arranged in hexagonal packing. The different lines correspond to selected values of the contact angle of building block colloid particles. The circular dots (•) represent the global minimum of the adsorption free surface energy of the porous supra–particle with respect to its contact angle for a fixed value of the contact angle of the building block particles, θ_o.....137
Figure 6.10. Dimensionless free energy of adsorption for a supra–particle impregnated with oil from the oil phase to the oil–water interface as a function of its macroscopic contact angle, θ (see Eq. (6.27)). The colloid particles on the supra–particle surface are arranged in square packing. The different lines correspond to selected values of the contact angle of building block colloid particles. The circular dots (•) represent the global minimum of the adsorption free surface energy of the porous supra–particle with respect to its contact angle for a fixed value of the contact angle of the building block particles, θ_o.....139
Figure 7.1. Schematic representation of the process of adsorption of a composite porous particle (supra–particle) and the building block particles: from the oil phase (A and C) to the oil-water interface (B and D) and from the water phase (E and G) to the oil-water interface (F and H). Similar considerations hold for the adsorption of the porous particle to the air-water interface in which the oil phase is formally replaced with air. 144

Figure 7.2. SEM micrograph of sulphate latex particles of an average diameter of 2.6 ± 0.1 μm imaged with a GTT for determining their three-phase contact angle θ_o at: (A) air-water interface, the particle suspensions dispersed in ethanol were injected from the air phase; (B) air-water interface, the particles were injected from the water phase; (C) hexadecane-water interface, particle suspensions dispersed in ethanol were injected from the hexadecane phase; and (D) hexadecane-water interface, particles were injected from the water phase. The value of θ_o was averaged out of 10 different particles protruding from the PDMS substrate obtained by templating the particles at the liquid interface. The scale bar is 1 μm on all images. The average area per sulphate group on the particles surface is 3.84 nm^2/SO_4, and the number of charged groups per particle is approximately 6×10^6. 146
Figure 7.3. Schematic representation of a water droplet attached to porous supra-particles at the oil-water interface. (A) The initial attachment of porous particles to a water droplet, (B) after pushing the porous particles into the water droplet and (C) the maximum attachment of porous particles to the water droplet. 149
Figure 7.4. Optical photograph of the porous supra-particles attached to an air bubble produced on the syringe needle of a DSA 10 setup. The porous particle was impregnated with water before being attached to the air-water surface. The porous supra-particles were produced by the evaporation method from 40 wt% latex suspensions.....151
Figure 7.5. Photograph of the porous supra-particles contact angle at (a, b, c and d) an air-water surface for dry porous supra-particles. 152
Figure 7.6. Contact angle of dry porous particles (2.2 mm) at the a/w interface as a function of the ratio between the radius of particles (R_p) and the radius of water as a fluid ($R_{droplet}$): (□) initial contact angles for a flat liquid surface (FCA), (○) initial contact angles for a curved liquid surface (CCA), (■) final contact angle for a flat liquid surface (FCA), (●) final contact angle for a curved liquid surface (CCA). The error bars denote the average of contact angle values for three-repeated calculations of the 2.2 mm particles at different stages using macro script in Image Pro Plus 6.....155
Figure 7.7. Average contact angle of dry, porous supra-particles adsorbed to a water droplet at an air-water interface as a function of the supra-particle diameter: (□) initial contact angle for a flat liquid surface (FCA), (○) initial contact angle for a curved liquid surface (CCA), (■) final contact angle for a flat liquid surface (FCA) and (●)

final contact angle for a curved liquid surface (CCA). The difference in the contact angle between the initial contact angle and the final contact angle is 60°. The error bars denote the average of contact angle values for three to five particles of the same diameter. 156
Figure 7.8. Contact angle of dry porous particles (1.7 mm) at an air-NaCl (aq) solution as a function of the ratio between the radius of the particles (R_p) and the curvature radius of the a/w water surface ($R_{droplet}$): (□) initial contact angles for a flat liquid surface (FCA), (○) initial contact angles for a curved liquid surface (CCA), (■) final contact angle for a flat liquid surface (FCA) and (●) final contact angle for a curved liquid surface (CCA). The error bars denote the average of contact angle values for three repeated calculations of the 1.7 mm particles at different stages using macro script in Image Pro Plus 6. 158
Figure 7.9. Average contact angle of three sizes of dry porous supra-particles adsorbed to a NaCl (aq) solution droplet in air versus the particle diameter: (□) initial contact angles for a flat liquid surface (FCA), (○) initial contact angles for a curved liquid surface (CCA), (■) the final contact angle for a flat liquid surface (FCA), (●) final contact angle for a curved liquid surface (CCA). The error bars denote the average of contact angle values for five particles of the same size. 160
Figure 7.10. Contact angle of water-filled porous particles (1.75 mm) at a/w depending on the ratio between the radius of particles (R_p) and the radius of the air bubble (R_{bubble}): (□) initial contact angle for a flat liquid surface (FCA), (○) initial contact angle for a curved liquid surface(CCA), (■) final contact angle for a flat liquid surface (FCA), (●) final contact angle for a curved liquid surface (CCA). The error bars denote the average of contact angle values for three repeated calculations of the 1.75 mm particles at different stages using macro script in Image Pro Plus 6. 162
Figure 7.11. Average contact angle of water-infused porous supra-particles adsorbed to a water droplet at an air-water interface versus the supra-particle diameter: (□) initial contact angles for a flat liquid surface (FCA), (○) initial contact angles for a curve liquid surface (CCA), (■) final contact angle for a flat liquid surface (FCA), (●) final contact angle for a curved liquid surface (CCA). 163
Figure 7.12. Contact angle of a dry porous particle (1.67 mm) attached to an air bubble in a NaCl (aq) solution as a function of the ratio of the particle radius (R_p) and the

bubble curvature radius (R_{bubble}): (□) initial contact angle for a flat liquid surface (FCA), (○) initial contact angle for a curved liquid surface(CCA), (■) final contact angle for a flat liquid surface (FCA), (●) final contact angle for a curved liquid surface (CCA). The error bars denote the average of contact angle values for three repeated calculations of the 1.67 mm particles at different stages using macro script in Image Pro Plus 6. 165
Figure 7.13. Average contact angle of water-infused porous supra-particles adsorbed to an air bubble in a 0.1 M NaCl(aq) solution: (□) initial contact angle for a flat liquid surface (FCA), (○) initial contact angle for a curved liquid surface(CCA), (■) final contact angle for a flat liquid surface (FCA), (●) final contact angle for a curve liquid surface (CCA). 166
Figure 7.14. Contact angle of water-infused porous supra-particles (of diameter 1.83 mm) attached to a hexadecane drop in water as a function of the ratio between the particle radius (R_p) and the radius of the hexadecane droplet ($R_{droplet}$). The particles were approached to the oil droplet from the aqueous phase: (□) initial contact angle for a flat liquid surface (FCA), (○) initial contact angle for a curved liquid surface (CCA), (■) final contact angle for a flat liquid surface (FCA), (●) final contact angle for a curved liquid surface (CCA).....168
Figure 7.15. Contact angle of porous supra-particles (1.83 mm in diameter, pre-filled with 0.1 M NaCl (aq) solution) at the hexadecane-NaCl (aq) solution interface as a function of the ratio between the particle radius (R_p) and the oil droplet radius ($R_{droplet}$): (□) initial contact angle for a flat liquid surface (FCA), (○) initial contact angle for a curved liquid surface (CCA), (■) final contact angle for a flat liquid surface (FCA), (●) final contact angle for a curved liquid surface (CCA). The error bars denote the average of contact angle values for three repeated calculations of the 1.83 mm particles at different stages using macro script in Image Pro Plus 6. 170
Figure 7.16. Average contact angle of porous supra-particles (infused with 0.1 M NaCl (aq) solution) adsorbed to the interface of hexadecane droplets in a NaCl(aq) solution. The particles were attached from the aqueous phase: (□) initial contact angle for a flat liquid surface (FCA), (○) initial contact angle for a curved liquid surface (CCA), (■) final contact angle for a flat liquid surface (FCA), (●) final contact angle for a curved liquid surface (CCA). 171

Figure 7.17. Contact angle of hexadecane pre-filled porous supra-particles (diameter of 1.83 mm) at the hexadecane-water interface as a function of the ratio of the particles (R_p) and the water drop radius ($R_{droplet}$): (□) initial contact angle for a flat liquid surface (FCA), (○) initial contact angle for a curved liquid surface (CCA), (■)final contact angle for a flat liquid surface (FCA), (●) final contact angle for a curved liquid surface (CCA). The error bars denote the average of contact angle values for three repeated calculations of the 1.83 mm particles at different stages using macro script in Image Pro Plus 6. 173
Figure 7.18. Average contact angle of hexadecane-infused porous supra-particles attached to a water droplet in water. The particles are approached to the oil-water interface through the oil-phase: (□) initial contact angle for a flat liquid surface (FCA), (○) initial contact angle for a curved liquid surface (CCA), (■) final contact angle for a flat liquid surface (FCA), (●) final contact angle for a curved liquid surface (CCA). 174
Figure 7.19. Contact angle of hexadecane-infused porous supra-particles (diameter of 1.83 mm) at the hexadecane-NaCl(aq) solution interface as a function of the ratio of the particle radius (R_p) and the aqueous drop radius ($R_{droplet}$): (□) initial contact angle for a flat liquid surface (FCA), (○) initial contact angle for a curved liquid surface (CCA), (■) final contact angle for a flat liquid surface (FCA), (●) final contact angle for a curved liquid surface (CCA). The error bars denote the average of contact angle values for three repeated calculations of the 1.7 mm particles at different stages using macro script in Image Pro Plus 6. 176
Figure 7.20. Average contact angle of hexadecane-infused porous supra-particles attached to a drop of a 0.1 M NaCl(aq) solution in hexadecane. The particle was approached to the liquid interface through the oil-phase: (□) initial contact angle for a flat liquid surface (FCA), (○) initial contact angle for a curve liquid surface (CCA), (■) final contact angle for a flat liquid surface (FCA), (●) final contact angle for a curved liquid surface (CCA). 177
Figure 7.21. Contact angle of dry porous particles at the a/w interface after applying ultrasonication at different amplitudes, which reflects the drift of the contact angle from the initial metastable state towards an equilibrium position. The contact angle is

reduced from a higher contact angle to the lowest possible after sonicating the system with the attached porous supra-particles. 180
Figure 7.22. Side images of initially dry porous particles attached to the air-water interface after ultrasonication at different amplitudes. The supra-particle diameter is 1.7 ± 0.2 mm. 181
Figure 7.23. Side camera images from DSA 10 for water-wet porous supra-particles adsorbed at the a/w interface for different durations of sonication in an ultrasonic bath after: (A) 3 min, (B) 6 min, (C) 9 min, (D) 15 min, (E) 20 min and (F) 30 min (floated). The particles were attached to the air-water interface after initial sucking and the subsequent insertion of water. The water sucking step corresponds to the a/w surface pressing the particles towards the bottom of the cuvette, while the water addition step lifts the particles and the a/w interface into a viewing position. 182
Figure 7.24. The supra-particle contact angle at the air-water interface as a function of the duration of sonication. The solid line corresponds to supra-particles treated using an ultrasonic bath and the dashed line using an ultrasonic probe as they were attached at the air-water interface..... 183
Figure 7.25. Side camera images from DSA 10 for water-wet supra-particles attached at the a/w interfaces for different sonication times in the ultrasonic bath after: (A) 3 min, (B) 6 min and (C) 9 min. The particles were initially attached at the a/w surface using a spatula. 184
Figure 7.26. Side camera images from DSA 10 for supra-particles (1.9 mm in diameter) attached at the a/w interface. The supra-particles were infused with 0.1 M NaCl and subjected to different durations of sonication by an ultrasonic probe (40 %, 2 second pulse) at the air-NaCl(aq) solution surface: (A) 3 min, (B) 6 min, (C) 9 min, (D) 15 min and (E) 20 min. 184
Figure 7.27. Porous supra-particles of diameters of 1.7 ± 0.2 mm initially impregnated with water and sonicated for different durations using an ultrasonic bath after being attached to the hexadecane-water interface. The number denotes the vibration time in minutes. The bubbles were observed due to the vibration generated by the ultrasound bath. 185
Figure 7.28. The three-phase contact angle of supra-particles with a diameter of 1.7 ± 0.2 mm pre-filled with water and attached to the hexadecane-water interfaces using a spatula. The particle contact angle is plotted versus the sonication time..... 186

Figure 7.29. The three-phase contact angle of supra-particles with the diameter of 1.7 ± 0.2 mm pre-filled with hexadecane and attached to the hexadecane-water interfaces using a spatula. The supra-particle contact angle is plotted versus the sonication time. The three graphs correspond to three different individual particles with several runs for each particle. The supra-particle contact angle reaches 70° and 110° after sonication. 188
Figure 7.30. Porous supra-particles (diameter of 1.7 mm) impregnated with hexadecane at the hexadecane-water interface. The contact angle quickly reached 80° and then levelled off further after sonication. 189
Figure 7.31. Side camera images from DSA 10 for oil-wet particles attached at the o/w interfaces at different sonication durations in ultrasonic bath time: 0–27 min. The number on the images corresponds to the sonication time in minutes. The oil is hexadecane. 189
Figure 7.32. MRI images of composite porous supra-particles made from 40% 2.6 μm sulphate latex particles suspension by the evaporation and thermal annealing method. The image shows the position of the air-water surface on the porous particle surface. (a) Air imbedded inside the particle pores, as the air shows a dark region; (b) water penetrated into the porous particles at the air-water surface is seen in grey colour. The particles show different resolutions when infused with water, as the interior of the particle becomes grey, the liquid water corresponds to white and the air is represented by a black colour. The scale bar in all images is 1 mm. 191
Figure 7.33. MRI images for particles pre-infused with water at (a) the air-water and (b) oil-water interface. In this image, the water contained gadolinium chloride (10^{-3} M) as a contrast agent, and the oil is hexadecane. The contrast agent increased the water brightness but turns the inside colour into black when added to the oil in (b). The scale bar in all images is 1 mm. 192
Figure 7.34. MRI images for particles filled with oil (hexadecane) at (a) air-oil and (b) oil-water interfaces. The imbibition of water is quite difficult to identify in these images, as the interior of the particle does not change much. The scale bar in all images is 1 mm. 192

List of tables

Table 2.1. Organic solvents used in the experiments. 30
Table 2.2. Properties of CML particles. 31
Table 4.1. Data for the CML particles of different sizes and the particle three–phase contact angles measured at the air–water and oil–water interfaces after injecting the particle through the water or oil phase. The contact angle values reported are an average of at least 10 measurements obtained from several SEM images of different particles, over at least two repeated samples. The error bars represent the standard deviation of the contact angle data. 72
Table 4.2. Contact angle of CML particles after placing the particles in the fridge at 4°C for 10–20 min. 78
Table 5.1. Mass density and porosity of porous supra–particles obtained by drying and annealing of latex particle suspension at various concentrations, 8–70 wt%. The annealing temperature was 106 ^{o}C for all particles. These supra–particles were measured, as described in 2.2.5.6. Here ϕ is the latex particle volume fraction in the supra–particle, calculated from the mass measurements. ρ_p is the supra–particle mass density. 106
Table 7.1. Contact angle of the sulphate latex particles measured at the air-water and oil-water interfaces and its theoretical relation (in Chapter 6) with the contact angles of porous supra-particles packed in hexagonal packing, θ_h and square packing and θ_s on the supra–particle surface. 147
Table 7.2. Measured contact angle of porous supra-particles pre-wetted with water at the hexadecane-water interface in two situations: (i) when the particles are only attached to the oil droplet and (ii) when they are inserted into the oil droplet, both from the aqueous phase. The contact angles were measured at two stages: when the oil droplet was flattened by withdrawing oil from the syringe (FCA) and also for oil droplets of a fixed curvature (CCA). 167
Table 7.3. Summary of the experimental values for porous supra-particles' contact angle impregnated with hexadecane or air at the hexadecane-water and the air-water interfaces related to the theoretical values predicted in Chapter 6. 178
Table 7.4. Summary of the experimental values for porous supra-particles contact angle impregnated with water at the hexadecane-water and the air-water interfaces related to the theoretical values predicted in Chapter 6. 178

Table 7.5. Summary of the experimental values for porous supra-particles' contact angle impregnated with air, water or hexadecane at the air-water and hexadecane-water interfaces related to the theoretical values predicted in Chapter 6. 190
Table 8.1. Experimental data for the contact angles of dry porous supra–particles adsorbed at the air–water interface. $H_{initial}$ is the initial particle protrusion. 203
Table 8.2. Summary of the contact angles of dry porous supra–particles adsorbed at the air–water interface (from the above table) compared to the theoretical model. 205
Table 8.3. Experimental data for the contact angles of dry porous supra–particles adsorbed at the air–water interface where the aqueous phase is 0.1 M NaCl solution. 206
Table 8.4. Summary of the the contact angles of dry porous supra–particles adsorbed at the air–water interface where the aqueous phase is 0.1 M NaCl solution (from the above table) compared to the theoretical model. 207
Table 8.5. Experimental data for the contact angles of water–infused porous supra–particles adsorbed at the air–water interface. 208
Table 8.6. Summary of the contact angles of water–infused porous supra–particles adsorbed at the air–water interface (from the above table) compared to the theoretical model. 209
Table 8.7. Experimental data for the contact angles of porous supra–particles infused with 0.1 M NaCl(aq) solution adsorbed at the air–NaCl(aq) solution interface. 210
Table 8.8. Summary of the contact angles of porous supra–particles infused with 0.1 M NaCl(aq) solution adsorbed at the air–NaCl(aq) solution interface (from the above table) compared to the theoretical model. 211
Table 8.9. Experimental data for the contact angles of water–infused porous supra–particles adsorbed at the hexadecane–water interface. 212
Table 8.10. Summary of the contact angles of water–infused porous supra–particles adsorbed at the hexadecane–water interface (from the above table) compared to the theoretical model. 212
Table 8.11. Experimental data for the contact angles of porous supra–particles infused with 0.1 M NaCl(aq), adsorbed at the hexadecane– NaCl (aq) interface. 213
Table 8.12. Summary of the contact angles of porous supra–particles infused with 0.1 M NaCl(aq), adsorbed at the hexadecane– NaCl (aq) interface (from the above table) compared to the theoretical model. 214

Table 8.13. Experimental data for the contact angles of hexadecane–infused porous supra–particles adsorbed at the hexadecane–water interface. 215
Table 8.14. Summary of the contact angles of hexadecane–infused porous supra–particles adsorbed at the hexadecane–water interface (from the above table) compared to the theoretical model. 216
Table 8.15. Experimental data for the contact angles of hexadecane infused porous supra–particles adsorbed at the hexadecane–NaCl(aq) solution interface 217
Table 8.16. Summary of the contact angles of hexadecane infused porous supra–particles adsorbed at the hexadecane–NaCl(aq) solution interface (from the above table) compared to the theoretical model. 218

List of abbreviations

S	Spreading coefficient
γ_{WA}	Specific surface energies (interfacial tensions) water–air interfaces
γ_{SW}	Specific surface energies (interfacial tensions) solid–water interfaces
γ_{SA}	Specific surface energies (interfacial tensions) solid–air interfaces
W_c	Work of cohesion
W_{ad}	Work of adhesion
q	Equilibrium contact angle
r	Roughness ratio
A	Actual liquid–solid area,
A_o	Apparent liquid–solid area
f_1	Area fractions of the liquid
f_2	Area fractions of the solid
θ_a	Apparent (macroscopic) contact angle
θ_{rec}	Receding contact angle
θ_{adv}	Advancing contact angle
$\Delta\theta$	Contact angle hysteresis
γ_{op}	Oil–particle interfacial energy
γ_{wp},	Water–particle interfacial energy
γ_{ow}	Oil–water interfacial tension
ΔE	Energy
kT	Thermal energy
PS	Polystyrene
r_2	Radius of the three phase contact line
$R_{2,}$	Radius of the particle
b_2	Depth of particle immersion in the lower phase
ψ_2	Meniscus angle
Cryo–SEM	Cryo–scanning electron microscopy
FCM	Film calliper method
FRESCA	Freeze fracture shadow casting
m_w	Is the monolith wet mass
m_d	The monolith dry mass
ρ	The water density
L	The cylindrical length
ϕ	The porosity of a cylindrical monolith
R	Radius monolith
fcc	Face–centred cubic
bcc	Body–centred cubic
hcp	Hexagonal packing
o/w	Oil–in–water
w/o	Water–in–oil
surfactants	Surface active agents
CML	Carboxylate–modified latex
rpm	Round per minutes
FITC	Fluorescein 5(6)–isothiocyanate
D	Particle diameter
d_c	The particle contact line diameter

DSA	Drop shape analysis
b	Particle protrusion through water
θ_{Flat}	Flat liquid surface contact angle (FCA)
θ_{Curv}	Curved liquid surface contact angle (CCA)
MRI	Magnetic resonance imaging
V_p	Porous supra–particle total volume
m_d	Porous supra–particle dry mass
m_w	M_w, is the porous supra–particle wet mass
ρ_{water}	Water density
ρ_{latex}	Latex density
ρ_p	Porous supra–particle density
ϕ	Latex volume fraction
MSME	Multi spin multi echo
ΔG_{el}	Gibbs free energy
σ_0	Surface charge density
e	Electronic charge,
N_A	Avogadro's number,
ε_o	Vacuum permittivity
ε	Dielectric constant of water
T	Absolute temperature
k	Boltzmann constant
Z	Valence of the electrolyte (Z:Z)
ψ_0	Surface electric potential
C_e	Electrolyte concentration
ψ_{aw}	Air–water surface potential
ψ_{pw}	CML particle surface potential is
γ_{aw}	Air–water surface tension
ΔG_{el} (ψ_{aw})	Surface free energies of formation of the electric double layers at the particle–water
ΔG_{el} (ψ_{pw})	Surface free energies of formation of the electric double layers at the air–water surface

Chapter 1: Introduction

1.1 Research objectives and thesis presentation

The wettability of powder particles by liquids has attracted a considerable amount of interest during the last few decades owing to its importance in the formulation of pharmaceutical, cosmetic, and food products; preparation of building materials and paints; waste water treatment; and secondary oil recovery.[1-5] In all these cases, small solid particles adsorb at or are transferred through the interface between a liquid phase and another fluid. The affinity of these particles to the adjacent fluid phases is characterised by the equilibrium three–phase contact angle, θ, which is related to the surface energies of the liquid–fluid interface and the particle–fluid interface exposed to the two fluid phases.

Many experimental and theoretical studies deal with spherical solid particles at air–water or oil–water interfaces in relation to their ability to stabilise foams and emulsions. However, a vast majority of products and formulations used in practice contain solid particles, which have anisotropic shapes, varying from needle–like microcrystals to particles with cubic symmetry as well as fibre–like particles with very large aspect ratios. In addition, many powder particles used in formulations are porous or agglomerated from smaller particle aggregates. The adsorption behaviours of such complex particles cannot be described only by the value of the three–phase contact angle since the particle shape and internal structuring can play an important role in their orientation at the liquid interface. The main objectives of the work presented in this thesis are (i) to investigate the attachment of a spherical and non–spherical particles at liquid interfaces, (ii) to develop theoretical approaches for the attachment energy and contact angles at liquid–fluid interfaces of colloidosomes and porous supra–particles assembled from small spherical particle building blocks, and (iii) to fabricate a model of porous supra–particles and investigate its wetting properties in relation to the contact angle of the building particles used.

This thesis consists of eight chapters. Chapter 1 introduces, summarises, and reviews the current scientific knowledge surrounding the wetting phenomena of macroscopic surfaces and colloidal particles as well as the fabrication of porous particles and emulsions. Chapter 2 describes the materials and methods used in this study.

Chapter 3 examines how different types of anisotropic particles attach and orientate at the air–water and oil–water interfaces following the use of a Gel Trapping Technique (GTT).

The GTT is used to study the behaviour and wettability of carboxylic modified latex (CML) particles with different sizes and carboxylic group (–COOH) densities at oil–water and air–water interfaces. The results are presented in Chapter 4.

The adsorption of aggregated porous particles at the liquid–fluid interface is common in emulsion fabrications. Chapter 5 describes the development of a new method for fabricating model porous supra–particles using small latex particles as building blocks. The porosity of these porous particles allows impregnation of different fluids inside the pores. This enables one to investigate the impact of the impregnated liquid on wetting behaviour. This behaviour will be introduced, both theoretically and experimentally, via a model designed in Chapter 5.

Chapter 6 will introduce a theoretical model for the attachment energy and contact angles of porous supra–particles or colloidosomes at fluid interfaces. Additionally, Chapter 6 will discuss the influence of impregnated fluid on the wetting behaviour of these porous particles. Different fluid will be used to impregnate the porous particles, so as to observe their effects on wetting behaviour. Air and hexadecane were uses as nonpolar phase, while mill–Q water and 0.1 M NaCl aqueous solution were used as polar phases. In Chapter 7, experimental results for the wettability of porous supra–particles at air–water and oil–water interfaces will be presented.

Lastly, in Chapter 8, a summary of the main findings and suggestions for future work will be presented.

1.2 Basic concepts in solid wetting

Wetting can be described as the interaction and behaviour occurring between fluid/solid and fluid/liquid interfaces. An interface is described as the boundary between two phases, e.g. solid–gas, solid–liquid, liquid–liquid, or liquid–gas. Molecules in the bulk of liquid have cohesion energies that are larger than those of molecules at the interface layer. Therefore, the molecules on the surface have greater energy than those in the bulk. The increase in the interfacial area leads to an increase in the free energy of the surface. Interfacial tension is the energy needed to create a unit surface area. It is usually measured in N/m or J/m^2 and frequently represented by

the symbol γ (or σ). There are a number of methods for measuring interfacial tensions of liquid–fluid interfaces, including the Wilhelmy plate, Du Nouy ring, pendant drop, drop volume, and sessile drop methods.[6-7]

The behaviour of a liquid in contact with a solid surface was first described by Thomas Young who introduced the concept of the contact angle.[8] When a liquid droplet is placed onto a solid surface, three scenarios can result: the droplet would partially spread over the solid surface attaining a dome shape (partial wetting), the droplet would spread over the surface completely forming a liquid film (complete wetting), or it would not wet the surface at all (complete dewetting), as illustrated Figure 1.1[1]. The contact angle, θ, is the angle measured between the tangent to the liquid vapour interface drawn at any point of the three–phase contact line and the solid surface (Figure 1.1A).[1]

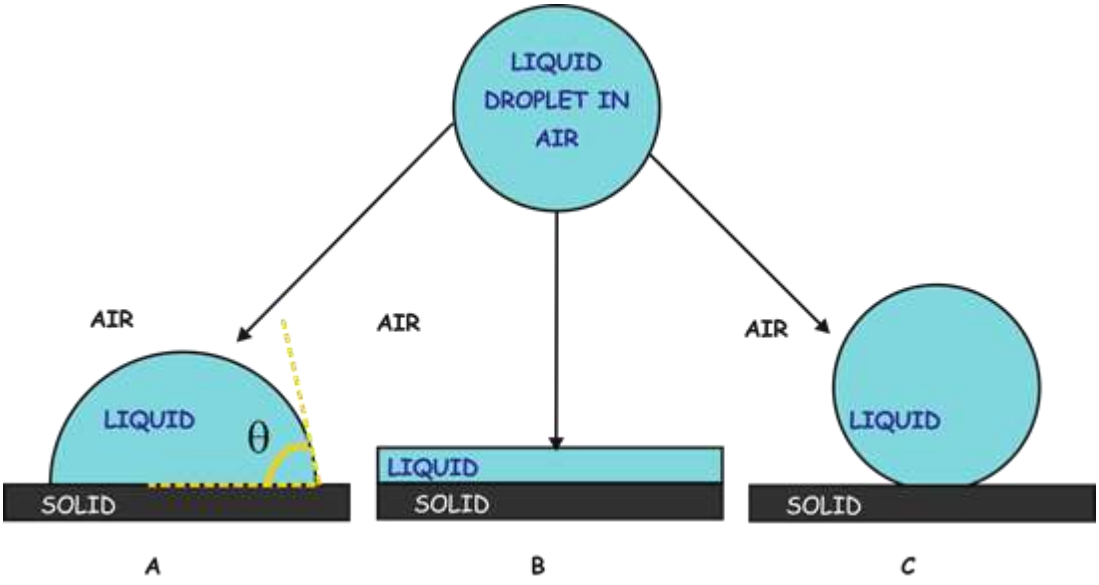

Figure 1.1. Liquid drop behaviour on a solid surface. (A) partial wetting, (B) complete wetting, and (C) complete dewetting.[1]

1.3 Spreading coefficient and works of adhesion and cohesion

A liquid in contact with a solid surface may partially wet the surface or spread across the surface to form a film. The spreading coefficient (S) measures the difference in the surface energy (per unit area) between a dry solid surface and a liquid film that totally spreads across the solid surface.[9]

$$S = \gamma_{SA} - (\gamma_{SW} + \gamma_{WA}) \tag{1.1}$$

Where γ_{SA}, γ_{SW}, and γ_{WA} are the specific surface energies (interfacial tensions) at the solid–air, solid–water, and water–air interfaces, respectively. If the spreading coefficient is positive (S > 0), the liquid droplet will spread completely (θ = 0°) to lower the surface energy. If the spreading coefficient is negative (S < 0), the liquid droplet will partially wet the surface, forming a droplet with a finite equilibrium contact angle θ > 0°.[1, 9]

The behaviour of a liquid drop (i.e. water) on a solid surface can be better understood by considering the works of cohesion and adhesion which are related to interfacial energies.

$$W_c = 2\gamma_{WA} \tag{1.2}$$

$$W_{ad} = \gamma_{WA} + \gamma_{SA} - \gamma_{WS} \tag{1.3}$$

In the case of a homogenous phase separated into two halves, the work of cohesion (W_c) is defined by eq. (**1.2**). In the case of two dissimilar phases separated at a distance beyond the range of interaction forces between newly created surfaces, the work of adhesion (W_{ad}) is defined by eq. (**1.3**). These concepts are illustrated in Figure 1.2.[9-10]

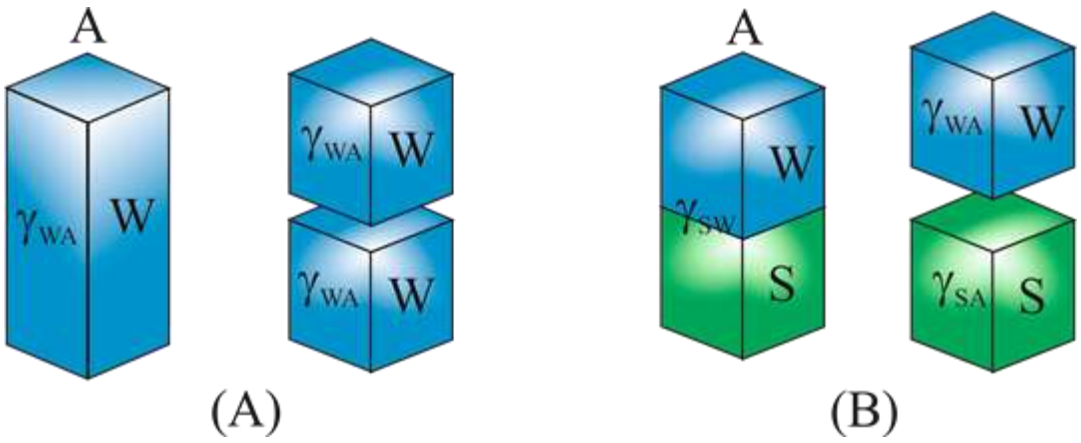

Figure 1.2. A diagram illustrating (A) the work of cohesion, which is the energy required to reversibly split a column of a pure liquid (water), W, thus forming two water–air, WA, interfaces with surface tension and unit areas; and (B) the work of adhesion, which is the energy required to separate reversibly a liquid in contact with

solid, S, by forming solid–air, SA, and liquid–vapour surfaces with unit areas and the respective interfacial tensions.

Works of adhesion and cohesion are related to the contact angle, as follows:

$$\cos\ \theta = 2\left(\frac{W_{ad}}{W_c}\right) - 1 \qquad (1.4)$$

Equation (**1.4**) suggests that the contact angle is controlled by the cohesion between liquid droplets and the adhesion between the solid surface and the liquid droplet, as illustrated in Figure 1.1 above. If the work of cohesion equals the work of adhesion, the contact angle is equal to 0° and the liquid spreads over the solid. This corresponds to complete wetting (Figure 1.1 B). If the work of adhesion is equal to zero, the contact angle should be equal to 180° (complete dewetting, Figure 1.1 C). In all other cases, when the work of adhesion is smaller than the work of cohesion, the contact angle value is between 0° and 180° (partial wetting, Figure 1.1 A).[10]

1.4 Wetting of ideal solid surfaces and the Young equation

An ideal solid surface can be defined as a smooth, rigid, non–reactive, isotropic, chemically and physically homogeneous, insoluble, and non–deformable surface. As first suggested by Young,[8] the equilibrium contact angle, θ, of a liquid droplet on such a surface can be linked to the interfacial tensions (specific surface energies) of the three phases in contact (solid, water, and air) by considering the balance of interfacial tensions at the three–phase contact line (Figure 1.3).[8, 11]

$$\cos\ \theta = \frac{\gamma_{SA} - \gamma_{SW}}{\gamma_{WA}} \qquad (1.5)$$

Equation (**1.5**) is known as the Young equation, where γ_{SA}, γ_{SW}, and γ_{WA} are the interfacial tensions of the solid–air, solid–water, and water–air interfaces, respectively, and θ is the equilibrium contact angle measured through the polar phase (water).[12-14]

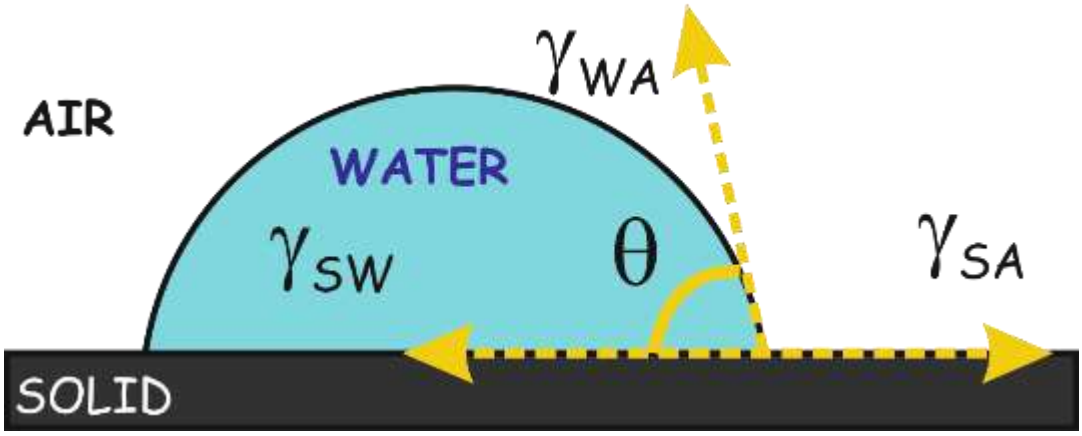

Figure 1.3. Schematic of a water droplet (cross–section) resting at equilibrium on an ideal smooth solid surface in air.

The solid–air and solid–water interfacial tensions cannot be easily measured experimentally, while the air–water interfacial tension γ_{WA} can be easily determined by a variety of methods.[5] The degree of wetting is indicated and characterised by the contact angle. For example, surfaces with contact angles lower than 90° are considered hydrophilic and wettable by water. In contrast, surfaces with contact angles larger than 90° are classified as hydrophobic. Surfaces with contact angles larger than 150° are called superhydrophobic surfaces.[15]

1.5 Wetting of rough surfaces

Many studies on the wettability of droplets on rough surfaces show that wettability is affected by the surface roughness of a solid substrate. Two models for wetting of rough solid surfaces have been proposed.

1.5.1 The Wenzel model

The Wenzel model assumes that the liquid fills the surface depressions created by the roughness (Figure 1.4), thus increasing the liquid–solid area of contact in comparison to a smooth surface of the same material. The roughness ratio (r) is defined as the ratio of the actual liquid–solid area, A, to the apparent liquid–solid area (the projection in the plane of the solid surface), A_o.[16]

$$r = \frac{A}{A_o} \geq 1 \tag{1.6}$$

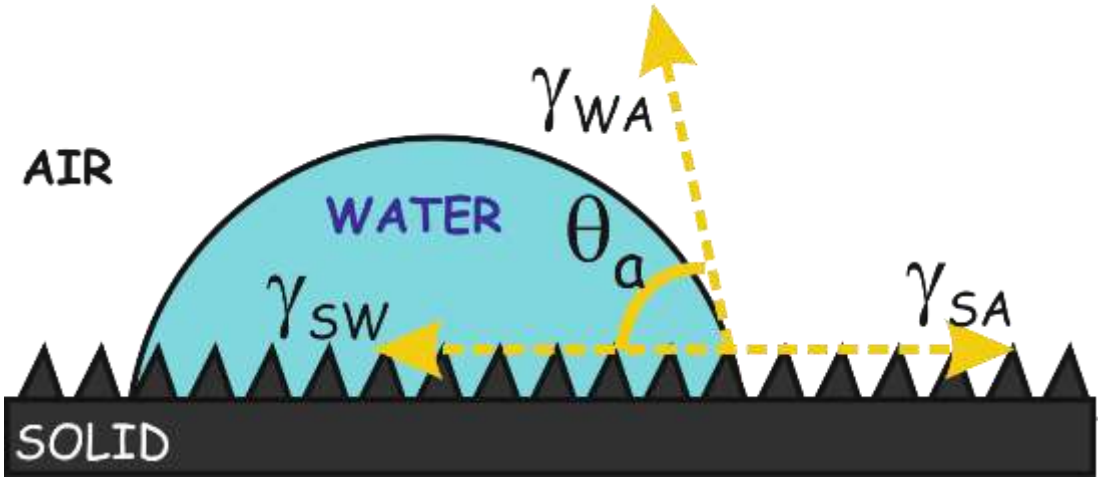

Figure 1.4. A diagram illustrating the Wenzel model for the apparent contact angle of a water droplet on a rough surface. The surface roughness is exaggerated.

Therefore, for a rough surface, the minimum free energy state is given by the apparent contact angle (θ_a) rather than Young's contact angle (θ) owing to the increased liquid–solid interfacial area.[17]

$$\cos\ \theta_a = r\ \cos\ \theta \tag{1.7}$$

Hence, the Young equation for a rough surface should be corrected to read[17-19]

$$\cos\ \theta_a = \frac{r\,(\gamma_{SA} - \gamma_{SW})}{\gamma_{WA}} \tag{1.8}$$

When $\theta < 90°$, the effect of roughness is to reduce the apparent contact angle towards 0°, but when $\theta > 90°$, the roughness will lead to an increase in the apparent contact angle towards 180°. Therefore, the roughness factor magnifies the tendency of a surface towards complete wetting or complete non–wetting.[17-18, 20]

1.5.2 The Cassie and Baxter model for heterogeneous wetting

This model of wetting deals with droplets on surfaces that are smooth but chemically heterogeneous, i.e. the surface consists of two types of microscopic regions with Young's contact angles θ_1 and θ_2, respectively. The apparent contact angle in the considered case can be written as:

$$\cos\ \theta_a = f_1 \cos\ \theta_1 + f_2 \cos\ \theta_2 \qquad (1.9)$$

Where f_1 and f_2 are the area fractions of the respective regions of the liquid–solid interface. For a porous surface in air, assuming complete dewetting for the water–air interface (i.e. $\theta_2 = 180°$) eq. 1.9 is reduced to

$$\cos\ \theta_a = f_1 \cos\ \theta_1 - f_2 \qquad (1.10)$$

Where θ_a is the apparent (macroscopic) contact angle on the composite solid surface. For very rough (porous) surfaces of hydrophobic material (i.e. $\theta_1 > 90°$), the liquid–solid fraction f_1 is much smaller than the liquid–air fraction f_2, and the apparent contact angle could be significantly larger than 90° (Figure 1.5).

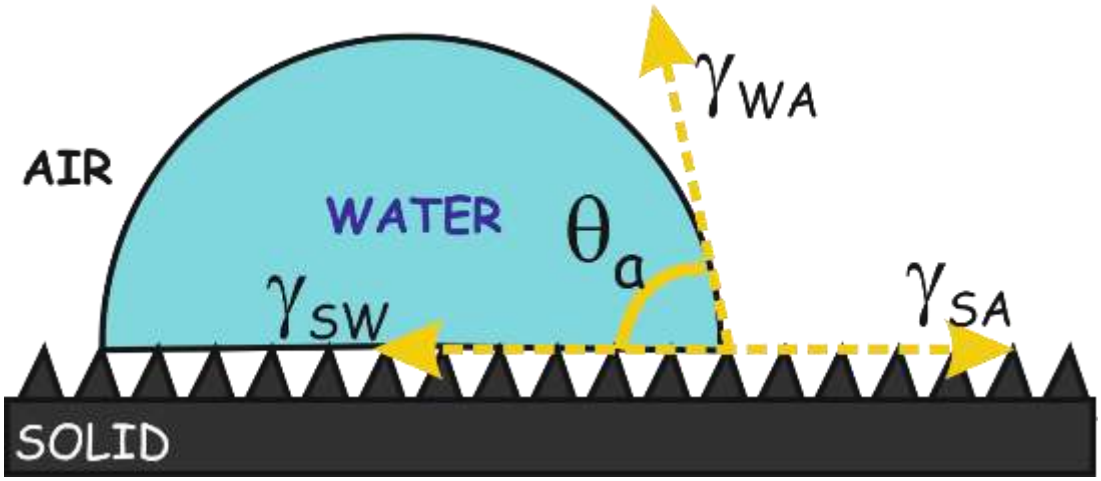

Figure 1.5. Cassie–Baxter model for apparent contact angle of a droplet on a rough surface of hydrophobic material.

1.6 Contact angle hysteresis

As described above, Young's equation explains the contact angle of water droplets on ideal surfaces, but the macroscopic (apparent) contact angle on non–ideal surfaces could be affected by roughness and heterogeneity. The latter factors prevent the free movement of the three–phase contact line by pinning; hence, the contact angle may deviate from its equilibrium value. This can be observed by tilting the solid surface with a droplet on it (Figure 1.6). The contact angle at the upper end of the droplet, θ_{rec}, is smaller than that on its lower end, θ_{adv}, just before the droplet starts sliding on the

surface. θ_{rec} is called as the receding contact angle, while θ_{adv} is called as the advancing contact angle. On a horizontal solid surface (Figure 1.6b), changing the

$$\Delta\theta = \theta_{adv} - \theta_{rec} \tag{1.11}$$

droplet size by increasing the drop volume will result in an increase in the contact angle to the maximum value, θ_{adv}, just before the three–phase contact line expands (advances) over the surface. Similarly, reducing the droplet volume would lead to a decrease in the contact angle to its minimum value, θ_{rec}, corresponding to the receding contact angle just before the three–phase contact line shrinks (recedes) over the solid surface. The difference between advancing contact angle and receding contact angle is called as contact angle hysteresis, $\Delta\theta$ (eq. 1.11).

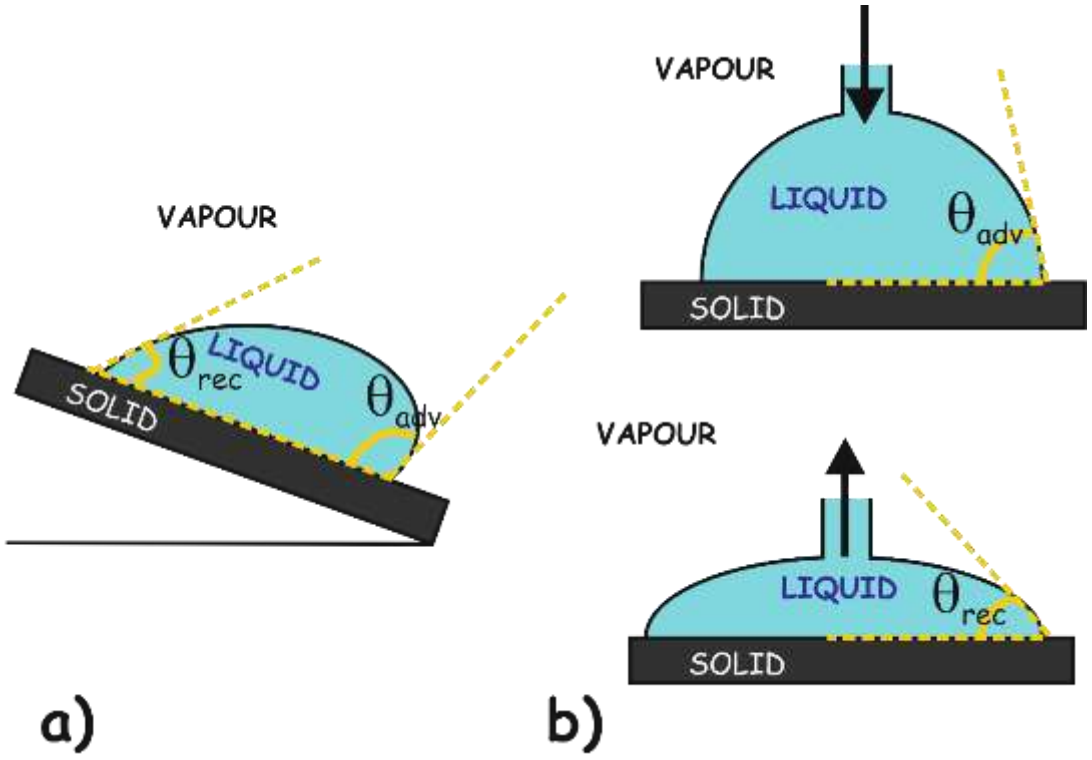

Figure 1.6. (a) Illustration of the advancing and receding contact angles of a droplet on a tilted solid surface[21] and (b) adding an amount of liquid results in advancing and reducing an amount of liquid results in receding of the contact angle.[22]

1.7 Particle contact angles and energies at liquid interfaces

The wettability of particles by a fluid phase has attracted considerable interest during the last two decades owing to its important application in different areas of life, such as pharmaceutical products, cosmetics, food, water treatments, building materials, paint, and secondary oil recovery.[4] Particle wettability, quantified by the three–phase contact angle, θ, is very important for many practical applications. Knowledge of particle contact angle is a requirement for characterising and understanding the interaction and behaviour of solid particles at liquid interfaces.[19]

When a small spherical solid particle is attached to a planar fluid–water interface, the contact angle is measured between the tangent to the particle surface at any point of the three–phase contact line and the flat liquid surface through the water (Figure 1.7). For a spherical particle at the oil–water interface, the Young equation reads as follows:

$$\gamma_{\mathrm{op}} = \gamma_{wp} + \gamma_{ow}\cos\theta \tag{1.12}$$

Here, γ_{op} is the oil–particle interfacial energy, γ_{wp} is the water–particle interfacial energy, γ_{ow} is the oil–water interfacial tension, and θ is the equilibrium contact angle.[7, 18] The particle position with respect to the flat liquid interface depends on the particle contact angle (Figure 1.7). Pieranski[23] pointed out that the interfacial particles are trapped at the liquid interface with energies much larger than the thermal energy. The energy, ΔE, required to detach a spherical particle with radius, R, from the oil–water interface into a bulk liquid depends on the particle contact angle according the equation[24-25]

$$\Delta E = \pi R^2 \gamma_{ow}(1 \pm \cos\theta)^2 \tag{1.13}$$

Where γ_{ow} is the water–oil interfacial tension and θ is the particle contact angle. The positive sign refers to the detachment of particles in oil, while the negative sign refers to the detachment of particles in water. ΔE is the maximum at θ = 90° and even for small particles, it can be much larger than the thermal energy (kT) as illustrated in Figure 1.7b. This also suggests that although the colloidal particles are not amphiphilic, they are surface active and can spontaneously assemble at the air–water or oil–water interface to reduce the interfacial energy of the system.

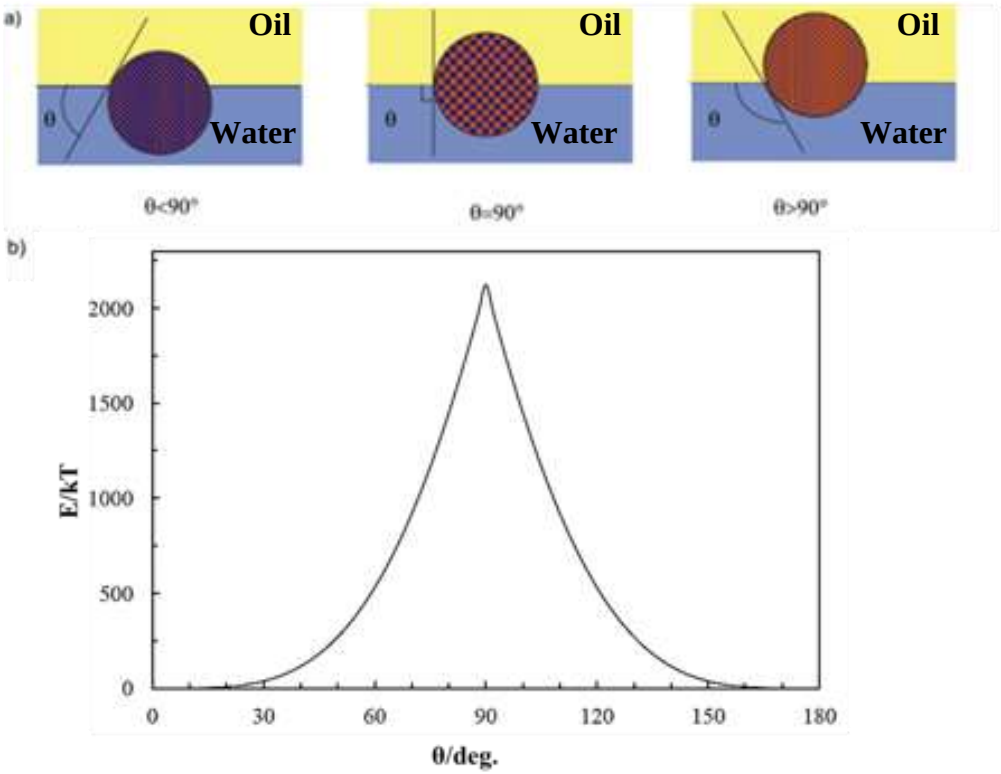

Figure 1.7. (a) Diagrams showing the position of spherical particles with different contact angles, θ, at the oil–water interface. (b) The energy required to remove a spherical particle with radius 10 nm from a liquid interfaces with interfacial tension 27 mN/m at 298 K into a bulk liquid as a function of the particle contact angle (adapted from[26] and[27]).

When particles are smaller than ~10 μm in diameter, the deformations of the liquid interface, due to gravity, can be neglected, and the liquid interface can be considered as flat up to the particle's surface. However, for larger particles, the force of gravity becomes important [24, 28-30] and could generate significant deformations in the liquid interface in the vicinity of the particle (Figure 1.8) that cause detachment and a non–equilibrium position. Extrand et al found that the surface tension of water can suspend large particles (up to 10 mm) at the air–water interface.[31]. The surface deformation is highly dependent on the wettability of the particle's surface. The more hydrophobic the surface of the particle, the more stably it attaches to the interface.[32] Liu et al.[33] studied the effect of different forces (surface tension, buoyancy and gravity), when varying the diameter of a hydrophobic glass sphere, and made visual observations of the floating behaviour[34]. They found that the gravity force was small when the surface tension force played a more important role than the buoyancy force; however, when

the particles were big enough, the buoyancy force contributed more, which balanced the weight. In the same study, the hydrophilic particles of 1–4 mm could neither float either in air–water nor air–NaCl interfaces. Once these particles were etched (i.e. rough surface), they became hydrophobic and floated on the surface of either the water or the NaCl solution[33]. The more hydrophobic the surface of the particle, the more stably it attached to the interface [35]. Danov et al. [36]. studied the interfacial deformation around spherical particles of 4–6 mm at the air–water and oil–water interface. The effect of gravity's force on the particle's deformation was found at around $\psi 2 = 0.7^{o}$. For the sake of simplicity, the influence of those forces on the millimetre size's porous particles adsorbed to liquid interfaces were neglected in Chapters 6 and 7.[31]

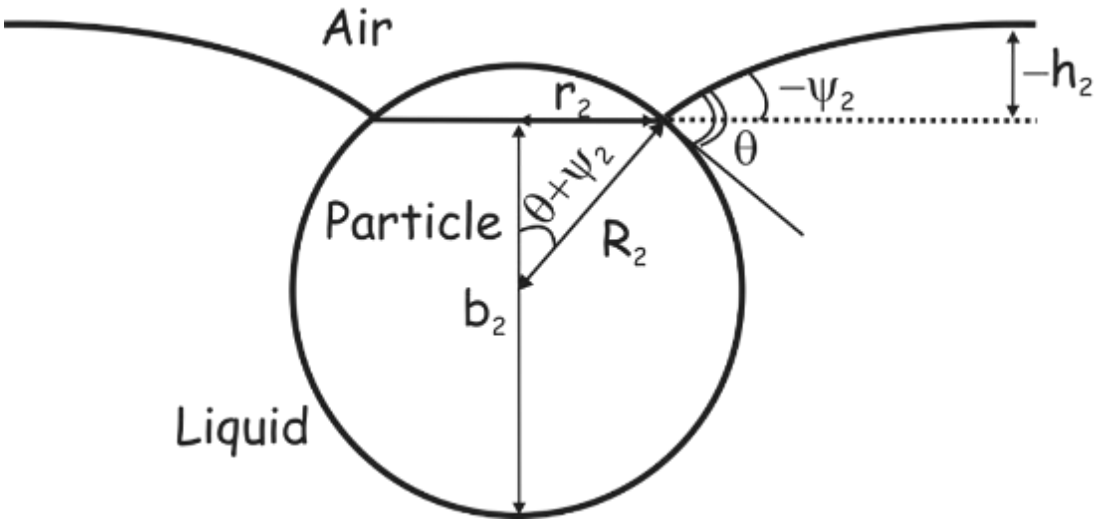

Figure 1.8. A diagram showing a large dense spherical particle attached to a liquid interface.[37]

The orientation and equilibrium position of anisotropic particles at liquid interfaces have been studied for different shapes. These studies assumed that anisotropic particles are adsorbed at the planar liquid interface. The orientation of an individual ellipsoidal or cylindrical particle can be perpendicular or parallel to the interface, which depends on the energy barriers to reorientation. For instance, the cylinder particles that adsorbed to the liquid interface achieved minimum energy when the

particles were parallel to the interface. Figures 1.9 show the equilibrium values.[38-41]

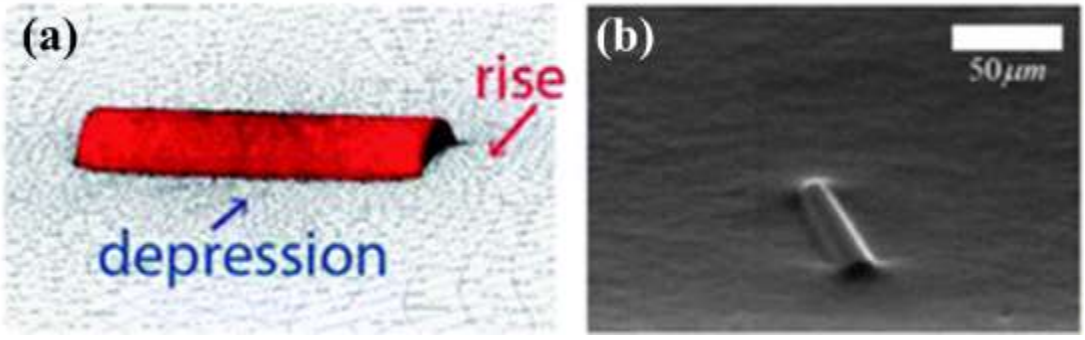

Figure 1.9. Individual cylindrical particle adsorbed at planar air–water interface. (a) Simulated shape with contact angle θ = 80 ± 2° and (b) SEM image of SU–8 cylinder at air–water interface [38, 40].

1.8 Methods for measuring particle contact angles

1.8.1 Methods using multiple particles (integral methods)

There are a number of experimental methods for measuring the contact angle of particles at liquid interfaces. Some of these methods are limited for measuring the air–water interface, as it is difficult to measure the contact angle on oil–water surfaces.

1.8.1.1 *Compact powder method*

This method is adapted from the contact angle measurement of a liquid droplet on solid, flat surfaces. The powdered particles are first compacted into a tablet, and the contact angle of a liquid droplet placed on the tablet is then measured by taking a side image. Although this method is simple, it has serious disadvantages related to the penetration of the liquid into the pores of the tablet and to the surface roughness. The latter will affect the apparent contact angle which could be significantly different from the actual particle contact angle.[42-43]

1.8.1.2 *Washburn method*

The Washburn method (capillary rise wetting method) relies on determining the rate of liquid penetration into a packed powder bed. It is generally used when a large amount of solid particles are available for preparation of a powder bed.[4, 42, 44-45] The sample is loaded into a cylindrical tube whose base has cavities at the bottom to support the particles while allowing the liquid to penetrate (Figure **1.10**).[46-47] The test

liquid is raised to touch the tip of the cylindrical tube that is attached to an electronic balance. When the liquid starts to penetrate into the compact powder sample, the change in the mass of the tube with time enables calculation of the contact angle depending on the rate of penetration. This method depends on several factors that affect the validity and determination of the contact angle. These factors include the liquid's viscosity, uniformity of the powder shape, amount of powder, reproducibility of packing, and the reference wetting liquid. Regardless of all of these disadvantages, the Washburn method is used widely because it is automated, fast, economical, and easy to use.[46-48]

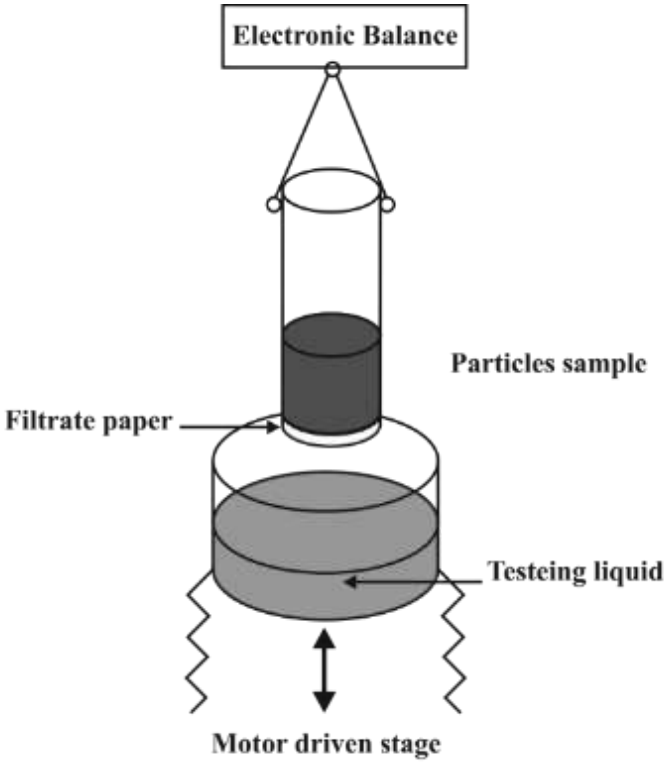

Figure 1.10. Illustrative view of the capillary rise wetting method.[47, 49]

1.8.1.3 *Wicking method*

This method is similar to the Washburn method but requires a much smaller amount of particles. The particles are first dispersed in a liquid and then spread to form a film onto the surface of a solid plate. After the evaporation of the liquid film, the end of the powder–coated plate is immersed into the test liquid. Then, the contact angle is calculated from the recorded rate of the liquid front penetration through the powder coating.[42]

1.8.1.4 *Pressure compensation method*

Most of the methods described above are not suitable for measuring hydrophobic particles with contact angles of $\theta \geq 90°$. This drawback is addressed by the pressure compensation method proposed by Bartell et al. and is based on the evacuation of air from the packed powder by liquid. The displacement (capillary) pressure is used to determine the contact angle based on the adhesion tension between the liquid and solid. This capillary pressure is equal to the Laplace pressure.[42, 50] Advancing and receding contact angles can be determined from the difference between the initial pressure and the final pressure.[51]

1.8.2 Methods for measuring contact angles of individual particles

For large solid particles, the contact angle can be determined by taking side images of an individual particle attached to the liquid interface. For example, Velev et al.[37] measured the contact angle, θ, of spherical copper beads of millimetre size (Figure 1.8) attached to a fluid interface. In their calculation, they assumed that the interfacial tension and densities of the particle and the two fluid phases are known. From the side photos, they were able to determine the radius of the three–phase contact line, r_2, the radius of the particle, R_2, and the depth of particle immersion in the lower phase, b_2. From the values of R_2 and r_2, they calculated the contact angle and the meniscus angle (ψ_2). This method can be used for measuring three–phase contact angles of sub–millimetre and millimetre size particles.[37, 52-53]

$$\theta = \arcsin\left(\frac{r_2}{R_2}\right) - \psi_2 \qquad (1.14)$$

It is challenging to determine the contact angle of individual micron and submicron particles at a liquid interface. Several methods have been proposed recently using X–ray microscopy,[54] cryo–scanning electron microscopy (cryo–SEM),[25] the film calliper method (FCM),[19] and the gel–trapping technique (GTT).[4, 55] Some of these are briefly described below.

1.8.2.1 *The Gel Trapping Technique*

Paunov[4] developed a method that can be used to measure the contact angles of micron or sub–micron particles, known as the Gel Trapping Technique (GTT), using scanning

electron microscopy (SEM). The GTT uses a hot aqueous solution of a non–adsorbing gelling agent (gellan gum) as a sub–phase. The gellan gum[56] is not surface active hydrocolloid polymer which mean they do not adsorb to the particles–water and fluid–liquid interfaces the reasons behind that is the double helix formation upon cooling.[4, 57-58] In the case of the air–water interface, the particles dispersed in a spreading solvent (e.g. isopropyl alcohol) are injected at the surface of the hot gellan solution at 50–55°C in a Petri dish (Figure **1.11**, A). Then, the system is cooled down to room temperature in the sealed Petri dish for 30 min to set the gel. For the oil–water interface, the oil (e.g. decane) pre–warmed at 50°C is poured on top of the hot gellan; then, the particles are spread at the oil–water interface as shown in Figure **1.11**, B. Once the gellan solution is gelled, the oil is removed and a layer of polydimethylsiloxane (PDMS) mixed with a curing agent is placed on top of the gel. [59]

After two days of curing at room temperature, the PDMS elastomer with partially embedded interfacial particles is removed by peeling off from the aqueous gel. The PDMS–particles sample is treated with hot deionised water and a 10 mM solution of EDTA disodium salt to remove any gel remaining at the PDMS surface.[4] Finally, the PDMS mould with the partially embedded particles is coated with a thin layer of carbon and imaged by SEM. The particles' contact angle is determined by circle fitting the particle profile (Figure **1.11** C and D). [4] The method was further developed by using AFM[55] to find the wettability of nano–sized particles as small as 37 nm at oil–water and air–water interfaces.[24, 55, 60-61]

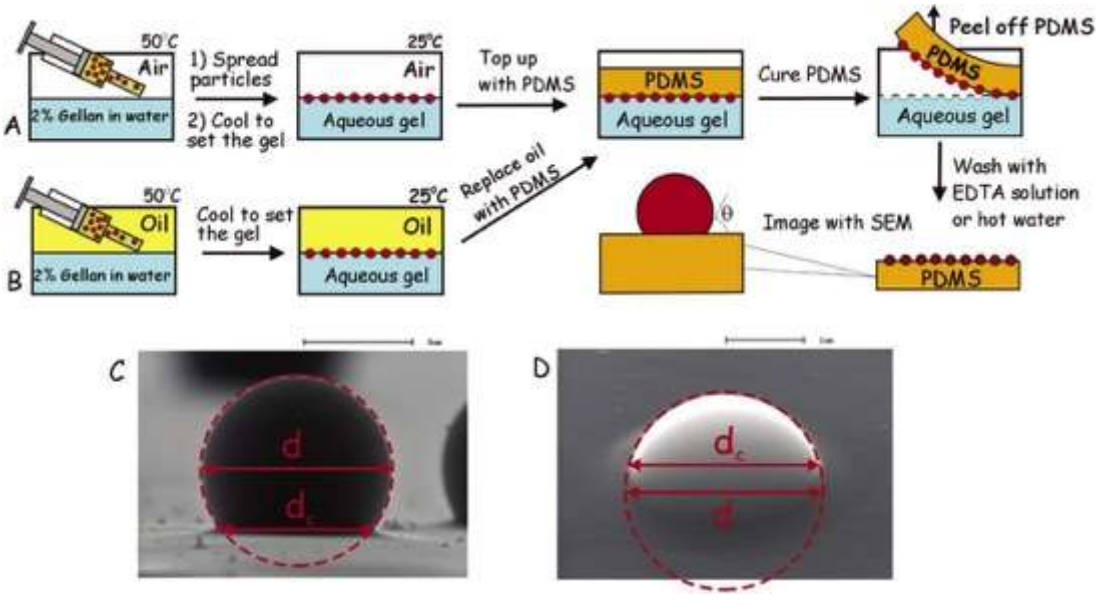

Figure 1.11. Schematic diagram of sample preparation for measuring the contact angle of particles at (A) air–water and (B) oil–water interfaces. The equatorial particle diameter, d, can be determined directly (C) or after profiling the particle with a circle (D). The GTT method is used with SEM or AFM.[4, 55, 59]

Maestro et al.[24] investigated the effect of the spreading solvent by determining the contact angle of different types of particles at air (oil)–water interfaces. They found that different surface activities of methanol and isopropanol did not change the surface tension when adding the same amount alcohols and particle suspension to the air (oil)–water interface.[24] This method was used to measure the contact angle of spherical[62] and anisotropic particles[63] (see Chapters 3 and 4).

1.8.2.2 *The Film–Calliper Method*

Contact angles of micrometre and sub–micrometre particles at an air–water interface have been measured by a new method called the Film Calliper Method (FCM) recently developed by Horozov.[19, 64-65] This method requires the particles to be attached simultaneously to both surfaces of the liquid film, thus forming a particle bridge. The particles are injected and spread at a horizontal water–air interface to create a dilute monolayer. Then, the liquid interface is crossed by a glass ring connected to a syringe. This creates a thick liquid film inside the ring. The film thickness can be controlled by using the syringe. Pumping the liquid into the circular frame (the ring) gives a thicker film, while sucking it out makes the film thinner. When the liquid is rapidly sucked out, some particles become attached to both film surfaces, thus bridging them. The liquid film is observed with a horizontal microscope in reflected monochromatic light.[19, 64-65]

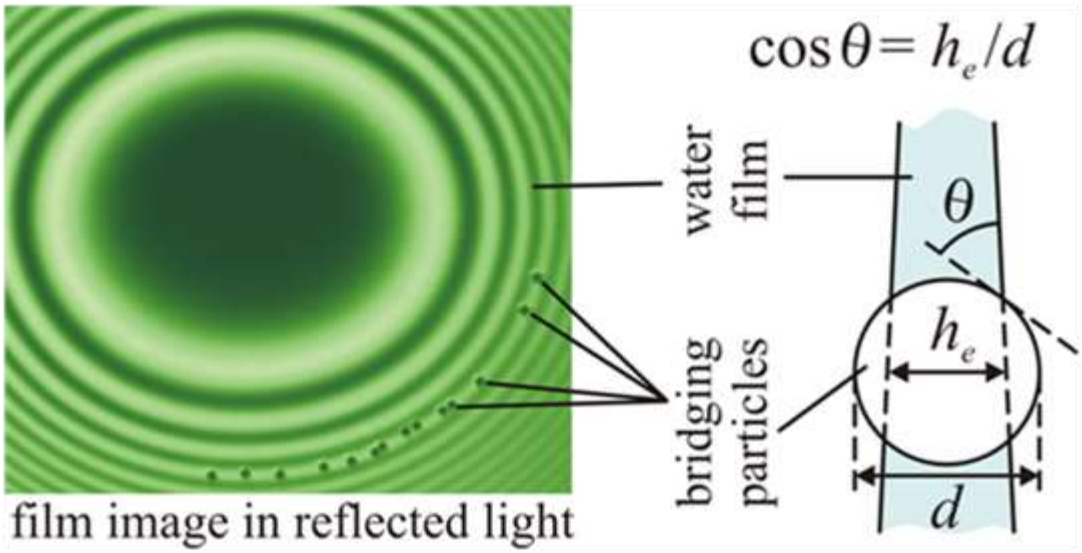

Figure 1.12. Illustration of the contact angle measurements using the film calliper method. The image on the left shows interference fringes of a water film in air with 2 μm bridging particles in the film meniscus.[19]

The interference pattern and particles are clearly seen in the images (Fig. 1.11). The bridging particles move into the thicker part of the meniscus to diminish the deformations of the liquid interface.

$$\cos\theta = \frac{h_e}{d} \qquad (1.15)$$

The equilibrium position of particles in the meniscus is established at a certain radial distance from the centre of the film (Figure **1.13**, bottom).

The film thickness is determined from the interference pattern; consequently, the contact angle can be calculated from the film thickness (h_e) and the particle diameter (d) using equation 1.15.[19] This method is simple and makes it possible to measure the contact angles of micron and sub–micron particles in real time if the particles attached simultaneously to the film surfaces form stable particle bridges. It is also necessary to know the particle diameter.[19, 65] FCM and the GTT have been used to measure the wetting of hydrophilic latex particles with polymers grafted onto their surface.[66]

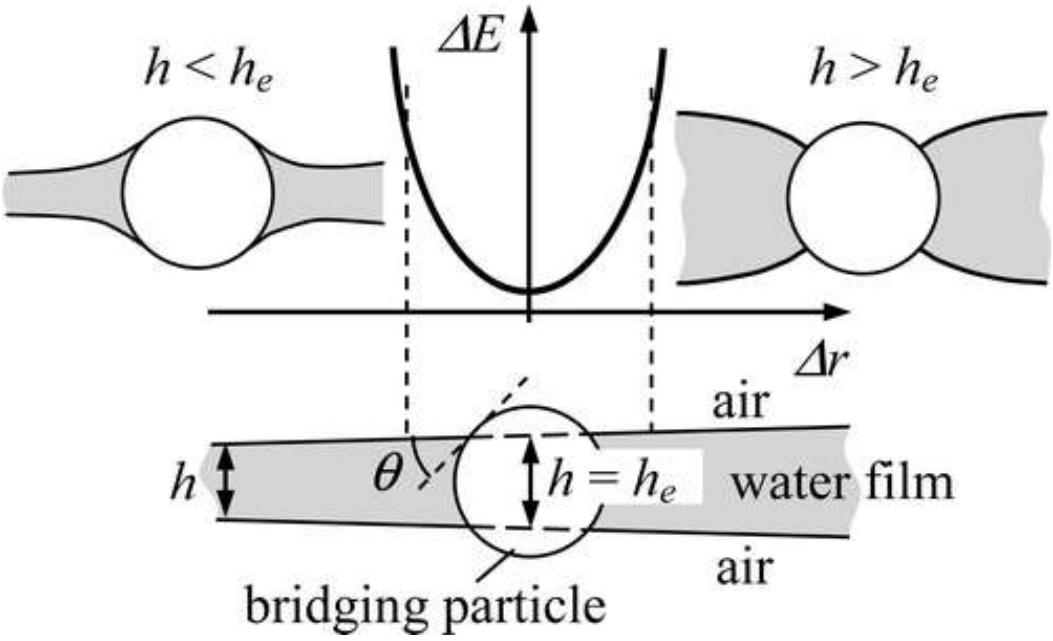

Figure 1.13. A sketch of the bridging particles in the air–water interface for particle movements in thicker or thinner liquid interfaces. [19]

1.8.2.3 *The freeze fracture shadow casting (FRESCA) method*

Isa et al.[25] presented an *in–situ* method for determining the single particle contact angle using cryo–scanning electron microscopy (cryo–SEM) conjugated with freeze–fracture and shadow–casting. Using this method, the contact angles of particles of different sizes (down to 10 nm) and types (organic, inorganic, hydrophilic and hydrophobic) have been measured with high accuracy. The contact angle has been determined when the particle monolayer at the liquid interface is frozen and then cracked and coated with metal, creating a shadow just behind the particles at the solidified liquid interface (Figure **1.14**). The advantage of this method is its high accuracy owing to the large number of measurements.

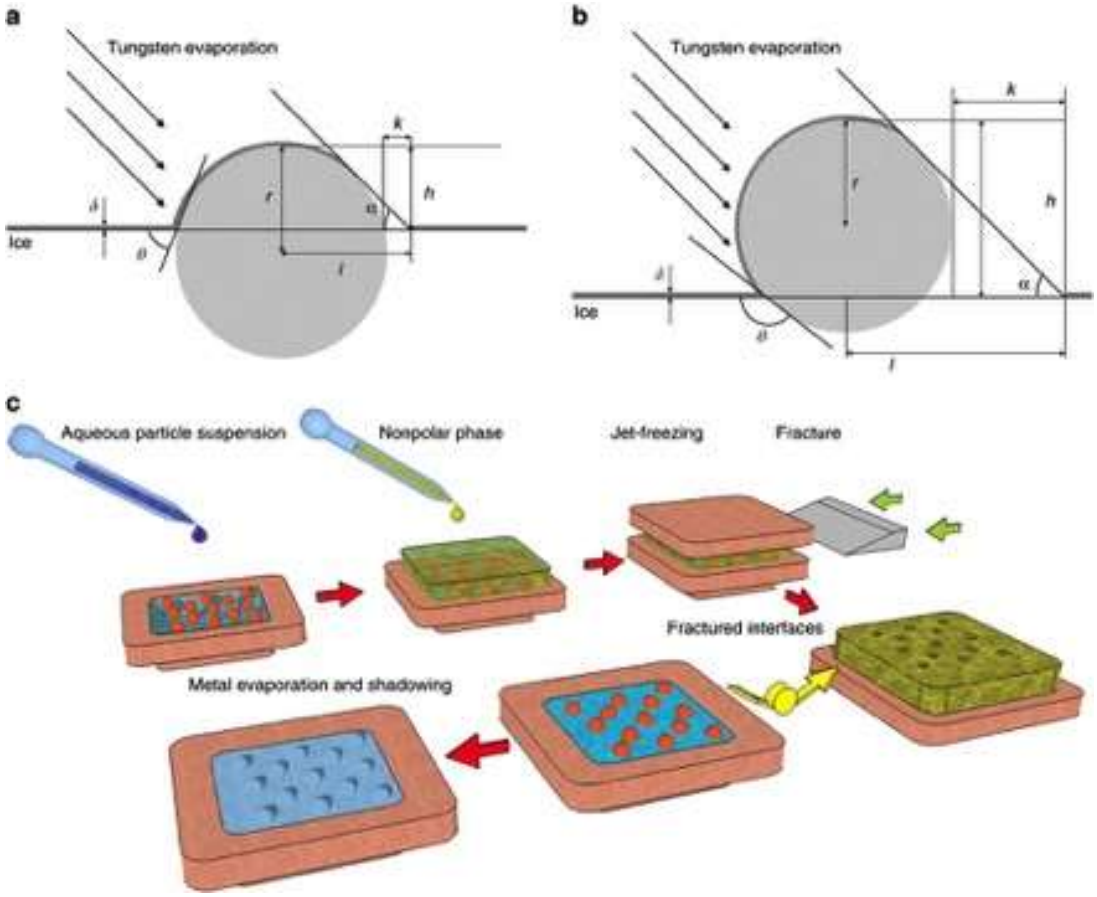

Figure 1.14. Illustration of particle adsorption at the frozen liquid after coating with metal: (a) hydrophilic particles and (b) hydrophobic particles. (c) Demonstration sample preparation for cryo–SEM Fresca imaging.

1.8.2.4 *Particle wettability by X–ray microscopy*

This method has been developed by Weon et al. using full–field transmission X–ray microscopy (Figure **1.15**).[54] An emulsion droplet of water coated with polystyrene latex particles in decalin is inserted into a 10–μm thick capillary filled with decalin. A very short exposure (~1 ms) of X–ray imaging was used to visualise the particle adsorption at the decalin–water interface in the emulsion droplet.[67] The contact angle was determined from the depth of immersion of the particles in the oil phase, h, and their radius, r, using equation 1.16. The contact angle of the polystyrene particles was found to be 167.4° ± 12.0°.[54]

$$\theta = \text{acos}\left(1 - \frac{h}{r}\right) \tag{1.16}$$

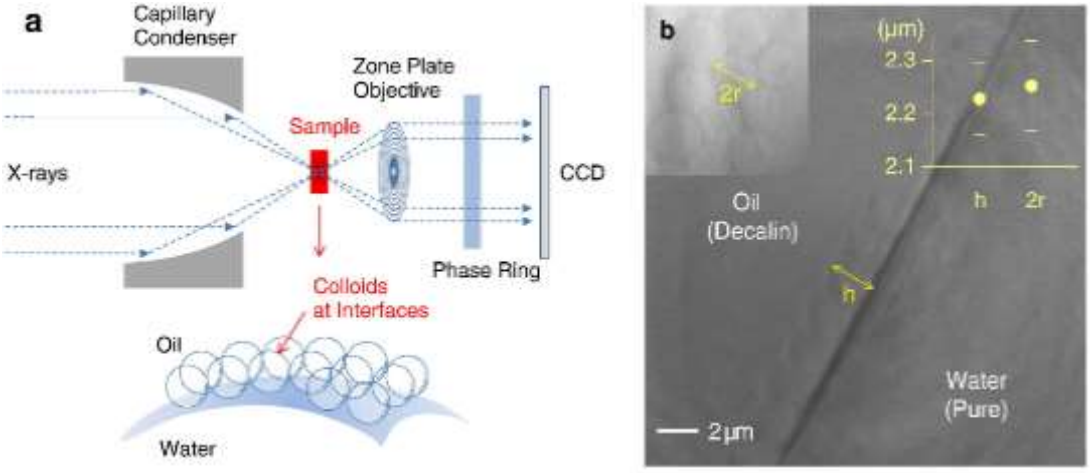

Figure 1.15. (a) Illustration of X–ray imaging technique to visualise particle adsorption at the oil–water interface. (b) In–situ X–ray image of polystyrene latex particles at the decalin–water interface.[54]

1.9 Porous particles

1.9.1 Properties and characterisation of porous particles

Porous particles have been used in numerous applications for decades. Porous particle applications include the production and development of pharmaceutical products, building materials, catalysts, sintered materials, ceramics, adsorbents, pigments, chromatography components, and filters. Each application seems to have an optimal specific pore size.[68] On the basis of size, pores are categorised into three classes: macropores (pore diameter: >50 nm), mesopores (pore diameter: 2–50 nm), and micropores (pore diameter: <2 nm).[69] Particles containing unsaturated bonds at their surfaces form a loosely coherent particle known as an aggregate, owing to the presence of weak bonds. If the particles are combined rigidly, as could happen under the influence of temperature or pressure, these types of particles are termed agglomerates.[70-72]

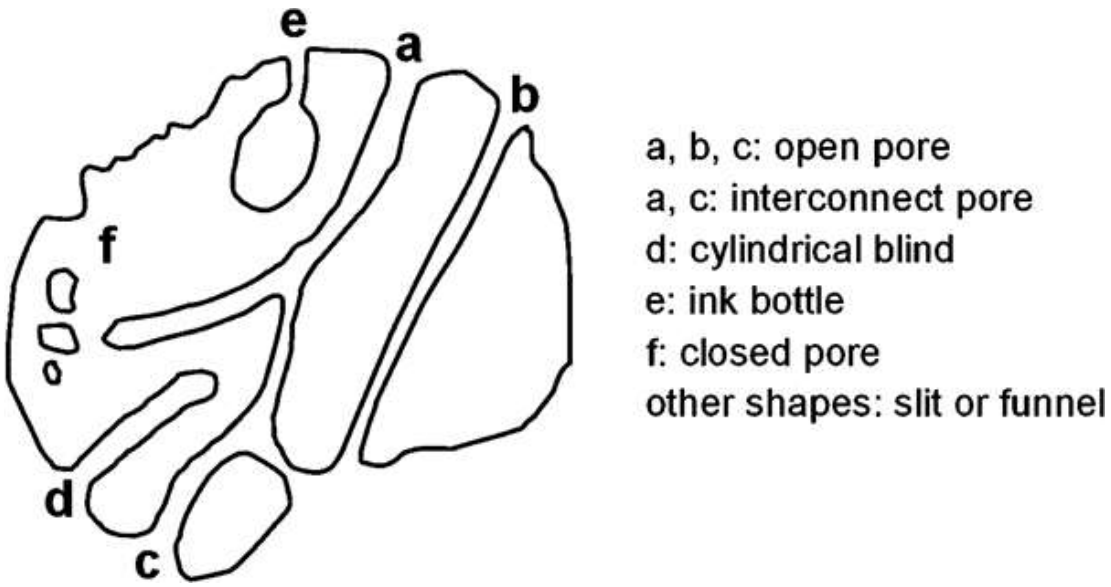

Figure 1.16. Porous solid physical properties.[73]

As shown in Figure 1.16, pores can be classified into different types (a, b, c: open pore; d: cylindrical blind; e: ink bottle; f: closed pore).[73] Nitrogen (at 77 K) is the suggested adsorptive for determining the pore size and surface area distribution of particles. Mercury porosimetry is an alternative method for determining porosity. A known weight of a dry sample of any shape is placed in a chamber of mercury, which is not a wetting fluid and does not enter the pores spontaneously. When placed under pressure, the mercury gradually flows into the pores and gives rise to a capillary pressure curve.[73-74] Fletcher et al.[75] suggested that the porosity of a silica monolith can be determined by measuring the particle weight when the substance is dry and wet. Based on the particle weight, the porosity of a cylindrical monolith (ϕ) can be determined using the following equation:

$$\phi = \frac{m_w - m_d}{\rho L R^2 \pi} \tag{1.17}$$

where m_w is the monolith wet mass, m_d is the monolith dry mass, ρ is the water density, L is the cylindrical length, and R is the radius.[75]

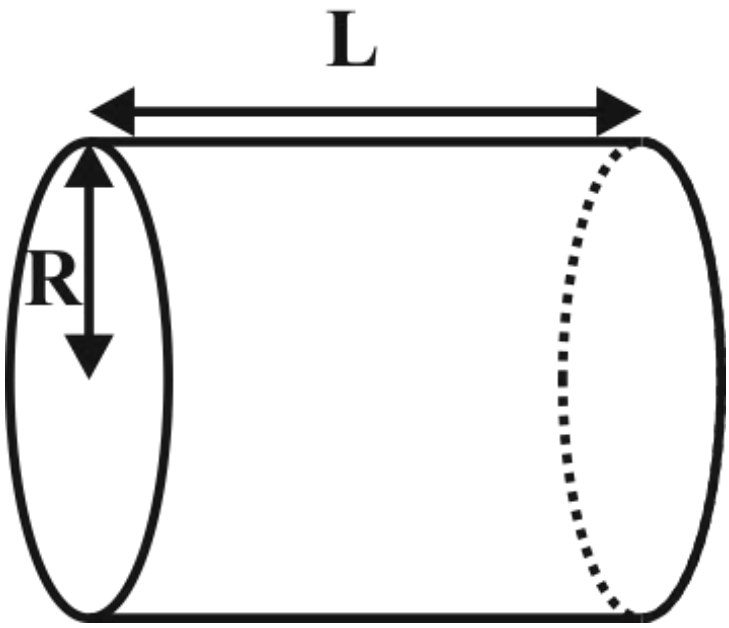

Figure 1.17. A diagram showing a monolith where L is the cylindrical length, and R is the radius

Particles of different sizes, shapes, and surface chemistry are used in composites. Therefore, these composites depend on the how they interrelate with each other and the materials' mixture. The particle packing arrangement is restricted to the fine spherical system. Nevertheless, particle packing depends on the arrangement process as well as the material properties and characteristics. These arrangements can be classified into two categories: loose or dense packing.[76] Loose packing can easily lead to particle movement, while dense packing does not usually lead to particle movement. The ideal arrangement of particle packing relates to the cohesion and dispersion that take place between monodisperse spherical particles. Hexagonal packing (hcp) and square close packing (i.e. face–centred cubic [fcc] or body–centred cubic [bcc] packing) are the most common packing structures (see Figure 1.18). The porosity for hcp and fcc is nearly 26 %, indicating minimum free energy, while the porosity for bcc is nearly 31 %, which makes for a highly porous structure.[76] Porous particles have been used in numerous applications for decades. For example, porous sizes in the range of 100 to 500 µm are important for the development of synthetic bone.[77] Porous particles have large surface areas, size dispersity, and the capacity to uptake solvents of different chemical natures and functions.[78] Different analytical methods can be used to determine porosity. These analytical methods include mercury porosimetry, scanning electron microscopy (SEM), radiation scattering (light, X–ray, and neutrons),

and gas and liquid adsorption. Gas adsorption measurements are broadly used for the characterisation of various porous particles, including polymers, zeolites, carbons, and oxides.

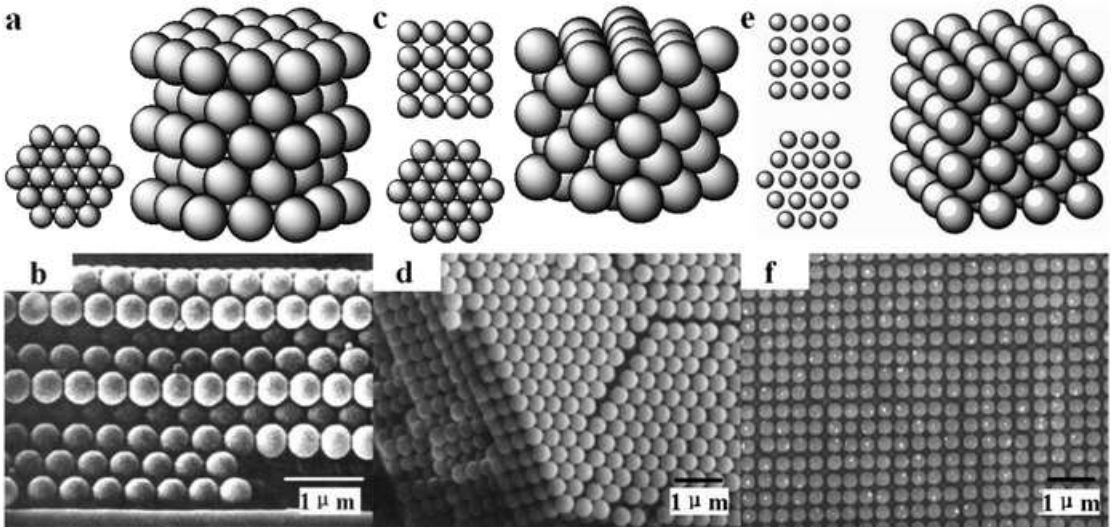

Figure 1.18. Packing density for colloidal particle arrangements: (a) and (b) diagram and SEM micrograph of hcp packing, (c) and (d) diagram and SEM micrograph of fcc packing, (e) and (f) diagram and SEM micrograph of bcc packing.[76].

1.9.2 Preparation of porous supra–particles

A number of approaches have been developed to assemble inorganic or organic particles into a dense packing of colloidal particles.[79] Several techniques have been used to arrange the particles into macroscopic spherical structures that can encapsulate proteins, drugs, and other components; such arrangements are called as supra–particles, supraballs, or colloidosomes (Figure 1.16).[76, 79-82]

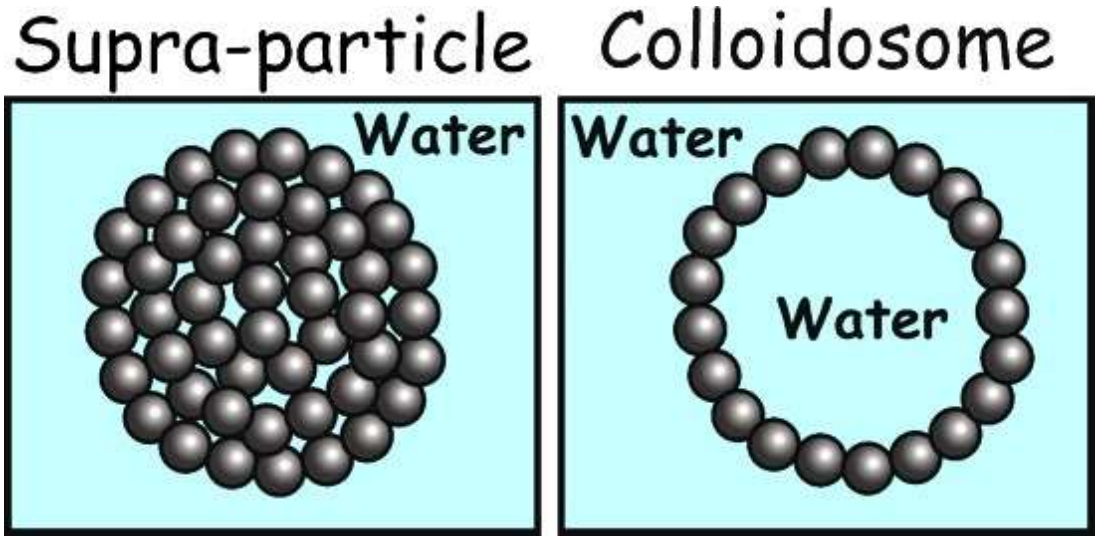

Figure 1.19. A diagram showing a supra–particle and a colloidosome

Dinsmore et al. showed the use of a permeable capsule made from composite colloidal particles called as colloidosomes (Figure 1.19).[83] The colloidosomes were produced via the self–assembly of polystyrene particles into emulsion droplets. In order to produce a dry and stable colloidosome, the researchers fused the shell particles at their glass temperature of 105°C.[81, 83-84] Moreover, hollow–structure particles were formed via different techniques, including microfluidic devices [85-86], solvent evaporation,[73] emulsion,[81, 87-88] and solvent evaporation.[89-90] Nevertheless, these approaches are appropriate for large–scale assembly.[82] On the other hand, supra–particles are made from concentrated monodisperse particle suspensions. Additionally, monodisperse composite porous supra–particles can be obtained via microfluidic devices,[91-92] ink–jet dripping technology, or micropipette injections.[93-94]

The aggregation of colloidal particles in three–dimensional structures can be achieved via the slow evaporation of droplet particle suspensions.[95] Researchers have proposed an emulsion technique for the preparation of supra–particles from monodisperse colloidal particle suspension[96,97] templates to manufacture microstructure hollow particles[98] and ball–like aggregates.[99] Another methodology for the production of porous supra–particles is the evaporation of a particle suspension on superhydrophobic surfaces. Particle crystal formation can be achieved by evaporating the droplet at room temperature. The size and shape of the particles depend on the volume and the wettability of the surface.[79, 100-101] This method has been used to create hemispherical particles,[101] spheroidal supraballs,[95] photonic balls,[91, 94] anisotropic particles,[102] dimpled particles, and doughnut–like structures.[79]

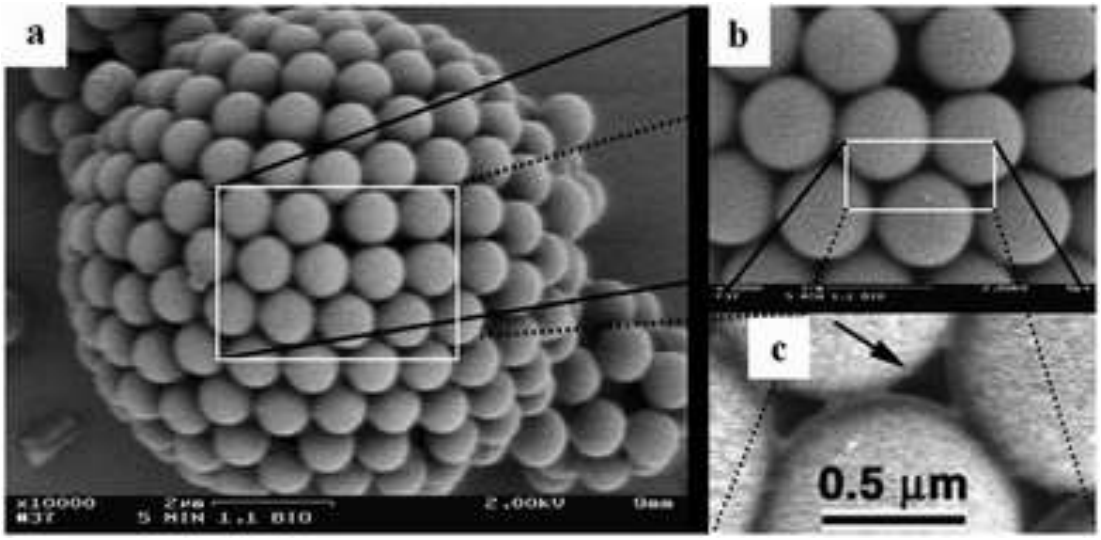

Figure 1.20. SEM micrographs for colloidosomes made by emulsion assembly (oil droplet dispersed in water): (a) dry colloidosome composed (10 µm) of 0.9 µm polystyrene particles and (b, c) close–ups of a, b, respectively. 0.15 µm holes, denoted by an arrow, express the penetrability.[76, 103]

Velev et al.[79] evaporated droplets of particle suspension on the surface of fluorinated oil, which is immiscible with water. A Petri dish with Teflon tape on its wall was used to prevent meniscus formation between the oil and the Petri dish. This is important because meniscus formation can deform the droplet shape via capillary forces (Figure **1.21**). The initial concentration of the microliter droplet was between 5 and 30 v%. Subsequently, the Petri dish was kept in a desiccating chamber for twelve hours. This procedure yielded spherical supra–particles of homogeneous size (100–500 µm) and appearance.[79] Highly ordered composite porous supra–particles with hexagonal arrangement had a volume packing fraction of <0.7404, representing the maximum packing fraction.

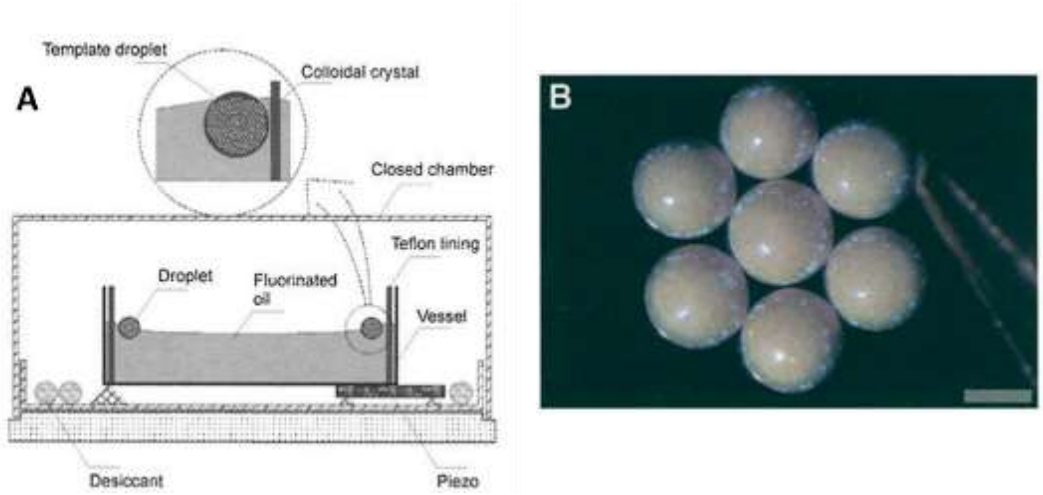

Figure 1.21. (A) Schematic diagram for the preparation of porous particles. (B) Optical micrograph of supra–particles made from 320 nm latex particles.[79]

Another method involves the use of a colloidal suspension dried on a superhydrophobic surface.[84, 95] The superhydrophobic surface is prepared via low–density polyethylene (LDPE), as it is hydrophobic with the solvent (xylene) and non–solvent (methyl ethyl ketone). Methyl ethyl ketone was used to make the surface more rough and, thus, increase the contact angle. The latex particle suspension decreased in volume during the 60 minutes evaporation process and formed supra–particles built from hexagonal close–packed monodisperse particles.

1.10 Emulsions

An emulsion[104] is a mixture of two immiscible liquids (usually oil and water) in which one of the liquids, called as the disperse phase, is dispersed as droplets in the other liquid, called as the continuous phase. When oil droplets are dispersed in an aqueous continuous phase, the type of emulsion obtained is oil–in–water (o/w). Conversely, when water droplets are dispersed in an oil solution, the type of emulsion obtained is water–in–oil (w/o). Aside from the so–called microemulsions (which are formed spontaneously and are thermodynamically stable), the formation of emulsions (i.e. macro–emulsions) also requires energy input. Macro–emulsions are thermodynamically unstable and could break down to the bulk liquid phases via several processes (Figure 1.20).

Creaming/sedimentation is a process caused by external forces (i.e. centrifugation or the earth's gravitational field) that act on fluid droplets in liquid–fluid emulsions. The

low density of the fluid dispersed in the liquid medium causes creaming, moving the droplets to the top. The droplets do, however, tend to sediment at the bottom if the fluid is denser than the liquid medium. Depending on the droplet volume occupied in the liquid phase, the fluid droplets can form a random or ordered close packed structure.[104]

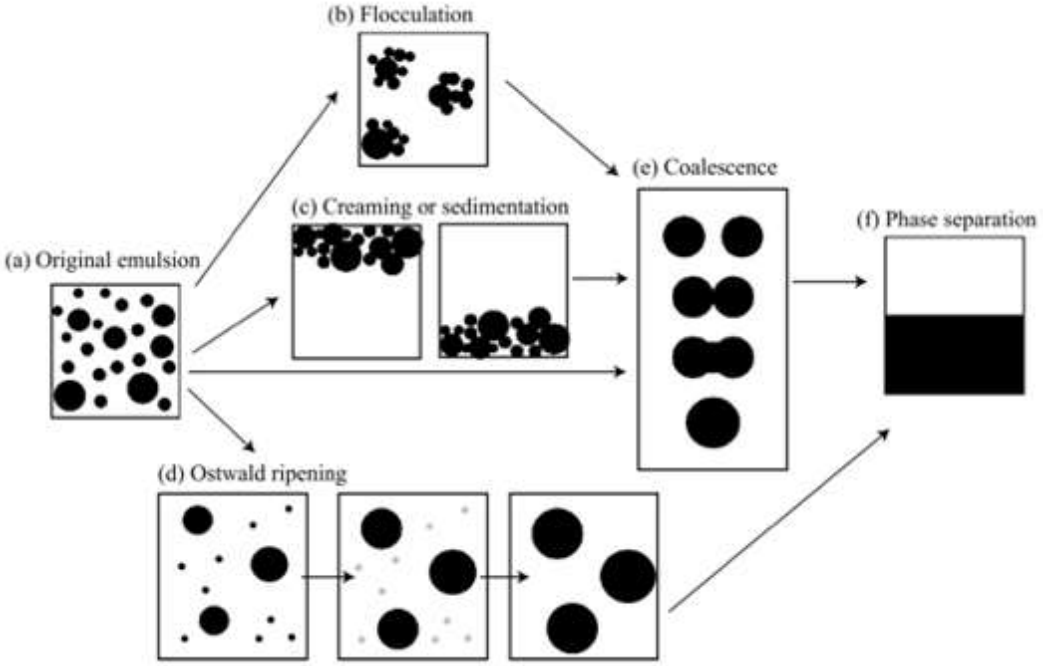

Figure 1.22. Schematic representation of the different mechanisms involved in the breakdown of an unstable emulsion.[105]

Additionally, flocculation is a process whereby fluid droplets collude and aggregate into larger units without droplet rupture or changes in size.[106] Flocculation occurs because of the van der Waals attraction, as well as the low repulsion forces between fluid droplets. The resulting flocs sediment faster than individual fluid droplets, leading to more rapid creaming or sedimentation.

Coalescence is a process whereby fluid droplets interact with each other and rupture the film interface via disruption and thinning, thereby forming larger droplets. This is due to the increase in the attraction energy, causing the film to rupture and the two fluids to separate. It is assumed that the coalescence stability of emulsions correlates to with the favoured curving and rigidity of the stabilising particles at the liquid–fluid interface.[107]

Ostwald ripening is caused by the limited solubility of fluid droplets in the liquid medium.[108] Small fluid droplets merge into larger droplets until they disappear and the fluid separates from the liquid. The internal pressure in the small fluid droplet is higher than in the larger droplet.[104]

In the all–purpose approach, unstable emulsion breakdown can occur through a combination of all four processes, which may progress simultaneously at different rates. As emulsions are thermodynamically unstable, they ostensibly separate over a long-term period. Flocculation and coalescence are more likely to occur if the surface area to volume ratio is high and the surface energy between the fluid and liquid is high.

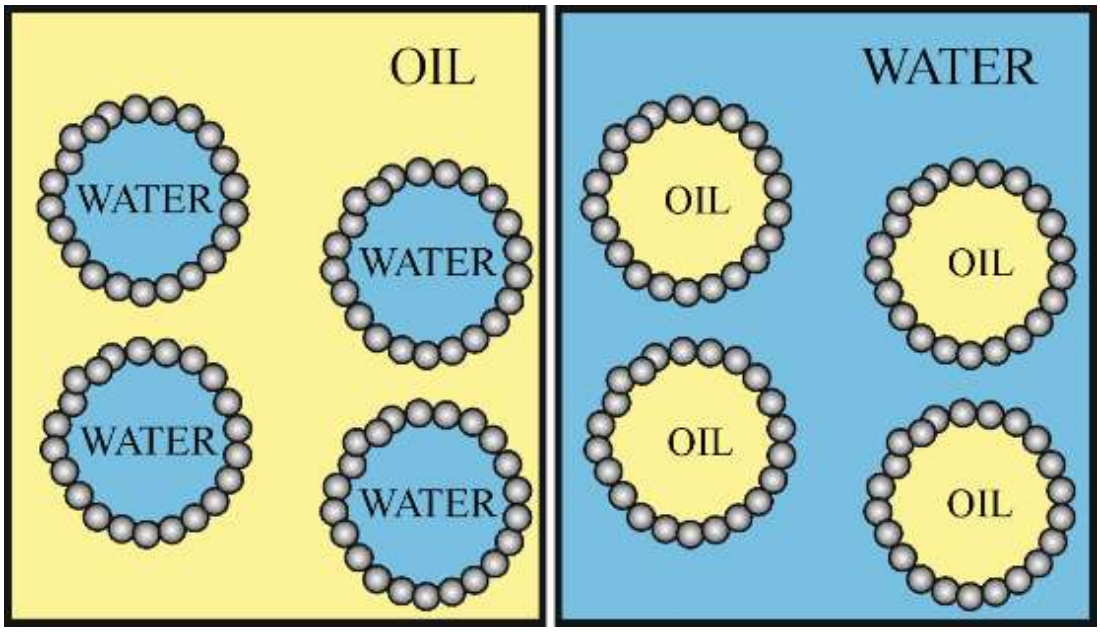

Figure 1.23. Schematic representation of water–in–oil (left) and oil–in–water (right) emulsions stabilised by hydrophobic and hydrophilic particles, respectively.

Macro–emulsions could be kinetically stabilised through the addition of surface–active agents (i.e. surfactants) or colloidal powder particles. Particle–stabilised emulsions are usually much more stable than those stabilised by surfactants, as the colloidal particles are strongly and irreversibly attached to the oil–water interface. The particle contact angle dictates the preferred emulsion type. The stability and the type of emulsion stabilised by silica nanoparticles that are pre–hydrophobised to different extents has been investigated.[109] It has been confirmed that the type of emulsion formed depends on particle wettability. Hydrophilic and hydrophobic particles form oil–in–water and water–in–oil emulsions, respectively (Figure 1.21).[109]

Chapter 2: Materials and methods

2.1 Materials

2.1.1 Water

All aqueous solutions were prepared with de–ionised water obtained from a Millipore Milli–Q Plus water purification system through a 0.22 μm membrane. The water resistivity was around 18.2 MΩ/cm, the pH was 6.7, and the surface tension was 72.3 ± 0.6 mN/m, as measured by the drop shape analysis instrument (MK10, Kruss).

2.1.2 Organic solvents and other chemicals

The organic liquids used in this study are shown in Table **2.1**. Dodecane, hexadecane, and n–decane were used as the oil phase in the gel trapping technique (GTT) for measuring contact angles of sulphate latex particles. Methanol and isopropanol were used as spreading agents for latex particles at air–water and oil–water interfaces in those experiments. The oils were purified by passing them through activated alumina three times before use.

Table 2.1. Organic solvents used in the experiments.

Organic Solvent	Supplier	Purity
Methanol	**Fisher Scientific**	**≥99%**
Isopropanol	**Fisher Scientific**	**≥99%**
Ethanol	**Fisher Scientific**	**≥99%**
Dodecane	**Sigma–Aldrich**	**≥99%**
Hexadecane	**Sigma–Aldrich**	**99%**
n–Decane	**Acros organic**	**99+%**

2.1.3 Other materials

Activated aluminium oxide (STD grade, Merck) was used to remove any polar impurities from the oils. Gellan gum (Kelcogel®) was a gift from CPKelco (USA). The curable elastomer Sylgard 184 (polydimethylsiloxane, PDMS) was obtained from

Dow Corning. A functionalised silica chromatographic column (Strata C18 Gigatube, 60 mL, from Phenomenex) was used to remove any hydrophobic or surface–active impurities from aqueous gellan gum solutions before the GTT experiment. Ethylenediaminetetraacetic acid disodium salt (EDTA, 99.6%) and sodium hydroxide (NaOH, 99.6%) were purchased from Sigma. Sodium chloride (NaCl, 99.5%) was supplied by BDH. Hydrochloric acid (HCl, 37% from Acros Organic) was used to adjust the pH. Dichlorodimethylsilane (DCDMS, 99.5%, GC) was obtained from Fluka. Chloroform (99.99%) was obtained from Fisher Scientific. Ethylene glycol (reagent plus, >99%), which has a higher boiling point than water (197.3 °C), was used as the polar phase and replacement for water. Chrome steel ball bearings 2 mm and 3 mm in diameter (AISI 52100), were used to make hollow cavities in curable PDMS elastomer. Microsyringes with a flat needle (outer diameter is 0.494 mm) (SGH) were used to insert sulphate latex suspension into the hollow cavities in PDMS elastomer moulds and to inject the sulphate latex suspension in the air–water and oil–water interfaces. Gadolinium (III) chloride (Aldrich) was added to the water phase in some experiments.

2.1.4 Spherical latex particles

2.1.4.1 *Carboxylate–modified latex particles*

Carboxylate–modified latex (CML) particles with diameters in the range of 0.9–3 μm (Invitrogen) were used as received (see Table **2.2**). These particles have a negative surface charge in aqueous media due to the dissociation of the carboxyl groups on their surface. The carboxylate groups of the CML particle surface are expected to be fully ionised at very high pH (e.g. above pH 10). The particles were washed two times before use by Milli–Q water to remove any impurities.

Table 2.2. Properties of CML particles.

CML diameter/ μm	Percent of solid w/v%	Specific surface area/cm^2/g	Area per surface group /nm^2
0.9	**4.2**	**6.30×10^4**	**4.6**
1.2	**4.3**	**4.70×10^4**	**1.3**
2	**4.2**	**2.80×10^4**	**0.3**
3	**4.4**	**1.90×10^4**	**0.9**

2.1.4.2 *Sulphate latex particles*

Surfactant–free sulphate polystyrene (PS) latex particles with diameter 2.5 ± 0.3 µm were obtained from Invitrogen as an 8.1 wt% aqueous suspension. Polystyrene has a density of 1.055 g/cm^3 at 20°C, a glass transition temperature (Tg) of 100–110°C, and a refractive index of 1.59 at 590 nm. These particles were soluble in benzene, chloroform, cyclohexane, toluene, acetone, and xylene but insoluble in ethanol, methanol, and water. The solubility data were important for choose the best solvent which not effect on the particles surface properties. The sulphate latex particles were washed two times before use by milli–Q water to remove any impurities.

2.1.5 Non–spherical and porous microparticles

2.1.5.1 *Needle–like aragonite microcrystals*

The aragonite crystals (Figure 2.1, a)were prepared by holding a solution containing 0.25 M $CaCl_2$ dihydrate and 2.25 M urea at 90°C for 7 hours.[110] The crystals were then collected by filtration, washed, and air–dried. Images obtained by scanning electron microscopy showed that the crystals had a needle–like or tubular shape and a length of about 20–40 µm. Reaction below is illustrate the basic reaction that occurs between urea and calcium chloride:

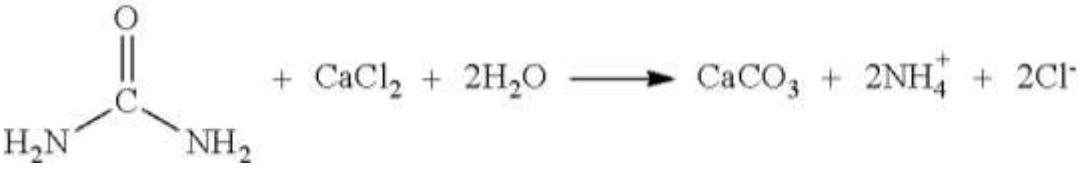

2.1.5.2 *Rhombohedral–like calcite microcrystals*

The calcite cubes (rhombohedral, Figure 2.1, c) were produced by mixing equal volumes of 10 µM $CaCl_2$ dihydrate and 10 mM Na_2CO_3.[111-112] The solution was stirred briefly and left undisturbed for four days. The crystals were then collected by filtration, washed, and air–dried. The crystals were rhombohedral–shaped and ~10 µm in size.

$$2Na^+ + CO_3^{2-} + H_2O \rightleftharpoons 2Na^+ + 2OH^- + H_2CO_3, \quad (1)$$

$$2Na^+ + 2OH^- + H_2CO_3 + Ca^{2+} + 2Cl^- \rightarrow \downarrow CaCO_3 + 2H_2O + 2Na^+ + 2Cl^-. \quad (2)$$

2.1.5.3 *Ethyl cellulose micro–fibres*

The ethyl cellulose micro–fibres (figure 2.1, d) were produced using the "in shear solvent attrition method".[113] They were used immediately after washing to prevent excessive aggregation. A 15 wt% solution of ethyl cellulose in tetrahydrofuran (THF) was injected into an 85 wt% glycerol–in–water solution that was stirred using a high–speed shearing head (2000 rpm) for 10 minutes. The fibres were then filtered and washed with water which then characterised by SEM and optical microscopy (figure 2.1, d).

2.1.5.4 *Porous silica microparticle*

Powders of highly porous fumed silica particles VP Aeroperl® 300/30 (hydrophilic, Degussa lot#9110122, Figure 2.1, b) and VP Aeroperl R806/30 (hydrophobic, Degussa, lot# 9110123) with an average diameter of about 30 μm and BET surface area of 300 ± 30 m^2/g were used as received.

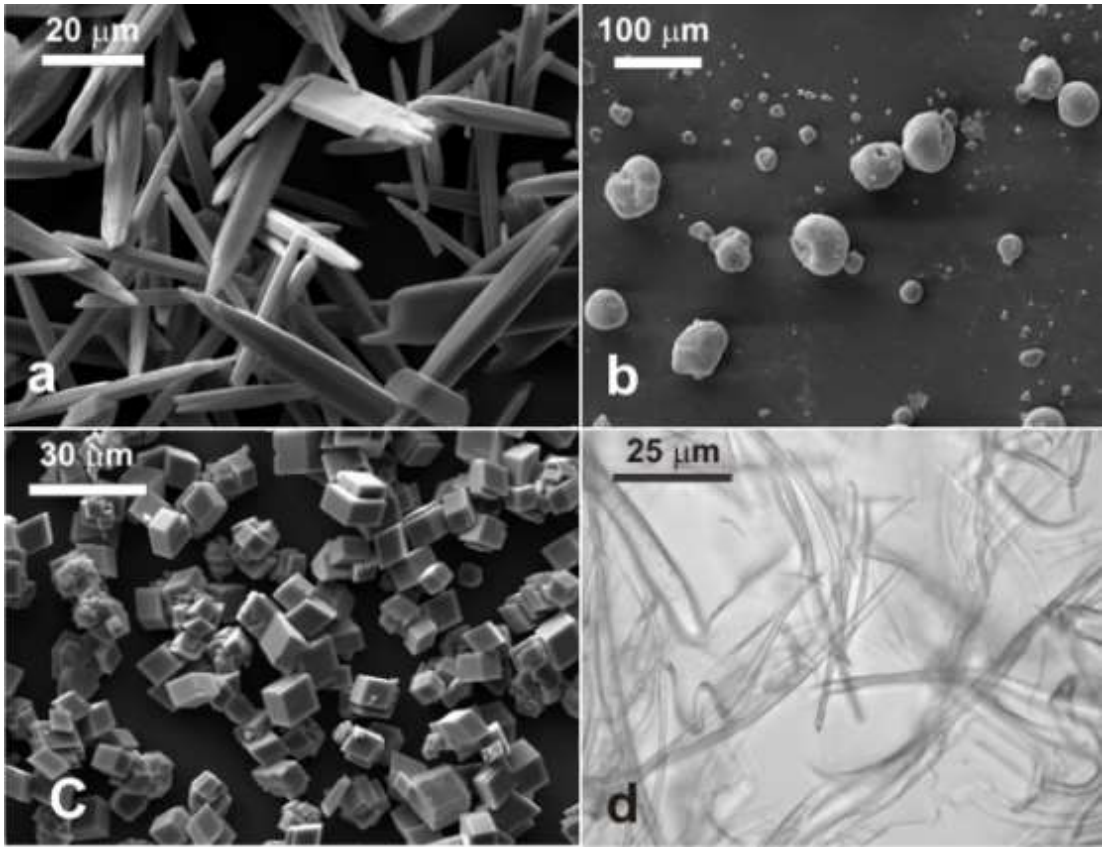

Figure 2.1. SEM images of (a) aragonite microcrystals, (b) hydrophilic porous silica microparticles (VP Aeroperl® 300/30), and (c) calcite microcrystals. (d) Optical microscopy images of ethyl cellulose microrods in aqueous solution.

2.1.6 Fluorescent dyes

In our studies, different fluorescent dyes were used, including Rhodamine 6G, 99% and fluorescein 5(6)–isothiocyanate (FITC, Sigma–Aldrich Ltd, UK) (Fig. 2.1).

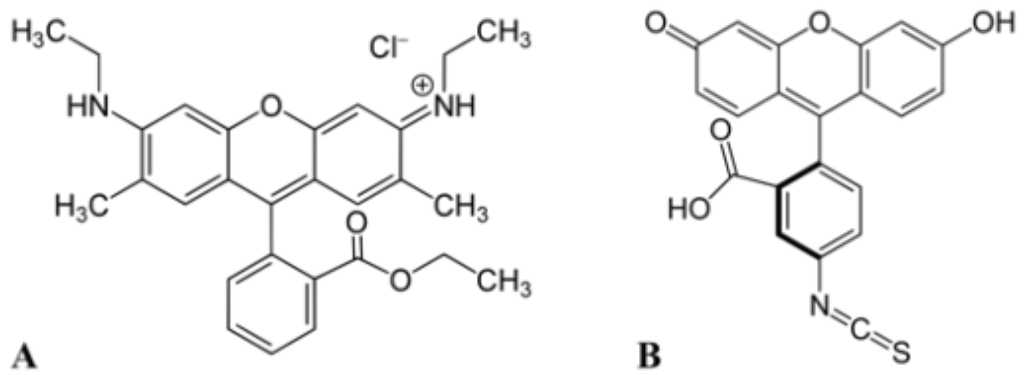

Figure 2.2. Chemical structure of (A) Rhodamine 6G, (B) Fluorescein 5(6)–isothiocyanate (FITC).

2.2 Methods

2.2.1 Cleaning procedures for glassware

The glassware was cleaned by soaking in a freshly prepared solution of KOH in ethanol, (150 g KOH dissolved in 1 L ethanol) for 30 min. Then, the glassware was washed with large amounts of Milli–Q water and rinsed with deionised water. Finally, the glassware was dried in an oven at 60°C overnight.

2.2.2 Measuring the surface and interfacial tensions

The surface and interfacial tension of liquids were determined by the pendant drop method. In this method, a pendant drop is formed at the tip of a needle with a known diameter in air or other fluid and an image is taken with a camera. The surface or interfacial tension is calculated from the shape of the pendant drop using the Laplace equation for capillarity.

Measurements of the surface tension of deionised water and 0.1 M NaCl (Riedel–de Haen, extra pure) aqueous solutions were taken using a drop shape analyser (DSA 10, Kruss) and a needle with diameter of 1.657 mm. The densities of water (0.9978 g/cm^3) and the 0.1 M NaCl solution (1.0016 g/cm^3) were measured using the Anton Paar densitometer (model DMA35N). The surface tension of deionised water and 0.1 M NaCl solution was found to be 71.4 ± 0.9 mN/m and 72.6 ± 0.4 mN/m, respectively. The interfacial tensions of dodecane–water and hexadecane–water surfaces were measured using pendant drops of water in oils. The interfacial tension of dodecane–water was 50.7 ± 0.5 mN/m, while that of hexadecane–water was 51.2 ± 0.6 mN/m, both in agreement with the values in the literature.[114-115]

2.2.3 Zeta potential

The zeta potential of particles in water were measured using the Zetasizer nano instrument (Malvern). The effect of pH on the particle charge was also studied using an auto titrator fit to the instrument. The pH of particles suspended in 1×10^{-3} M NaCl solutions was adjusted by adding a few drops of 0.25 M NaOH or 0.25 M HCl.

2.2.4 Measuring particle contact angles with the Gel Trapping Technique

The Gel Trapping Technique (GTT), already discussed in the introductory chapter, was used with some modifications as the main method of investigation in Chapters 3 and 4. Therefore, this method is described in detail below.

2.2.4.1 *Preparation and purification of gellan hydrogel*

A non–adsorbing hydrogel solution (gellan gum) was used as the water phase in this technique. Gellan gum[116-118] is a linear anionic polysaccharide produced by the microorganism *Pseudomonas elodea*.[4]

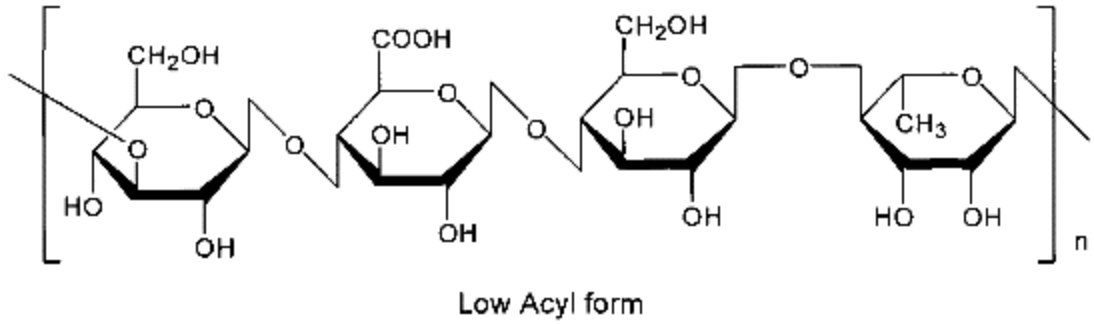

Figure 2.3. Gellan gum structure.

The gellan gum used in the GTT was purified to remove any surface–active impurities. A 3.0–g portion of gellan gum powder was dispersed in 600 mL Milli–Q water at 95°C in a water bath for 30 minutes to hydrate the polymer. The 0.5 wt% gellan solution obtained was passed twice through a pre–activated C_{18}–silica chromatographic column connected to a vacuum filtration set. The column was pre–activated using an acetonitrile–water mixture (80 : 20) and flushed several times with hot Milli–Q water before the hot gellan solution was passed through it. The C_{18}–silica column was heated from outside during the filtration of the hot gellan solution to prevent gelling inside the column. The temperature of the purified gellan solution could be kept above its gelling temperature in an oven at 50°C for 1–2 days. Finally, after the purification step, the concentration of the gellan solution was increased by evaporation at 90°C, from 0.5 wt% in 600 mL to approximately 2 wt% in 150 mL.[4, 60] The final concentration of gellan was confirmed gravimetrically by completely evaporating an aliquot of the solution. The concentrated solution was kept at 60°C in a sealed flask until its use in the GTT experiments.

2.2.4.2 *Preparation of PDMS mixture for moulding*

The mixture of PDMS and curing agent (10:1 by volume) was centrifuged (4000 rpm, 5 min) to remove any air bubbles formed during mixing with a spatula. Once prepared, the mixture could be kept in a liquid state for about 2 days in a refrigerator at 4°C or for 7 days in a freezer.

2.2.4.3 *Gel preparation and measuring procedure*

In the experiments involving particle adsorption at the air–water surface, a 3–4 mm thick layer of hot (50°C) 2 wt% gellan solution was poured into a non–treated polystyrene Petri dish (35 mm diameter). Then, a sample of 10 μL of the spreading suspension (i.e. methanol) of particles was injected at the liquid interface using a microsyringe. The Petri dish with the sample was then cooled to room temperature and left for 30 min until the gel was set. In the experiments at the decane–water interface, the decane phase was pre–equilibrated to the same temperature as the gellan solution. A thin layer of gellan solution was poured into the Petri dish and a thin layer (2–3 mm) of oil poured on top of the aqueous phase. The particle suspension in a spreading solution was then injected at the oil–water interface, and the sample was left to cool and set at room temperature. Once the gel was set, the oil layer was gently removed by decanting the oil off and using the edge of a tissue paper to remove the excess oil from the sides of the Petri dish. For both the air–water and oil–water experiments, a 1–mm thick PDMS layer (at room temperature) was poured on top of the gellan sample in the Petri dish and left for 48–72 hours to fully harden and then the PDMS was peeled off and washed in hot water. The PDMS moulds were coated with a carbon nanolayer for imaging with SEM. In the SEM images of the PDMS replica of the liquid surface, the PDMS itself represents the phase that has been replaced – the air phase, in an air–water system, or the oil phase, in an oil–water system. Most of the SEM images were taken at an angle of 65° of the electron beam to the sample surface. The particle contact angle values were determined from the SEM micrographs using the following equations: Equation (2.1) if the particles were immersed in the oil or air and the contact line diameter was below the equatorial diameter (hydrophilic particles; <90°):

$$\sin\ \theta = \frac{d_c}{D} \qquad (2.1)$$

Equation (2.2) for hydrophobic particles (>90°), where the contact line diameter is above the particles' equatorial diameter and the protrusion height is large the contact angle is obtained by this equation:

$$\sin\ (\pi - \theta\ ) = \frac{d_c}{D} \qquad (2.2)$$

D is the particle diameter, d_c is the particle contact line diameter, and θ is the contact angle.

In the experiments with CML and sulphate latex particles, their aqueous suspensions were mixed with methanol (50 : 50 by mass, 2 wt%) and used as a spreading solvent. Also, for the non–spherical and porous microparticles isopropanol was used as spreading agent at concentration of 1 wt%. In order to determine whether the phase through which the particles spread at the interface has any influence on the particle contact angle the particles were spread at the oil–water interface by injecting (20 µL, 2 wt%) the spreading suspension (i) through the oil phase or (ii) through the water phase close to the liquid interface, as illustrated in Figure **2.4**.

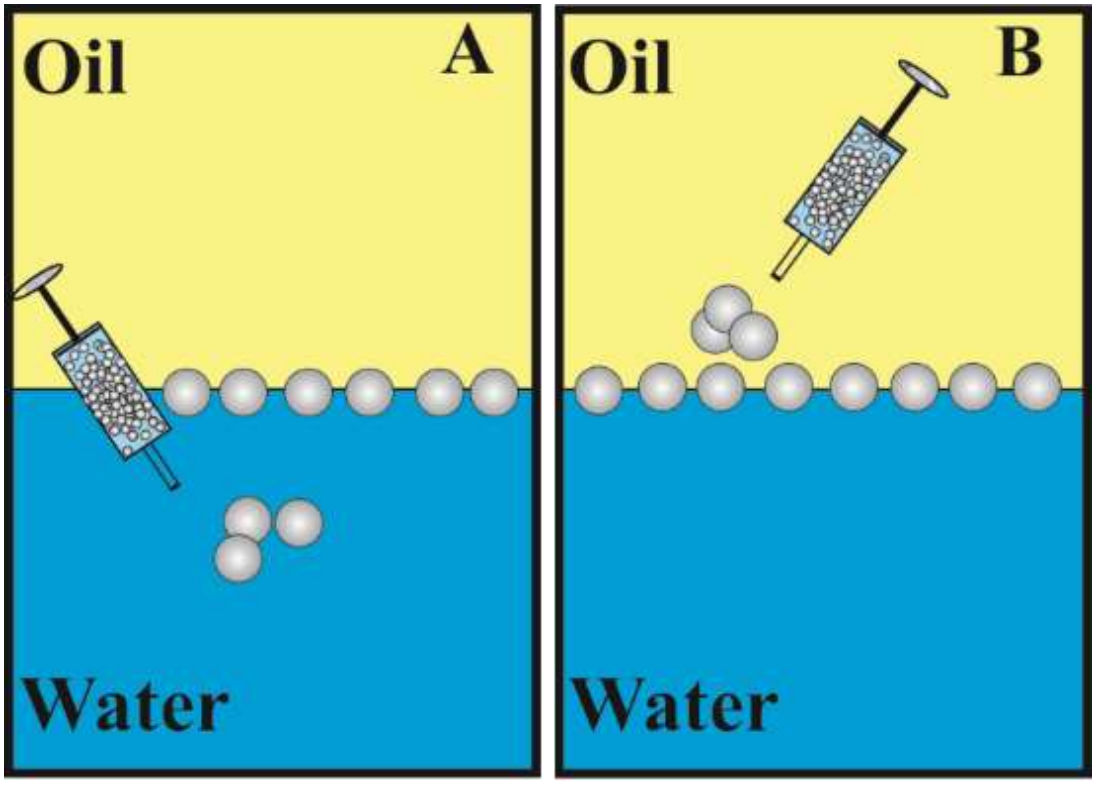

Figure 2.4. Illustrations showing how the particles adsorbed and spread on the surface of the gellan solution. (A) Injecting the particles through the water phase and (B) injecting the particles through the air–oil phase.

Then, the procedure for embedding the interfacial particles into a PDMS mould, as described above, was followed. After peeling off the solidified PDMS layer with the particles, the samples were incubated in hot aqueous solutions 90^{o} C of 20 mM EDTA disodium salt, 20 mM NaOH, and deionised water for 20 min each, consecutively, to wash off the gellan residue from the PDMS surface. This procedure was used for CML particles adsorbed at the dodecane–water and hexadecane–water interfaces. In the case of particles at the air–water interface, the procedure was very similar; however, the Petri dish was sealed during the gelation process to avoid evaporation of water and development of cracks at the hydrogel–air interface. In this case, the particle monolayer was microcast with PDMS directly from the surface of the set gellan solution.

2.2.4.4 *Effect of salt in the gellan solution on the particle contact angle*

The effect of the addition of NaCl to the aqueous phase on the three–phase contact angle of 3 μm CML particles at the liquid interface was investigated. Solid NaCl was added directly to the purified gellan solution to adjust the salt concentration to 1 mM of NaCl. The aqueous suspension of the 3 μm CML particles was mixed with methanol at a ratio of 50:50 by mass and then spread at the liquid interface. The oil phases used in this experiment were dodecane and hexadecane. Sample preparation was carried out as described in the previous section.

2.2.4.5 *Effect of gel syneresis on the contact angle of CML particles at different interfaces*

Four sizes of CML particles were used: 0.9 μm, 1.2 μm, 2 μm, and 3 μm. For the air–water surface, the gellan solution (2 wt%) was added to the Petri dish, spread the particles onto the gellan solution (2 wt%) surface, and then kept it in the fridge for 10–20 minutes. On the other hand, for the oil–water (dodecane–water) interface, the hot gellan was added to the dish while the oil was poured on the top phase carefully using

a pipette. The latex particles were added using a microsyringe (Hamilton, 100 µL), and the dish was placed for 10–20 minutes in the refrigerator.

2.2.4.6 *Scanning Electron Microscopy (SEM)*

SEM images were obtained using an Evo 60 field emission scanning electron microscope (Carl Zeiss, Gmbh) at a magnification in the range of 10×–1,000,000× and resolution of 2 nm. The samples were pre–coated with either carbon or gold monolayers to enhance their surface electro–conductivity.

2.2.4.7 *Preparation and characterisation of emulsions*

A 22 mL aqueous suspension of 5 wt% CML particles in 1 mM NaCl was stained with 10^{-5} M fluorescein sodium salt. Then, 2 mL of dodecane was added and mixed by vigorous hand shaking for 30 seconds at 25°C. The emulsion samples were imaged immediately after their preparation, and the type of droplet phase was determined using fluorescence microscopy (Olympus BX–51 microscope fitted with a FITC filter set).

2.2.5 Fabrication of model of porous supra–particles

2.2.5.1 *Fabrication of porous supra–particles using a PDMS mould.*

PDMS was mixed with a curing agent at a 10:1 ratio and degassed using a vacuum desiccator for 30 minutes to gain a clear solution. Ball bearings of diameters 2, and 3 mm were used to make spherical holes in the PDMS. The balls were placed in Petri dishes and PDMS was poured over them. They were allowed to solidify for 3 hours in an oven at 50°C. In some cases, the balls tended to aggregate during the solidifying process. Berry pins (diameter: 0.6 mm) were used to make holes towards the balls, and the balls were removed from the cured PDMS using a scalpel.

Sulphate latex particles (1 mL) were dispersed in ethylene glycol after removing the water using a centrifuge at 3000 rpm for 3 minutes, and then shaken for 3 minutes, before being finally degassed using a vacuum desiccator. The particles suspension was prepared by the weigh by weight percentage. After removing the water the needed amount of ethylene glycol was used to produce 30wt% and 70 wt% of particles

suspension. The syringe contains particles were shaken gently during the insertion of particles into the cavities in order to prevent any blocking in the needles. Meanwhile, the PDMS was placed on top of the Anotop filter (Whatman polycarbonate, 0.2 µm), which was laid on top of a Whatman filter paper (pore size, 3 µm; Whatman 6) and then placed in a Petri dish with a hole. These filters allowed the ethylene glycol to pass through but not the particles or any gas trapped in the mould cavities(see Figure 2.5),. The PDMS and filters were then tightly clamped and the particles were injected using the microsyringe (Hamilton, 100 µL) . The particles were injected using one of three different methods (see Figure 2.6), i.e. by hand, using a calliper, or a syringe pump (flow rate, 1 mL/h). After adding the latex in the PDMS cavities, the samples were placed in an oven at 106°C for 2 hours. The volume of suspension required to fill 2 mm sized cavities measuring 2 mm and 3 mm was, respectively, ~15 µL and ~50 µL of 70 wt% of sulphate latex particles suspension in ethylene glycol. The effect of viscosity of 70 wt% was noticed after keeping them for a while in the syringe without moving the particles which sediment the particles and block the needles. The ethylene glycol was used as a polar phase instead of water because of its high boiling point – 197.3°C – to prevent any gas generation when using an oven at 106°C for 2 hours.

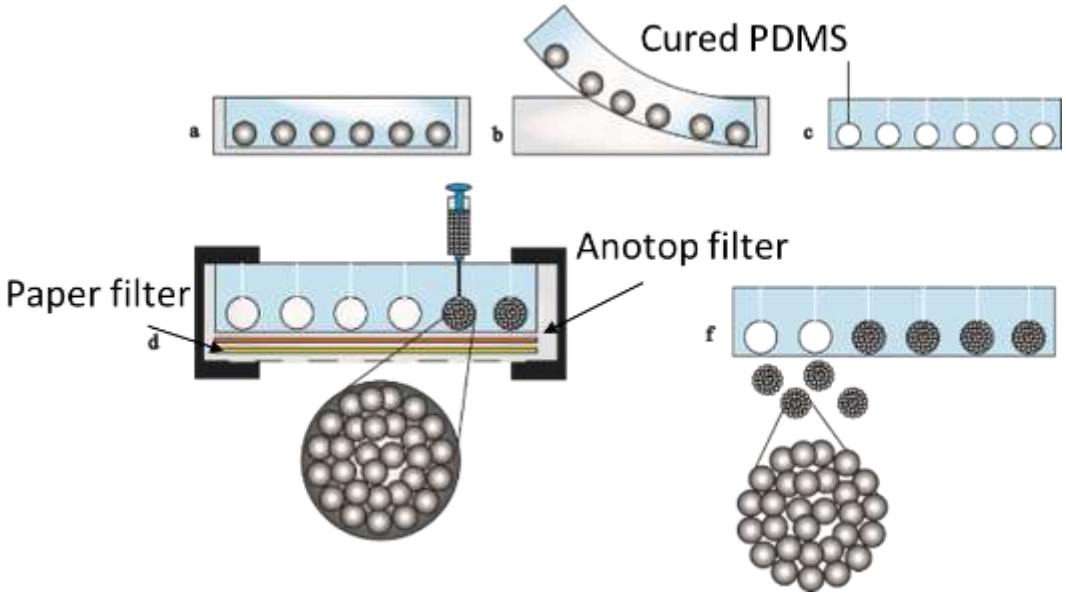

Figure 2.5. Schematic diagram illustrating supra–particles prepared using the PDMS template. (a) The PDMS with the curing agent was poured onto the stainless steel balls. (b) The cured PDMS elastomer was peeled off at 50°C in the oven. (c) The steel balls were removed, creating a well cavity, and holes were made towards the wells. (d) The PDMS on top of the 0.02 µm Anotop filter, a 3 µm filter paper, and a Petri dish with

holes were clamped to allow the injection of the particle suspension into the wells. (f) The particle suspension was allowed to fuse and the suspension was evaporated at 106°C.

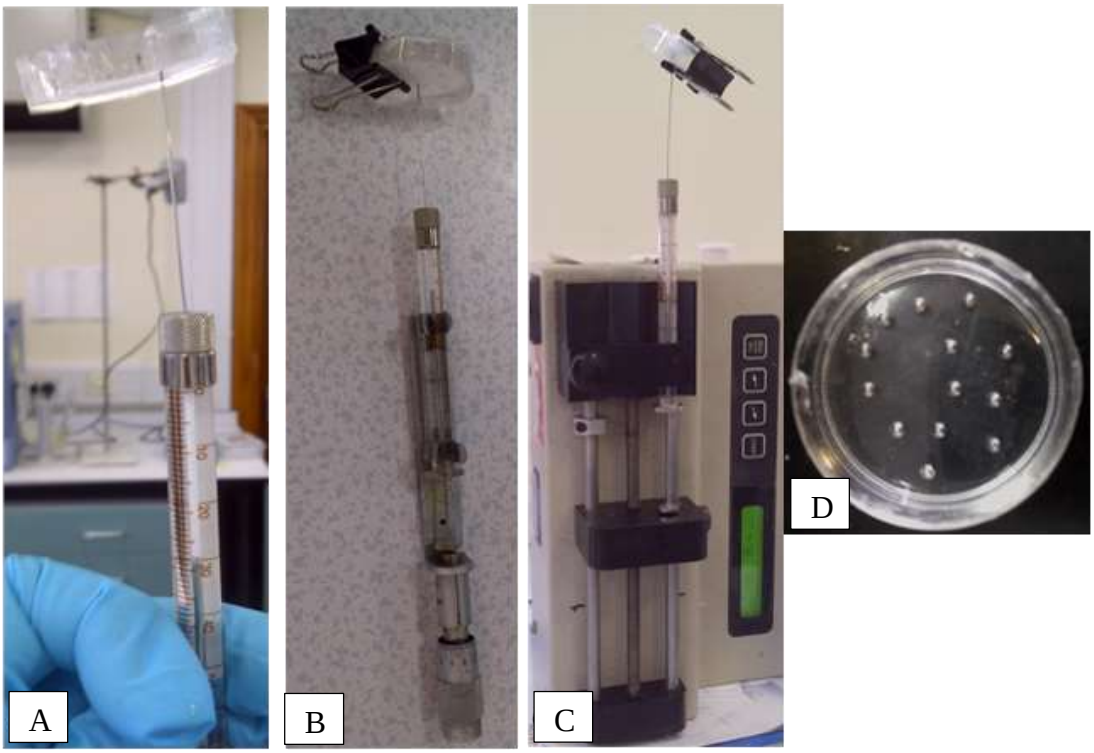

Figure 2.6. Methods used to insert the sulphate latex suspensions into the ball cavities in the PDMS template: (A) by hand, (B) calliper, and (C) syringe pump. (D) The image on the right shows steel balls in the PDMS template.

2.2.5.2 *Fabrication of model porous supra–particles by evaporating drops of latex suspension on a superhydrophobic surface.*

The porous supra–particles were fabricated from polystyrene sulphate latex particles by evaporating drops of their aqueous suspensions during rolling on a superhydrophobic surface. The preparation of superhydrophobic surfaces was as follows. Glassware was cleaned with KOH/ethanol for 1 hour and then washed with water and acetone in an ultrasonic bath for 10 min at room temperature and then dried in the oven. Glass surfaces were functionalised using the vapour hydrophobisation method along with DCDMS by adding 1 mL DCDMS to glass in a sealed box overnight and then washing the glass with hexane, which helped to remove any excess DCDMS from the glass surface. Hydrophobic fumed silica particles (R202 Degussa,

AEROSIL®) were dispersed in ethanol at 5 wt% using an ultrasonic probe (Digital Model 250, Branson) operating at 50% amplitude with a 2 sec pulse every 5 sec for a total of 20 min. Then, a 0.5 mL – 1 mL silica suspension was spread onto the glassware surfaces and dried for 20 min in an oven at 50°C.

2.2.5.3 *Preparation of composite porous supra–particles using a vortex mixer*

A dimple glass (watch glass) with a superhydrophobic surface was prepared as described above, taped on the vortex mixer (Vortex Mixter SA7, Stura), and used to make supra–particles by rotating 10 µL of 8.1 wt% and 40 wt% sulphate latex on the glass at speeds below 200 rpm, as higher speeds would make the droplet roll off the dimple glass surface. The latex suspension was vibrated and rolled on the superhydrophobic surface for 1 hour, after which the latex suspension became viscous and stuck to the superhydrophobic surface, forming a dimple shape. A fan heater was used to speed up the evaporation rate in order to create the porous supra particles faster.

2.2.5.4 *Preparation of composite porous supra–particles by manual rolling of latex suspensions on hot superhydrophobic surfaces*

Glass beakers with superhydrophobic coating (see above) were used in these experiments. The composite porous particles were prepared using 2.6 ± 0.1 µm polystyrene sulphate latex particle suspensions with different concentrations in the range of 8.1–70 wt%. The concentrations above 8.1 wt% were prepared by settling the particles using a centrifuge at 4000 rpm for 3 min. The concentrated suspension was then degassed using a vacuum desiccator. Different volumes of latex particle suspensions (2.5–20 µL) were added to a pre–heated beaker with a superhydrophobic surface and rolled manually by shaking the beaker on top of a hot plate set at 90°C until the latex suspension droplet evaporated and dried (Fig. 2.6). The time needed to make one porous particle was between 1 and 10 min, depending on the initial concentration and volume of the particle suspension. Finally, the particles were fused together by heating at 106°C just above the glass transition temperature of polystyrene using an oven, dry block heating system (QBD1, Grant), or oil bath for a period of 30

min to 2 h as described below. Figure **2.7** summarises the main steps in the preparation of the model porous particles used in this thesis.

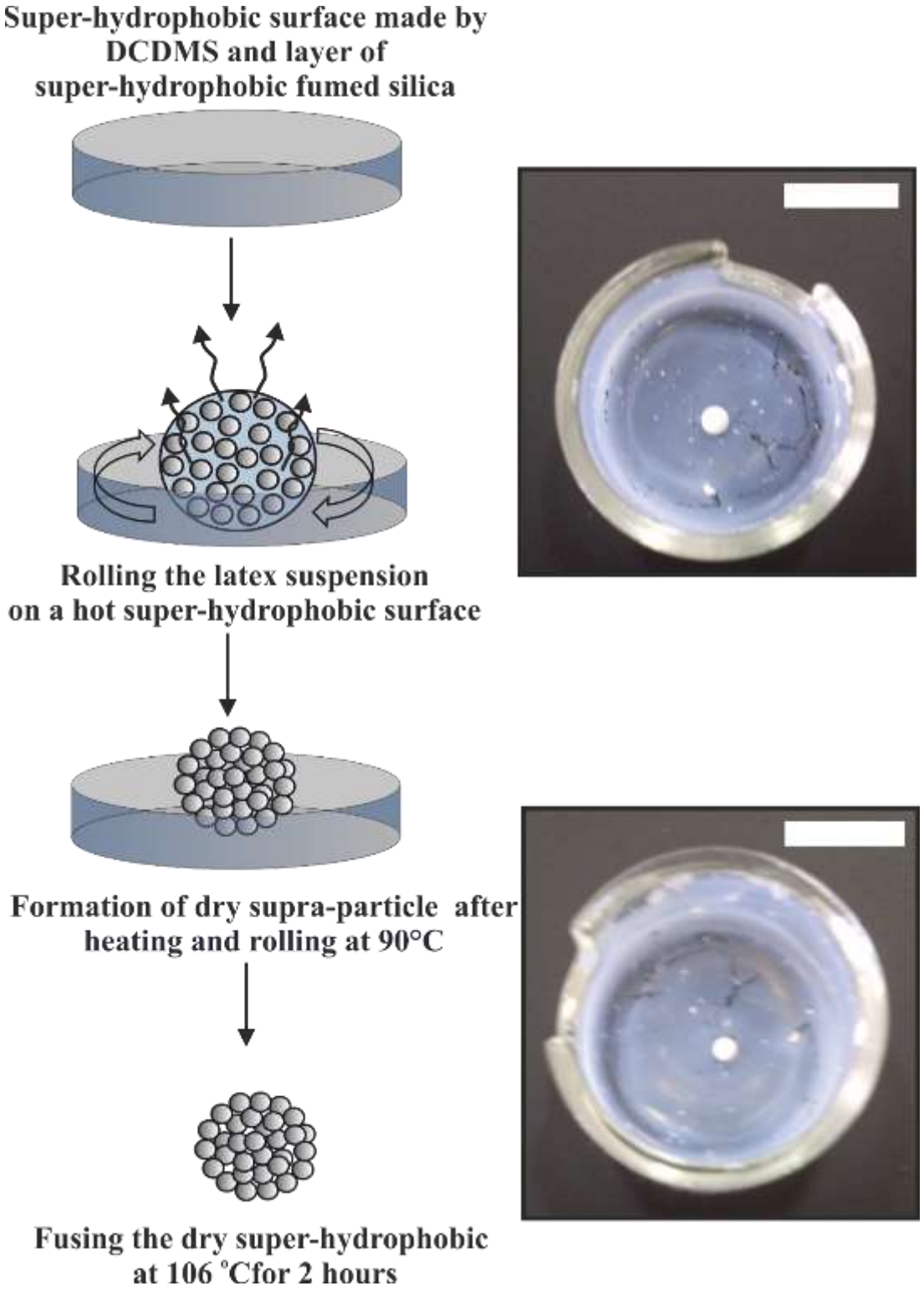

Figure 2.7. Representation of the formation of a dry porous supra–particle from a drop of concentrated polystyrene latex suspension which was evaporated at 90°C. The dry porous particles (2 mm) were partially fused at 106°C to form a stable porous supra–

particle for our studies on porous particle adsorption at liquid surfaces. The scale bar is 10 mm.

2.2.5.5 *Annealing of the porous supra–particles*

The following methods of temperature control for fusing the supra–particles at specific temperatures were investigated. Supra–particles used in this investigation were prepared using 10 µL of 50 wt% sulphate latex suspension and were fused for 2 hours.

2.2.5.5.1 Fusing the particles using the hotplate method

This method involves the use of a hot plate with an oil bath. The hotplate controls the temperature with a probe that is insert in oil bath, which used to maintain the temperature at 107°C. The particles obtained were stable in ethanol and water.

2.2.5.5.2 Fusing the particles using a dry block heating system

In this method, the Grant (QBD1) dry block heating system is used to fuse the building block particles. This system has interchangeable heating blocks, QB–E2, with a 35–mm–deep hole to fit a sample tube. Its temperature was first set at 103°C. Two mercury thermometers were used to measure the actual temperature of the block: the first one was immersed in the oil bath (97.6°C) and the second was directly in contact with the block surface (96.1°C). Once the particles cooled to reach room temperature, they were washed in ethanol but they disassembled immediately, thus indicating that the latex particles were not fused together at this temperature. Increasing the temperature to 107°C resulted in the formation of fused particles which were stable in ethanol and water. Therefore, heating the supra–particles to 103–105°C was sufficient for fusing the building block particles.

2.2.5.5.3 Investigating the effect of temperature during evaporation of the latex suspension on the supra–particle structure

Sulphate latex particle suspensions (15 µL of 50 w/w%) were added to pre–heated glass beakers and evaporated during manual rolling at temperatures of 60, 80 and 105°C. The supra–particles obtained were in a dry vessel then inserted into an oil bath for 2 h at 103°C to fuse the individual sulphate latex particles together. Images of the supra–particles formed were taken using a table top scanning electron microscope (SEM–TM1000, Hitachi) without coating the samples with carbon or gold.

2.2.5.6 *Determining the packing density and porosity of supra–particles*

To calculate the particle packing density and porosity of the supra–particles, their masses were measured twice, when dry and wet. The dry particles were measured immediately after fusion at 106 ± 1°C, while the wet mass was measured by permeating the particles with ethanol followed by water. The water was then sucked out using a pipette, and the particles were moved to a filter paper (Whatman) to remove all the excess water on the supra–particles' surface. The wet mass of the particles was then measured. Finally, the supra–particles were placed onto a balance (Sartorius precision balance). Here, the supra–particle volume was calculated by assuming the dry mass and the wet mass using the following formulae, assuming that the dry supra–particles were fully filled with air and the wet particles were fully filled with water:

Dry mass:

$$m_d = V_p \phi \rho_{latex} \tag{2.3}$$

Wet mass:

$$m_w = V_p \phi \rho_{latex} + V_p (1-\phi) \rho_{water} \tag{2.4}$$

From the above values, the volume of the supra–particles can obtain:

$$V_p = \frac{1}{\rho_{water}} [m_w - m_d + (\frac{m_d \times \rho_{water}}{\rho_{latex}})] \tag{2.5}$$

The particles density can be calculated by

$$\rho_p = \frac{m_d}{V_p} \tag{2.6}$$

The volume fraction of supra–particles can be calculated as follows:

$$\phi = \frac{m_d}{V_p \rho_{latex}} \tag{2.7}$$

Where V_p is the porous supra–particle total volume, m_d is the porous supra–particle dry mass m_w, is the porous supra–particle wet mass, ρ_{water} is the water density, ρ_{latex} is the latex density, ρ_p is the porous supra–particle density, and ϕ is the latex volume fraction.

2.2.6 Supra–particle attachments and contact angle measurements at fluid interfaces using drop shape analysis (DSA)

A drop shape analysis instrument (DSA–10 MK2, Kruss) was used to photograph the side images of the particles at the air–water and oil–water interfaces. Different approaches were used to attach the porous supra–particles at the fluid interface. In the first method, a syringe was connected to a glass tube with an outer diameter of 8.1 mm and an inner diameter of 5 mm. In the second one, polystyrene cuvettes were used, and these allowed to form a flat interface of water and air and thus prevent meniscus formation. For oil–water interfaces, a glass cuvette was used. In this case, a flat interface between the two liquids was formed by adjusting the oil and water volume ratio.

2.2.6.1 *Impregnation of porous supra–particles with a fluid phase*

In order to attach the porous supra–particles to a liquid droplet or gas bubble, the pores need to be impregnated with the bulk phase medium. In the following experiments, the method used for impregnating the particles with water, NaCl(aq) solution, hexadecane or gas and then attaching them to air–water and hexadecane–water interfaces are described.

Impregnation with ethanol was the intermediate step in impregnating the particles with water. The porous supra–particles were impregnated with ethanol as air bubbles were found to move out from the pores. After 10 min in ethanol, the particles were transferred to the bulk of Milli–Q water, 10–20 mL, and kept there overnight. On the other hand, the dry porous supra–particles were immersed into hexadecane, 10–20 mL, and the air bubbles were eliminated from the particles by immersing them overnight to ensure that the pores were completely filled with oil.

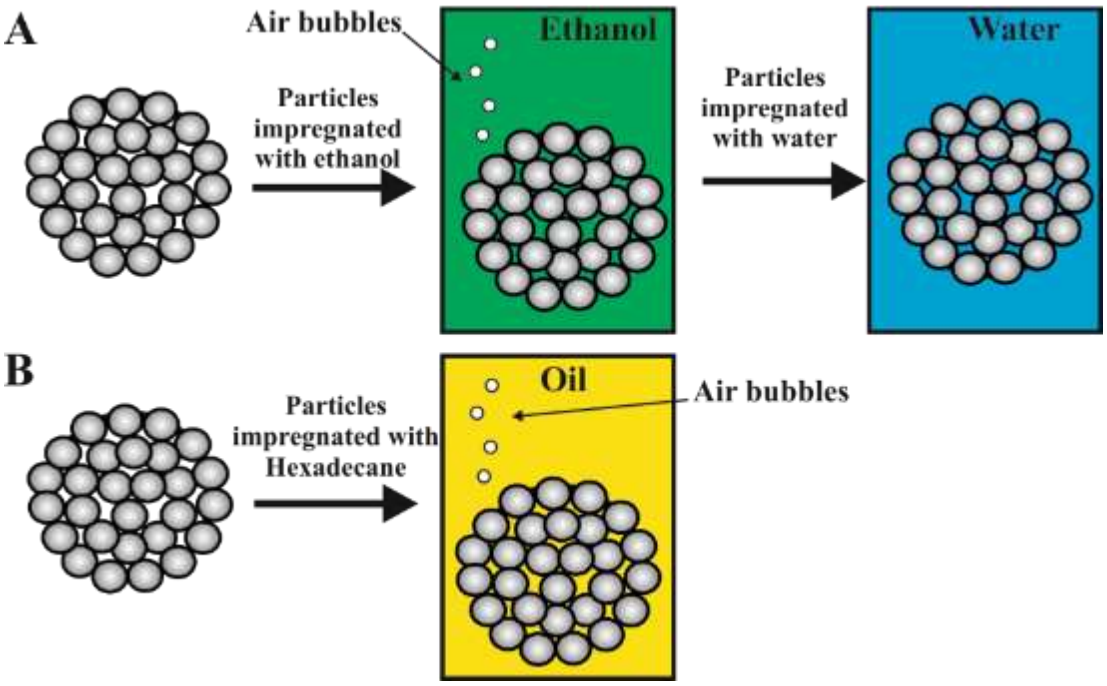

Figure 2.8. Illustration of impregnation of pores with liquids. (A) Particles filled with water need an intermediate solution (i.e. ethanol) to get fully impregnated with an aqueous solution. (B) Particles impregnated with hexadecane. Air bubbles were observed when ethanol and hexadecane were used to impregnate the particles. The particles were placed in water and hexadecane overnight to make sure they were fully impregnated.

To explore the penetration of the liquid front into a dry porous supra–particles were washed in ethanol for 10 min then immersed into a 10^{-5} M solution of Rhodamine 6G (Acros Organic, 99%) for 1 hour and overnight. These particles were characterised using florescent microscopy and confocal microscopy. Another experiment silver nitrate (0.1 M) was also used to determine the penetration into the pores. The particle was first immersed in ethanol, then in water, then transferred into the silver nitrate solution for 30 min under a light source. The particle appeared to be filled with white dots, which reflect the silver nitrate particles.

2.2.6.2 *Porous supra–particles attachment to air–water interfaces*

The aqueous phase in this study was either deionised water or 1 mM NaCl(aq) solution. Two different scenarios were investigated. In the first one, the attachment of a dry supra–particle to the air–water interface was studied (Fig. 2.8). The dry supra–particle

was placed in an empty glass cuvette (20 × 20 × 20 mm, Hellma); then, a glass tube connected to a syringe filled with the aqueous phase was inserted into the cuvette. A water droplet was created at the tip of the tube and the cuvette with the dry supra–particle was moved towards the water pendant drop until the particle was attached to the droplet. After the particle was attached to the water droplet, force was applied by pushing the particle into the water droplet to the maximum to reach the equilibrium contact angle and a series of side images were taken by the camera of the DSA 10 instrument. After the experiment, the particle was washed in ethanol, dried overnight at room temperature and used again. In the second series of experiments, the supra–particle was first impregnated with the aqueous phase and placed in a cuvette filled with water. Then, the tube connected to the syringe filled with air was immersed in the cuvette, forming a bubble at the tube tip. The wet supra–particle was attached to the bubble surface by lifting the cuvette with the particle, and the procedure for the attachment of dry particle described above was followed.

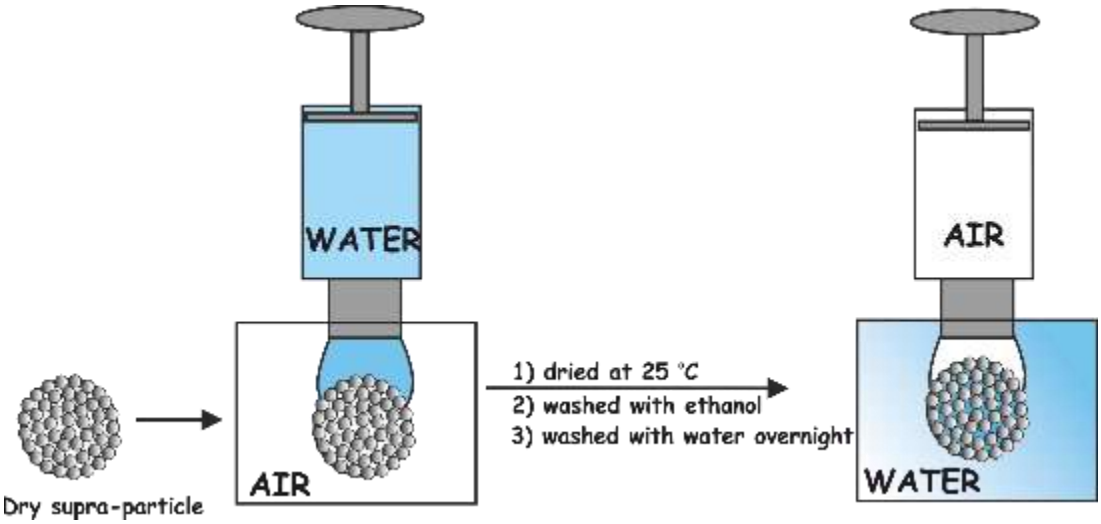

Figure 2.9. Schematic for dry (left) and wet (right) porous supra–particle attachment to air–water interfaces.

2.2.6.3 *Porous supra–particle attachment to hexadecane–water interfaces*

The procedures followed in these experiments were similar to those followed for the air–water interface experiments. Again, two sets of experiments were performed: (i) the supra–particle impregnated with oil was attached to the oil–water interface from

the oil phase and (ii) the supra–particle impregnated with water was attached to the oil–water interface from the aqueous phase (Fig. 2.9).

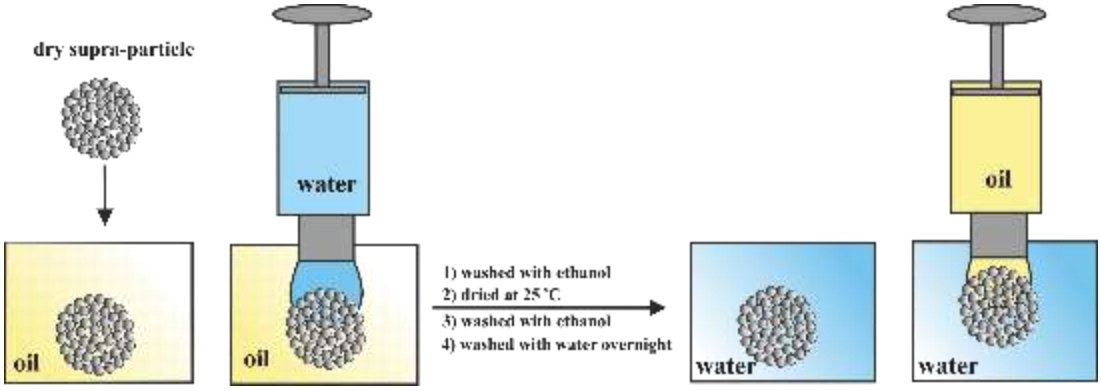

Figure 2.10. Illustration showing how the water penetrates into the pores and how the particle was attached to the water pendant droplet or air bubble.

2.2.6.4 *Vibrational method to determine the global minimum energy for the equilibrium contact angle for porous particles at oil–water interfaces.*

Mechanical vibrational methods were developed using two different approaches to find the equilibrium contact angle, i.e. by using an ultrasonic probe or ultrasonic bath.

For studying the dry porous particles, they were placed at the air–water surface and vibrated using a Vibra–Cell ultrasonic probe (3 mm in diameter, Sonics & Materials) at different amplitudes ranging from 0% to 100% in continuous mode for 10 min (Fig. 2.10).

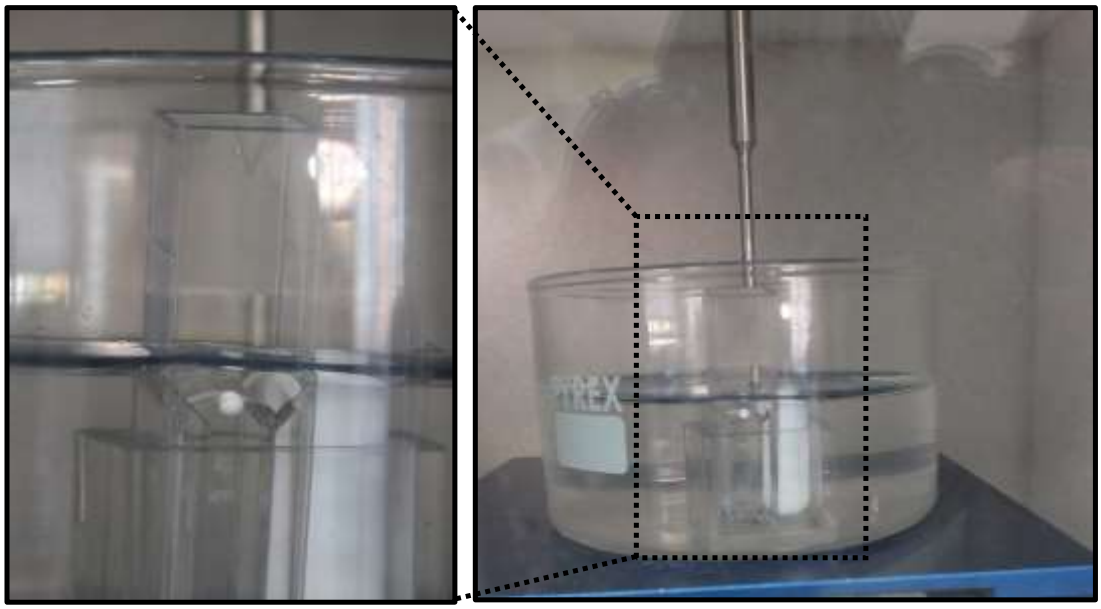

Figure 2.11. Photograph of dry porous supra–particles (1.7 ± 0.2 mm) at the air–water interface using an ultrasonic probe ranging from 0% amplitude to 100% amplitude.

2.2.6.4.1 Wet particles with water

In the experiments with wet porous supra–particles, the dry porous particles were initially washed with ethanol to extract all the air from the pores. These particles were then immersed in water or 1 mM NaCl(aq) in a glass cuvette to replace the ethanol overnight. The water was sucked out almost completely until the particle was covered with a thin layer of water (Fig. 2.11A). Then, ultrasonication was applied for different periods of time (1–30 minutes) using an ultrasonic bath (U100, Ultrawave) or an ultrasonic probe. Then, water was added to raise the particles gradually. Alternatively, a wet porous particle is attached to water using a spatula at the air–water interface and vibrated the particle.

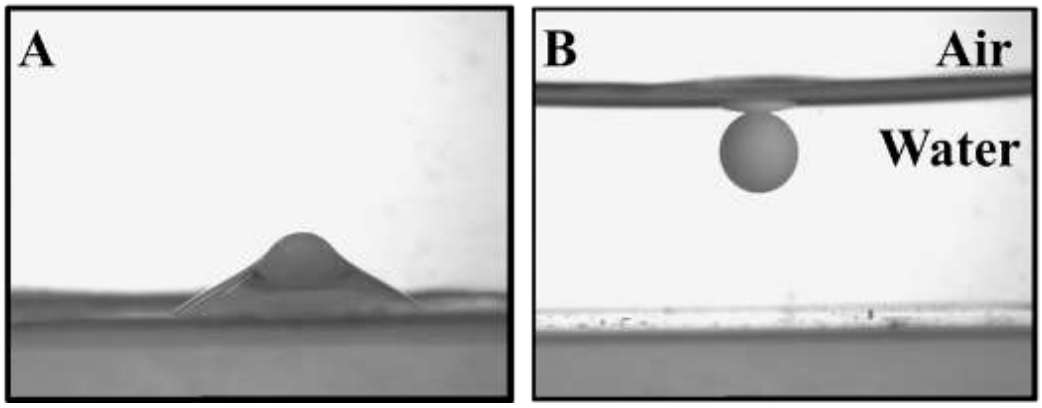

Figure 2.12. Attachment of wet porous particles at air–water interface after (a) vibrating the particles at thin film and (B) injecting water to make the particles float.

2.2.6.4.2 Wet particle with hexadecane

In the experiments with the oil–water interface, the dry particles were first impregnated with hexadecane. After that, the cuvette was filled with water, and oil was added on top of it, followed by the particles. Different images were taken before and after attachment. Then, ultra–sonication was applied for different periods of time (1–20 minutes) using an ultrasonic bath (U100, Ultrawave).

2.2.6.5 *Calculation of the contact angle of supra–particles*

In order calculate the contact angle of the porous particles attached to air–water and oil–water interfaces, a macro script was developed on Image Pro Plus V6 to account for the curved contact line. The apparent macroscopic contact angle of the porous supra–particles attached to the liquid interface was determined from their side images using a drop shape analysis system. The contact angle degree for particles filled with water attached to air–water or hexadecane–water interfaces was determined using the following equation:

$$\cos\theta = 1 - \frac{2b}{D} \tag{2.8}$$

Where D is the particle diameter, b is the particle protrusion through water, and θ is the contact angle. The apparent contact angle of supra–particles filled with air or oil was calculated using the formula below:

$$\cos(\pi-\theta)=1-\frac{2b}{D} \tag{2.9}$$

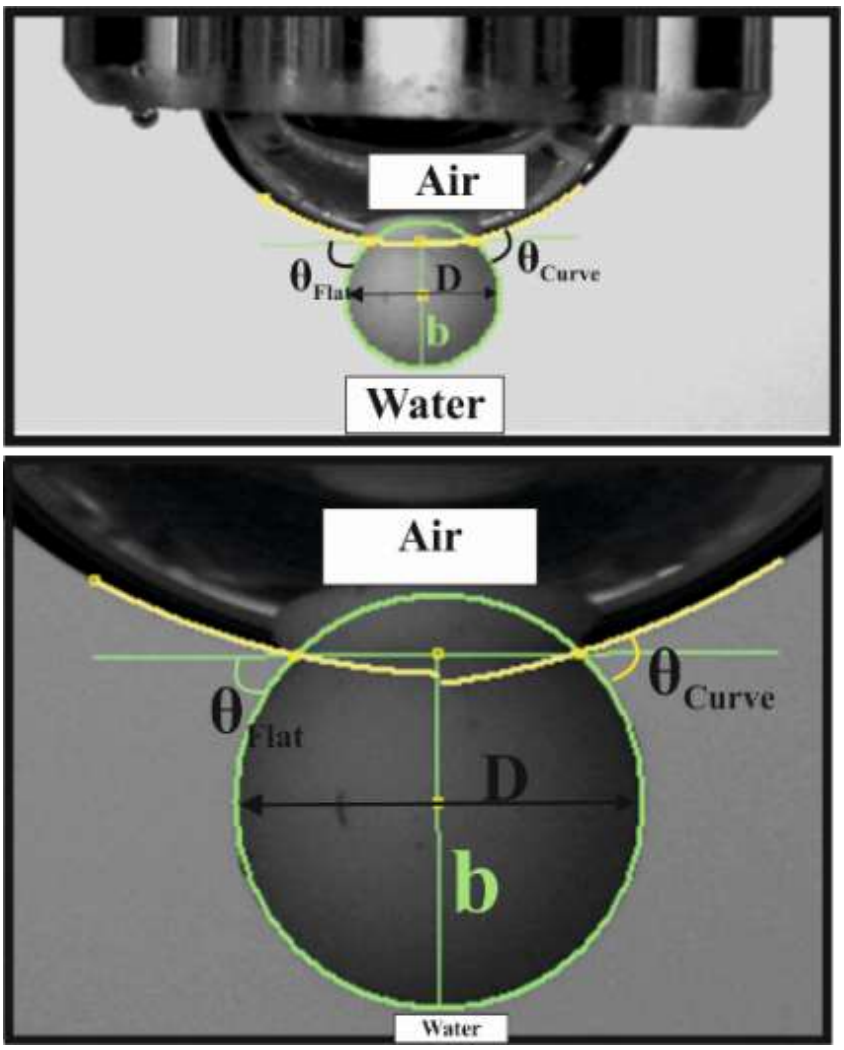

Figure 2.13. Side image obtained from DSA 10 for a porous supra–particle (1.7 0.2 mm) filled with water attached to an air bubble. D is the particle diameter, b is the particle protrusion through water, and θ_{Flat} and θ_{Curve} are the contact angles for flat liquid surface contact angle (FCA) and curved liquid surface contact angle (CCA), respectively.

2.2.6.6 *Magnetic resonance imaging method for determining the liquid front penetration in porous supra–particles attached to liquid interfaces*

Magnetic resonance imaging (MRI) is a method used for generating images of the interior parts of objects by using magnetic field and pulses of radio wave. In our study, MRI was used to investigate the penetration of liquid into porous supra–particles with

adequate resolution and satisfactory contrast. Porous supra–particles (1 mm) were used dry or initially infused with different fluids (hexadecane, water, or 1 mM gadolinium (III) chloride solution). In order to wet the particle with water or gadolinium solution, ethanol (Fisher) was used as an intermediate phase between air and water. The ethanol helped in the penetration of water into the particle pores overnight. A vacuum desiccator (10 min) was used to improve the penetration of ethanol and water into the particle pores. Hexadecane was used as the oil phase, which penetrated directly into the dry particle pores. A vacuum desiccator (10 min) was used to remove any air remaining inside the particle pores. The particle (1 mm) was inserted into a capillary tube and then into a coil holder attached to the NMR probe. The particle was wetted with water then imaged using MRI. After that, hexadecane was added in order to see how the oil could penetrate into the pores. The nuclear magnetic resonance (NMR) detect the presence of proton (i.e. Hydrogens) by applying a magnetic field to the samples. For that reason, the oil has a brighter colour than water, due to variation in proton density, thereby decreasing the contrast inside the particle.

A composite supra–particle (1 mm) was imaged using the Bruker AVANCE 2 wide bore 11.74 T magnet fitted with a Bruker microimaging probe with a 2 mm solenoid coil (Figure. 2.13). Standard pulse sequences from the Bruker Paravision library were used. Multi Spin Multi Echo (MSME) sequences were acquired using the solenoid coil and Bruker's MSME_Bas sequence. The image slice thickness was 0.17 mm, and the resolution was about 20 µm. The readings were taken under a constant temperature of 18–20°C; each image capture took approximately 1 hour.

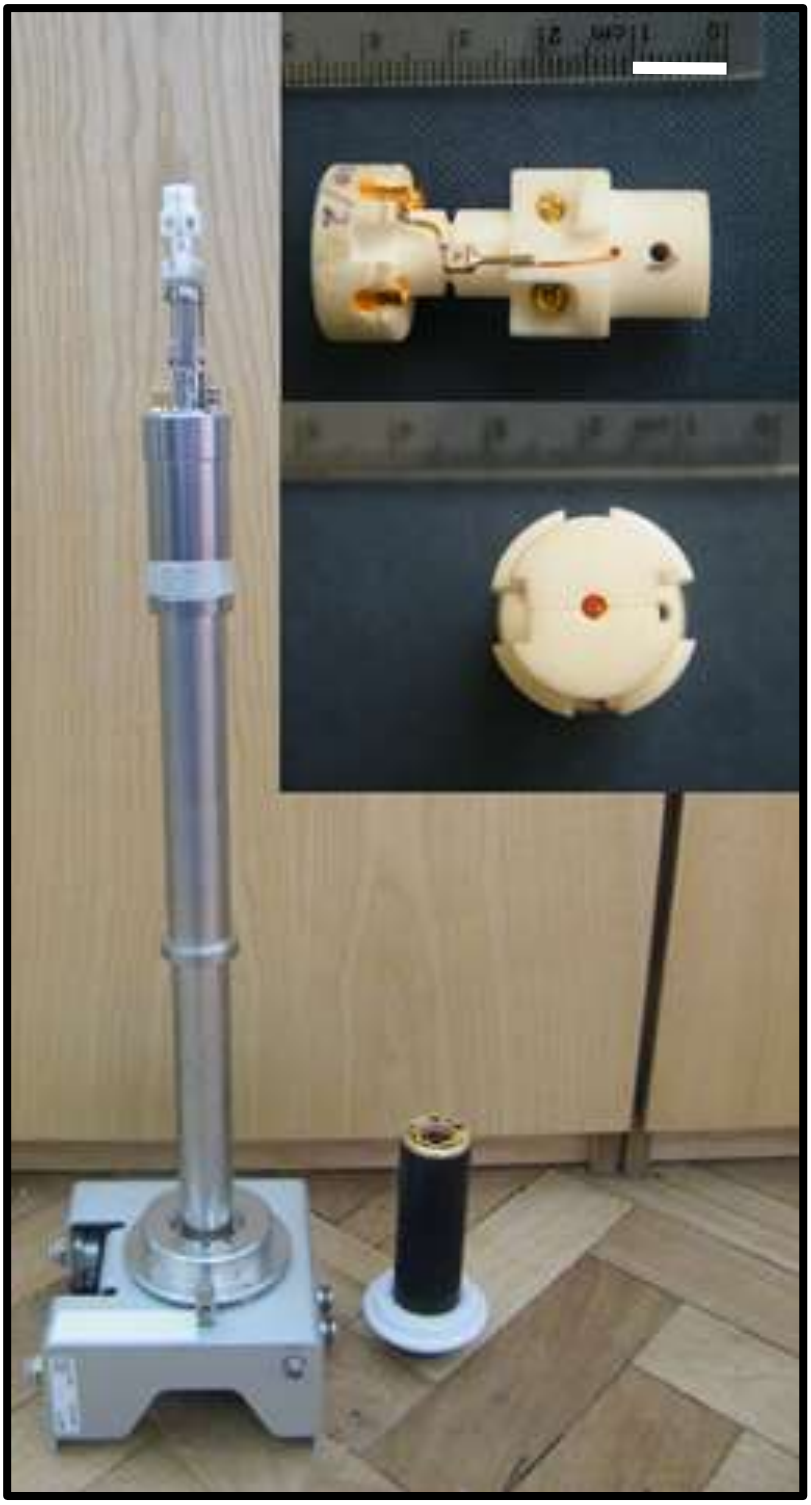

Figure 2.14. Pictures of the probe used for the MRI experiment to visualise the penetration of liquid into the porous particles. Photographs (side and top) of the 2 mm solenoid coil attached to the Bruker microimaging probe.

Chapter 3: Adsorption of shape–anisotropic and porous particles at the air–water and the decane–water interfaces studied by the Gel Trapping Technique

3.1 Introduction

The use of solid particles as foaming agents and emulsion stabilisers has found applications in the formulation of food, pharmaceutical, and cosmetic products.[61, 119-122] Over the last 15 years, the importance of the wetting properties of solid microparticles and nanoparticles at liquid surfaces[4, 119-120, 123-133] has been recognised and studied intensively in relation to the stability and the types of Pickering emulsions.[134] The behaviour of spherical particles at liquid interfaces is governed by the particle three–phase contact angle, θ, and is well studied and understood. The wetting properties of both hydrophilic ($\theta < 90°$) and hydrophobic ($\theta > 90°$) particles depend on the particle surface properties, temperature, and electrolyte concentration in the system.[2, 5, 44, 123, 135] It is well documented that hydrophobic (hydrophilic) particles tend to stabilise water–in–oil (oil–in–water) emulsions at equal oil/water volume fractions.[134]

Many formulations, however, contain solid particles with anisotropic shapes, varying from needle–like microcrystals to particles of cubic symmetry as well as fibre–like particles of very large aspect ratios. In addition, many powder particles used in formulations are porous or agglomerated from smaller particle aggregates. The adsorption behaviours of such complex particles cannot be described solely by the value of the three–phase contact angle since the particle shape and internal structuring can play an important role in their orientation at the liquid interface (see Figure **3.1**). For example, multiple orientations of adsorbed anisotropic particles are possible at the liquid interface.[122] In addition, the interparticle interaction can also play an important role in how shape–anisotropic particles organise themselves in dense layers at the liquid interface[38, 40, 136-137]. The determination of wettability and adsorption behaviour of particles of different shapes and sizes in particular on the nano– and microscale at liquid surfaces has been an area attracting much interest for a long time and is of

importance for many advances in food science,[61, 121] cosmetics, and pharmaceuticals.[119]

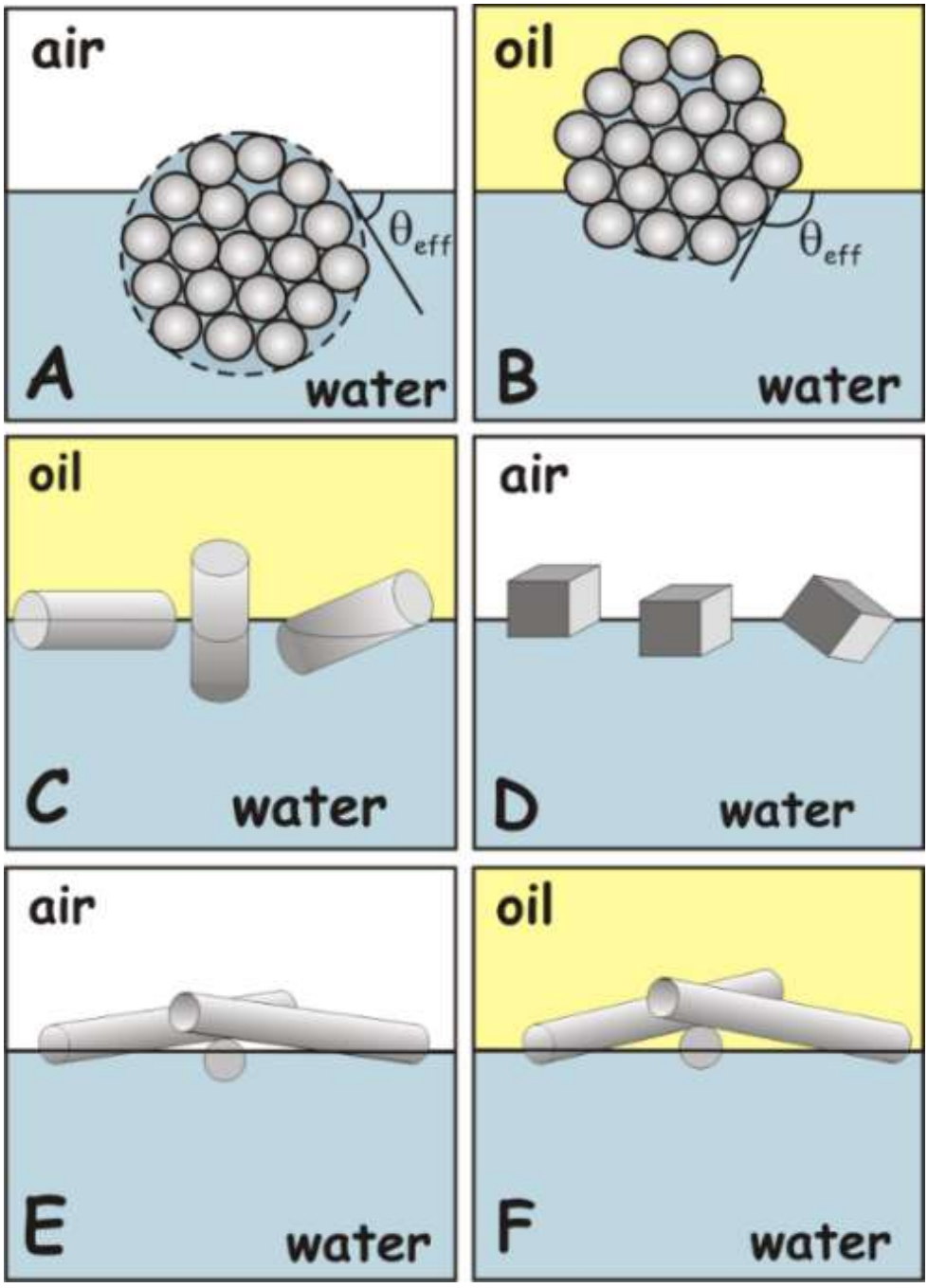

Figure 3.1. Scheme of a solid porous microparticle adsorbed at (A) the air–water and (B) the oil–water interface. The position of the porous particle (or a particle aggregate) when adsorbed at the liquid interface depends on the effective contact angle, θ_{eff}, which is different from the contact angle of the individual particles in the aggregate. Needle–like (C) and rhombohedra–like microcrystals (D) may have several possible orientations at the liquid interface. (E–F) The orientation of microfiber particles when

adsorbed at liquid surfaces may also depend on the packing conditions and their surface concentration at the air–water and the oil–water interface.

In this chapter, the GTT were used, described in section 2.2.4, to investigate how anisotropic particles of different types adsorb and orientate at the air–water and oil–water interfaces. calcite microcrystals with rhombohedra–like shape and an average size of around 10–15 µm and needle–like aragonite microcrystals with an aspect ratio of 5–10 and lengths of up to several tens of micrometres, and much longer microfibers of ethyl cellulose were explored at the air–water and the oil–water interfaces. In addition, also the adsorption of two types of highly porous silica particles (up to 95% porosity) at the air–water and decane–water interfaces were examined. The GTT is a very robust method for visualising the microstructure and the orientation of the anisotropic particles within the adsorbed particulate layer at the liquid surface.

Samples of the Aeroperl® 300/30 hydrophilic particles and VP Aeroperl R806/30 – hydrophobic silica particles were dispersed in isopropyl alcohol (IPA) and spread at the liquid interface in the GTT experiments. The PDMS mould of the set gellan solution was washed in a hot aqueous solution of EDTA to remove gellan residues, dried, and imaged by SEM after coating with carbon.

3.2 Results and Discussion

3.2.1 Anisotropic particles

The needle–like aragonite microcrystals, calcite rhombohedra–like microparticles, and ethyl cellulose microfibers were expected to adsorb at the liquid interface differently to spherical particles, such as latex, owing to their inherent shape anisotropy. Although it is not practical to estimate the contact angle of these particles, SEM images can reveal the possible orientations at the liquid surface and their preference to one of the adjacent phases.

3.2.1.1 Aragonite microcrystals

The needle–like aragonite microcrystals spread at the air–water interface were successfully moulded in the PDMS by the GTT. Figure **3.2** a shows the surface of the PDMS. There was a high surface concentration of adsorbed aragonite microcrystals which seemed to aggregate. The majority of the microcrystals were parallel to the

plane of the interface. The ones that were perpendicular to the interface tended to be part of the aggregates where there was not enough surface area to accommodate them in parallel orientation. It can also be seen that the surface of the PDMS around the uprightly orientated aragonite microcrystals was not flat, as the PDMS replica had also captured the shape of the liquid meniscus around the particles. This can be seen more clearly in Figure **3.2** b and Figure **3.2** c, which show a close–up of some aragonite crystals on the PDMS. This indicates that the aragonite microcrystals at high surface concentration are also subject to lateral capillary forces which enhance the particle clustering at the interface.[138] The sample with aragonite microcrystals spread at the decane–water interface, however, shows a different picture. The number of adsorbed microcrystals present at the surface replica is vastly reduced, and because of this, the crystals that are present seem to be isolated and not aggregated as seen in Figure **3.2** d. All microcrystals in this case were found to orientate along the interface. Ballard et. al [139] proposed a computational model which predict the adhesion energy and the equilibrium orientations of anisotropic particles at interfaces. They found that individual ellipsoidal particles at the interface energetically favoured to orientate parallel to the plane of the interfaces. Furthermore, the aggregated ellipsoidal particles prefer to orientate perpendicular to the plane of the interface [139]. The adsorption of individual and aggregated aragonite microcrystal particles at the interface agrees with this model. Although in the cases of both the air–water and decane–water interfaces, a large proportion of the spread aragonite microcrystals remained in the water phase and did not attach themselves to the interfaces. However, as shown in Figure 3.3 these particles seemed to attach themselves strongly (and at higher concentration) to the air–water interface. At present, this adsorption behaviour is not completely clear and it does not seem to be directly related to the particle contact angle but could be related to the adsorption barrier of the microcrystals at the respective liquid interfaces. The adsorption barrier is existed between the particles and the interface which can be overcome once the particles adsorbed to the interface by using isopropanol as spreading solvent[140].

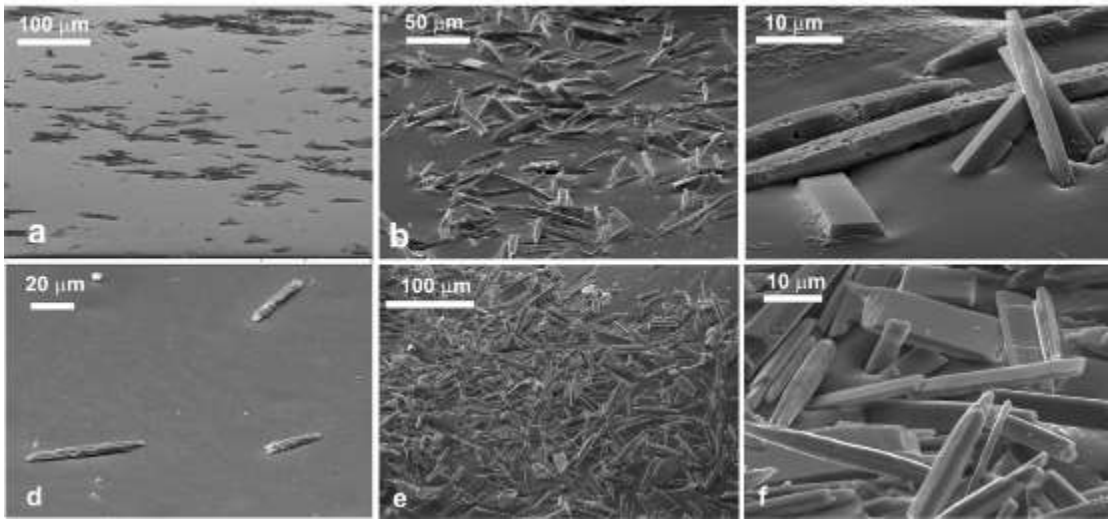

Figure 3.2. (a)–(c) SEM images of aragonite microcrystals adsorbed at the air–water interface followed by its replication with PDMS by using the Gel Trapping Technique (GTT). The parts of the aragonite microcrystals immersed in the PDMS have been exposed to the air phase when adsorbed at the air–water interface. Sample area of low (a) and high (b–c) surface concentration of aragonite microcrystals; (d)–(f) SEM images of aragonite microcrystals adsorbed at the decane–water interface followed by its replication with PDMS by the GTT. The exposed parts of the microcrystals were originally immersed in the aqueous phase. Sample areas of low (d) and high (e), (f) surface concentration of aragonite microcrystals.

3.2.1.2 Calcite microcrystals

The rhombohedra–like calcite microcrystals adsorbed at the air–water interface were successfully moulded with PDMS. The SEM images of the PDMS replica of the surface showed that some of the calcite microcrystals were attached to the PDMS (replacing the air phase) with the face of a rhombohedral in the plane of the interface. Some cubes appear to have been removed due to the stretching of the PDMS surface during the SEM sample preparation. Moreover, problems were faced with the complete removal of traces of gellan on the PDMS replica as excessive heating or EDTA treatment led to the dissolution of the calcite microcrystals as well as the gellan residues. When spread at the decane–water interface, very similar attachment was observed of calcite microcrystals at the interface as at the air–water interface. the configurations of adsorbed individual calcite microcrystals was counted at the liquid interface after being replicated with PDMS at the air–water and oil–water interfaces.

However the method were used in section 2.1.5.2 produced a non–homogenous and polydisperse calcite microcrystal particles. The particles were differentiated as face–on–surface, half–way through and tilted, by their different adsorption behaviour at the interfaces. The face on particles are the adsorbed particles but did not wet and they are just attached to the interface (as shown in Figure 3.3 a and e). While Figure 3.3, b and c shows the half–way particles which are fully adsorbed (i.e. sunken into the PDMS replica surface) with different height. In addition, the tilted particles were also adsorbed to the interface in very small population. The results are presented in Figure **3.3** for three typical configurations which could be distinguish on the SEM images. The data show very similar frequencies of the occurrence of all these configurations for both air–water and decane–water interfaces. Typically, about 80% of the adsorbed calcite microcrystals were attached to one of the faces of the rhombohedral at the liquid interface as expected (Figure **3.3** a, b, e).

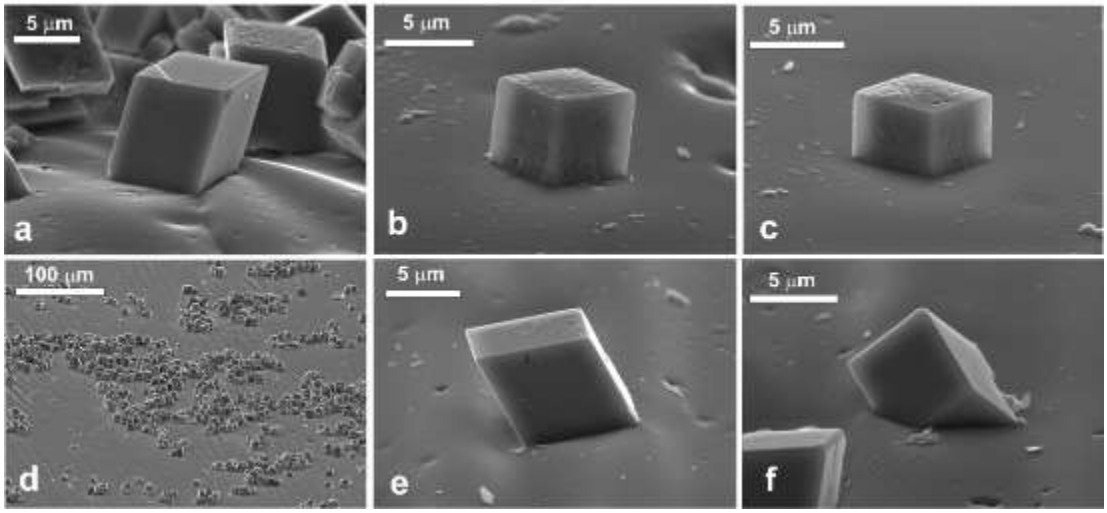

Figure 3.3. (a)–(c) SEM images of calcite microcrystals adsorbed at the air–water interface followed by its replication with PDMS using the GTT. The parts of the calcite microcrystals immersed in the PDMS have been exposed to the air phase when adsorbed at the air–water interface. (d)–(f) SEM images of calcite microcrystals adsorbed at the decane–water interface followed by its replication with PDMS using the GTT. Images viewed at angle of 65°.

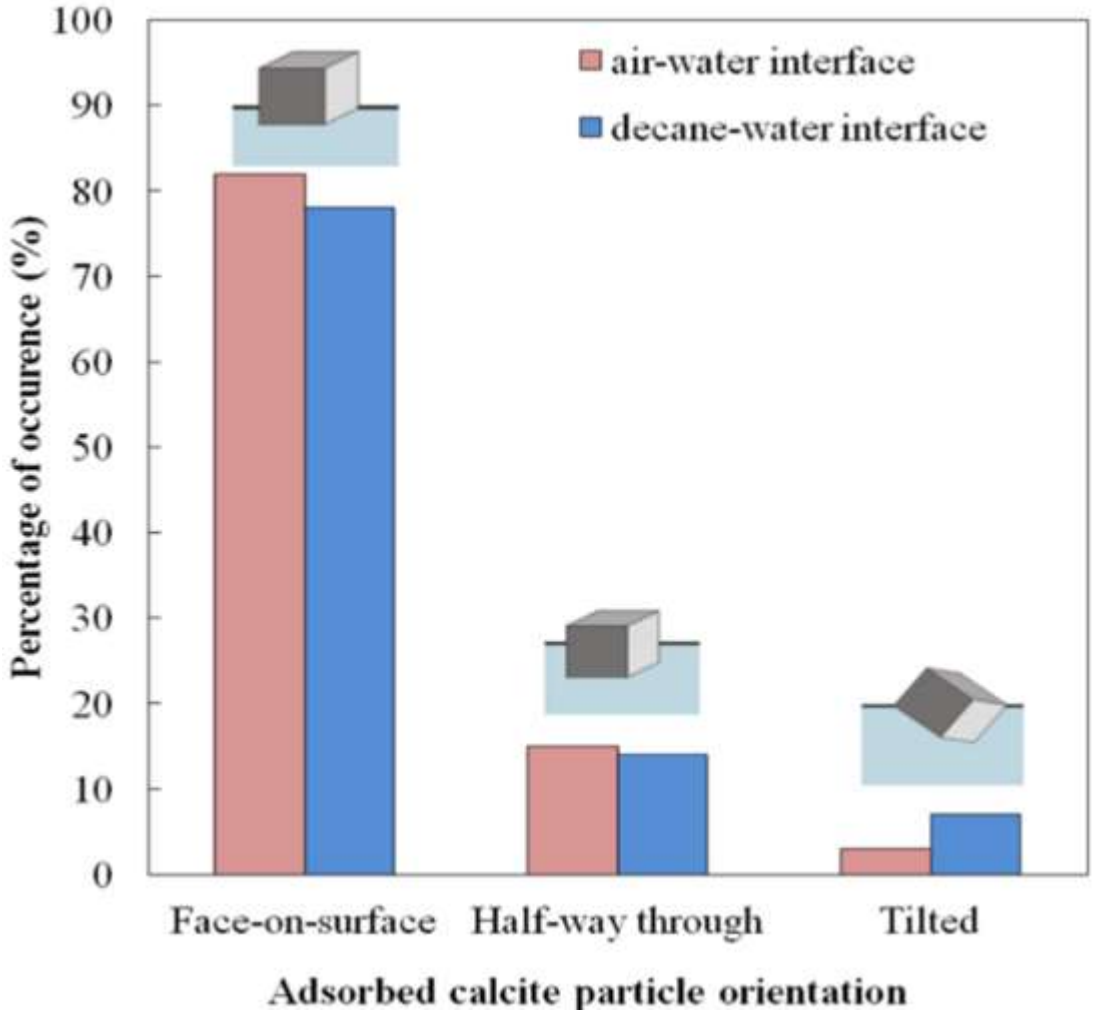

Figure 3.4. Percentages of the occurrence of particle surface orientations for three most typical configurations of adsorbed calcite microcrystals at the air–water and decane–water interfaces.

The second most typical configuration can be seen in Figure **3.3** c, accounting for about 14–15% of all configurations. The rest of the calcite particles were in tilted configurations. The clustering of the particles and the small frequency of occurrence of this configuration did not allow us to determine the distribution of the tilting angle of the adsorbed calcite particles. Several SEM images were taken from different parts of the sample surface. As seen on each SEM image taken with high resolution, there are tens and even hundreds of particles imaged at the interface, facilitating zooming on individual particles and evaluating their orientation with respect to the liquid interface. The data shown in Figure **3.4** are accumulated from 2–4 SEM images with several tens of particles, each for both air–water and oil–water interfaces.

3.2.2 Ethyl cellulose microfibres

The layer of ethyl cellulose fibres spread at the air–water interface was successfully replicated with PDMS using the GTT. A large population of fibres seem to aggregate. It is clear from the SEM images that the fibres are fairly polydisperse in terms of length and diameter. Figure **3.5** a shows a large number of fibres on the surface of the PDMS. It can be seen that although the majority of the length of the fibres is in the water phase, the ends tend to be sticking into the oil phase (represented in the PDMS replica). It can be seen that the fibres are present mainly in the aqueous phase (see the exposed part of the fibres surface in the PDMS replica). This indicates that the contact angle of the ethyl–cellulose fibres at the air–water interface is smaller than 90°, although it was difficult to determine this quantitatively from the images. Figure **3.5** b–c shows a close–up of some of the fibres. It can be seen that the fibres are quite textured (rough). This could explain their behaviour since surface roughness affects the wettability of a material, as mentioned in the introduction. According to Wenzel's model for wetting of rough surfaces,[141-142] if the smooth surface is hydrophilic, its rough surface equivalent is even more hydrophilic.

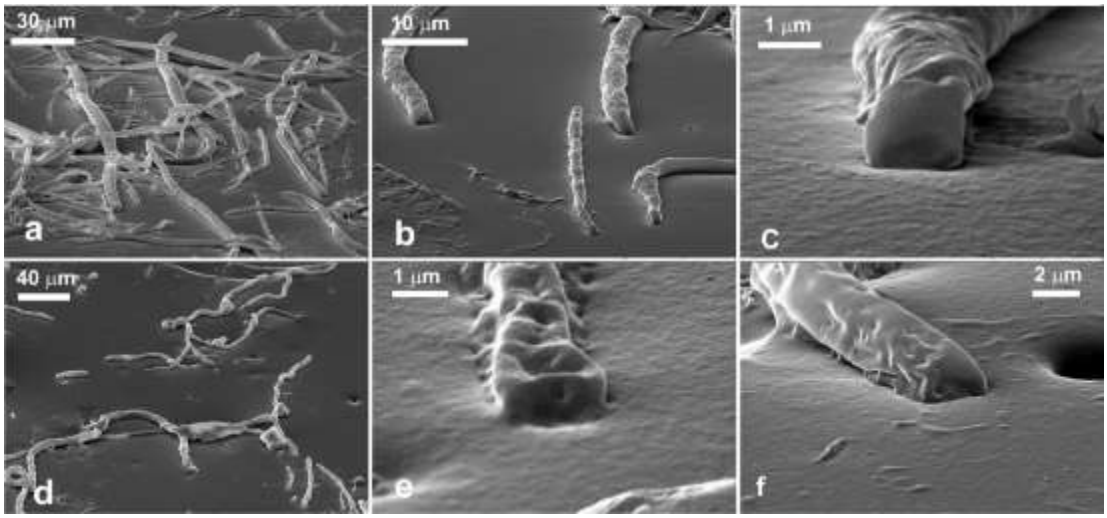

Figure 3.5. (a)–(c) SEM images of ethyl cellulose microfibres adsorbed at the air–water interface followed by replication with PDMS using the GTT. The parts of the microfibres immersed in the PDMS were exposed to the air phase when adsorbed at the air–water interface. (d)–(f) SEM images of aragonite microcrystals adsorbed at the decane–water interface followed by replication with PDMS using the GTT. The parts of the aragonite microcrystals immersed in the PDMS were originally immersed in the

decane phase when adsorbed at the decane–water interface. The exposed surface of the microfibres was originally immersed in the aqueous phase.

On the SEM images, it was observed that the ends of the ethyl–cellulose fibres were much smoother than the fibre surface along the length. This observation seems consistent with the fact that the fibre ends are less hydrophilic than the rest of the fibre surface owing to their roughness. The number of ethyl cellulose fibres present at the oil–water interface is lower than that present at the air–water interface. Similar to the crystal case, there seems to be less aggregation. The fibres that are at the interface seem to be twisted and have loops in them (Figure **3.5** d), in contrast to the air–water interface, where the fibres tend to be straight and untwisted. It was also observed that the ethyl–cellulose fibres are slightly less exposed to the aqueous phase when adsorbed at the decane–water interface. This intermediate hydrophobicity at both the air–water and oil–water interfaces is consistent with their ability to stabilise well both foams and emulsions.[143-145]

3.2.3 Hydrophilic porous silica microparticles

The VP Aeroperl® 300/30 particles spread and adsorbed at the air–water interface were successfully moulded with PDMS using the GTT. Figure 3.6 shows the surface of the PDMS replica. The particles appear to be sitting within the surface, and there is a large size distribution present. The particles behaved as anticipated. They are hydrophilic; hence, they were expected to be exposed preferentially to the water phase, when adsorbed at the liquid surface, as demonstrated in Figure 3.6 a. The hydrophilic porous silica particles spread at the decane–water interface were successfully moulded in the PDMS using the GTT as well. Figure 5 b shows the surface of the PDMS. Note that the average size of the particles present at the liquid interface is much smaller than that of the original polydisperse particle sample (Figure **3.2** b); on the liquid surface, the adsorbed particles were all smaller than 2 μm. It is also interesting to note the fact that there is no agglomeration of the particles at this interface. This could be due to repulsion of the particles from each other [143] at the original oil–water interface. Notably, much larger particles were present at the air–water system. It seems that only a fraction of smaller porous particles successfully spread and adsorbed at the decane–water interface with the IPA as a spreading solvent. The reasons behind this result are could be because of the weight of larger particles (i.e. 30^{o} μm) did not mentation their

position at decane-water interface. From the SEM images, the contact angles were estimated of these hydrophilic particles as 25 ± 5° when adsorbed at the air–water interface and 27 ± 4° at the decane–water interface.

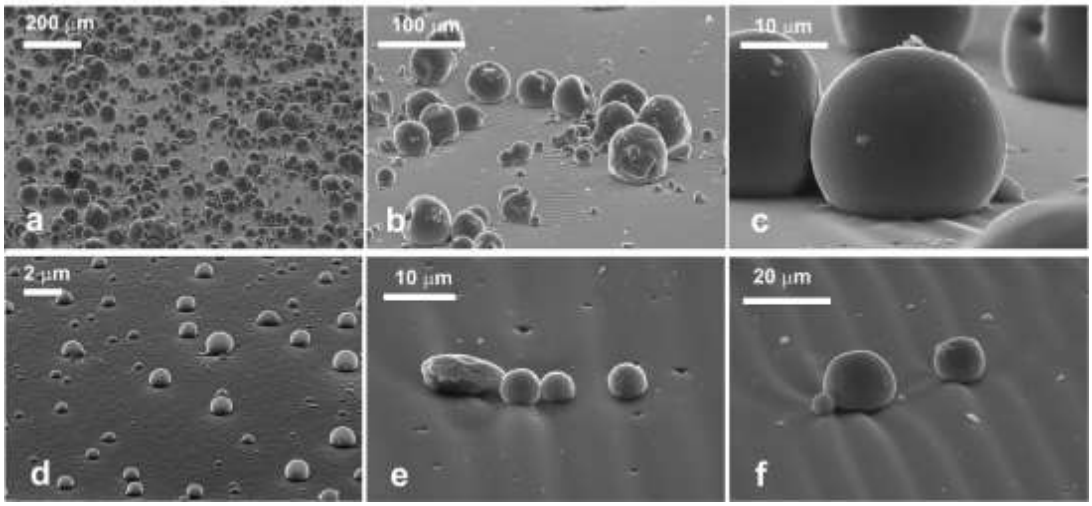

Figure 3.6. SEM images of hydrophilic porous silica particles (VP Aeroperl® 300/30) adsorbed at the air–water interface (a)–(c) and the decane–water interface (d)–(f) followed by the surface replication with PDMS using the GTT. The samples were imaged at a viewing angle of 65° between the electron beam and the detector. The exposed part of the particle surface was exposed to the aqueous phase when adsorbed at the air–water surface (a)–(c) and the decane–water interface (d)–(f).

3.2.4 Hydrophobic porous silica microparticles

The hydrophobic (VP Aeroperl® R806/30) porous particles were not successfully spread and mould at the air–water interface. The hydrophobic porous silica particles spread at the oil–water interface were successfully moulded in the PDMS using the GTT, as shown in Figure **3.7**. As expected, the particles were predominantly exposed to the decane phase (replaced by the PDMS in the replica) and it appears that there was a variety of particle sizes present. The SEM images indicate that the contact angle of the porous hydrophobic silica was well over 90° at the decane–water interface. The approximate value was estimated of the contact angle of these porous hydrophobic particles at the decane–water interface by extrapolating the particle profile with a circle; a large portion of the particle surface was embedded in the PDMS replica. This estimate gave an average particle contact angle of 149 ± 4°.

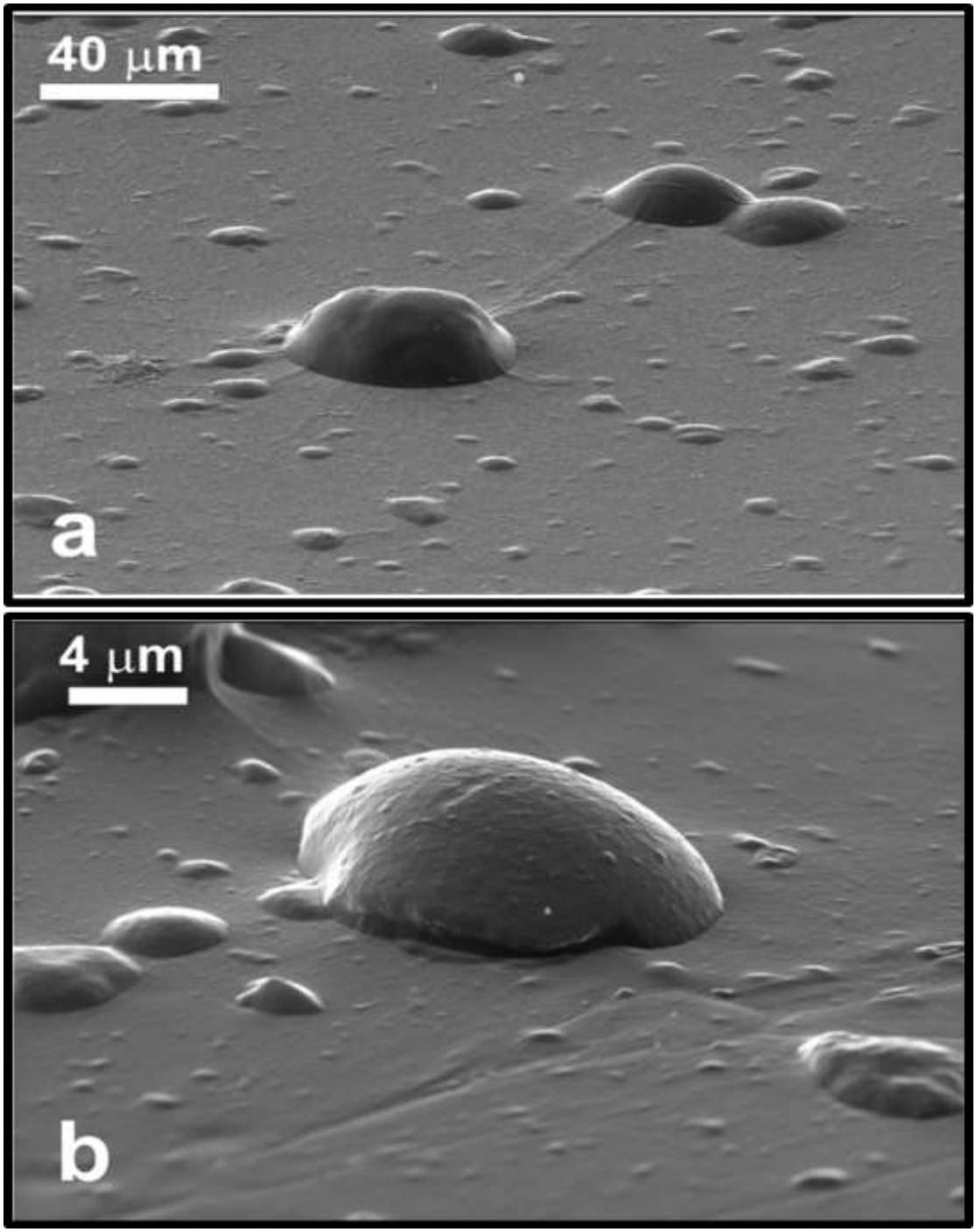

Figure 3.7. SEM images of hydrophobic porous silica particles (VP Aeroperl® R806/30) adsorbed at the decane–water interface followed by the liquid surface replication with PDMS using the GTT. The samples are imaged at a viewing angle of 65° between the electron beam and the detector. The exposed parts of the particle surface were immersed in the aqueous phase when adsorbed at the decane–water interface (a) and (b) correspond to different resolutions.

3.3 Conclusions

The GTT was used to explore how several different types of shape–anisotropic particles and porous silica microparticles adsorb and orientate at the air–water and oil–water interfaces. This approach involves the use of a hydrogel solution as the water phase, which "arrests" the position of the adsorbed particles at the liquid interface after setting. It is then moulded using PDMS and viewed using high–resolution SEM. The anisotropic particles used were calcite (rhombohedra–like microcrystals) and aragonite (needle–like microcrystals), both polymorphic forms of calcium carbonate. the adsorption of ethyl cellulose microfibers with much larger aspect ratios were investigated at both liquid interfaces. Although no particle contact angles were determined owing to the complex shapes of the anisotropic particles, some general trends in their attachment and orientation at the liquid interfaces were observed. The rhombohedral–like calcite microcrystals when attached (by spreading with IPA) at the air–water interface tended to have a face of the crystal in the plane of the interface, with almost the entire crystal in the water phase. The intermediate orientation of the calcite microcrystals at the interface were not observed any fixed angle, indicating that the microcrystals may be trapped in non–equilibrium positions because of contact angle hysteresis. The aragonite needle–like crystals were successfully moulded with PDMS at both the air–water and decane–water interfaces. At both interfaces, these microcrystals seem to preferentially lie in the plane of the interface. However, significant reorientation of the aragonite microcrystals to the upright position was observed when they were spread at a high concentration at the air–water interface. Ethyl cellulose fibres were successfully moulded with PDMS at both the air–water and the decane–water interfaces. The ethyl cellulose microfibers tended to aggregate at the liquid interface and in both cases, the ends of the microfibres seemed to prefer to be in the non–aqueous phase (air or oil), and this was attributed to surface roughness differences. The porous silica microparticles, both hydrophilic and hydrophobic, were also examined at the air–water and decane–water interfaces. The porous hydrophilic silica particles were positioned almost entirely in the aqueous phase when adsorbed at the both air–water and oil–water interfaces, although the size of the particles attached at the oil–water interface was much smaller (~2 μm) than the average particle size of the original polydisperse sample (~30 μm) . The reason for large hydrophilic particles would not adsorb to the decane–water interface is due to low contact angle and the

weight of these particles which deformed and detached from the interface. The hydrophobic porous silica particles were positioned almost entirely in the oil phase. Porous hydrophobic silica particles were not spread and moulded successfully at the air–water interface. For each particle type, there were more particles/fibres attached at the air–water interface than at the oil water interface, except for the hydrophobic porous silica particles. In conclusion, the GTT was applied successfully to anisotropic and porous particles to study their adsorption and orientation behaviour at liquid surfaces. The results can provide valuable information about the structuring of anisotropic particles at liquid surfaces in various industrial products and formulations containing anisotropic particles, as stabilisers of foams and emulsions.

Chapter 4: Adsorption of carboxylic–modified latex at a liquid–liquid interface studied by the gel trapping technique

4.1 Introduction

The wettability of solid particles has attracted considerable interest during the last few decades owing to its importance in many practical applications in the pharmaceutical, cosmetic, and food industries; preparation of building materials and paints; waste water treatment; and secondary oil recovery.[2-5] Small solid particles can spontaneously attach themselves to the interface between a liquid phase and another fluid, and the affinity of these particles to the adjacent fluid phases is characterised by the equilibrium three–phase contact angle, θ, which is related to the surface energies of the liquid–fluid interface and the particle–fluid interface exposed to the two fluid phases. Knowledge of the wettability of particles is required in order to understand their interactions and behaviour at liquid interfaces.[19, 146] For example, it is possible to predict the type of Pickering emulsion that may occur when using solid particles as emulsifiers by measuring the particle contact angle.[4, 19, 29-30, 61] Particles with contact angles smaller than 90° tend to stabilise oil–in–water emulsions while those with contact angles higher than 90° show that the solid particles are more likely to stabilise water–in–oil emulsions.[19, 24-25, 29-30, 147] Similar relationships exist between the particle three–phase contact angle and the formation of particle–stabilised foams and liquid marbles.[65, 148-150] The functionalisation of the particle surface with terminal groups of different polarity or ionisation ability than the particle core material allows the particle to change its wettability depending on the surrounding fluids, favouring lower or higher contact angles.[4, 146] However, the link between the degree of ionisation (i.e. the surface charge) and the particle contact angle is still not fully understood. This problem is addressed by our study in the current chapter. the GTT were used, described in section 2.2.4, to investigate the contact angles of carboxylate–modified latex (CML) particles with diameters in the range of 0.9–3 μm and carboxyl groups with different densities on their surface (Table 2.2) at the air–water and oil–water interfaces. It is expected that the density of carboxyl groups at the particle surface would affect the particle contact angle as illustrated in Fig. 4.1. The results obtained for their contact angles are linked to the type of emulsion stabilised by those particles. The effect of

small amounts of electrolytes added to the aqueous phase has been also investigated both theoretically and experimentally.

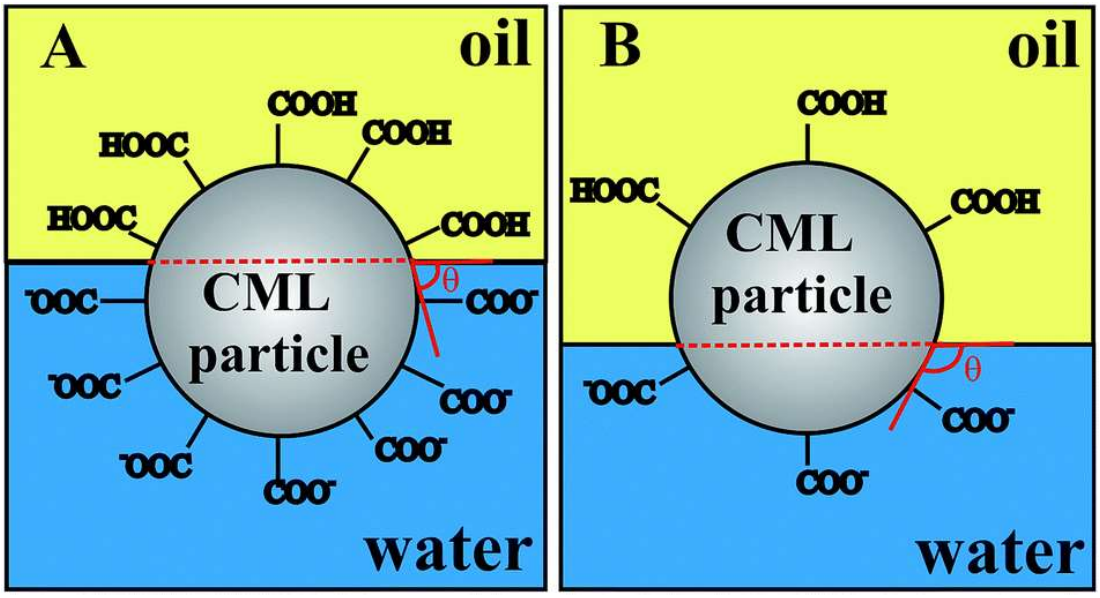

Figure 4.1. Schematic representation of the effect of carboxylic (–COOH) surface groups on particle adsorption and the three–phase contact angle at the oil–water interface: (A) high surface density of carboxylic groups on the particle surface makes them hydrophilic ($\theta < 90°$), while (B) low surface density of carboxylic groups on the latex particle surface makes them hydrophobic ($\theta > 90°$).

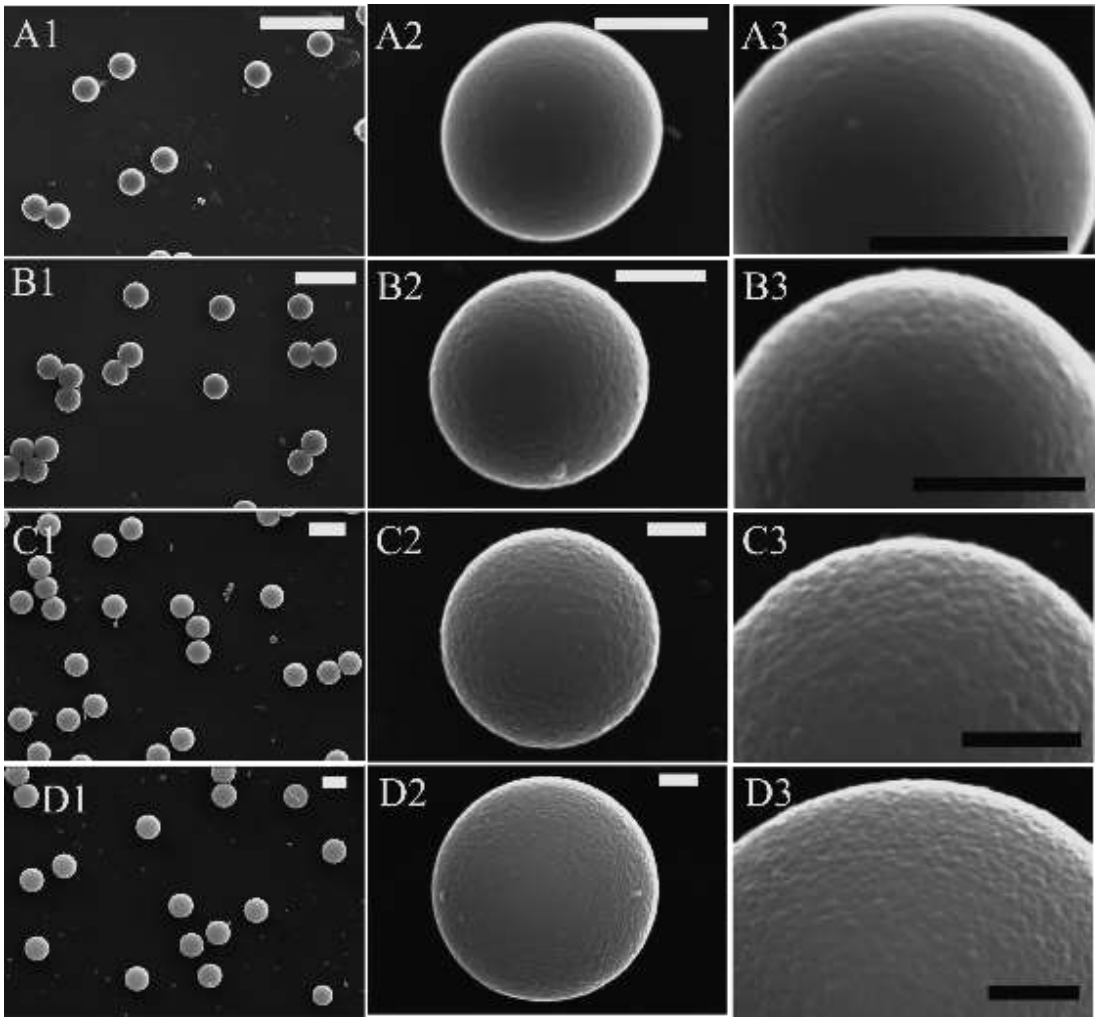

Figure 4.2. Scanning electron microscopy images of the CML particles of various diameters examined in this paper: (A1, A2, A3) 0.9 μm, (B1, B2, B3) 1.2 μm, (C1, C2, C3) 2 μm, and (D1, D2, D3) 3 μm. High–resolution SEM images (A2–D2) and (A3–D3) showing the local surface morphology of the CML particles. The scale bars are 3 μm for images (A1–D1) and 500 nm for images (A2–D2) and (A3–D3).

4.2 Results and discussion

4.2.1 Wettability of CML particles at liquid surfaces

The morphology of the CML particles of different sizes and COOH–group densities was studied by SEM. Figure **4.2** shows SEM micrographs of the used latex particles as provided by the manufacturer. Note that the surface of the 0.9 μm CML particle appears significantly smoother than that of the CML particles of a larger size. Figure **4.3** shows SEM micrographs of CML particles that were gel–trapped and

microcast with PDMS at the air–water surface, dodecane–water, and hexadecane–water interfaces.

The visible part of particle surfaces on the PDMS was immersed in the water phase while the particle surface immersed by the PDMS was originally in the air or oil phase. the particle contact angle was calculated by using equation (2.1) or ((2.2) after measuring the contact line diameter of the individual particles from the SEM images, d_c, and fitting a circular profile on the particles to determine their equatorial diameter, D. The contact angle values are summarised in Table 4.1.

Table 4.1. Data for the CML particles of different sizes and the particle three–phase contact angles measured at the air–water and oil–water interfaces after injecting the particle through the water or oil phase. The contact angle values reported are an average of at least 10 measurements obtained from several SEM images of different particles, over at least two repeated samples. The error bars represent the standard deviation of the contact angle data.

Particle diameter [a]/μm	Number of COOH groups per particle[a]	Area per surface carboxyl group[a]/nm^2	Air–water/θ°		Dodecane–water/θ°		Hexadecane–water/θ°	
			Injection through air	**Injection through water**	**Injection through dodecane**	**Injection through water**	**Injection through hexadecane**	**Injection through water**
0.9	5.5×10^6	4.6	63 ± 3	64 ± 4	96 ± 3	94 ± 2	97 ± 3	96 ± 3
1.2	3.5×10^7	1.3	64 ± 3	61 ± 4	67 ± 7	75 ± 5	82 ± 5	78 ± 4
3	3.0×10^8	0.9	47 ± 2	45 ± 2	71 ± 3	69 ± 3	69 ± 3	69 ± 2
2	4.1×10^8	0.3	50 ± 2	46 ± 4	61 ± 5	60 ± 2	60 ± 1	58 ± 4

[a] Provided by the manufacturer

The location of particle injection (in water or oil phases) during the sample preparation did not affect the particle contact angles. However, the CML particle contact angles were affected by the area per carboxylic group on the particle surface. A smaller surface density of carboxylic groups on the particle surface corresponds to a higher contact angle. CML particles of diameter 0.9 μm have the highest three–phase contact angle because of the low surface density of COOH groups. These particles are hydrophobic ($\theta \approx 96°$) at the oil–water interface (**Error! Reference source not found.** representing how the particle contact angle depends on the particle diameter. However, the dependence is not at a constant area per carboxylic group and reflects the variation in the polarity of the particle surface for a set of particles of varying sizes which have different numbers of carboxylic groups per unit area. The CML particle

contact angle decreases with increasing particle size as this corresponds to a higher surface density of carboxylic groups on the particle surface (Figure **4.4**). Which can be envisage that at a low surface density of carboxylic groups, the two fluid phases have a higher contact area with the bare polystyrene surface which has a high contact angle at the oil–water interface ($\theta > 120°$).[4] The CML particles with a diameter of 2 μm have the highest surface density of COOH groups which is reflected by their contact angle ($\theta \approx 60°$) at the oil–water interface. Notably, the CML particle contact angle at the air–water surface follows a similar trend to the area per carboxylic group as shown in Figure 4.5.

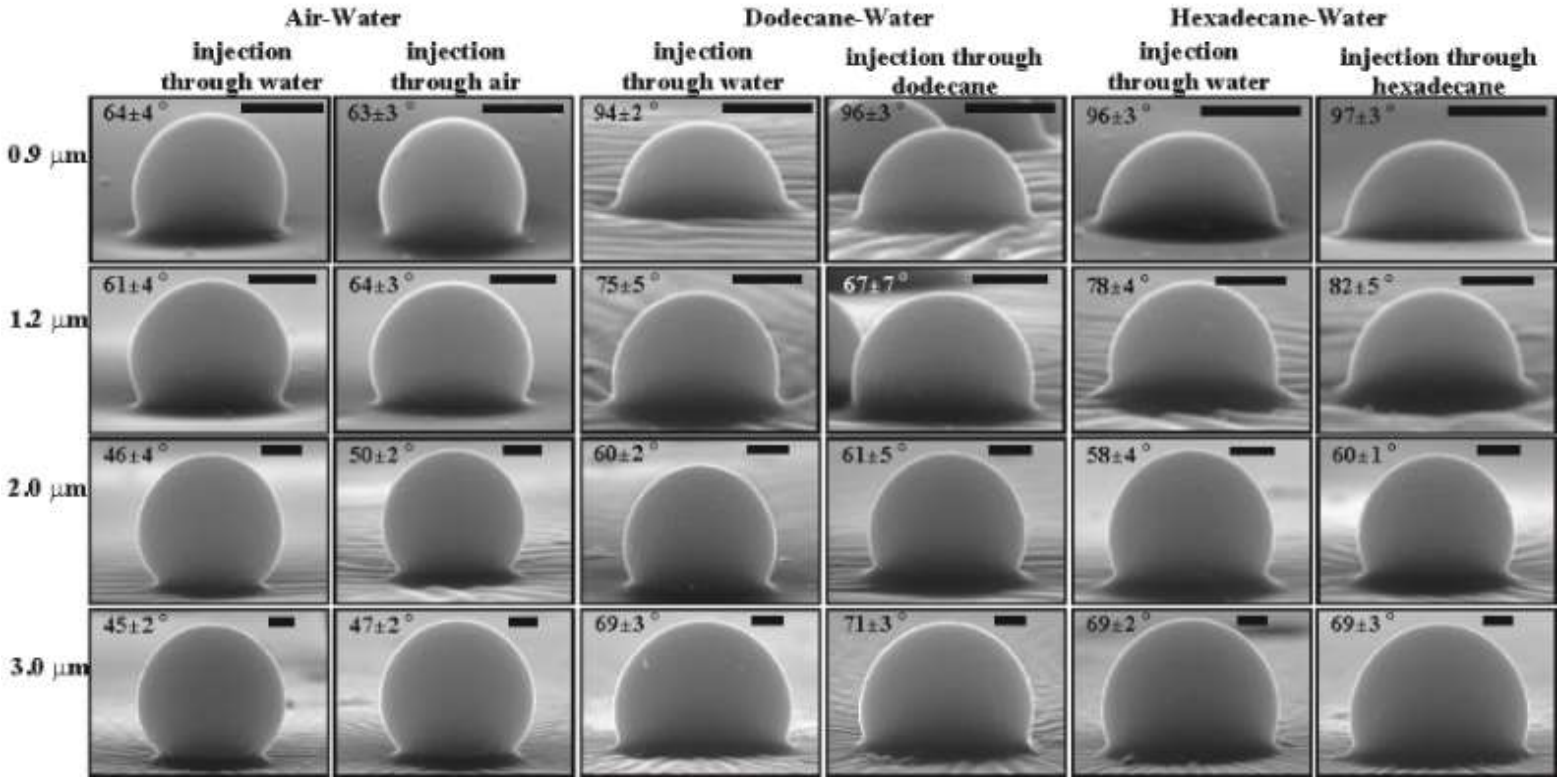

Figure 4.3. SEM micrographs of CML particles of different diameters and their contact angles at the air–water, dodecane–water, and hexadecane–water interfaces. The samples were prepared by injecting a particle dispersion in a spreading solvent into water or a non–polar phase near the liquid interface. The detector tilt angle used for imaging the particles was 85°. The scale bar is 500 nm for all images.

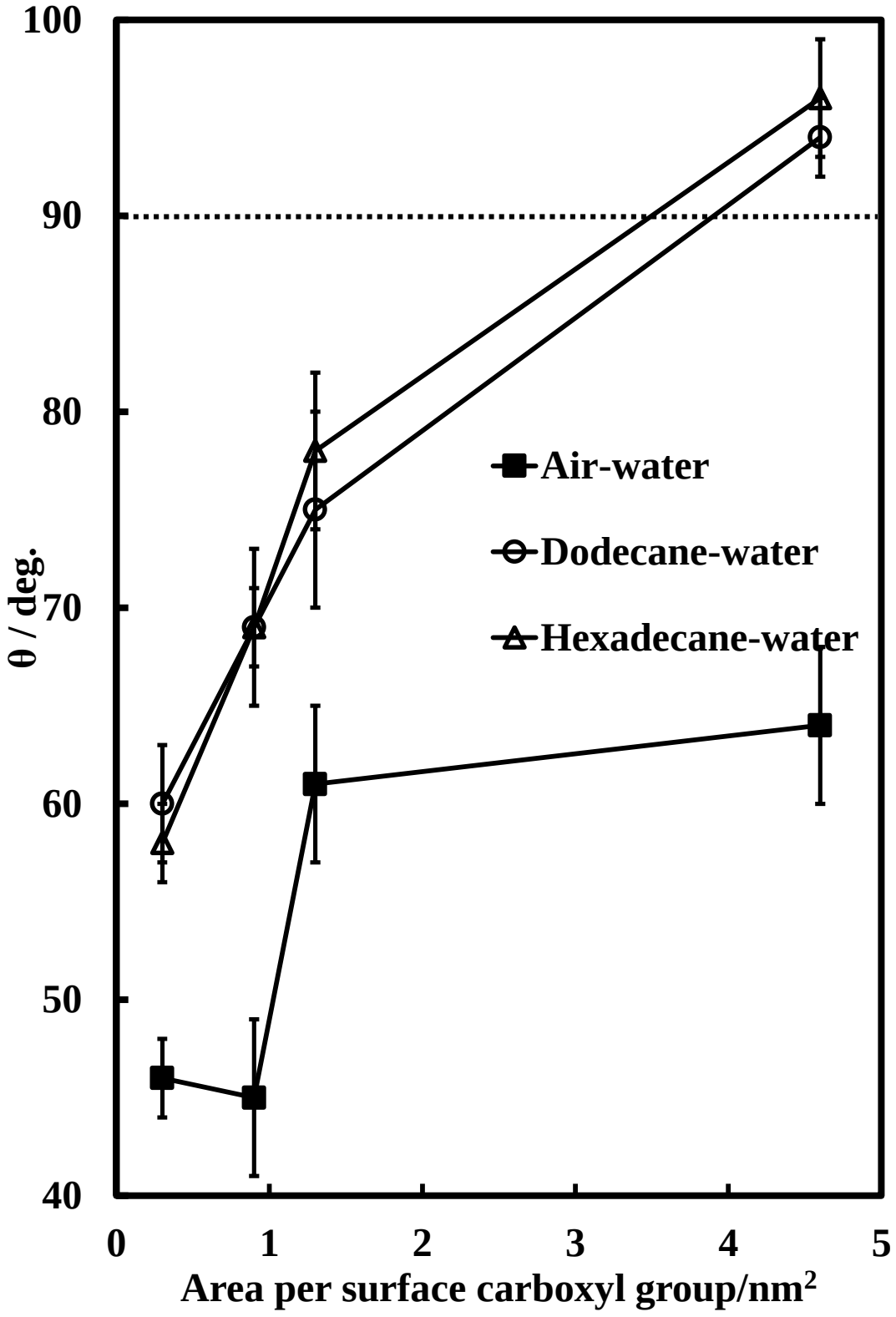

Figure 4.4. CML particle three–phase contact angle as a function of the area per carboxylic group on the particle surface. A Large area per –COOH group corresponds to hydrophobic particles, while a low area per –COOH group corresponds to hydrophilic particles. The lines between the data points are only guides to the eye.

4.2.2 Effect of syneresis on contact angle measurements

The effect of syneresis has been studied with different sized particles at air–water and dodecane–water interfaces. Syneresis occur when liquid exude of the solidified gel over time. Petri dishes were kept in the fridge at 4°C, containing the gel and the particles at air–water and dodecane–water interfaces, for 10–20 min in order to speed up gelation. The SEM images of the particles on the PDMS mould obtained by the GTT are shown in Fig. 4.6. The particles' contact angles are summarised in Table **4.2**. All the values obtained were below 90° in contrast to those obtained without cooling to 4°C (cf. Table 4.1).

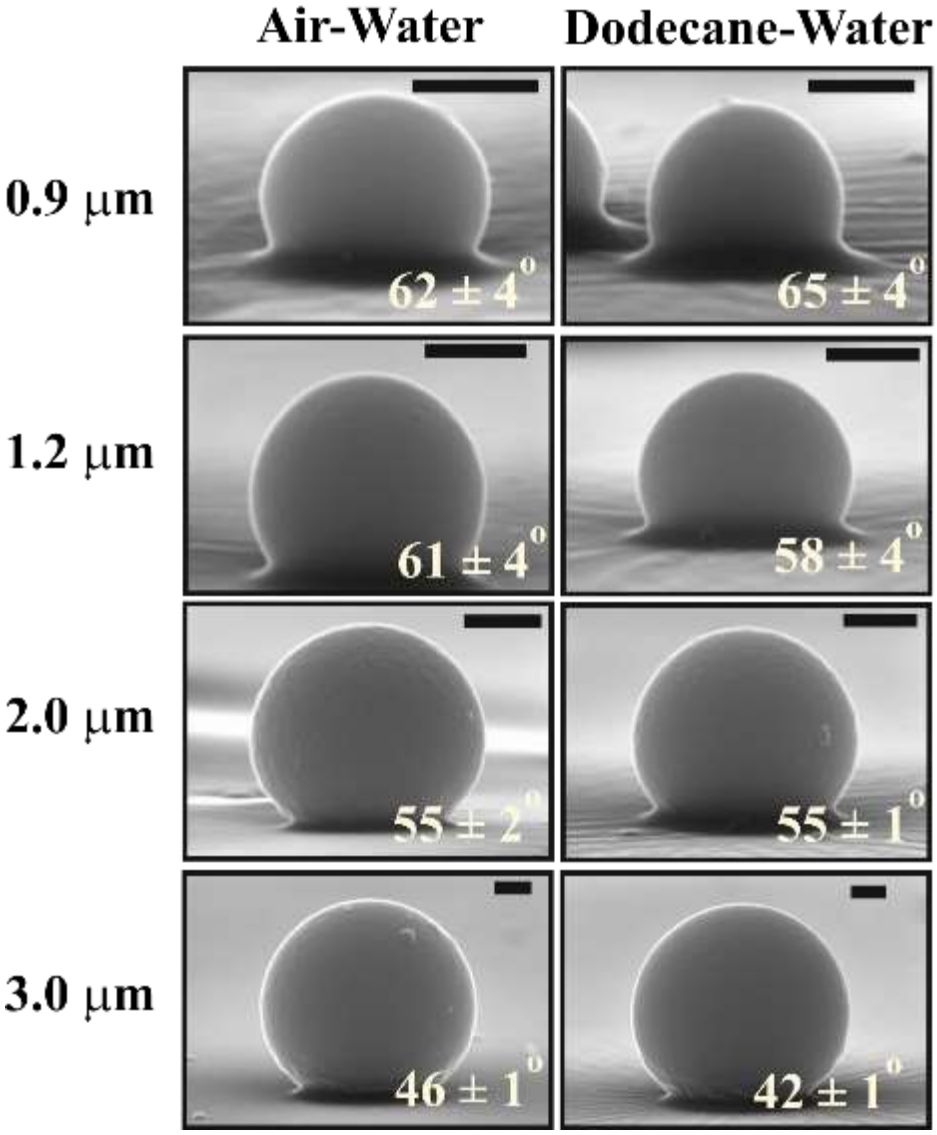

Figure 4.5. SEM micrographs of CML particles of different diameters and their contact angles at the air–water and dodecane–water interfaces. The samples were

prepared by injection of a particle dispersion in a spreading solvent into the water near the liquid interface and put in the fridge at 4°C for 10–20 min before PDMS curing. The detector tilt angle used for imaging the particles was 85°. The scale bar is 500 nm for all images.

This can be explained by the release of water at the top of the gel (gel syneresis) due to over cooling. As a result, the particles were not efficiently trapped during the PDMS curing; they readjusted their position with respect to the PDMS oil–water (gel) interface that affected the equilibrium contact angle of particles measured (Figure 4.6). These experiments show that proper sample preparation is very important for obtaining the particle contact angles using the GTT.

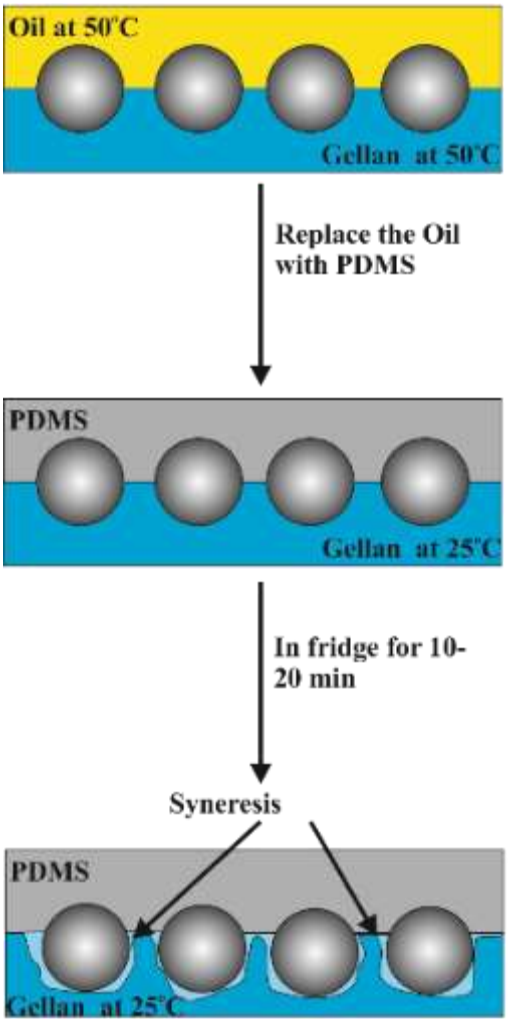

Figure 4.6. Schematic representation for syneresis effect on particles at oil–water interface after cooling for 10–20 min at 4 ºC.

Table 4.2. Contact angle of CML particles after placing the particles in the fridge at 4°C for 10–20 min.

Particle diameter[a]/μm	Air–water/θ°	Dodecane–water/θ°
3	46 ± 1	42 ± 1
2	55 ± 2	55 ± 1
1.2	61 ± 4	58 ± 4
0.9	62 ± 4	65 ± 4

[a] **Provided by the manufacturer**

4.2.3 Effect of salt concentration on the contact angle of CML particles at liquid surfaces

The contact angles of CML particles were compared at the air–water and oil–water interfaces for the cases with and without addition of NaCl. Salt was added to the purified gellan solution at a concentration of 1 mM NaCl in 2 wt% gellan at 90°C. The results in Figure **4.7** show that the addition of salt at these concentrations does not affect the contact angle. A higher concentration of salt were not tested as a solution with high ionic strength may interfere with the ability of gellan to form gels and strong hydrogels[151], and this may compromise the contact angle measurements with the GTT.

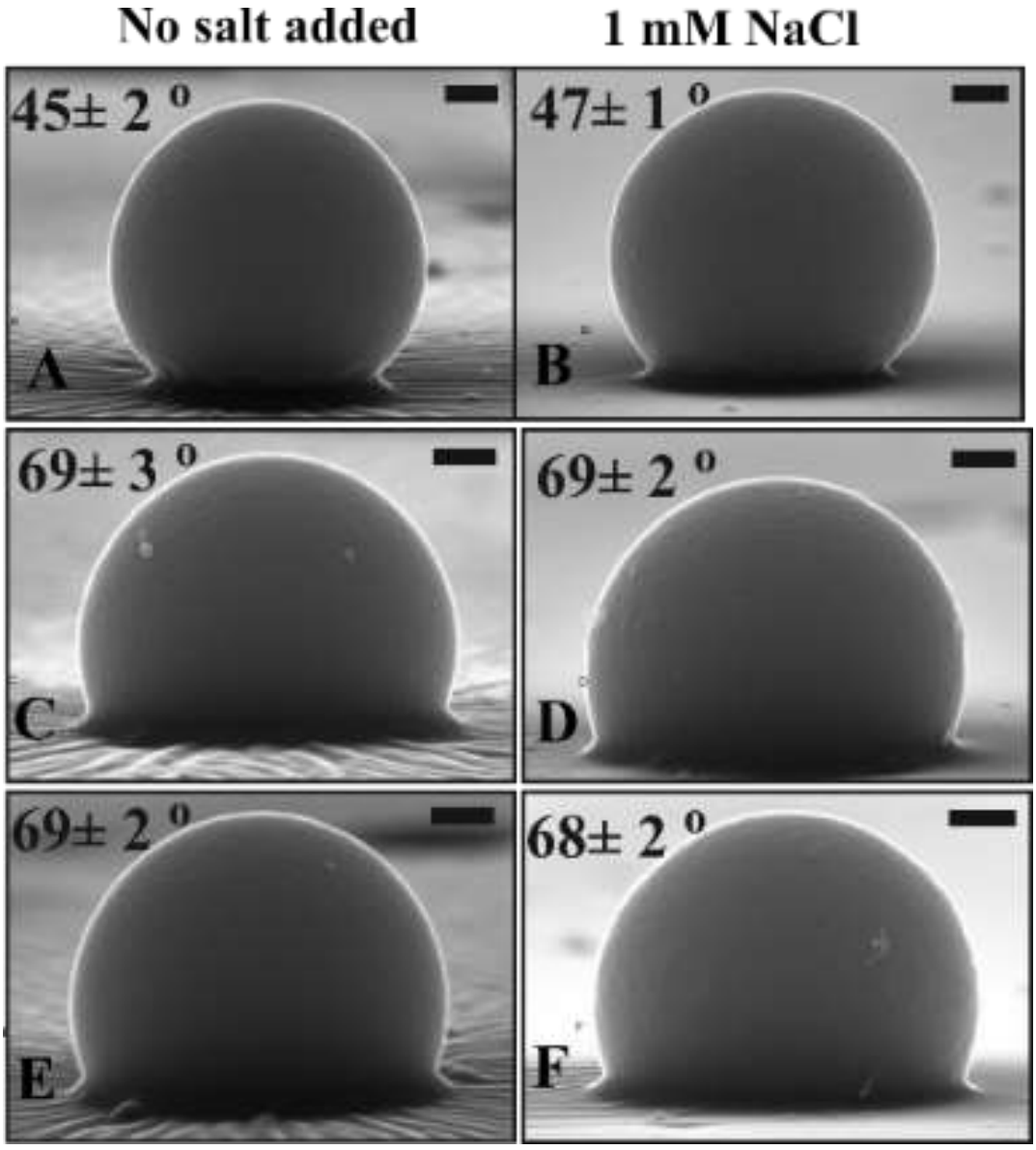

Figure 4.7. SEM images of 3 μm CML particles templated with PDMS at different liquid interfaces, where the particles are injected through the water phase. The contact angle does not change upon adding a known amount of NaCl (1 mM) to the aqueous phase (A and B). Typical SEM images of the CML particles at the air–water surface; (C and D) at the dodecane–water interface and (E and F) at the hexadecane–water interface. The scale bar is 500 nm for all images. Note that the three–phase contact angle of 3 μm CML particles at both the air–water and the oil–water interface does not change significantly upon the addition of salt to the aqueous phase.

The effect of the electrolyte concentration was estimated on the Gibbs free energy ΔG_{el} of the electric double layers at the particle–water interface and the air–water interface in an attempt to evaluate its influence on the particle contact angle.

Neglecting the particle surface curvature effects for the sake of simplicity, the relation between the surface charge density σ_o and the particle surface potential was used.[152]

$$\sigma_0 = \frac{2kT\varepsilon\varepsilon_0\kappa}{Ze}\sinh\left(\frac{\psi_0 Ze}{2kT}\right) \qquad 4.1$$

Then, the ΔG_{el} was calculated using the following equation:[152]

$$\Delta G_{el}\ (\psi_o) = -\left(\frac{2kT}{Ze}\right)^2 \kappa\varepsilon\varepsilon_o\left[\cosh\left(\frac{\psi_o Ze}{2kT}\right)-1\right] \qquad 4.2$$

Here, e is the electronic charge, N_A is the Avogadro number, ε_o is the vacuum permittivity, ε is the dielectric constant of water, T is the absolute temperature, k is the Boltzmann constant, Z is the valence of the electrolyte (Z : Z), and ψ_o is the surface electric potential. In equation (4.1) and (4.2), the Debye screening parameter is calculated from the formula below:

$$\kappa = \sqrt{\frac{2000\ Z^2e^2N_A^2C_{el}}{\varepsilon\varepsilon_o kT}} \qquad 4.3$$

Where C_{el} is the electrolyte concentration. For these calculations, the air–water surface potential, ψ_{aw}, was assumed to be −40 mv. The CML particle surface potential, ψ_{pw}, was −36 mv, which was approximated with its zeta potential in 1 mM NaCl at pH 5(**Figure 4.8**). If the particle contact angle corresponding to non–dissociated COOH groups was assumed to be θ_o, the effect of the electrolyte concentration on the particle contact angle can be estimated from the following expression:[153]

$$\cos\theta = \frac{\cos\theta_o - \Delta G_{el}(\psi_{pw})/\gamma_{aw}}{1+\Delta G_{el}(\psi_{aw})/\gamma_{aw}} \qquad 4.4$$

Here, γ_{aw} is the air–water surface tension, ΔG_{el} (ψ_{aw}) and ΔG_{el} (ψ_{pw}) are the surface free energies of formation of the electric double layers, respectively, at the air–water surface and particle–water surface, with surface potentials ψ_{aw} = −40 mv and ψ_{pw} = −36 mv at 1 mM NaCl. The three–phase contact angle vs. salt concentration was calculated by using equation (4.4), assuming a constant surface charge density for both the air–water and the particle–water interfaces. The calculation assumes a constant

surface charge at the air–water and the particle–water interface when the electrolyte concentration is varied. Our measurements showed that the 2% gellan solution had a pH of 5. The respective values of surface charge density σ_{aw} and σ_{pw} were calculated using equation (4.1) for the quoted values of the surface potentials at 1 mM NaCl and pH 5 (see Figure 4.8). Then, at constant surface charge densities, the salt concentration was varied and recalculated the surface potentials from equation (4.1) and the corresponding values of ΔG_{el} (ψ_{aw}) and ΔG_{el} (ψ_{pw}) from equation (4.2) and the contact angle from equation (4.4).

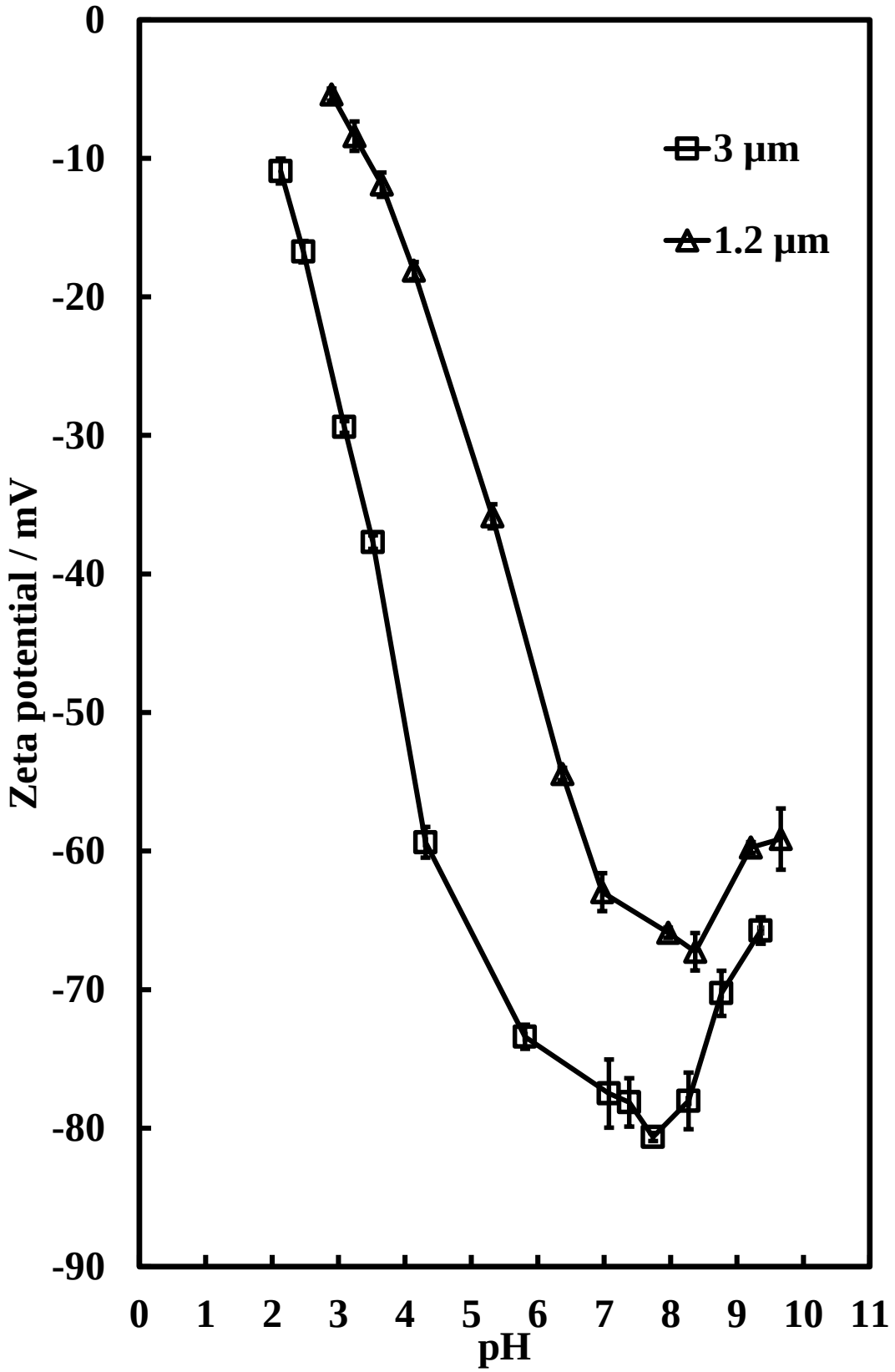

Figure 4.8. Zeta potential of the 1.2 µm and 3 µm CML particles as a function of pH at 1 mM NaCl in the aqueous solution. The zeta potential gradually changes with the pH. The lines between the data points are only guides to the eye.

Figure **4.9** shows the calculated effect of the salt concentration on the particle contact angle at the air–water surface. However, as the graph shows, the change in the microparticle contact angle for a wide variation in the salt concentration is very small, i.e. within 1°. Similar results were obtained upon variation of the particle surface charge density at a fixed value of the surface potential. The particle surface curvature effect on the electric double layer surface energy is important only when the particle radius of the curvature becomes comparable with the Debye screening length. [153] For 1 mM NaCl solution, the Debye screening length is two orders of magnitude smaller than the size of the microparticles used in this study. This is true even for microparticles in deionised water (typically of pH 5.5). For this reason, neglecting the surface curvature effects is justified. Nevertheless, even on neglecting the curvature effects, the overall contribution of the electric double layers to the variation of the particle contact angle was found to be very small, as shown in Figure **4.9**. Note that the particles have very different surface group densities and all of them show very small changes in the particle contact angle as the salt concentration increases to 1 mM. Hence, the change of the particle contact angle measured experimentally cannot be explained solely using the changes of the surface free energy of the electric double layer of the particles at the air–water surface as they are too small for particles of this size.[153] Although upon changing the pH and salt concentration the COOH groups on the particle surface can dissociate to produce a high surface charge density and the corresponding surface potential, as illustrated in Figure **4.9**, the value of the contact angle seems to be determined by the surface density of the COOH groups rather than their degree of ionisation. In addition to this argument, at the aqueous phase with the gellan in the GTT experiment, the pH is around 5.5, where a high percentage of COOH groups on the CML particle surface is not dissociated. Hence, the COOH group surface density is correlated to the particle contact angle at the liquid interface. The same arguments hold true for particles at the oil–water interface where a similar analysis can be conducted to show that the effect of the polar carboxylic group present on the surface is the main factor determining the changes in the particle contact angle.

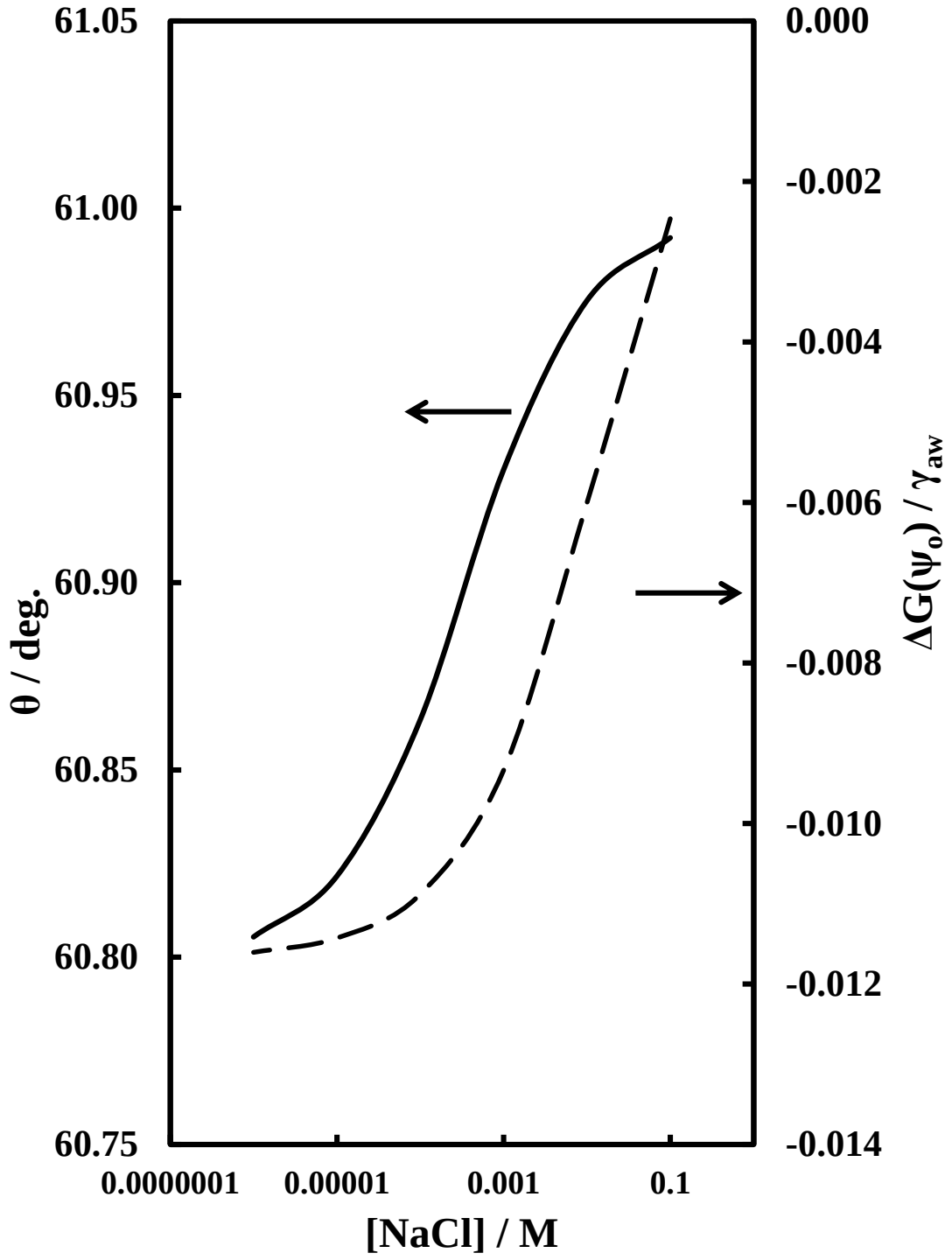

Figure 4.9. The estimated effect of the salt concentration on the CML particle contact angle based on the change of the electric double layer free energy. The calculations are based on the parameters of 1.2 μm CML particles. The value of the zeta potential is used here as a proxy for the respective surface electric potentials. The particle surface charge density is estimated from the value of the zeta potential, which is −36 mv for the particle at pH 5 and salt concentration of 1 mM (see Figure **4.8**).

The zeta potential of the air–water interface was assumed to be −40 mv. The electric double layer free energy was calculated from equation (4.2) and the particle contact angle from equation (4.4). Note that the effect was very small – the change in θ was within 1° over a range of salt concentrations. Here, for the non–charged particle was used $\theta_o = 61°$.

4.2.4 Emulsions stabilised by CML particles

Using dodecane as the oil phase, CML particles (5 wt%) as sole emulsifiers, and 1 mM NaCl aqueous solution stained with fluorescein di–sodium salt, an emulsion were produced for all particle sizes used in this study (Figure **4.10**). Oil–in–water emulsions were obtained for CML particles of diameters 1.2 μm, 2 μm, and 3 μm which, according to our GTT contact angle data, are hydrophilic particles as their contact angles are lower than 90°. On the other hand, with the 0.9–μm CML particles, whose contact angle at the decane–water interface was greater than 90°, water–in–oil emulsion was obtained. The general result obtained in this study is that the solid particle surfaces are more exposed to the phase outside the droplets in the preferred type of Pickering emulsion, as also shown by other studies[154-156]. However, the physical reasons behind this conclusion are barely discussed in the literature. The thermodynamic aspects of this result are considered in the recently published work a Kralchevsky et al.[157]

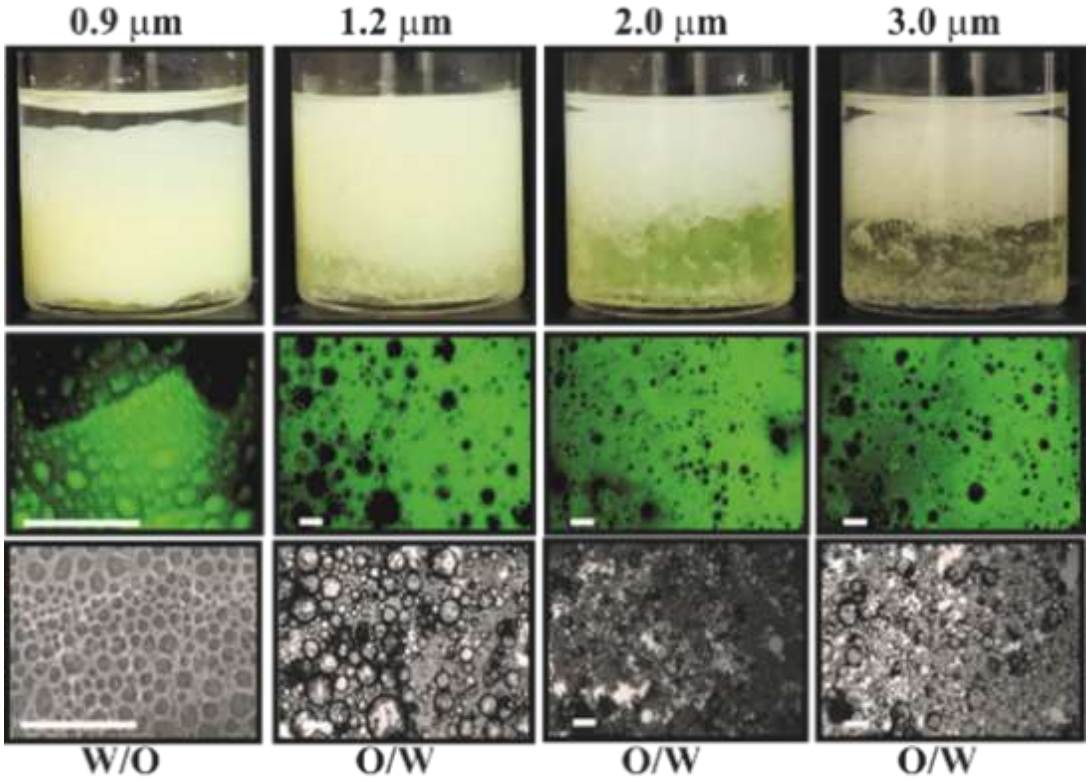

Figure 4.10. Optical photographs of emulsion made from 50 : 50 dodecane : water stabilised by 5 wt% CML particles in 1 mM NaCl immediately after emulsification. The emulsification was done by the hand–shaking method. Florescence and optical microscopy images of the particle–stabilised emulsions, where the aqueous phase was doped with fluorescein. The type of the emulsion changed from (w/o) water–in–oil emulsion to oil–in–water (o/w) emulsion not because of the different sizes of the particles but because of the decreasing area per COOH group on the particle surface which switches the nature of the particles from hydrophobic to hydrophilic. The scale bar is 200 μm for all images.

Here, an alternative view is suggested which is based on the fact that during emulsion preparation (e.g. at 50 : 50 oil : water), both water–in–oil emulsion to oil–in–water emulsion drops coated with adsorbed solid particles are formed simultaneously and undergo coalescence. It is very likely that their liquid interfaces are not closely packed with solid particles during this process as the emulsion is homogenised and the droplets come in contact with each other. Therefore, the bridging effect of the solid particles in the liquid films formed between the emulsion drops determines which type of emulsion survives and leads to the preferred emulsion type. Hydrophobic particles can form a stable oil film by bridging two water drops in oil but cannot form a stable aqueous film

by bridging two oil drops in water. Since the opposite is true for hydrophilic particles, this could explain the final outcome where hydrophobic particles stabilise water–in–oil Pickering emulsions while hydrophilic particles stabilise oil–in–water Pickering emulsions[30, 48].

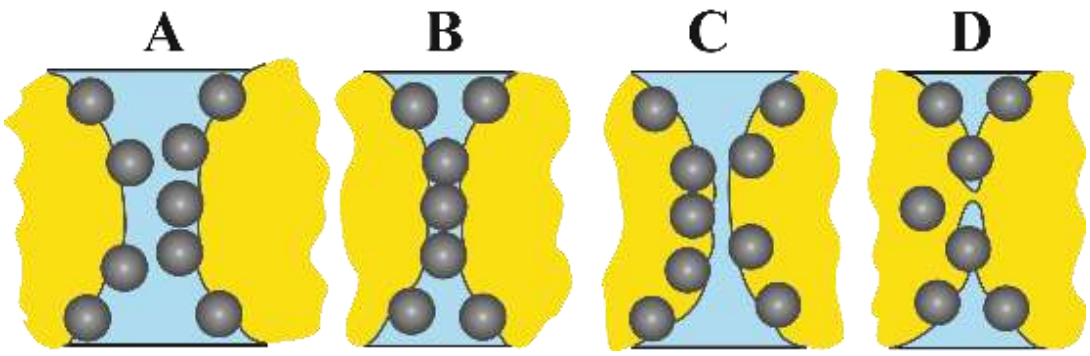

Figure 4.11. Schematic representation of the particles stabilise emulsion. the unsaturated surfaces of (A) two oil droplet with hydrophilic particles in water approaches to each other and form (B) a bridge particles stabilises the emulsion droplet. In the case of hydrophobic particles on surface of oil droplet the distance between the two droplets are close enough to rupture the file and cause coalescence.

4.3 Conclusions

In this work, the GTT was used to study the three–phase contact angle of CML particles of varying sizes at the air–water and the oil–water interfaces. It was found that although the particle contact angle varies with the particle size, the variation is due to the different surface densities of COOH groups on the surface of CML particles. The effect of ionisation of COOH groups at the particle surface and the free energy of the electric double layer on the particle contact angle were estimated but it proved to be too small to explain the variation in the particle contact angle. The role of the liquid phase from which the particles were injected to the liquid interface in the GTT experiment were examined. The effect of the initial phase of CML particles did not change the particle contact angle significantly within the experimental error. The consequence of syneresis was investigated and showed that the particles' adsorption was affected, thereby producing the same contact angle at air–water and dodecane–water interfaces. The effect of the presence of salt in the aqueous phase on the particle contact angle was investigated both experimentally and theoretically and found that it was negligible at least for moderate salt concentrations. The main conclusion is that

the CML particle contact angle is usually determined by the density of COOH groups on the particle surface rather than by their ionisation at the particle surface. It was also found that the CML particles with low densities of COOH groups had a contact angle higher than 90° at the oil–water interface and prefer to stabilise the water–in–oil emulsions. The CML particles of contact angle lower than 90° had a much higher surface density of COOH groups and stabilise the oil–in–water emulsions.

Chapter 5: Fabrication of porous supra–particles

5.1 Introduction

In Chapter 4, the effect of surface density of carboxylic groups on the surfaces of CML particles and the particle size were explored on the particle three–phase contact angle. Also the impact of the liquid phase was examined from which the particles are injected at the fluid interface in the GTT experiment. The study gave us important insights into how individual spherical CML microparticles with smooth surfaces adsorb at liquid surfaces. However, in many applications which involve formulation of powders with oil and water, the solid particles are highly agglomerated in porous clusters and aggregates, which do not behave as the individual solid particles from which they are formed. Porous particles and particle aggregates appear in the production and development of pharmaceutical products, building materials, catalysts, sintered materials, ceramics, adsorbents, pigments, chromatography, and filters.[68] Nevertheless, the arrangement of the particles depends on the packing process and their materials' properties. These arrangements are classified into two categories as either loose or dense packing. Wetting behaviour of porous particles at oil–water or air–water interfaces is poorly understood despite the numerous studies of contact angles of colloid particles and some progress in this area [59]. The possible reasons for the lack of comprehensive studies of the mechanism of adsorption of porous or complex particles is: (i) the lack of rigorous theoretical insights into the adsorption mechanism of porous particles or particle aggregates; (ii) the lack of consistent geometry of particle aggregates which makes any study difficult to reproduce and test by other authors. To overcome these difficulties, model porous particles of well characterised building blocks was fabricated, which would allow us to study consistently their wetting behaviour at liquid surfaces were used.

Here, in Chapter 5, a new method was develop for the fabrication of model porous supra–particles which consist of smaller colloid particles packed in a spherical aggregate. In addition, in the following Chapter 6, a new theoretical model was develop which describes the adsorption of such complex particles from the oil or water phase to the oil–water interface and link the contact angle of the complex supra–

particles to the three–phase contact angle of the small spherical particles from which they are built. Chapter 7 uses the porous supra–particles, developed in the present chapter, to measure their three–phase contact angles in different settings and test the theoretical predictions from the adsorption model of a supra–particle produced in Chapter 6.

The main focus in this chapter is the preparation of porous supra–particles, using a simple and quick method. The bulk of our results are obtained primarily by evaporation of a drop of 10 µl , 15 µl and 20 µl of monodisperse (2.6 µm) sulphate latex suspension of various particle concentrations 40–70 wt.% over a hot superhydrophobic surface, on a hot plate at ~90 ^{o}C. The supra–particles were further annealed at the polymer glass transition temperature (~106 ^{o}C) in order to strengthen the interparticle bonds and improve the supra–particle integrity upon adsorption at liquid surfaces. Figure 5.1 summarises the main steps in the preparation of the model porous particles used in this thesis.

The microstructure of the obtained supra–particles was controlled by: (i) the annealing temperature; (ii) the initial volume fraction of the latex suspension; and (iii) the drop evaporation rate at different temperatures 60–105 ^{o}C. The supra–particle size was controlled by the initial volume of the latex particle suspension for fixed particle concentration.

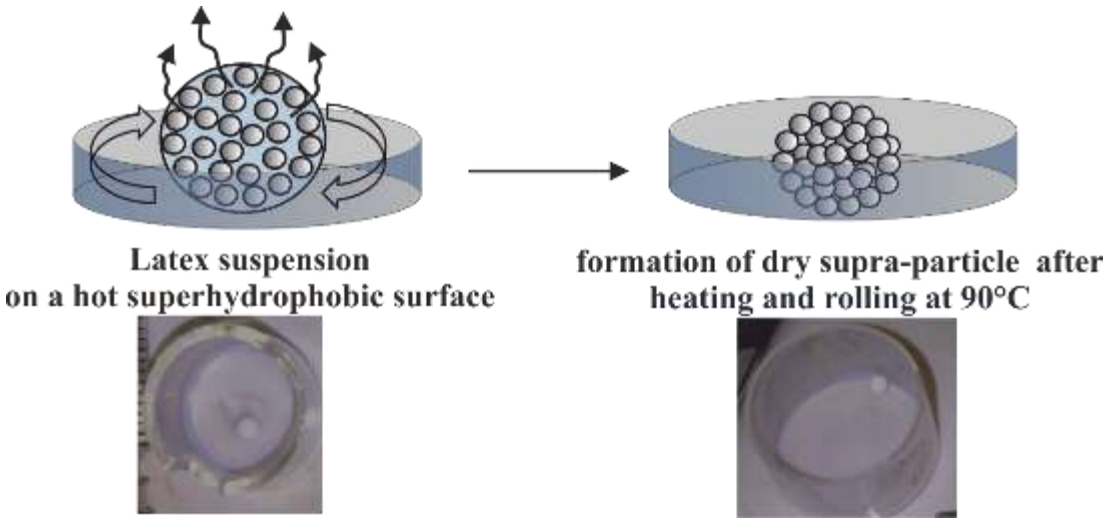

Figure 5.1. Representation of the formation of a dry porous supra–particle from a drop of concentrated polystyrene latex suspension (15µl, 40 wt%) which was evaporated at

90 ^{o}C. The dry porous particles (2 mm) were partially fused at 106 ^{o}C to form stable porous supra–particles for our studies of porous particle adsorption at liquid surfaces.

Also an alternative method for the preparation of porous particles was briefly explored by filtering a concentrate latex suspension through a prefabricated PDMS mould followed by their thermal fusion, as described below. Here, both methods with the obtained results are presented, although the further studies in the following chapters are produced by the suspension drop evaporation method over a hot superhydrophobic surface.

5.2 Results and discussion.

5.2.1 Porous supra–particles fabrication

5.2.1.1 *Porous supra–particles made by using PDMS mould*

The purpose of this experiment is to fabricate model porous particles (supra–particles) from much smaller colloid particles in order to study the effect of the supra–particle porosity on its contact angle. This approach has been described in section 1.2.5.1. Spherical cavities were produced in silicone rubber (PDMS) by templating spherical steel beads of various size, followed by their removal from the elastic PDMS matrix through a drilled channel. These PDMS cavity moulds were then injected with a concentrated particle dispersion (monodisperse sulphate latex 2.6 μm in diameter) in ethylene glycol. The injection was performed using three different approaches: employing a hand–driven syringe, a calliper and a syringe pump. The idea was to produce porous supra–particles by controlling the rate of injection of the particles' suspension in these cavities and filter out the excess of the ethylene glycol continuous phase through a microchannel. The latex particles in the cavity were fused further by heating the mould to the glass transition temperature of polystyrene, followed by their subsequent removal from the mould, washing with Milli–Q water and drying. Although this method produced porous supra–particles, they appeared to be loosely packed with latex particles which, even after partial fusion, did not achieve the required integrity for further studies at liquid interfaces. Figure **5.2** shows typical optical images of hollow supra–particles and half–sphere particles which have been formed in this process. This method tends to produce poor results due to the potentially

incomplete filtration of the ethylene glycol from the PDMS mould which hinders the thermal fusion between the particles.

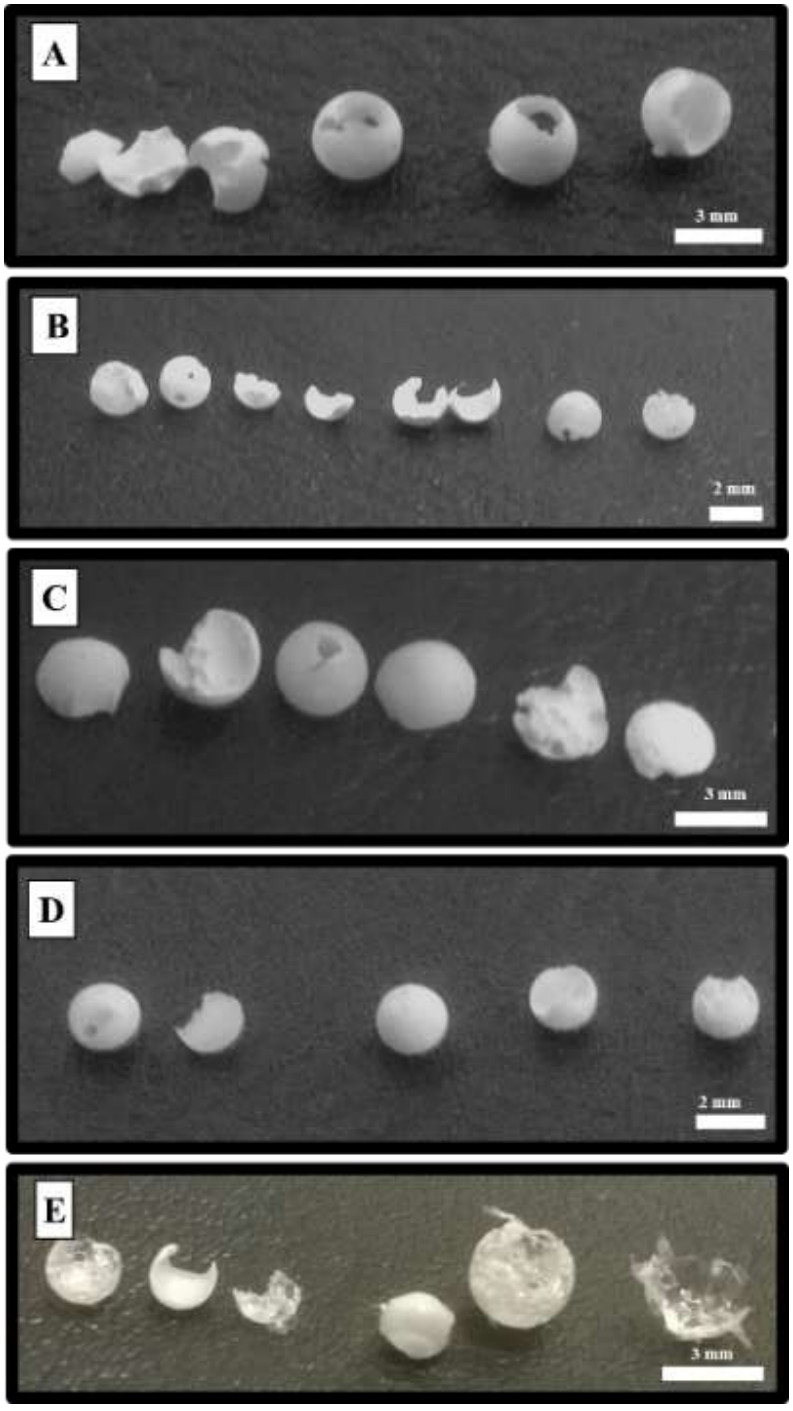

Figure 5.2. Optical photograph showing supra–particles made from partially fused latex particles (2.6 μm in diameter) using a PDMS mould. The irregularity of the shape is due to loose packing and incomplete removal of the ethylene glycol. A and B were made by the injection of particles via calliper, while C and D were produced via syringe pump and E, via hand.

This experiment nearly produced a supra–particle 2 mm cavity mould satisfactorily (**Figure 5.2** D), where the rate of injection of 70 w/w % of latex particles' suspension, filtered through the cavity, was about ~12 µl/h. However, for the 3 mm cavity size, spherical supra–particles were not formed due to the trapping of air in the cavity which was not prevented by initial degassing of the latex suspension.

Nonetheless, it seems that the syringe used to inject the suspension into the cavity mould also produced some air microbubbles inside the cavity. This approach led to irregularities in the supra–particle shape formed. Another drawback of this method was that after using high particle concentrations (i.e. >30 wt%), partial sedimentation occurred inside the needle during injection because of the different density of the ethylene glycol, thereby causing jamming. Due to these reasons, this method was abandoned and focused on the drop evaporation technique, as described in the next section.

5.2.2 Model supra–particles made by rolling latex particle suspension on hot superhydrophobic surface

5.2.2.1 *Formation of superhydrophobic surfaces*

The purpose of this experiment is to make a superhydrophobic surface in order to form supra–particles. As the DSDMS forms a superhydrophobic surface, the silica particles attached to it easily. Colloidal hydrophobic silica particles form a rough surface on the glass watch. Superhydrophobic glass surfaces were produced by spreading an ethanol suspension of hydrophobic silica particles (R202) on a glass Petri dish, as described in Chapter 2. Figure 5.3 shows the silica particle size distribution with a mean diameter at 256 nm, measured using a Mastersizer. After drying on the glass surface, the silica particles adhere to each other and form a rough hydrophobic surface which has significant durability, even at high temperatures.

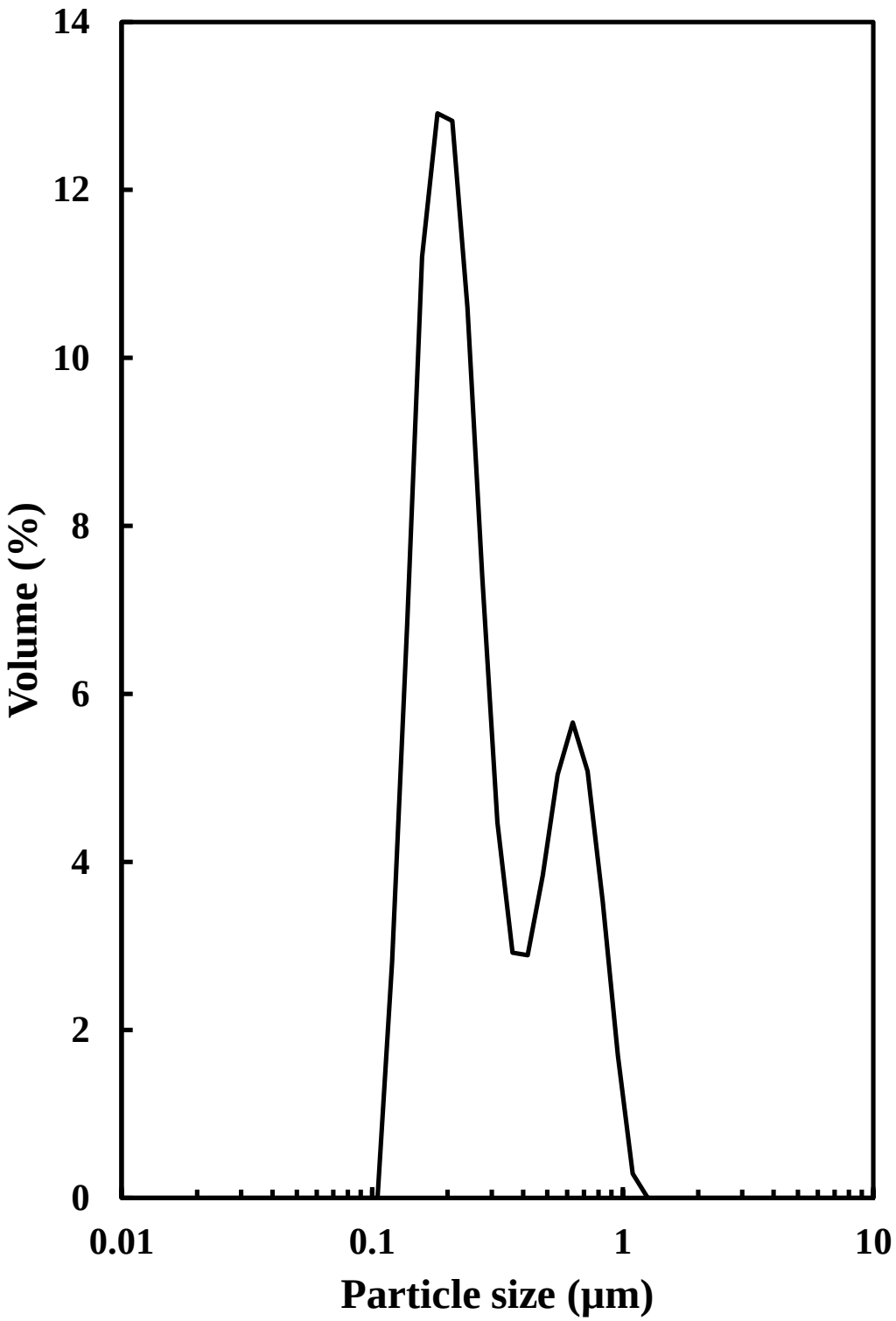

Figure 5.3. R 202 silica particle size in particle suspension, after using ultrasonic probe at 50% amplitude for 20 min, with pulse every 5 seconds for 2 seconds, for 5 % wt silica in ethanol. This suspension of hydrophobic silica particles (mean diameter 256 nm) was used in preparation of superhydrophobic surfaces for the drop evaporation technique.

5.2.2.2 *Model supra–particles made by rolling particle suspension on hydrophobic surface using mechanical vibration*

An initial volume of 10 µl both 8.1 wt%and 40 wt%monodisperse sulphate latex particle (2.6 µm) suspensions were used to produce porous supra–particles. An aliquot of the latex suspension was deposited on the superhydrophobic glass surface and then rolled until the aqueous phase evaporated to form a porous particle. In some of the experiments, a fan heater was used to increase the drop evaporation rate. The samples of 10 µl 8.1 wt% sulphate latex took around 1 hour, while the 40 wt% latex suspension took 30 minutes to fully evaporate using this method. However, due to the restricted amplitude of the vibrations, the drops and the resulting porous particles did not maintain a spherical shape. Figure 5.4 shows typical examples of such porous supra–particles. In many cases, the particles have a flat side and got stuck on the superhydrophobic surface upon evaporation. Such particles were not suitable for contact angle measurement due to their non–spherical shape. To overcome this problem, the method was modified of drying the particle suspension by using manual rolling instead of mechanical vibration.

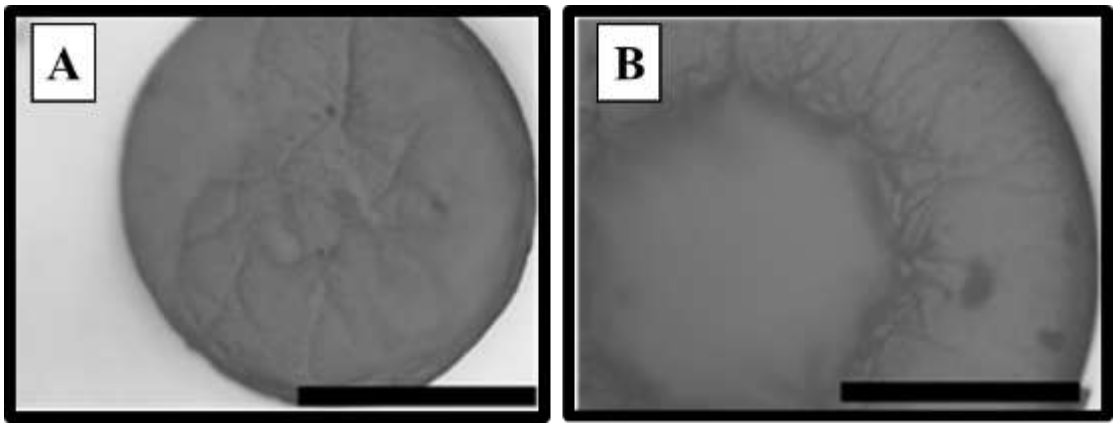

Figure 5.4. Optical microscopy images for (A) plate–like (B) dimple. The scale bar is 1 mm. Particles have different structures due to the effect of the viscosity of the sulphate latex after evaporation at room temperature and the fact that they stick to the hydrophobic surface. The structure is formed because of the high speed, at around 1000 rpm (A), and the low speed of 200 rpm (B).

5.2.2.3 *Model supra–particles made by rolling particle suspension on hydrophobic surface using manual rolling*

Porous supra–particles were successfully produced of different shape by using a hot superhydrophobic glass surface and different initial latex particle concentrations. the particles' concentration is an important factor in determining the final shape of the porous particles. Using 40%–70% w/w% of sulphate latex suspensions, spherical porous supra–particles was formed successfully. For samples made from the original suspension of particle concentration, 8.1 wt%, the supra–particles were not spherical, while for suspensions of 40%wt latex particle concentration, the formed supra–particles were spherical (see Figure **5.5**). It has to be noted that the particles formed from evaporating 20 µl of a latex suspension of concentrations (8.1 % and 30 %) produced shape–anisotropic particles, while the same amount of latex suspension of higher concentrations (40 %, 50 % and 70wt.%) produced spherical particles, with diameters 2.1 mm, 2.2 mm and 2.4 mm, respectively .

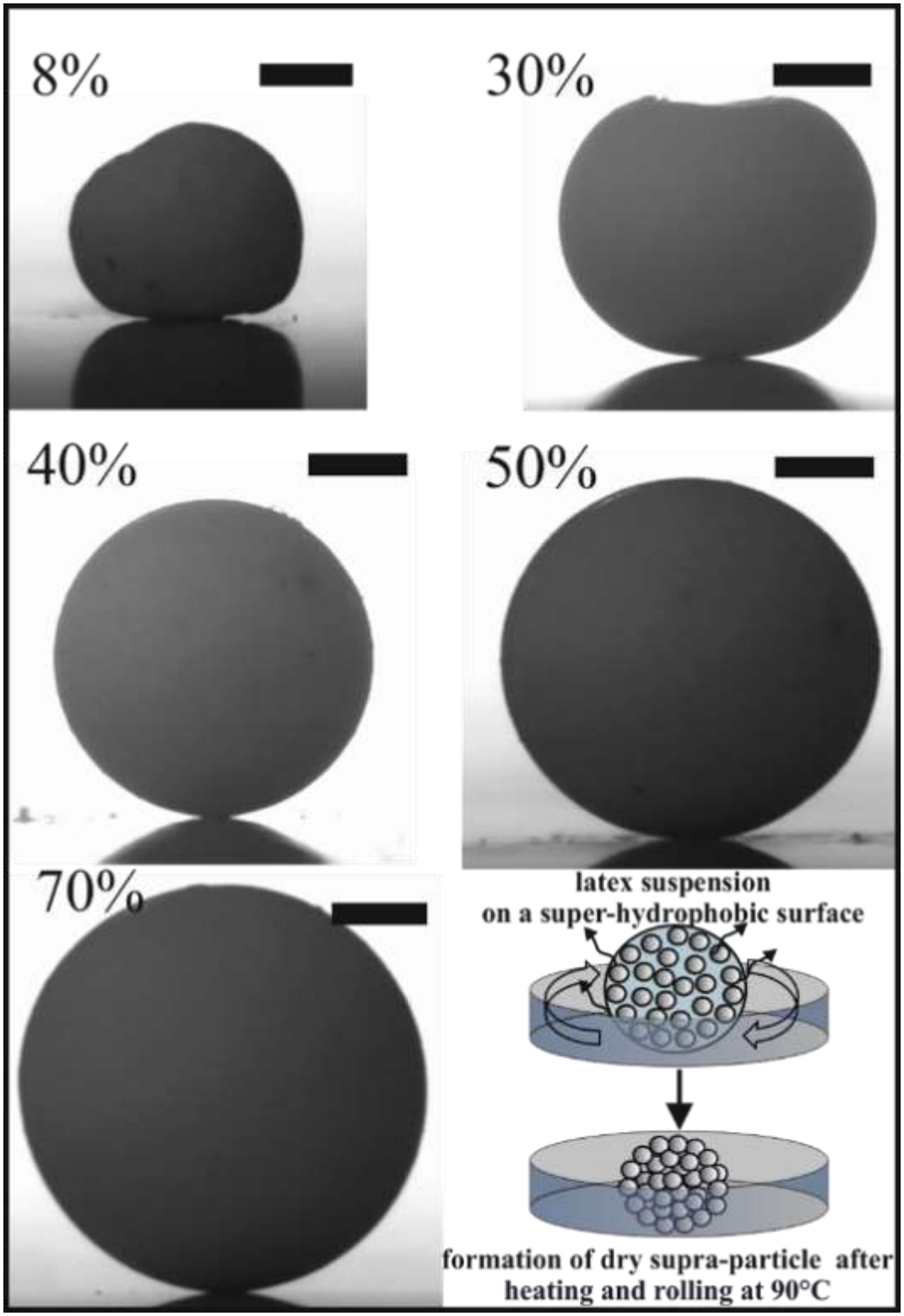

Figure 5.5. Optical images of supra–particles formed by evaporation of sulphate latex suspension of various particle concentrations 8–70 wt% on a superhydrophobic surface at 90 ^{o}C. The latex suspension drop was rolled over the hot superhydrophobic surface until complete evaporation occurred. The scale bars for these particles are 0.50 mm in all images.

5.2.3 Characterisation of the supra–particles morphology

The surface structure and the porosity of the porous supra–particles are affected by the initial concentration of the sulphate latex particle suspension. Figure **5.6** (A, B) shows that the produced supra–particle surface from 8.1 wt% latex particle concentration shows a randomly packed porous structure. As expected, upon increasing the particle concentration, the particles started forming a close–packing structure. At 40 wt% latex particles, as shown in Figure **5.6** (C, D), a much smoother surface was formed with some large pores, while at 50 wt% latex particles, close–packed structures with much lower porosity were produced on the supra–particle surface. Also, the number of defects (large pores) in the produced lattice is much smaller than those at lower particle concentrations. These results, to the best of our knowledge, have not been obtained by other authors and the dependence of the particle surface morphology on the small particle concentrations has not been discussed in the literature. [95-96]

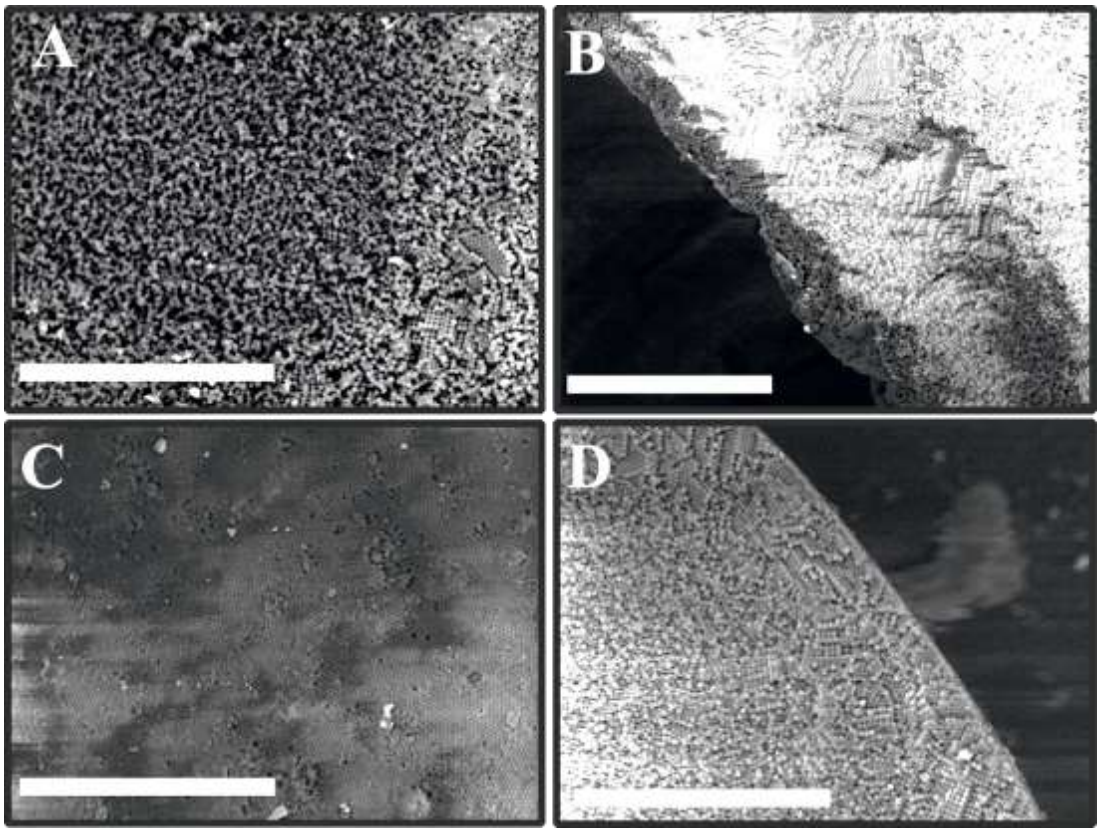

Figure 5.6. SEM images of the surface of supra–particles made from much smaller sulphate latex particles (2.6 μm in diameter) define the outer surface morphology of supra–particles at (A) 8.1 wt%, and (C) 40 wt%, and also show the inner structure at the edge of sectioned supra–particles for (B) 8 wt%, and (D) 40 wt% latex suspension,

respectively. The supra–particles in (B) and (D) were sectioned to reveal the internal structure of the latex particle assembly near the supra–particle surface. The scale bar is 100 μm in all images.

The surface morphology of supra–particles produced from 70 wt% latex particle suspension shows much more compact structures due to the increase in particle numbers, resulting in the rough but less porous surface (Figure **5.6** C, D). Supra–particles made from 40–70 wt% latex suspensions showed colloidal crystalline domains on their surface. The inner structure of the packed latex particles was investigated with a SEM, as seen in (Figure **5.6** and 5.7 B and D) at the edge of the porous supra–particles. The supra–particles were fractured to focus on latex particle assemblies at the edge of the section. Supra–particles obtained from 8.1 wt% latex particle suspension show significantly less ordered layers of composite sulphate latex as a result of the increased volume fraction of water in the process of supra–particle formation (Figure 5.6B). However, when the initial latex particle concentration increases, the edge structure of the formed supra–particle starts to show more densely packed structures (Figure 5.6D).

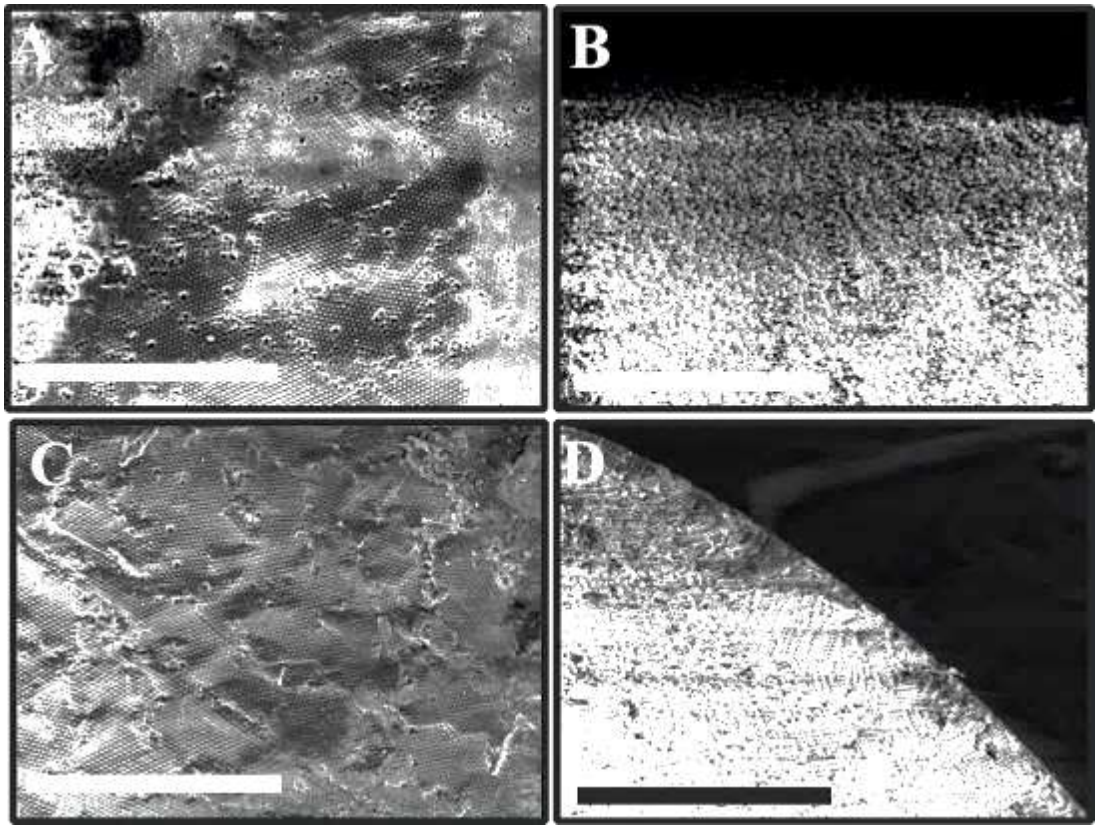

Figure 5.7. SEM images of the surface of supra–particles made from (2.6 μm) sulphate latex particles. The SEM images show the outer surface morphology of the supra–particles prepared from (A) 50 wt%, and (C) 70 wt% latex suspension; and shows the inner structure at the edge of supra–particles for (B) 50 wt%, and (D) 70 wt% initial latex particle concentrations, respectively. The supra–particles in (B) and (D) were sectioned to reveal the internal structure of the latex particle assembly near the supra–particle surface. The scale bar is 100 μm in all images.

The core structure for particles at 50–70 wt. % initial latex particle suspension showed some cavities due to air bubbles trapped inside them (see Figure **5.8**, A, B). This is undesirable as it may affect the overall mass density of the porous supra–particle and hence influence the supra–particle contact angle measurement when the particle is attached to a liquid surface. To avoid the trapping of air bubbles, the latex suspension was degassed before using it to produce the supra–particles. Note that the inner structure of the supra–particle near the surface has closer packing due to the rolling on the glass surface, while the latex particles tend to form a randomly packed structure towards the core of the particle because the rate of evaporation and removal of water is faster at the drop surface than those from the core of the particle. The difference between the water depletion rates at the forming supra–particle surface and its core

does not allow the supra–particles to develop fully homogenous packing of their building blocks.

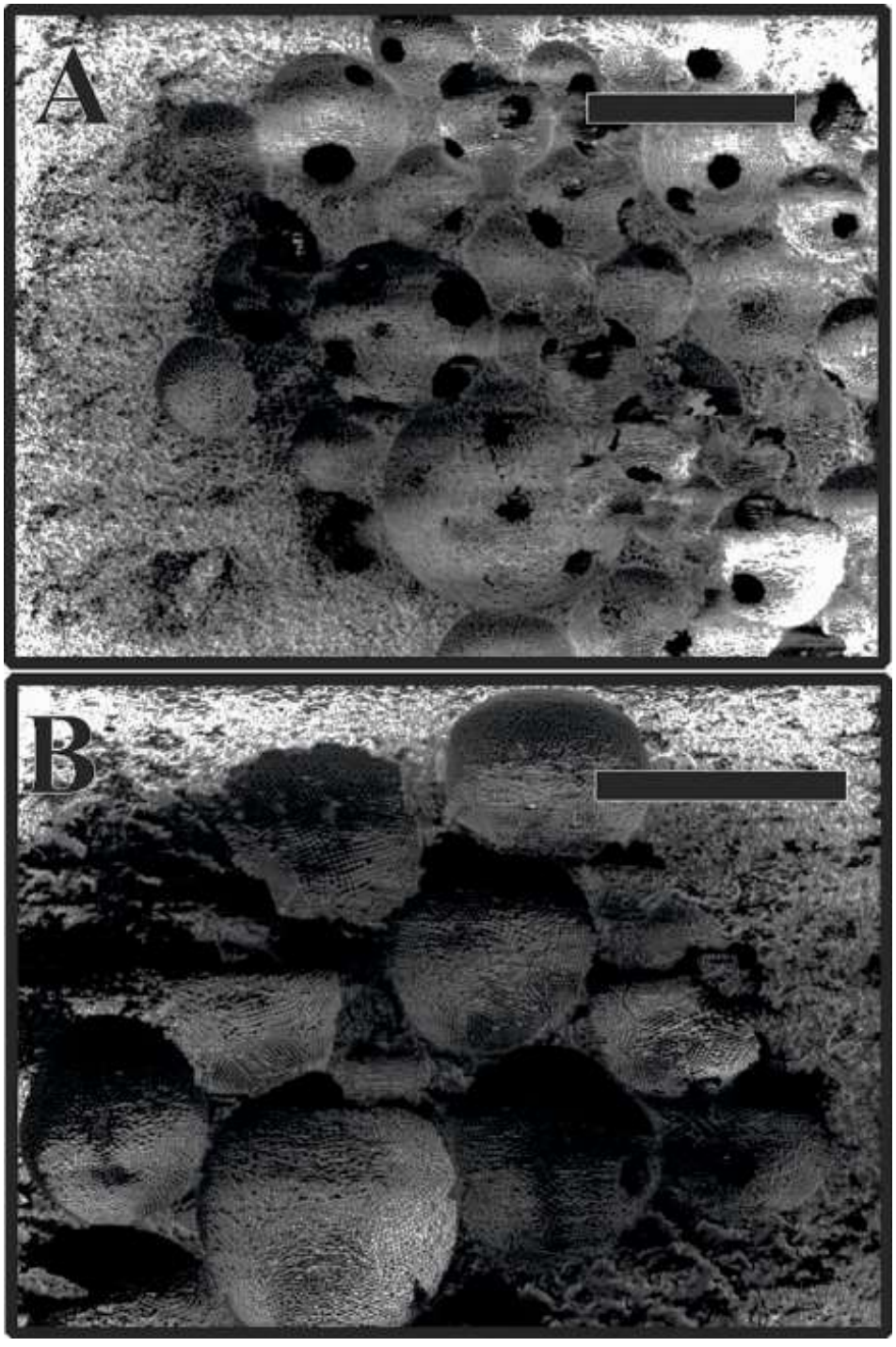

Figure 5.8. SEM images of the core of fragmented supra–particles made from 2.6 μm sulphate latex particles (A) 50 wt% and (B) 70 wt% initial latex concentration. These cavities appear only at the supra–particle core for particles formed from latex suspension above 50 wt%. The scale bar is 100 μm in all images.

Another factor which controls the surface morphology of the model supra–particles is the temperature of the hot superhydrophobic surface during the evaporation of the latex suspension. This effect was tested at several temperatures, right up to the polymer glass transition temperature. It can be seen that the latex particles start to be packed and organised with increasing temperatures from 60 to 105 °C (Figure **5.9**). However, the inner structure of the assembled latex particles shows that they are still randomly packed as the suspension gets jammed on the surface of the evaporating drop before the same phenomenon occurs in the core. Hence, the latex particles in the core can rearrange in a larger volume than those in the surface layer, which results in random packing in the core of the produced supra–particles.

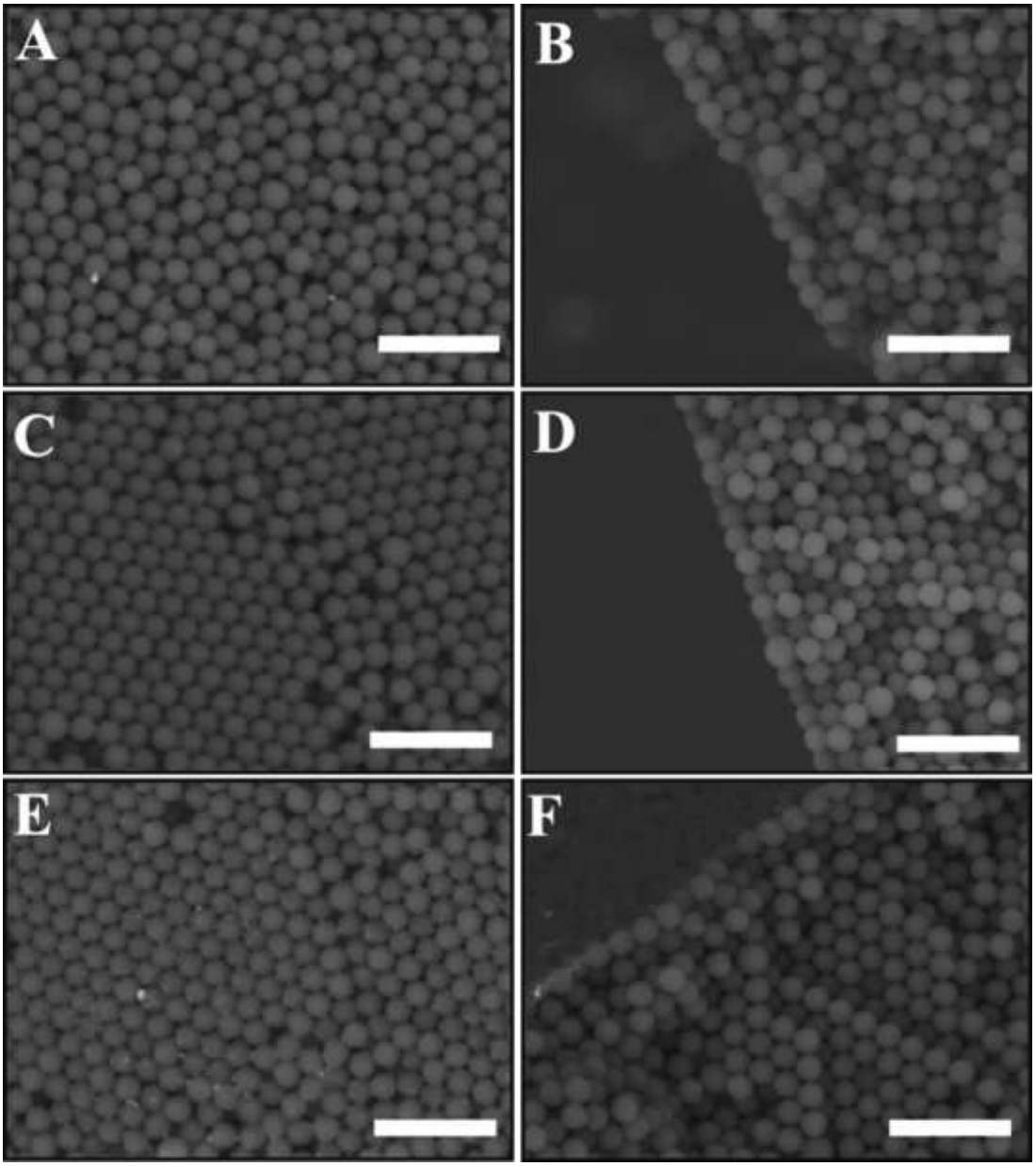

Figure 5.9. SEM images of porous supra–particles made by evaporating drops of 50 wt% latex suspension on a hot superhydrophobic surface, heated at 60 °C (A and B), 80 °C (C and D) and 105 °C (E and F). Surface morphology (A, C and E), and the inner structure at the edge of fragmented supra–particles (B, D, and F) can also be seen. The scale bar in all images is 10 μm.

5.2.4 Thermal annealing of the porous supra–particles

Latex particle fusion in the assembled supra–particles is affected by temperature. If the particles are held at temperatures above the glass transition temperature for polystyrene latex $T_g = 106\ ^oC$, i.e. $T > T_g$, the polystyrene particles started to partially

melt, the polymer turned soft and they fused together in the aggregate. (Figure **5.10**). When the latex particles were partially fused, they showed a glassy appearance and changed their composite colour to yellowish.

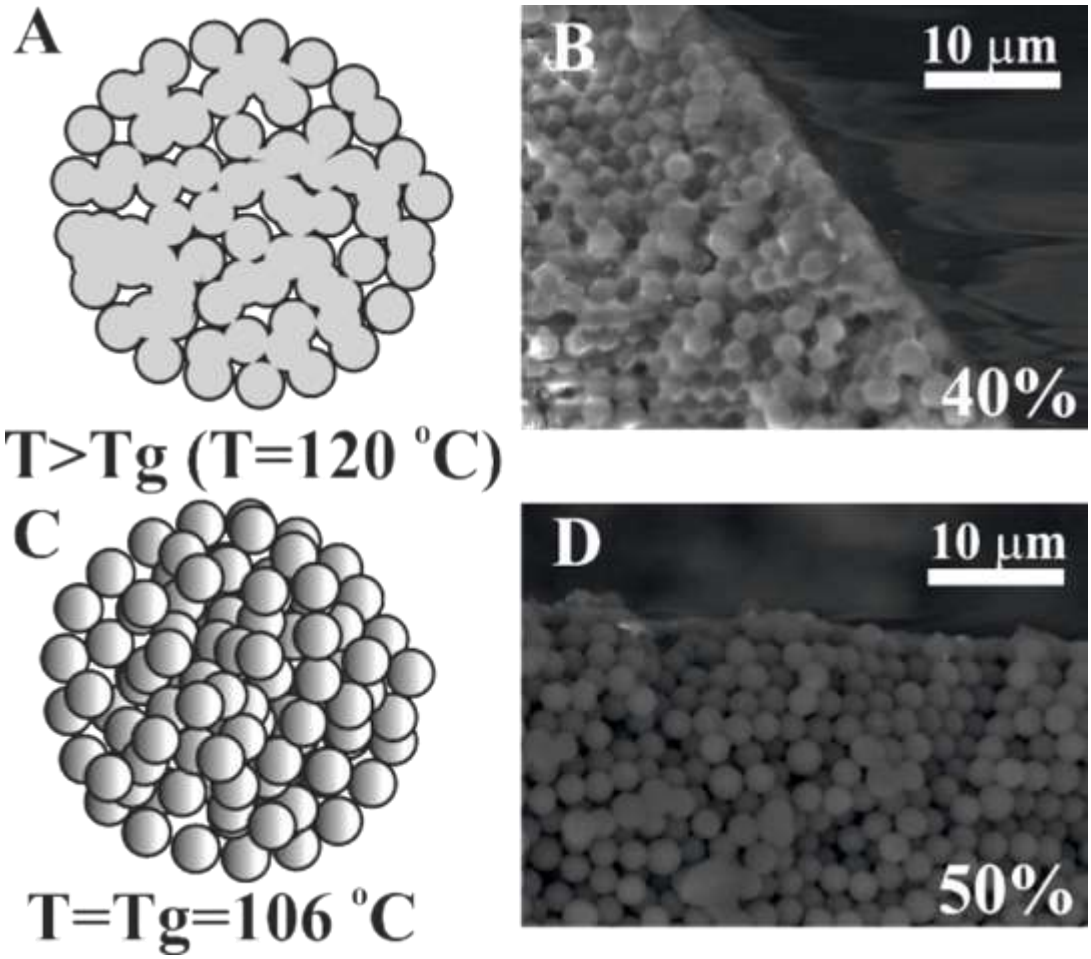

Figure 5.10. Illustration of the effect of temperature on the fusion of individual polystyrene latex particles inside a composite supra–particle: (A) schematics of the fusion of latex particles annealed at $T > T_g$; (B) SEM image of supra–particle made from 40 wt% latex particle suspension annealed at 120 ^oC; (C) schematics of a supra–particle annealed at the glass transition temperature (T_g) of polystyrene (106 ^oC); (D) SEM image of a fractured porous supra–particle made from 50 wt% particle suspension after annealing at T_g.

It was remarked that extensive fusion and melting of the latex particles would block all the pores and would not allow us to characterise the effect of the particle porosity on its three–phase contact angle at liquid surfaces. It was found that this is the case with particles annealed at 120 ^oC where the supra–particles melt and form glassy

supra–particles. However, supra–particles annealed below 103 ^{o}C were found to have poor stability and disintegrate when infused by a solvent (both water and oil).

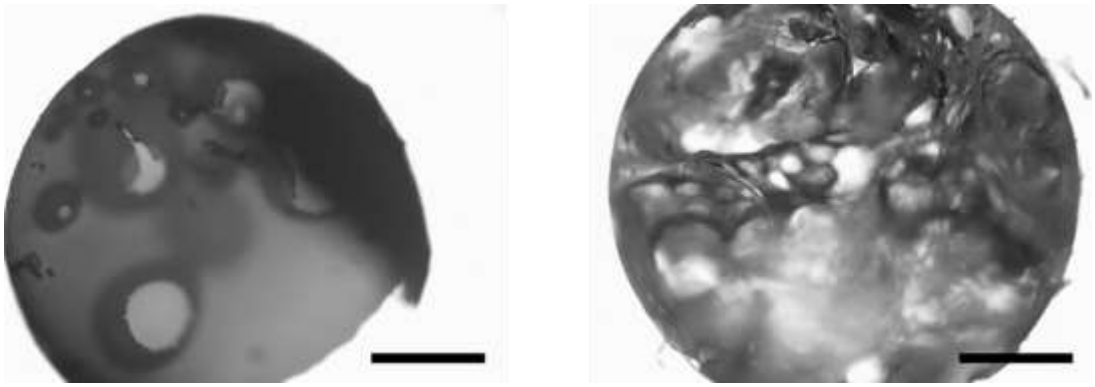

Figure 5.11. Optical microscopy images for melted (T>120 ^{o}C) particles prepared by injecting the building block particles into a PDMS mould. The scale bar is 500 μm.

5.2.5 Characterisation of the supra–particles' density and porosity

The aim of this experiment was to establish how the supra–particles mass density and the corresponding porosity depend on the initial particle concentration of the latex suspension. Generally, it was found that the supra–particle packing density increased with the increasing of the initial latex particle concentration. The highest packing density was obtained from 50 wt% latex suspension and remained unchanged for further increases in the particle concentration (60 wt% and 70 wt%). The density values were obtained using equation (2.6) and the porosity, by using the equation (2.7).

Table 5.1 summarises the mass densities and the volume fraction of particles in the obtained supra–particles as a function of the initial concentration of the latex suspension used to build these supra–particles. As expected, supra–particle porosity decreases when the concentration of the latex particles in the initial suspension is increased. Figure 5.12 represents the same data for the volume fraction of the latex particles versus the initial latex concentration.

Table 5.1. Mass density and porosity of porous supra–particles obtained by drying and annealing of latex particle suspension at various concentrations, 8–70 wt%. The annealing temperature was 106 ^{o}C for all particles. These supra–particles were measured, as described in 2.2.5.6. Here ϕ is the latex particle volume fraction in the supra–particle, calculated from the mass measurements. ρ_p is the supra–particle mass density.

Latex particles' initial concentration/ wt%	**ρ_p/ g cm^{-3}**	**ϕ**
8	**0.793 ± 0.020**	**0.629**
30	**0.853 ± 0.008**	**0.728**
40	**0.883 ± 0.010**	**0.780**
50	**0.987 ± 0.001**	**0.973**
60	**0.976 ± 0.002**	**0.953**
70	**0.984 ± 0.010**	**0.968**

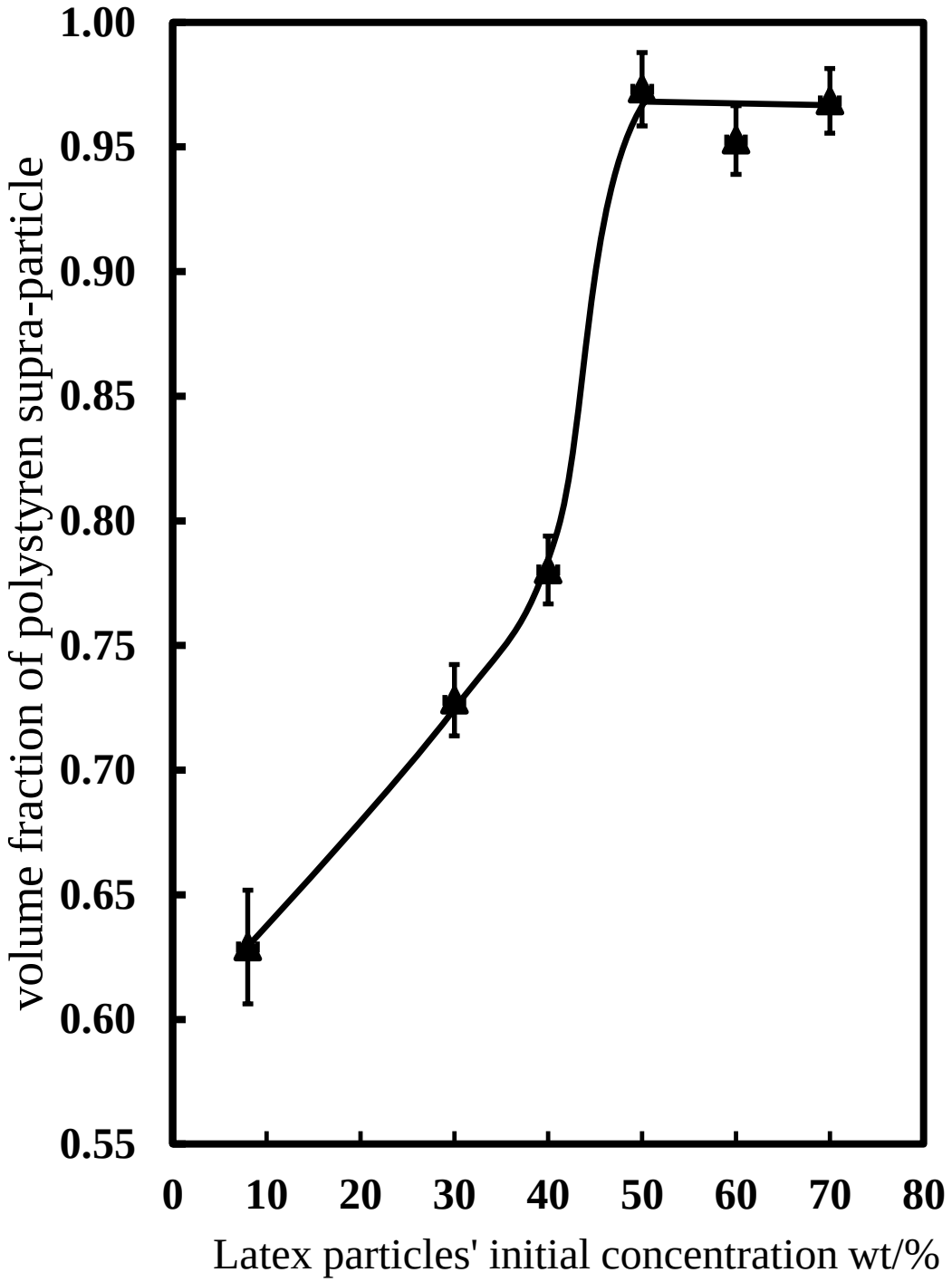

Figure 5.12. Relation between the latex particles' initial concentration in w/w % and the volume fraction of sulphate latex particles in the supra–particle. The volume fraction of these particles increased with the increase in the particles' initial concentration and reduced the pores' fraction of the total particles. Above 50 wt%, the particles' volume fraction levelled off.

In order to control the packing density of the supra–particles, the particles prepared from different suspension volumes were annealed in the two series of experiments. Firstly, the supra–particles were prepared and annealed for 2 hours at 106 ^{o}C, randomly at different times, which means that different patches of (1.7 mm, 2.0 mm and 2.2 mm) were fused individually for 2 hours in the oil bath. In the second experiment, the prepared supra–particles were annealed simultaneously, at the same temperature and set–up. It was found that the supra–particles which were annealed at different times showed different mass densities, whereas the supra–particles annealed simultaneously showed reproducible mass density values.

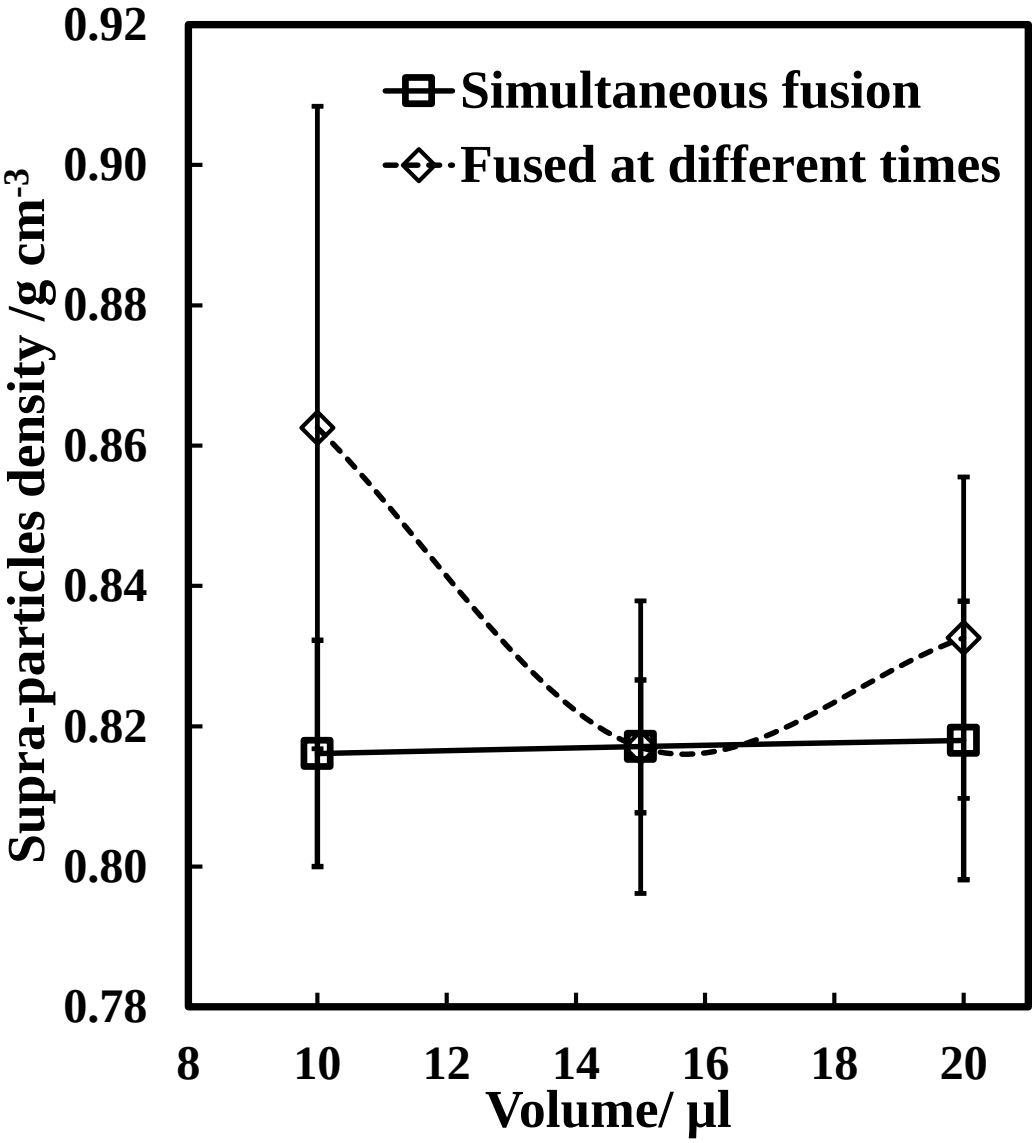

Figure 5.13. Supra–particles' packing density versus the initial volume of the latex suspension used for their prepration. This graph shows the importance of maintaining the same condtions for annealing all particles at the same time and the same set–up.

5.2.6 Observation of impregnation of the supra–particles with fluid

In order to find the best method to impregnate the pores of the supra–particles with liquids, two different experiments were carried out. The particles were pre–wetted in ethanol for 5 min and then in 10^{-5} M aqueous solution of Rhodamine 6G for 30 min and overnight. Optical and confocal fluorescence microscopy were used to observe the liquid phase penetration in the pores of the supra–particles. The results with optical fluorescence microscopy are presented in Figure 5.14 which shows incomplete infusion after 1 hour but complete infusion after overnight incubation in the solution. This delayed infusion can be explained by the slow dissolution of the air trapped inside of the supra–particle as it is inserted in the liquid phase.

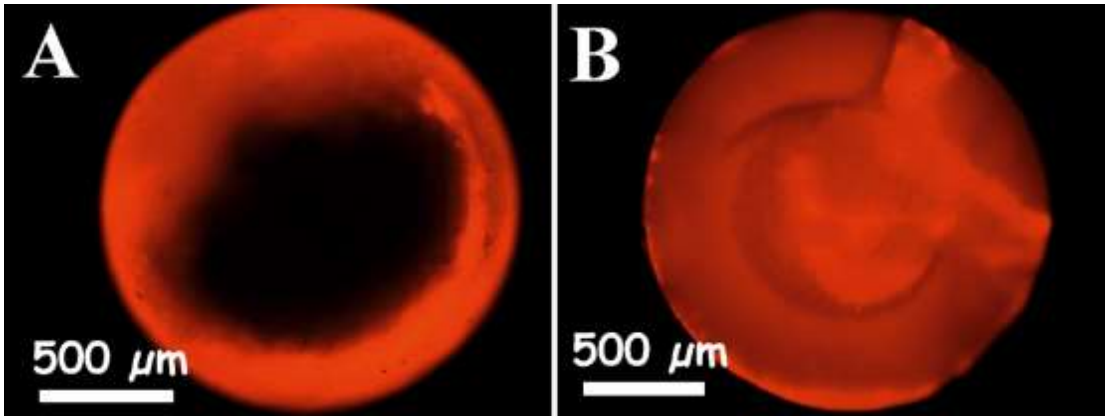

Figure 5.14. Fluorescence microscopy images of: (A) a porous supra–particle impregnated with 10^{-5} M Rhodamine 6G solution after 1 hour; (B) porous supra–particle impregnated with 10^{-5} M Rhodamine 6G overnight. The particles were fragmented after infusion with the liquid before being observed and imaged with a fluorescence microscope, with TRITC filter set.

Figure 5.15 shows the outer surface of particles filled with 10^{-5} M solution of Rhodamine 6G dye. This experiment was used to investigate the liquid impregnation by employing the dye as a fluorescent tracer of the liquid phase, using confocal fluorescent microscopy. The advantage of this method is that it obtains a 3D surface map and shows the inner distribution of the liquid for these particles, using scanning sheets. However, the depth of the laser scanning depends on the laser infusion through these particles which involves several latex particle diameters.

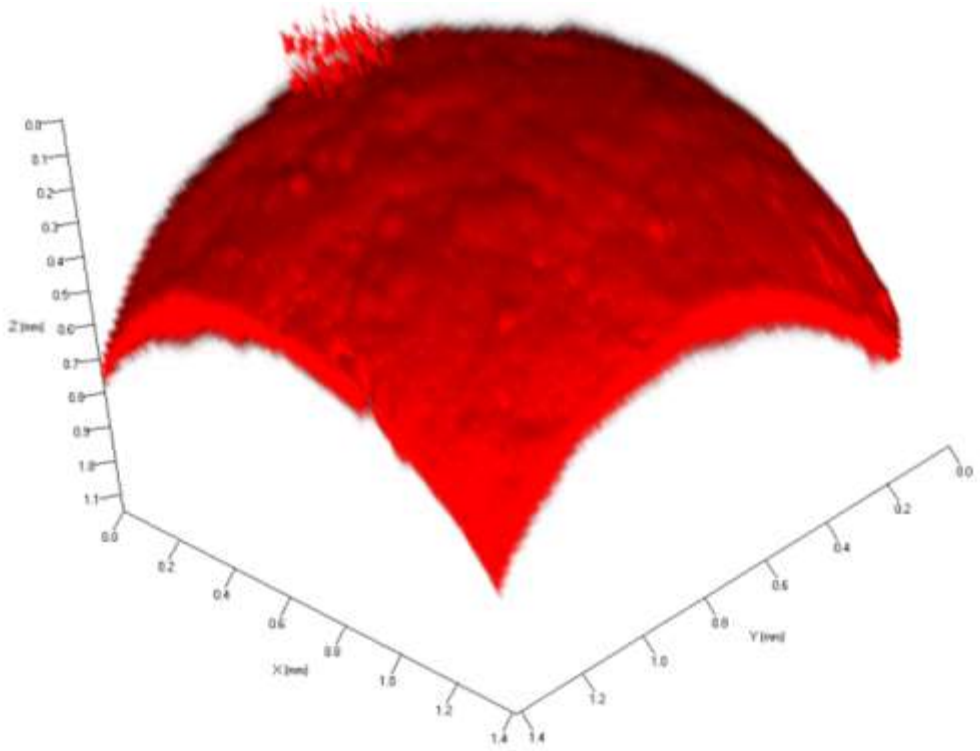

Figure 5.15. Confocal fluorescence microscope image for a supra–particle immersed in water. The water interface was 10^{-5} M solution of Rhodamine 6G. The scales X, Y and Z are in mm, while the depth of the imaged aqueous layer within the supra–particle is about 0.1 mm, which shows that the laser has only reached this depth and cannot enable the complete mapping of the liquid in–situ in such large supra–particles.

also silver salt was used as a tracer to investigate whether the water phase penetrated completely throughout the supra–particles. Figure **5.16** shows SEM images for supra–particles incubated with 0.1 M silver nitrate solution which, after drying, shows the silver salt crystals as white dots on the outer surface of the latex particles and inside the porous supra–particle.

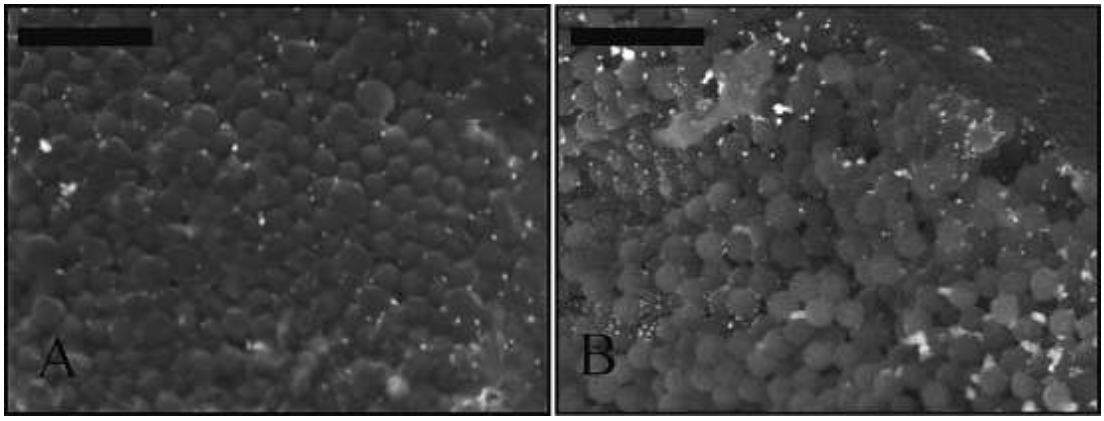

Figure 5.16. SEM images represent the infusion of an aqueous solution of silver nitrate inside the pores of a supra–particle; (A) is a SEM image of the supra–particle's outer surface, while (B) is a SEM image of the inner structure at the edge of a fractured supra–particle. The scale bar in both images is 10 µm. The particles have been removed from the solution and dried up before imaging.

5.3 Conclusions

Porous supra–particles were prepared by evaporation of a sulphate latex suspension on a hot superhydrophobic surface. Different supra–particle shapes were obtained, depending on the suspension drop evaporation technique used, which resulted in the formation of hollow shell, plate–like, spherical and dimple–like particles. Alternative techniques were explored using PDMS moulds with cavities produced by templating metal balls, rolling the suspension drop of latex particles on hydrophobic surfaces using shaker and hand rolling on a hot superhydrophobic surface. Of these techniques, only the last method was identified as successful in producing porous supra–particles. The supra–particles were further annealed to partially fuse the latex particle building blocks close to the polymer glass transition temperature. The supra–particles obtained had a rough surface, with a porous and amorphous structure. The supra–particle surface morphology and the inner structure were characterised by SEM imaging. This technique allows control of the supra–particle shape and size from a spherical structure by changing the drop evaporation temperature and droplet concentration and volume. Using latex suspension of particle concentration below 30 wt% produced supra–particles but not in spherical form. However, using suspension of the higher concentration, 40–70 wt%, spherical porous supra–particles were successfully produced. Moreover, the porosity of the porous supra–particles can be controlled by

the volume and the initial concentration of the latex particles' suspension and the rate of evaporation. Annealing of the supra–particles at the glass transition temperature for polystyrene shows no significant change when fused to form a rigid porous supra–particle, while annealing at higher temperatures formed hard, completely fused supra–particles of glassy appearance. The effect of the suspension concentration on the supra–particle mass density and porosity were investigated and found that above 50 wt% latex particle concentration, the obtained supra–particles become much denser and less porous than ones obtained with more diluted latex suspensions. The penetration of water inside the porous supra–particle upon incubation in aqueous solutions was studied by using aqueous fluorescent tracers and solutions of heavy metal salts. The timescale of complete infusion with water due to the existence of trapped air in the supra–particle upon incubation was demonstrated.

Chapter 6: Theory of the adsorption of porous particles and colloidosomes to a liquid–fluid interface.

6.1 Introduction

When colloidal particles adsorb at liquid surfaces, they decrease the free energy of the system [158, 159]. The adsorption energy of a colloid particle at the fluid interface (liquid–gas or liquid–liquid) (ΔF) could be many orders of magnitude higher than the thermal energy (kT). This indicates that colloid particles can adsorb irreversibly to the liquid–fluid interface. For that reason, colloid particles are used as emulsion stabilisers. Ramsden[160] and Pickering[161] reported the first emulsions systems stabilised by solid colloid particles. The particles wettability, surface chemistry, and shape influence how strongly the particles are adsorbed at the interface and their efficiency as emulsifiers.

Most of the theoretical considerations for the adsorption of colloid particles at liquid surface have been done on solid spherical particles with smooth surfaces[153, 162]. Although, the adsorption of surface anisotropic Janus particles[139, 163-170] and that of particles of non–spherical shape[40, 137, 171-174] have also been considered, a detailed theoretical description of the adsorption of porous spherical particles has not been reported in the literature.

In this chapter, a theoretical model of the adsorption of porous supra–particles from water or oil to the oil–water interface was develop. Composite porous particles made from smaller colloid particles will be considered as a model for a particle aggregate, which is a common occurrence in powdered materials. Our aim is to derive an equation connecting the three–phase contact angle, θ, of the supra–particle adsorbed at the liquid interface with the three–phase contact angle, θ_o of its building blocks, i.e. the smaller colloid particles from which it is formed. An equation were derive for the supra–particle adsorption energy and study the importance of the initial phase, from which the supra–particle approaches the liquid surface. the effect of the particle radius and the contact angle of the building blocks of the supra–particle on its wettability were studied. Here, also the energy of adsorption of a single colloid particle were compared with the energy of adsorption of a spherical aggregate of such particles. Furthermore the effect of the surface packing density of small particles was

investigated, on the supra–particle surface, on its effective three–phase contact angle. Interestingly, very similar considerations apply to the adsorption behaviour of spherical colloidosomes, which can be described with the same formulae.

One of the main assumptions of this chapter is that the adsorbing supra–particles attach to the liquid interface through a single layer of small colloid particles on the supra–particle surface. In this case, the liquid–fluid interface does not penetrate the core of the porous particles. This assumption seems reasonable as the potential penetration of the liquid surface front to the depth of the porous particle would require effective desorption of the surface layer of particles, requiring a very high energy input to occur. This means that a supra–particle (or a particle aggregate) is unlikely to spontaneously adjust the position of the liquid interface further than the surface layer of small colloid particles. In Chapter 7, will present the results of additional experiments with model porous supra–particles designed to visualise the penetration of the liquid interface with respect to the supra–particle surface, which confirms the validity of this hypothesis.

6.2 Theoretical background

6.2.1 Attachment of a single colloid particle at the liquid–fluid interface

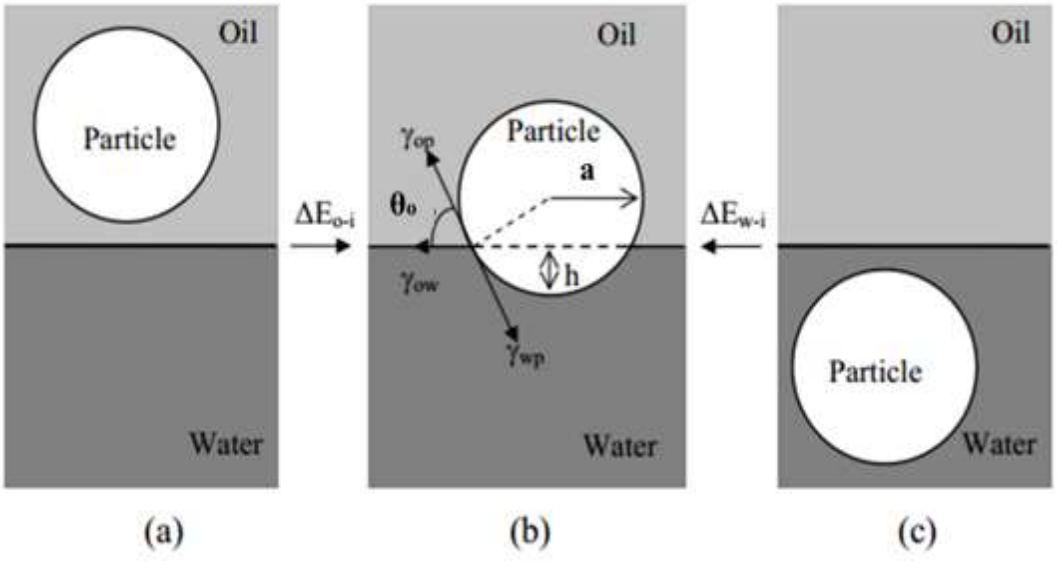

Figure 6.1. Schematics illustrating a smooth spherical colloidal particle (a) approaching the oil–water interface from the oil phase; (b) attached at the oil–water interface; and (c) approaching the oil–water interface from the water phase.[175]

The energy of attachment of a colloid particle at the oil–water interface is related to the interfacial tension of the oil–water interface, γ_{ow}, the particle three–phase contact angle measured through the more polar fluid phase (θ_o), and the particle radius, a. For a single colloid particle adsorbed at the oil–water interface (Figure **6.1**), the depth of immersion of the particle into the water phase (h) is[27, 175-176]

$$h = a\,(1 + \cos\theta_o) \tag{6.1}$$

The surface contact area of the adsorbed colloid particle with the water phase is given by:

$$A_{pw} = 2\pi ah = 2\pi a^2\,(1 + \cos\theta_o) \tag{6.2}$$

The surface contact area of the colloidal particle–oil at the oil–water interface is given by:

$$A_{po} = 2\pi a\,(2a - h) = 2\pi a^2\,(1 - \cos\theta_o) \tag{6.3}$$

(Therefore, the planar area of the oil–water interface excluded by the particle adsorption is given by:

$$A_{ow} = \pi a^2 \sin^2\theta_o = \pi a^2(1 - \cos^2\theta_o) \tag{6.4}$$

Assuming that the particle is small enough in order to neglect the gravity effect, the free energy of adsorption (or attachment) of a single spherical colloid particles from the fluid interface into the oil phase is given by:

$$-\Delta E_{attach} = A_{pw}\,(\gamma_{po} - \gamma_{pw}) + A_{pw}\,\gamma_{ow} \tag{6.5}$$

$$-\Delta E_{attach} = 2\pi a^2\,(1 + \cos\theta)\,(\gamma_{po} - \gamma_{pw}) + \pi a^2\,(1 - \cos^2\theta_o)\,\gamma_{ow} \tag{6.6}$$

By using Young's equation, $\gamma_{ow}\cos\theta_o = \gamma_{po} - \gamma_{pw}$, Eq (6.6) can be simplified to read:

a) for particle removal from the fluid interface into oil or air:

$$\Delta E_{attach} = -\pi a^2\,\gamma_{ow}\,(1 + \cos\theta_o)^2 \tag{6.7}$$

b) for particle removal from the fluid interface into water:

$$\Delta E_{attach} = -\pi a^2\,\gamma_{ow}\,(1 - \cos\theta_o)^2 \tag{6.8}$$

The γ_{ow} defines the applicable o/w interfacial tension while the p, w and o define the particle, water, and oil, respectively. Very similar considerations apply to the adsorption (attachment) of a colloid particle at the air–water interface, with the oil phase being replaced with air in all of the above formulas. Note that according to Eqs.

(6.7) and (6.8), the free energy of particle adsorption energy is negative, i.e. the process of particle adsorption at the liquid interface is spontaneous from both fluid phases, oil and water. As the above equations, (6.7) and (6.8) describe, more energy is required for the removal of hydrophilic particles ($\theta < 90°$) from the interface into oil compared with water, while the hydrophobic particles ($\theta > 90°$) has the same effect.[27, 175-176]

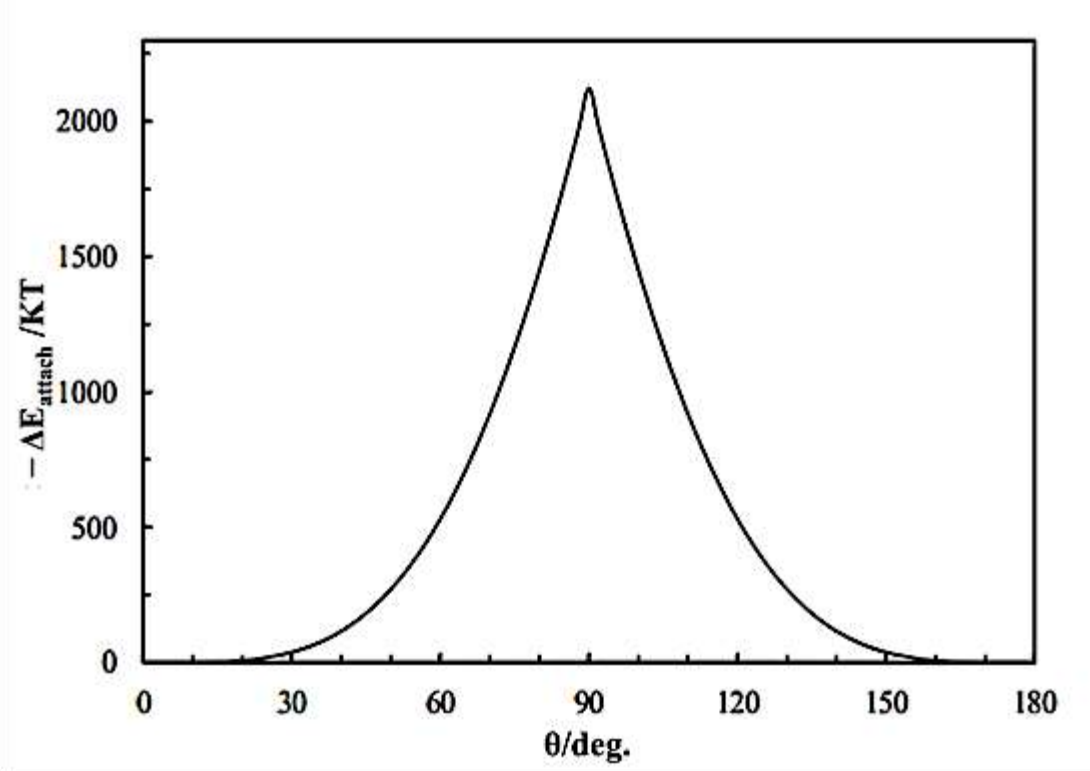

Figure 6.2. Variation of energy of attachment (ΔE_{attach}) of a colloidal particle of radius a = 10 nm from the water phase to a planar oil–water interface of interfacial tension γ_{ow} = 27 mN/m, at 298 K with contact angle θ.[134, 176]

The particle is strongly adsorbed at the oil–water interface when the contact angle is equal to 90°. However, the energy of attachment decreases rapidly (~ 10 kT or less) when the contact angle is superhydrophilic ($0° \leq \theta \leq 20°$) or superhydrophobic ($150° \leq \theta \leq 180°$)[27].

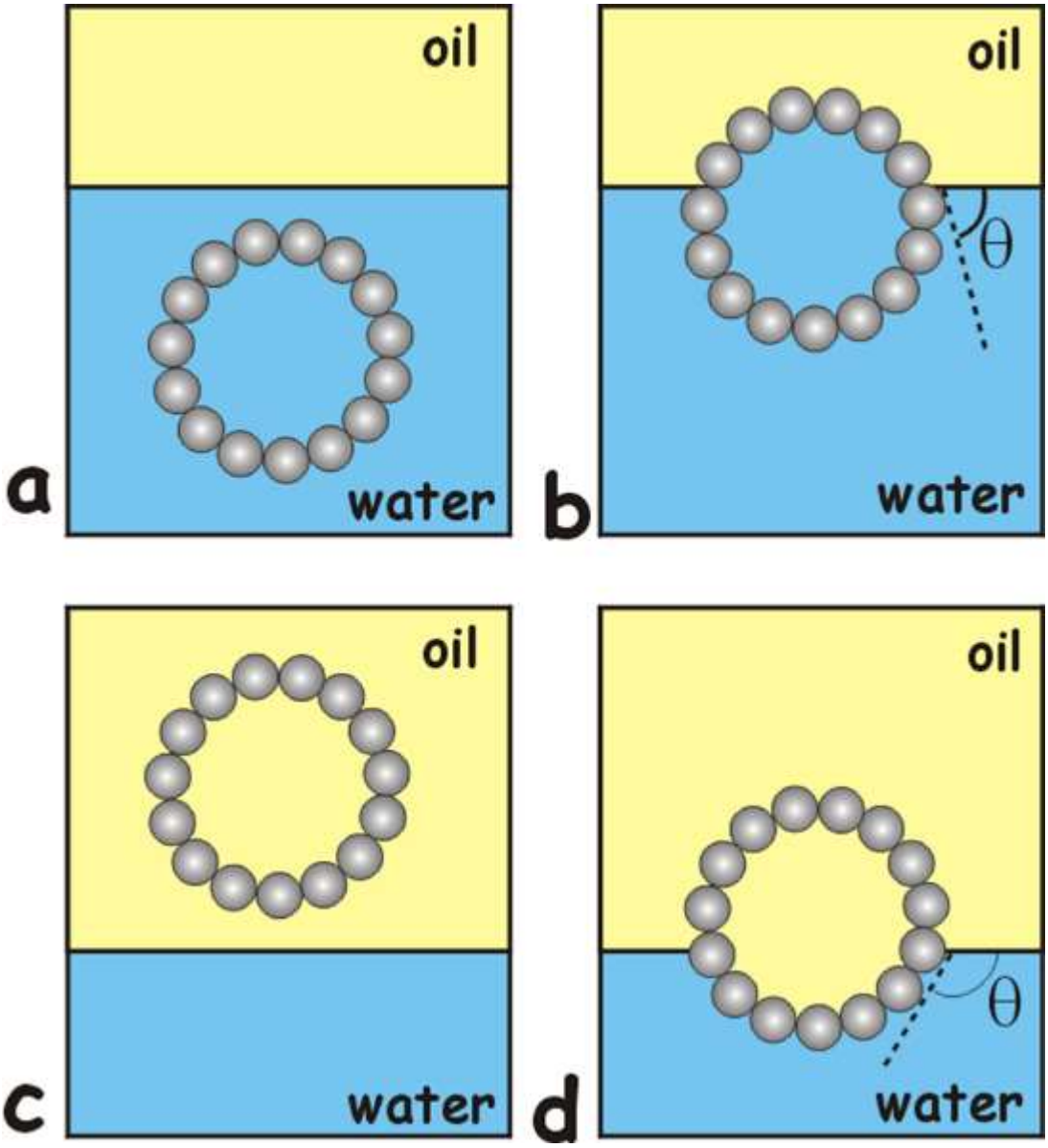

Figure 6.3. Schematic representation of the process of adsorption of a colloidosome capsule whose shell is made of smaller colloid particles: adsorption of colloidosome from the water phase (a) to the oil–water interface (b); adsorption from the oil phase (c) to the oil–water interface (d). Note that the contact angle of a water–infused colloidosome adsorbed at the oil–water interface (a)–(b) is different from the contact angle of the same colloidosome infused initially with oil (c)–(d). The theoretical model assumes that the oil–water interface is attached only on the surface layer of colloid particles of the adsorbed colloidosome and does not penetrate through its membrane.

6.3 Theoretical model for the adsorption of a porous spherical supra–particle (or a spherical colloidosome) at the oil–water interface

Let us consider the process of the adsorption of a porous spherical supra–particle or a spherical colloidosome capsule to an oil–water interface. Two cases will be considered: (i) when the porous supra–particle (or the colloidosome capsule) is initially in the aqueous phase (Figure **6.3**a, and Figure **6.4**a, respectively); and (ii) when the porous supra–particle (or the colloidosome capsule) is initially in the oil phase. In both cases, it is assumed that the porous supra–particle capsule is infused with the same fluid as in the continuous phase (i.e. water in case (i) and oil in case (ii)). The porous composite supra–particle and colloidosome capsule will be assumed to be spherical (with radius R) and encased by a shell with a monolayer of closely–packed spherical particles (with radius a). Our aim here is to find the connection between the three–phase contact angle (θ_o) of the colloid particles in the particle monolayer and the effective three–phase contact angle (θ) of the supra–particle (or the colloidosome), respectively) when adsorbed at an oil–water interface. Here and hereafter, the contact anglesθ and θ_o are defined through the water phase. Note that here, the theoretical considerations of the adsorption of a spherical colloidosome also apply to the adsorption of a spherical supra–particle (of the same radius R), which consists of closely–packed, small spherical particles (with radius a) and contact angle θ_o (compare Figure **6.3** and Figure **6.4**).

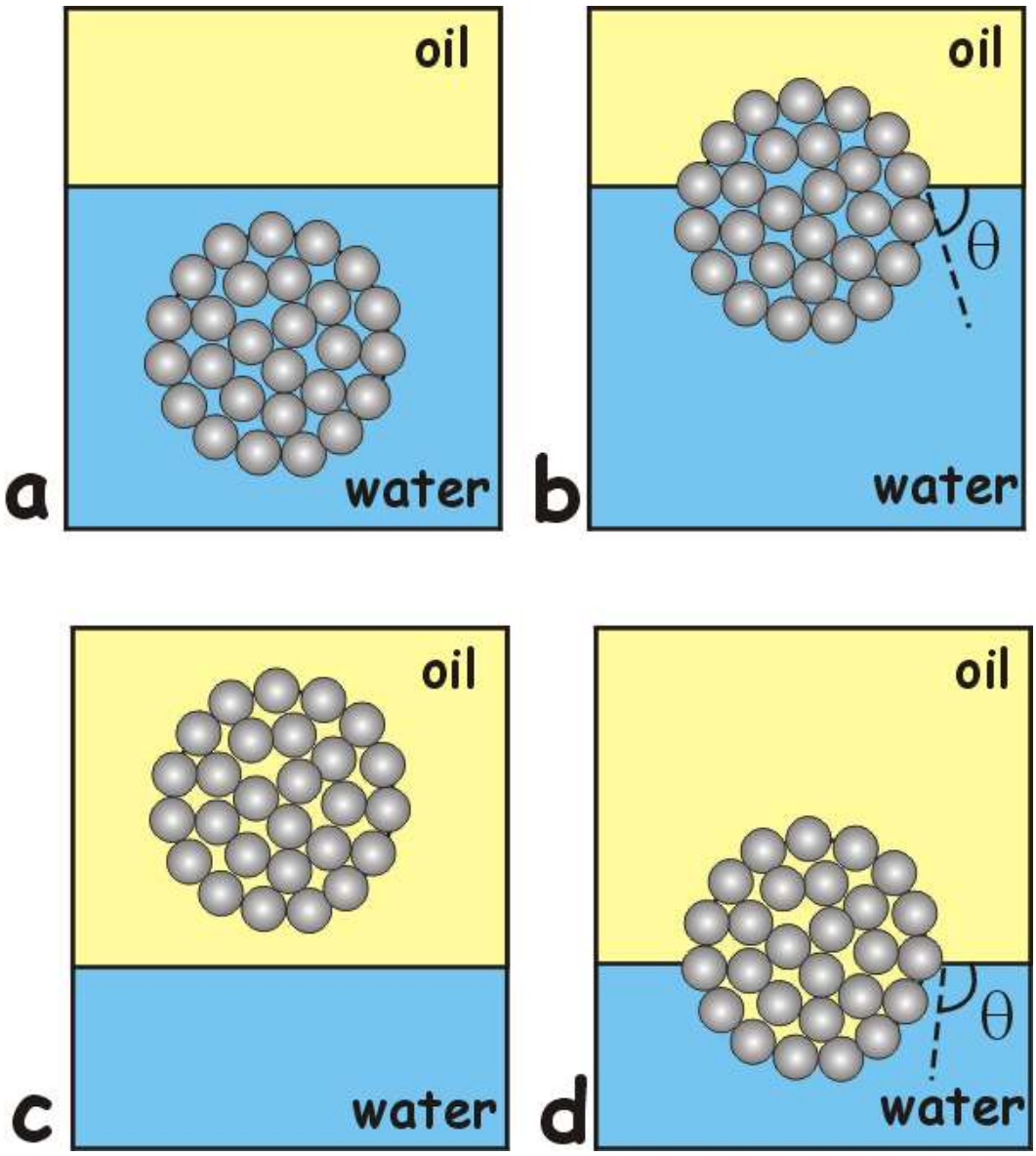

Figure 6.4. Schematic representation of the process of adsorption of a spherical composite supra–particle made of smaller colloid particles: adsorption of a supra–particle from the water phase (a) to the oil–water interface (b); adsorption from the oil phase (c) to the oil–water interface (d). Note that the contact angle of a water–infused supra–particle adsorbed at the oil–water interface (a)–(b) is different from the contact angle of the same supra–particle infused initially with oil (c)–(d). The theoretical model assumes that the oil–water interface is attached only on the surface layer of colloid particles of the adsorbed supra–particle.

All of the results are directly applicable to adsorption at the air–water interface, with the oil phase treated as air. As shown previously by many other authors (see Eqs. (6.7) and (6.8)), the adsorption energy of a single colloid particle of radius a and contact angle θ_o to the oil–water interface is:

$$\Delta E_1 = -\pi a^2 \gamma (1 - \cos\theta_0)^2, \qquad \Delta E_2 = -\pi a^2 \gamma (1 + \cos\theta_0)^2 \tag{6.9}$$

Here, γ is the oil–water interfacial tension while ΔE_1 and ΔE_2 correspond to adsorption from the water phase and the oil phase, respectively.

6.3.1 Adsorption of a porous supra–particle or a colloidosome from the aqueous phase to the oil–water interface.

The process of adsorption of the colloidosome from the bulk of the aqueous phase to the oil–water interface can be formally considered as a two–step process:

(i) The porous supra–particle (or colloidosome) displaces a portion of the oil–water interface of area encircled by its contact line:

$$A_c = \pi r_c^2 = \pi R_c^2 \sin^2\theta \tag{6.10}$$

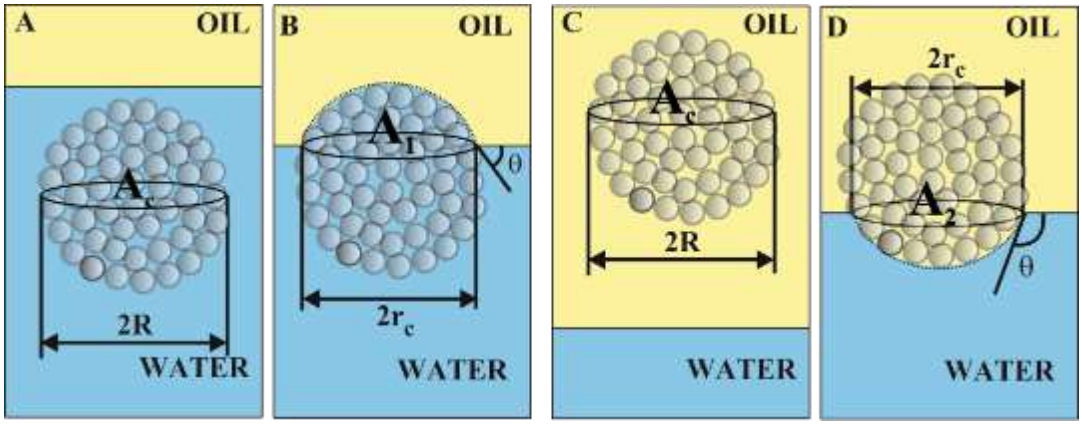

Figure 6.5. Schematic of the attachment energy of porous supraparticles to an oil–water interface (A) from water phase to (B) oil–water interfaces and from (C) oil interface to (D) oil–water interface.

but creates a curved oil–water interface with adsorbed particles of total area A_1 and a radius of curvature roughly the same (R) as that of the adsorbed supra–particle:

$$A_1 = 2\pi R^2 (1 - \cos\theta) \tag{6.11}$$

(ii) The colloid particles within this area on the supra–particle (or colloidosome surface) attach to the oil–water interface. For the sake of simplicity, the particles are assumed to be closely packed together within the porous supra–particle (or the colloidosome membrane). The possible effects of the fusion of particles within the supra–particle (or the colloidosome membrane) will not be accounted for as this complicates the analysis unnecessarily, although this can also be incorporated into a more refined model. The number of adsorbed particles can be calculated by approximating the area per small colloid particle on the porous supra–particle and colloidosome surface. This involves computing the area of a particles in hexagon packing, $A_h = 2\sqrt{3}a^2$:

$$N_1 = \frac{A_1}{A_h} = \frac{\pi R^2 (1-\cos\theta)}{\sqrt{3}a^2}, \text{ (for hexagonal packing),} \tag{6.12}$$

and area of particles in square packing , $A_s = 4a^2$:

$$N_1 = \frac{A_1}{A_s} = \frac{\pi R^2 (1-\cos\ \theta)}{2a^2} \text{ (for square packing).} \tag{6.13}$$

Thus, the free energy of adsorption ΔF_1 of the supra–particle (or colloidosome) from the water to the oil–water interface can be estimated as follows:

$$\Delta F_1 = \gamma A_1 - \gamma A_c + N_1 \Delta E_1 \tag{6.14}$$

For hexagonal packing, the substitution of Eqs. (6.9), (6.10), (6.11), and (6.12) into Eq. (6.14) gives:

$$\Delta F_1 = -\pi\gamma R^2 \left\{1-\cos^2\theta + (1-\cos\theta)\left[\frac{\pi}{\sqrt{3}}(1-\cos\theta_0)^2 - 2\right]\right\} \tag{6.15}$$

For square packing, the substitution of Eq. (6.9), (6.10), (6.11), and (6.13) into Eq. (6.14) gives:

$$\Delta F_1 = -\pi\gamma R^2 \left\{1-\cos^2\theta + (1-\cos\theta)\left[\frac{\pi}{2}(1-\cos\theta_0)^2 - 2\right]\right\} \tag{6.16}$$

With respect to the porous supra–particle (or colloidosome) contact angle, θ, the condition of a minimum of the surface free energy in the system requires that:

$$\frac{d\Delta F_1}{d\cos\theta} = -\pi\gamma R^2 \left\{ -2\cos\theta - \left[\frac{\pi}{\sqrt{3}} (1 - \cos\theta_0)^2 - 2 \right] \right\} = 0 \qquad (6.17)$$

for hexagonal packing of the particle building blocks on the supra–particle surface, and

$$\frac{d\Delta F_1}{d\cos\theta} = -\pi\gamma R^2 \left\{ -2\cos\theta - \left[\frac{\pi}{2} (1 - \cos\theta_0)^2 - 2 \right] \right\} = 0 \qquad (6.18)$$

for square packing, respectively. Depending on the arrangement of particles at the surface, Eqs. (6.15) and (6.16) allow to connect the supra–particle (or colloidosome) contact angle θ with the contact angle θ_o of its building blocks (i.e. the colloid particles in the porous supra–particle or colloidosome membrane, respectively).

For building block particles arranged in hexagonal packing on the supra–particle surface:

$$\cos\theta = 1 - \frac{\pi}{2\sqrt{3}} (1 - \cos\theta_o)^2 \qquad (6.19)$$

For building block particles arranged in square packing on the supra–particle surface:

$$\cos\theta = 1 - \frac{\pi}{4} (1 - \cos\theta_o)^2 \qquad (6.20)$$

The boundary condition for equations 6.17 and 6.18 can be observed when derived into (6.19 and 6.20). Note that the derived eq (6.19) and (6.20) does not depend on the radius of the colloid particles and the radius of the colloidosome. This equation also allows the contact angle θ_o of the colloid particles to be estimated by measuring the effective (macroscopic) contact angle θ of the composite porous particle and colloidosome capsule adsorbed at the oil-water interface. From eq (6.19) one can also see that there is a critical value of the particle contact angle if arranged in hexagonal packing $\theta_o \approx 119°$and eq (6.20) if the particles arranged in square packing $\theta_o \approx 126°$, above which eq (6.19) and (6.20) does not have a solution for the colloidosome contact angle. The interpretation of this fact is that if the particles in the composite porous particle and colloidosome membrane are so hydrophobic that their contact angle is larger than 119°, or 126° the composite porous particle and colloidosome (filled with water) would transfer completely from the water phase into the oil thus producing

water-in-oil Pickering drop rather than adsorb at the oil-water interface with a finite contact angle θ.

To the best of our knowledge, these two equations are original results derived by us in this thesis. The substitution of Eq. (6.19) back into Eq. (6.15) gives the free energy of adsorption of the water–infused supra–particle (or colloidosome) as a function of its radius R and the contact angle θ_o of the colloid particles on the surface of the porous supra–particle or colloidosome:

$$\Delta F_1 = -\frac{1}{12}\pi^3\gamma R^2(1-\cos\theta_o)^4 \qquad \text{(for hexagonal packing)} \qquad (6.21a)$$

$$\Delta F_1 = -\frac{1}{16}\pi^3\gamma R^2(1-\cos\theta_o)^4 \qquad \text{(for square packing)} \qquad (6.21b)$$

6.3.2 Adsorption of a porous supra–particle or a colloidosome from the oil phase to the oil–water interface

Analogous to the consideration in the previous section, the process of supra–particle (or colloidosome) adsorption from the oil phase to the oil–water interface can also be formally split into two steps (Figure **6.3**c and Figure **6.4**c):

(i) The porous supra–particle and colloidosome displace a portion of the oil–water interface of area A_c, thereby creating a curved oil–water interface of area A_2:

$$A_2 = 2\pi R^2(1+\cos\theta) \qquad (6.22)$$

(ii) The colloid particles within this area on the colloidosome surface adsorb to the oil–water interface. The number of adsorbed particles is:

$$N_2 = \frac{A_2}{A_h} = \frac{\pi R^2(1+\cos\theta)}{\sqrt{3}a^2} \qquad \text{(for hexagonal packing)} \qquad (6.23)$$

$$N_2 = \frac{A_2}{A_s} = \frac{\pi R^2(1+\cos\theta)}{2a^2} \qquad \text{(for square packing)} \qquad (6.24)$$

Thus, the free energy of adsorption of the porous supra–particle and colloidosome from the oil phase to the oil–water interface is:

$$\Delta F_2 = \gamma A_2 - \gamma A_S + N_2\Delta E_2 \qquad (6.25)$$

For hexagonal packing of particles on the supra–particle surface, the substitution of Eqs. (6.9), (6.10), (6.22) and (6.23) into Eq. (6.25) gives:

$$\Delta F_2 = -\pi\gamma R^2 \left\{1-\cos^2\theta+(1+\cos\theta)\left[\frac{\pi}{\sqrt{3}}(1+\cos\theta_0)^2-2\right]\right\} \qquad (6.26)$$

For square packing, respectively, the substitution of Eqs. (6.9), (6.10), (6.22), and (6.24) into Eq. (6.25) gives:

$$\Delta F_2 = -\pi\gamma R^2 \left\{1-\cos^2\theta+(1+\cos\theta)\left[\frac{\pi}{2}(1+\cos\theta_0)^2-2\right]\right\} \qquad (6.27)$$

With respect to the supra–particle (or colloidosome) contact angle, the condition of minimal surface free energy in the system requires that:

$$\frac{d\Delta F_2}{d\cos\theta} = -\pi\gamma R^2 \left\{-2\cos\theta+\left[\frac{\pi}{\sqrt{3}}(1+\cos\theta_0)^2-2\right]\right\} = 0 \qquad (6.28)$$

$$\frac{d\Delta F_2}{d\cos\theta} = -\pi\gamma R^2 \left\{-2\cos\theta+\left[\frac{\pi}{2}(1-\cos\theta_0)^2-2\right]\right\} = 0 \qquad (6.29)$$

For colloid particles organised in hexagonal packing on the supra–particle surface, Eq. (6.28) is analogous to Eq. (6.17) in that it provides the relationship between the porous supra–particle (or colloidosome) contact angle (θ) and the small particles' contact angle (θ_o) upon adsorption from the oil phase. This is given by:

$$\cos\theta = \frac{\pi}{2\sqrt{3}}(1+\cos\theta_o)^2 - 1 \quad \text{(for hexagonal packing)} \qquad (6.30)$$

For building block particles organised in square packing, the corresponding equation is:

$$\cos\theta = \frac{\pi}{4}(1+\cos\theta_o)^2 - 1 \quad \text{(for square packing)} \qquad (6.31)$$

One should note that Eqs. (6.19) and (6.30) predict different values of the supra–particle (or colloidosome) equilibrium contact angle at the oil–water interface, depending on the fluid phase of origin (water or oil). There is no contradiction here. This is due to the fact that the porous supra–particle (or colloidosome) is filled with water in the case of Eq. (6.19) and with oil in the case of Eq. (6.30). This is a fundamental result, which differentiates composite porous supra–particles or colloidosome capsules from the building block solid colloid particles that would

acquire the same equilibrium contact angle θ_o when adsorbed from both water and oil to the oil–water interface. According to Eq. (6.30), for hexagonal packing of spherical colloid particles on the supra–particle (or colloidosome) surface, there is a critical value of the particle contact angle: $\theta_o \approx 61°$. For the square packing, however, equation (6.31) suggests a critical value of $\theta_o \approx 54°$. Above this critical value, Eqs. (6.30) and (6.31) do not provide a real solution for the porous supra–particle and colloidosome contact angle (θ). This means that, if the particles in the colloidosome membrane are so hydrophilic that their contact angle is smaller than ~61^o, the porous supra–particle or colloidosome (filled with oil) would transfer completely from the oil phase into the water. For the case of a colloidosome initially filled with oil phase, this model predicts that for hexagonal packing of small particles of contact angle smaller than 61^o on the colloidosome membrane, this would produce an oil–in–water Pickering drop rather than an oil–filled colloidosome adsorbed at the oil–water interface with a finite three–phase contact angle, θ.

Similarly to Eq. (6.21), an expression can be derived for the free energy of adsorption of the supra–particle (or colloidosome) from the oil phase to the oil–water interface. The substitution of Eq. (6.30) back into Eq. (6.26) gives the energy of adsorption of the oil–infused porous supra–particle (or colloidosome) as a function of its radius R and the contact angle θ_o of the colloid particles forming the porous supra–particle (or colloidosome membrane):

$$\Delta F_2 = -\frac{1}{12}\pi^3 \gamma R^2 (1+\cos\theta_o)^4 \quad \text{(for hexagonal packing)} \qquad (6.32a)$$

$$\Delta F_2 = -\frac{1}{16}\pi^3 \gamma R^2 (1+\cos\theta_o)^4 \quad \text{(for square packing)} \qquad (6.33b)$$

Once again, the adsorption energy of the porous supra–particle (or colloidosome) from the oil to the oil–water interface is independent, in the first approximation, of the size of the colloid particles in its membrane. This result holds for both supra–particles and colloidosomes with densely packed surfaces with smaller particles. Both Eqs. (6.21) and (6.32) predict that the adsorption free energy is negative and the adsorption (attachment) process is thermodynamically spontaneous independently from which fluid phase the supra–particle is coming to adsorb at the oil–water interface. The energy of adsorption is different depending on whether the supra–particle is infused with oil (from the oil phase) or water (from the aqueous phase). Note, however, that

the value of the contact angle θ_o corresponds to spontaneous adsorption only for finite values of the particle contact angle, θ, according to Eqs. (6.30) and (6.31) for oil–infused particles. Comparing the adsorption energy of the porous spherical composite supra–particle, e.g. Eq. (6.32), with its analogue for the adsorption of its building blocks (small spherical colloid particles), and Eq. (6.9), one sees a much stronger dependence on the contact angle θ_o of the small particles on the adsorption energy of the composite particle.

6.4 Results and discussions

In this section, the adsorption energy of porous supra–particles or the colloidosome at the liquid interface will be discussed. These contact angles are related to the contact angle of individual building block particles. Additionally, the impact of the packing arrangement (i.e. hexagonal and square) of the supra–particle building blocks on the contact angle and the free energy of its attachment to the liquid–fluid interface will be studied numerically. Also the importance of the initial fluid phase infused into these porous supra–particles will be discussed, which affects the particle free energy of absorption at the liquid interface.

6.4.1 Contact angle of a porous supra–particle (or colloidosome) adsorbed from the aqueous phase to the oil–water interface.

Figure 6.5 shows the contact angle of the porous supra–particle as a function of the contact angle of the building block particles. Note that the resulting equations, (6.19) and (6.20), do not depend (in first approximation) on the radius of the small colloid particles, a, although they depend on the radius R of the porous supra–particle (or colloidosome, respectively). This equation also allows, in principle, the contact angle θ_o of the colloid particles (building blocks) to be estimated by measuring the effective (macroscopic) contact angle θ of the porous supra–particle (or colloidosome capsule) adsorbed at the oil–water interface.

From Eqs. (6.19) and (6.20), one can also see that there is a critical value of the small colloid particles' contact angle (for hexagonal packing, $\theta_o \approx 119°$ and square packing, $\theta_o \approx 126°$). Above these critical angles, Eqs. (6.19) and (6.20) do not have solutions for the porous supra–particle (or colloidosome) contact angle, θ. This suggests that, if the constituting particles in the porous supra–particle (or colloidosome membrane) are so

hydrophobic that their contact angle is larger than 119° (hexagonal packing) or 126° (square packing), the porous supra–particle (or colloidosome) would transfer completely from the water phase into the oil phase. In the case of a colloidosome in these conditions, which is a particular case of this consideration, this would result in the spontaneous formation of a water–in–oil Pickering drop on the other side of the liquid surface rather than its adsorption at the oil–water interface with a finite contact angle, θ. It could be remark that this is true only if such a colloidosome is already preformed and filled with water before it approaches the oil–water interface.

Depending on the building block particles' contact angle, θ_o, Figure **6.7** and Figure **6.8** represent the free energy required by porous supra–particles to attach to the liquid–fluid interface. For instance, if the building block is hydrophilic (e.g. $\theta_o \approx 61^o$), then the predicted contact angle for porous supra–particles would be $\theta \approx 41^o$ for hexagonal packing or $\theta \approx 38^o$ for square packing. In comparison, with hydrophobic building block particles (e.g. $\theta_o \approx 110^o$), the predicted supra–particle contact angles would be $\theta \approx 114^o$ and $\theta \approx 129^o$ for square and hexagonal packing, respectively.

One can also see that the adsorption energy of the supra–particle (or colloidosome) at the oil–water interface is independent (in first approximation) of the size, a, of its building blocks and depends on the square of the supra–particle radius, R. Its value is always negative and corresponds to spontaneous adsorption for finite values of the particle contact angle θ_o, lower than the critical value of $\theta_o \approx 119°$ (for hexagonal packing) or $\theta_o \approx 126°$ (for square packing). Note that according to Eqs. (6.21a) and (6.21b), the adsorption energy of hexagonally packed supra–particles is greater in magnitude than that of square–packed supra–particles. This result is not trivial as macroscopic contact angles of the supra–particles are also different for hexagonal and square packing.

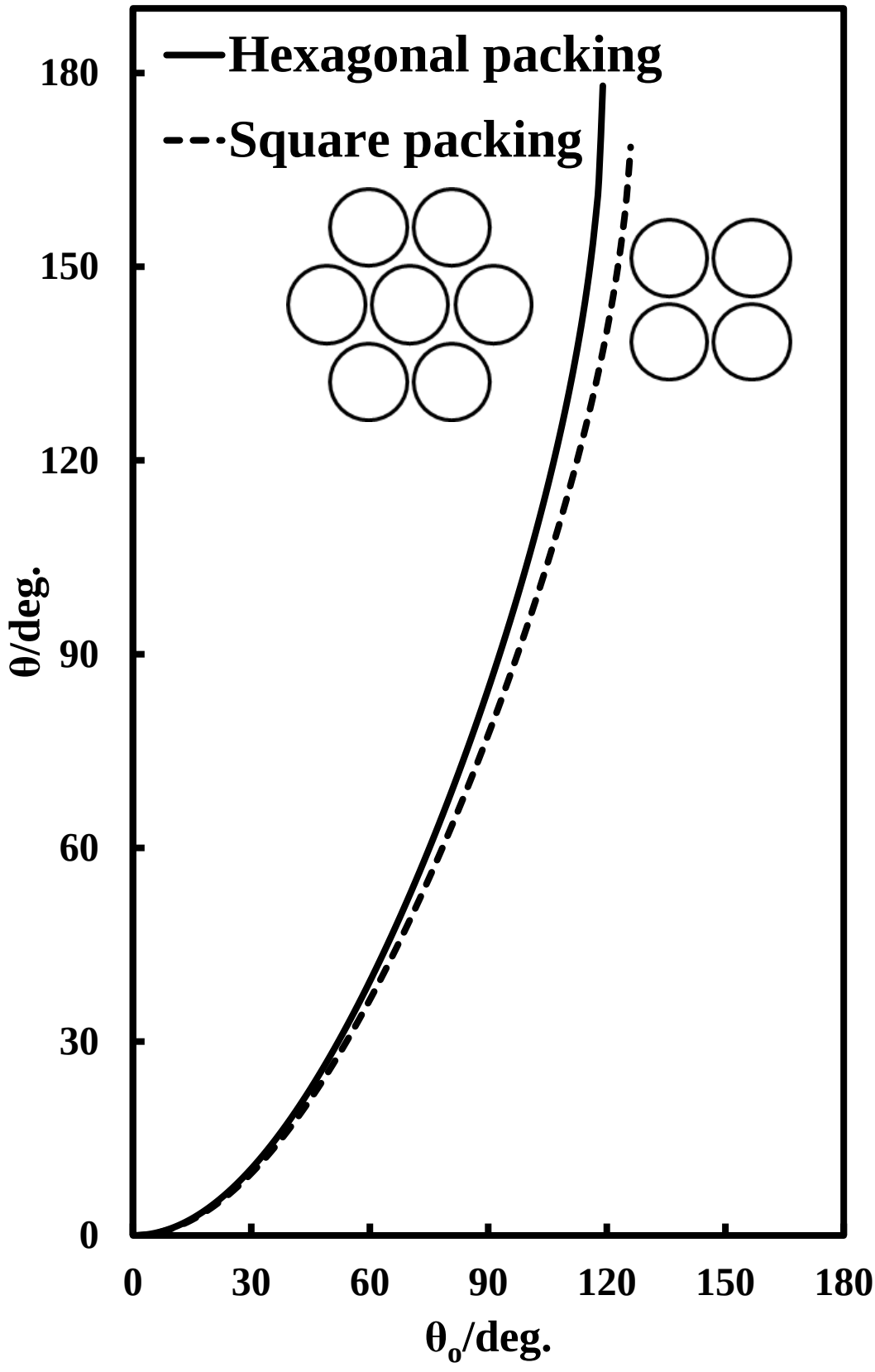

Figure 6.6. Theoretical dependence of the three–phase contact angle, θ, of a water–filled porous supra–particle (or a colloidosome) adsorbed at the oil–water interface and the three–phase contact angle of their "building block" colloid particles, θ_o.

In figure 6.5 present the theoretical dependence of the three–phase contact angle, θ, of a water–filled porous supra–particle (or a colloidosome) adsorbed at the oil–water interface and the three–phase contact angle of their "building block" colloid particles, θ_o. The solid line represents the contact angle for "building block" colloid particles arranged in hexagonal packing at the surface of the porous supra–particles (i.e. θ reaches maximum at $\theta_o \approx 119°$). On the other hand, square packing of the colloid particles on the supra–particle surface corresponds to the dashed line (θ reaches maximum value at a critical contact angle value of $\theta_o \approx 126°$). Beyond these critical values of θ, Eqs. (6.19) and (6.20) have no real physical solution, i.e. the free surface energy of the system has no global minimum as a function of θ. Note that this analysis also holds for the adsorption of water–filled supra–particles from the water to the air–water interface. The same analysis is valid for a water–filled colloidosome made from the same building block particles. Interestingly, the equations predict that above the critical value of θ_o, as pointed out above, the colloidosome would spontaneously transfer through the air–water surface and form a liquid marble [177-180], however, such high values for the small particle contact angle, θ_o, which would allow such a prediction of the theory to be tested experimentally, are difficult to achieve at the air–water interface for smooth surfaces.

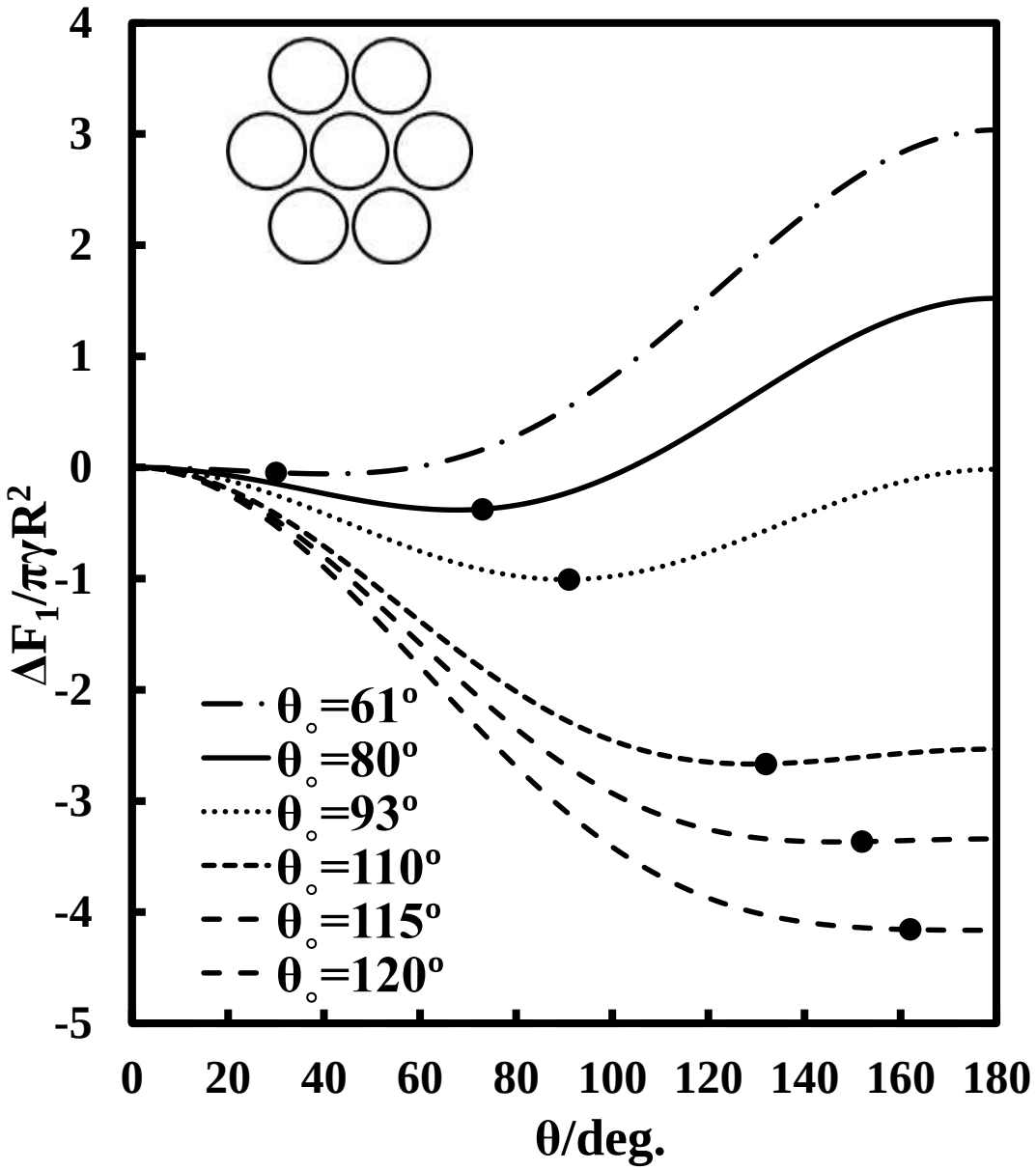

Figure 6.7. Dimensionless free energy of adsorption for a supra–particle impregnated by water from the water phase to the oil–water interface as a function of its macroscopic contact angle, θ (see Eq. (6.15)). The colloid particles on the supra–particle surface are arranged in hexagonal packing. The different lines correspond to selected values of the contact angle of building block colloid particles. The circular dots (•) represent the global minimum of the adsorption free surface energy of the porous supra–particle, with respect to its contact angle for a fixed value of the contact angle of the building block particles, θ_o. In this case, the macroscopic contact angle of the supra–particle (or colloidosome), θ, is determined from Eq. (6.20) for the respective value of θ_o, which corresponds to the minimum of the free energy curve presented on this graph.

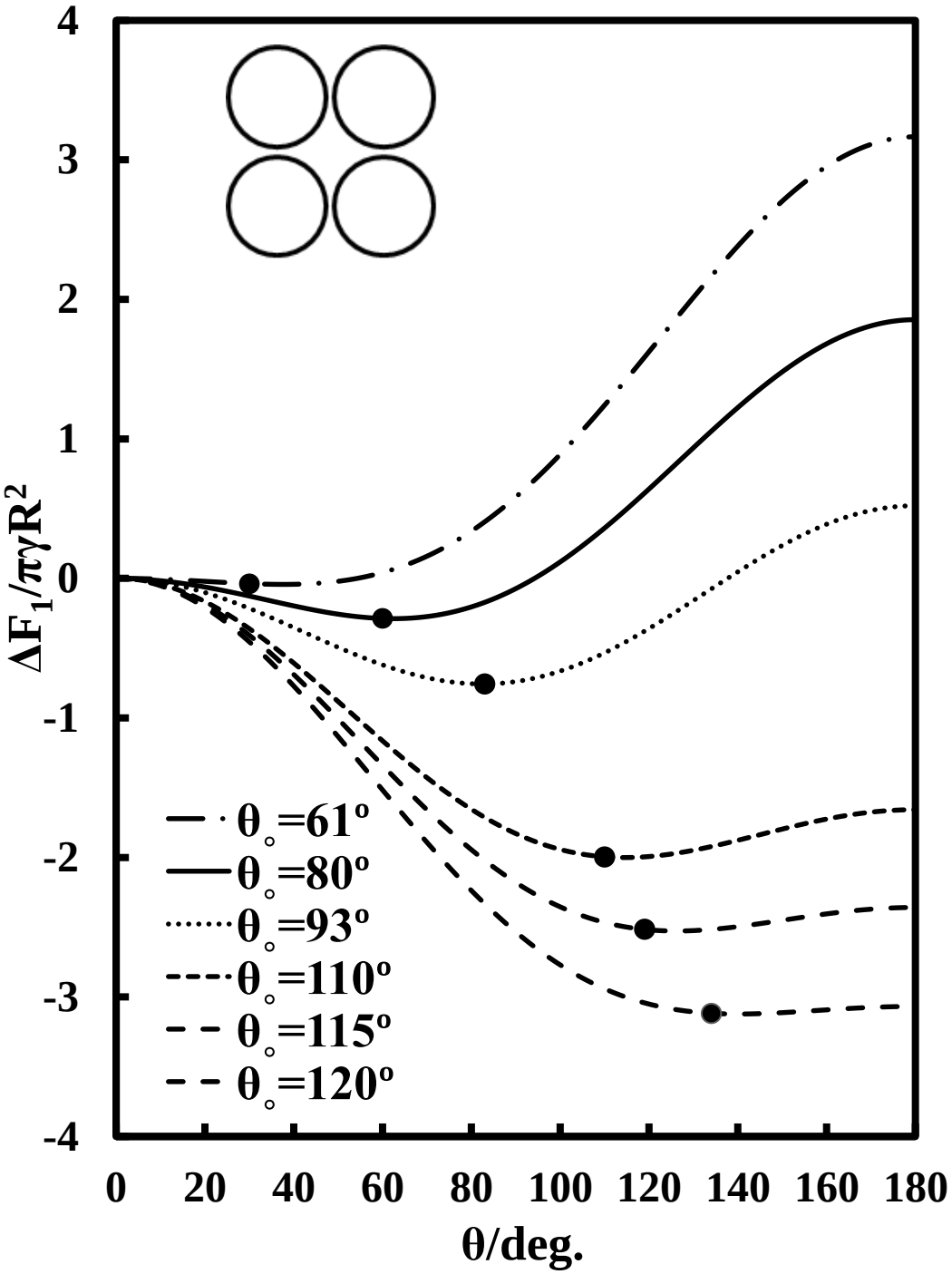

Figure 6.8. Dimensionless free energy of adsorption for a supra–particle impregnated with water from the water phase to the oil–water interface as a function of its macroscopic contact angle, θ (see Eq. (6.16)). The colloid particles on the supra–particle surface are arranged in square packing. The different lines correspond to selected values of the contact angle of building block colloid particles. The circular dots (•) represent the global minimum of the adsorption free surface energy of the porous supra–particle with respect to its contact angle for a fixed value of the contact angle of the building block particles, θ_o.

Figure 6.7 shows the adsorption energy of the supra–particle versus its macroscopic contact angle for square packing of its building block particles on its surface. One sees that each free energy curve, which corresponds to a fixed value of θ_o, has a minimum at different positions, compared with hexagonal packing (see Figure 6.6). In this case, the macroscopic contact angle of the supra–particle (or colloidosome), θ, is determined from Eq. (6.19) for the respective value of θ_o which corresponds to the minimum of the free energy curve presented on this graph.

6.4.2 Contact angle of a porous supra–particle (or colloidosome) adsorbed from the oil phase to the oil–water interface.

Impregnation of the pores in the porous supra–particles with oil or keeping it dry, i.e. full of air, has a different effect on its adsorption behaviour compared with water–impregnated porous particles made of the same building block particles. This affects the attachment energy of the supra–particles at the liquid interface and their equilibrium macroscopic contact angle, θ, at the liquid surface. One should note that Eqs. (6.19), (6.20), (6.30), and (6.31) predict different values of the porous supra–particles (or colloidosome) equilibrium contact angle at the oil–water interface, depending on the phase of origin. These results are not, in fact, contradictory. This is due to the fact that the porous supra–particle and colloidosome are filled with water in the case of Eqs. (6.19) and (6.20), but with oil for the case of Eqs. (6.30) and (6.31). This is a fundamental result, which differentiates porous supra–particles (or colloidosome capsules) from the solid non–porous building block colloid particles that would acquire the same equilibrium contact angle when adsorbed from both water and oil to the oil–water interface. According to Eq. (6.30), for hexagonal packing of the small particles on the supra–particle surface, there is a critical value of the colloid particle contact angle: $\theta_o \approx 61°$. For square packing conditions, Eq. (6.31) yields a critical value of $\theta_o \approx 54°$, below which Eqs. (6.30) and (6.31) do not have a real physical solution for the porous supra–particle (or colloidosome) contact angle, θ. This means that, if the particles in the porous supra–particles' surface (or the colloidosome membrane) are so hydrophilic that their contact angle is smaller than $\sim 61^o$ or 54^o, the porous supra–particle (or colloidosome) filled with oil would transfer completely from the oil phase into the water. the effect of the particle buoyancy in this theoretical consideration have been neglected. In the case of a colloidosome filled with oil, this would result in the formation of an oil–in–water Pickering drop rather than its adsorption from the oil phase to the oil–water interface with a finite contact angle, θ.

Similarly to Eq. (6.21), an expression can be derived for the energy of adsorption of the supra–particle (or colloidosome) from the oil phase to the oil–water interface. The substitution of Eq. (6.30) back into Eq. (6.26) gives the energy of adsorption of the porous supra–particle as a function of its radius and the contact angle of the colloid particles in the porous supra–particle (or colloidosome membrane). The adsorption

energy of the porous supra–particle at the oil–water interface is independent (in first approximation) of the size of the colloid particles on its surface and has negative values i.e. corresponds to spontaneous adsorption for finite values of the particle contact angle greater than the critical value of $\theta_o \approx 61^o$ for hexagonal packing or $\theta_o \approx 54^o$ for square packing conditions

The minimum of the surface free energy depends on the individual building block contact angle. For example, if the building block particle's contact angle is $\theta_o = 119^o$, then the porous supra–particle contact angle would be 139^o and 142^o for square and hexagonal packing, respectively. However, if the individual particles are hydrophilic (i.e. $\theta_o < 61^o$), then the porous supra–particles' contact angle could be $\theta \approx 43^o$ for square packing and $\theta_o \approx 0^o$ for hexagonal packing conditions.

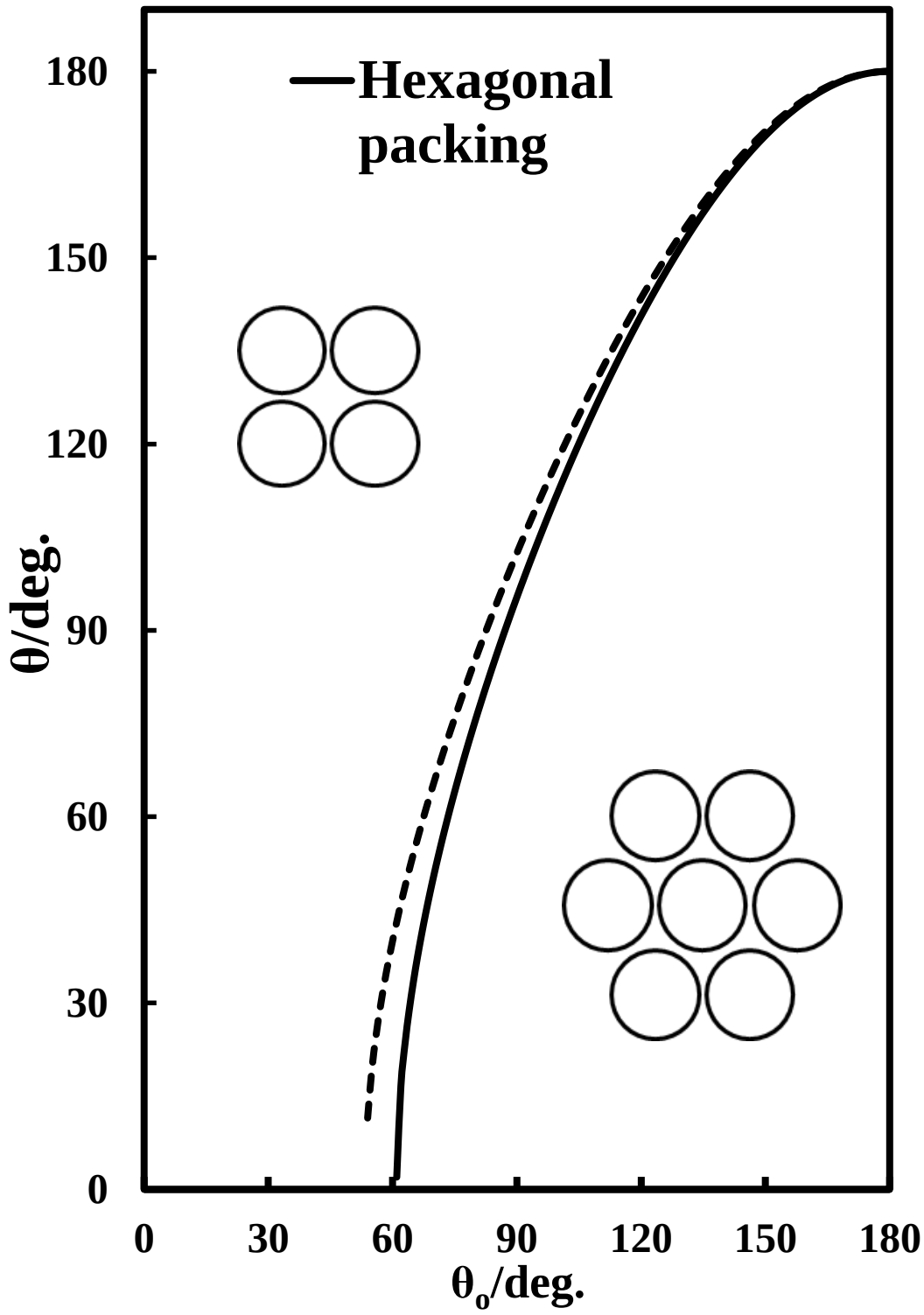

Figure 6.8. Theoretical dependence of the three–phase contact angle, θ, of an oil–filled porous supra–particle (or a colloidosome) adsorbed at the oil–water interface and the three–phase contact angle of their "building block" colloid particles, θ_o. The building block particles are packed in a hexagonal lattice on the surface of the supra–particle.

It can be seen that in Figure 6.8 the theoretical dependence of the three–phase contact angle, θ, of an oil–filled porous supra–particle (or a colloidosome) adsorbed at the oil–water interface and the three–phase contact angle of their "building block" colloid particles, θ_o. The solid line represents the macroscopic contact angle for the "building block" colloid particles arranged in a hexagonal packing at the surface of the porous supra–particles (i.e. θ reaches zero at approximately $\theta_o \approx 61°$). On the other hand, for square packing of the colloid particles on the supra–particle surface (the dashed line), θ reaches zero at a critical contact angle value of $\theta_o \approx 54°$). Below these critical values of θ, Eqs. (6.30) and (6.31) have no real physical solution for θ, i.e. the free surface energy of the system has no global minimum as a function of θ. Note that this analysis also holds for the adsorption of a dry, air–filled supra–particle from the air phase to the air–water interface. The same analysis is valid for a hollow, air–filled colloidosome made from the same building block particles.

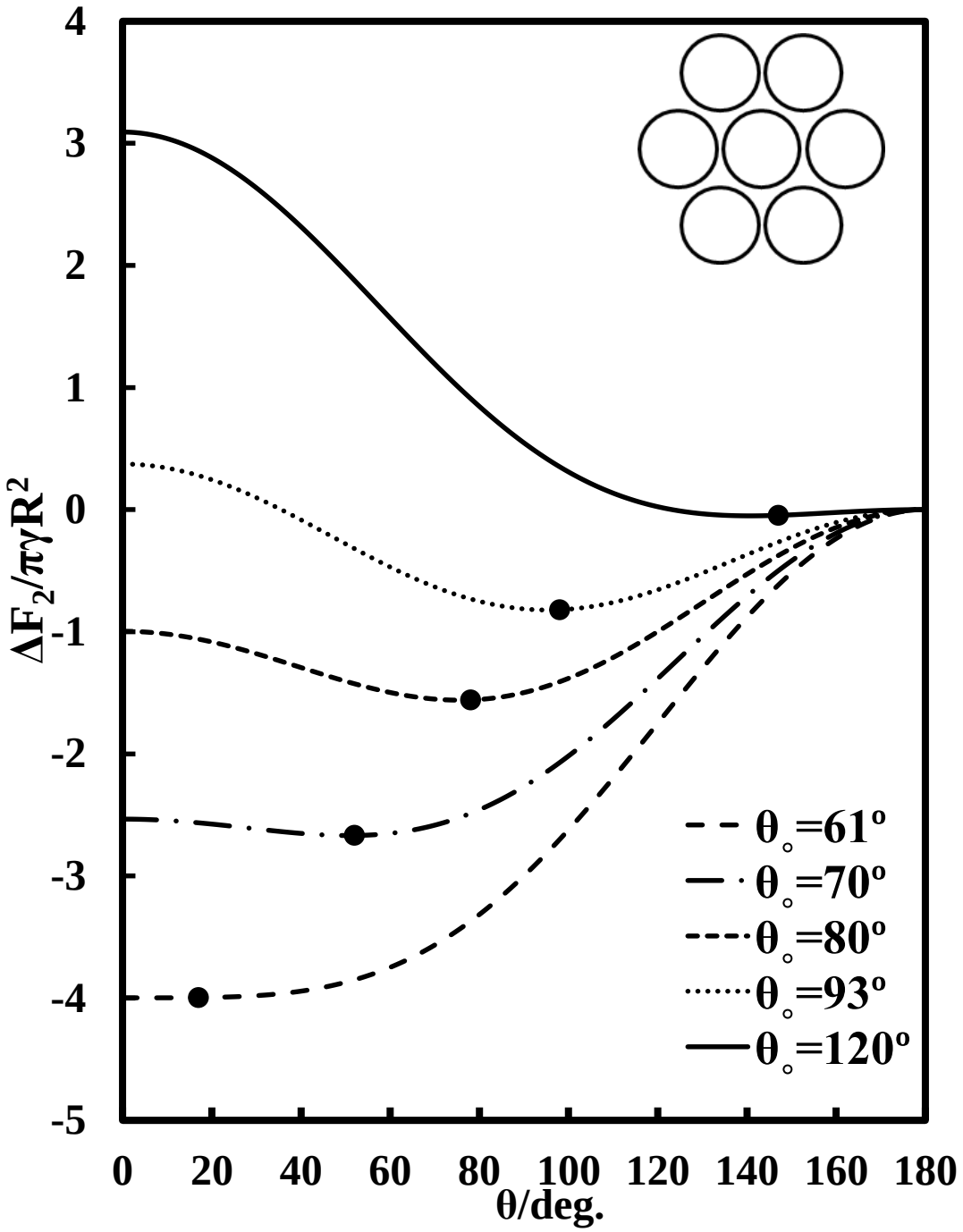

Figure 6.9. Dimensionless free energy of adsorption for a supra–particle impregnated with oil from the oil phase to the oil–water interface as a function of its macroscopic contact angle, θ (see Eq. (6.26)). The colloid particles on the supra–particle surface are arranged in hexagonal packing. The different lines correspond to selected values of the contact angle of building block colloid particles. The circular dots (•) represent the global minimum of the adsorption free surface energy of the porous supra–particle with respect to its contact angle for a fixed value of the contact angle of the building block particles, θ_o.

Figure 6.9 gives the surface free energy of the system with respect to oil–infused porous supra–particles at selected contact angles (θ_o) of building block particles. The dots represent the minimum of the free energy of the system versus the porous supra–particle contact angle, θ. In this case, the macroscopic contact angle of the supra–particle (or colloidosome), θ, can be determined from Eq. (6.30) for the respective value of θ_o, which corresponds to the minimum of the free energy curve presented on this graph.

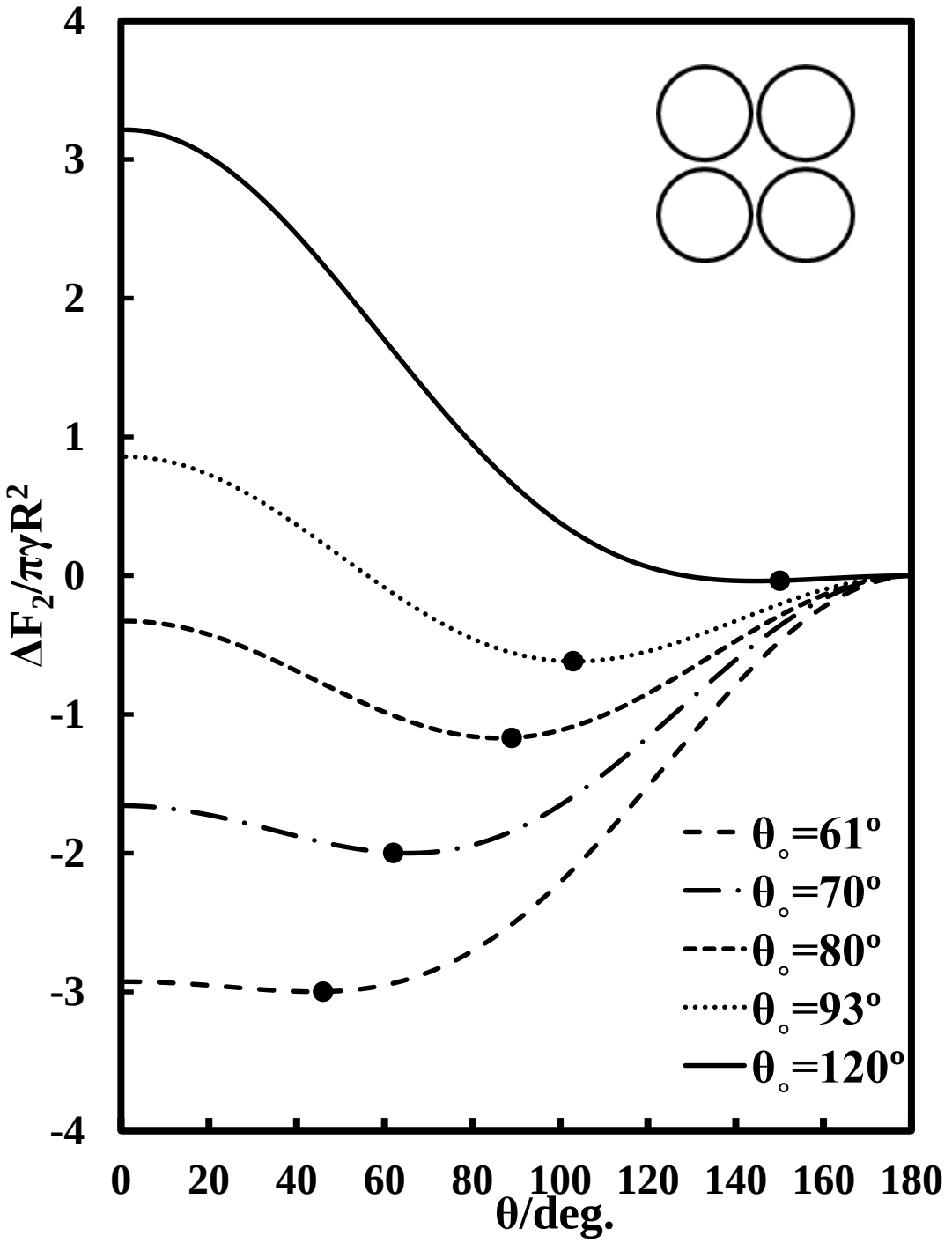

Figure 6.10. Dimensionless free energy of adsorption for a supra–particle impregnated with oil from the oil phase to the oil–water interface as a function of its macroscopic contact angle, θ (see Eq. (6.27)). The colloid particles on the supra–particle surface are arranged in square packing. The different lines correspond to selected values of the contact angle of building block colloid particles. The circular dots (•) represent the global minimum of the adsorption free surface energy of the porous supra–particle with respect to its contact angle for a fixed value of the contact angle of the building block particles, θ_o.

Figure 6.10 shows the adsorption energy of the supra–particle versus its macroscopic contact angle for square packing of its building block particles on its surface. One sees that each free energy curve at fixed value of θ_o, has a minimum in different positions, compared with square packing (see Figure 6.9). In this case, the macroscopic contact angle of the supra–particle (or colloidosome), θ, is determined from Eq. (6.31) for the respective value of θ_o, which corresponds to the minimum of the free energy curve presented on this graph.

6.5 Conclusions

In this chapter, a theoretical model of the adsorption of porous supra–particles at a liquid–fluid interface was developed. This model was developed for composite supra–particles built from smaller spherical colloid particles with smooth surfaces, which is the case for agglomerated particles in powdered materials. The case of water–infused porous supra–particles adsorbed at the oil–water interface from the water phase were considered as well as the case of oil–infused supra–particles adsorbed at the oil–water interface from the oil–phase. It was assumed that only the liquid interface attaches on the first layer of small colloid particles on the supra–particle surface. Because of this assumption, the results presented in this chapter are equally valid for adsorption of colloidosomes as they would also attach to oil–water similarly to the porous supra–particles. Two different packing conditions of small particles on the supra–particle surface were considered.

The connection between the contact angle of the microscopic contact angle of the porous supra–particles and the contact angle of the small "building block" colloid particles was derived for both types of packing conditions. The model predicts that the supra–particles would have different macroscopic contact angles depending on which fluid phase they originate from before they attach at the oil–water interface. This means that the porous particle would have a different attachment position and macroscopic contact angle if it is infused with water, compared with those of the same particle infused with oil. Interestingly, the macroscopic contact angle of the supra–particles does not depend on the size of its building block colloid particles or the size of the supra–particle itself. This behaviour differs from the adsorption of non–porous spherical colloid particles of smooth solid surfaces, which have the same equilibrium contact angle at the liquid interface, independently of the liquid phase from which they originate.

Equations for the energy of adsorption of porous spherical supra–particles at the oil–water interface was derived for the cases of initial infusion with water or oil. It was found that for supra–particles infused with water, the supra–particle contact angle at the oil–water interface has a physical solution only for values of the building block particle contact angle smaller than, or equal to, approximately 119^{o} at hexagonal packing. For square packing conditions, such a solution exists only for a building block

particle contact angle smaller than, or equal to, approximately 126^{o}. More hydrophobic small particles would favour a complete transfer of the water–infused particle to the oil phase. For supra–particles initially infused with oil, the supra–particle contact angle at the oil–water interface has a physical solution only for values of the building block particle contact angle larger than, or equal to, approximately 61^{o} at hexagonal packing conditions. For square packing conditions, such a solution exists only for a building block particle contact angle smaller than, or equal to, approximately 54^{o}. More hydrophilic small particle building blocks would favour a complete transfer of the oil–filled particle into the water phase.

Interestingly, the theory predicts that supra–particles with hexagonal packing of small particles would exhibit larger adsorption energy compared with the same size of supra–particle with square packing of building block particles. The considerations in this chapter are also valid for the adsorption of supra–particles or colloidosomes at the air–water interface with air, instead of the oil phase in all derived equations.

Chapter 7: Measurement of the three-phase contact angle of porous composite supra-particles at the air-water and oil-water interfaces

7.1 Introduction

In Chapter 5, a simple method was presented for the fabrication of a model for porous supra-particles, which consist of smaller colloid particles packed in a spherical aggregate. Theoretical approaches were discussed in Chapter 6 on the effect of colloid particles arrangements in the surface structure on the supra-particles, which can affect the adsorption of porous particles to the fluid interfaces. This effect is important because it shows how the agglomeration conditions and the packing of powder particles in the aggregates can affect their wettability in the liquid phase. The effective contact angle of the porous supra-particles was linked with the contact angle of their building blocks (i.e. the small colloid particles) at the same liquid-fluid interface. Also, the role of the initial fluid by which the particles are infused with on their adsorption to the liquid-fluid interface was considered theoretically. According to the theoretical model discussed in Chapter 6, if one assumes that the supra-particles attach to the liquid surface only by their outer layer of small colloid particles, the same considerations are valid for the adsorption of colloidosomes, whose membranes are made of the same colloid particle building blocks.

In this chapter, several types of experiments used for studying the effect of the surface structure, porosity and the infusion of the porous particles by one of the liquid phases on their adsorption at the fluid-liquid interfaces are discussed. The aim was to accumulate experimental data about the way porous supra-particles adsorb at liquid surfaces and to explore the link between the wettability of the supra-particle building blocks (smaller colloid particles) and the macroscopic (apparent) contact angle of the porous particles at liquid surfaces.

The contact angles of the individual colloid particles at air-water and oil-water interfaces were investigated using the gel trapping technique (GTT)[4] by injecting a small sample of the particles suspension in a spreading solvent through a polar and non-polar phase. In a separate series of experiments, the porous supra-particle contact angles were also studied. Also the effect of the fluid phase by which the porous

particles are initially infused on their adsorption at the liquid-fluid interface was studied experimentally. Finally, the link between the wettability of the particle building blocks and the macroscopic (apparent) contact angle of the porous particles at liquid surfaces were investigated. The porous supra-particles' wettability at both oil-water and air-water interfaces were investigated. For example, for the oil-water interface, the supra-particle wettability for particles initially infused with water (from the aqueous phase) and particles initially infused with oil (from the oil phase) was studied. For the air-water interface, the adsorption of porous supra-particles initially infused with water (from the aqueous phase) and dry porous supra-particles (coming from the air) to the air-water surface was investigated.

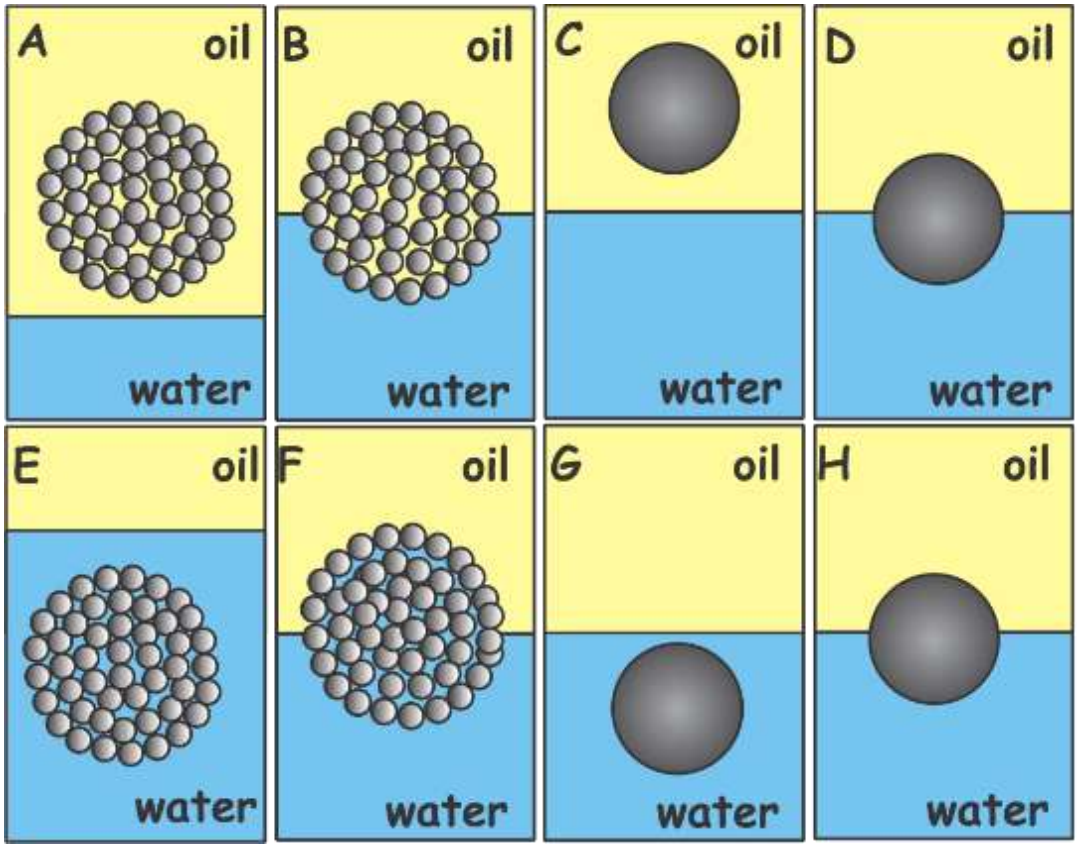

Figure 7.1. Schematic representation of the process of adsorption of a composite porous particle (supra–particle) and the building block particles: from the oil phase (A and C) to the oil-water interface (B and D) and from the water phase (E and G) to the oil-water interface (F and H). Similar considerations hold for the adsorption of the porous particle to the air-water interface in which the oil phase is formally replaced with air.

Furthermore, in this chapter, magnetic resonance imaging (MRI) was applied as a method for generating images of the interior of the porous supra-particles by using a magnetic field and pulses of radio waves. In this study, the penetration of liquid into porous supra-particles with an adequate resolution and a satisfactory contrast was investigated. Penetration of the fluid into porous particles is important, as they may change the wettability of porous particles at the liquid interfaces and hence affect the particle adsorption energy and its effective contact angle at the liquid-fluid interface.

7.2 Contact angle of sulphate latex particles at the air-water interface studied using the gel-trapping technique

The gel-trapping technique was used to measure the three-phase contact angle of 2.6 µm sulphate latex particles at the air-water (a/w) and the hexadecane-water (o/w) interfaces. Figure **7.2** shows the position of the sulphate latex particle on the surface of the PDMS from the GTT experiment after injecting the particles' suspensions through the air (A) or water (B) at the air-water interface. It was observed that the wettability of non-porous particles does not significantly change, as they are adsorbed from both the aqueous phase and the air phase. For individual sulphate latex particles adsorbed from the nonpolar phase (i.e. air), the contact angle was 63 ± 3º, and from the polar phase, the contact angle was 65 ± 1º at air-water interfaces. A similar observation was obtained when the particles were injected in the hexadecane (C) or through the water (D). The results show that the adsorption of particles from hexadecane is practically the same as for the particles adsorbed from the water phase. The contact angle observed for nonporous particles from the water phase was 94 ± 1º, and from the hexadecane phase, it was 93 ± 1º at the oil-water interfaces. These data provide a general idea of the wettability of the building blocks of the composite porous supra-particles, which are made of the same particles.

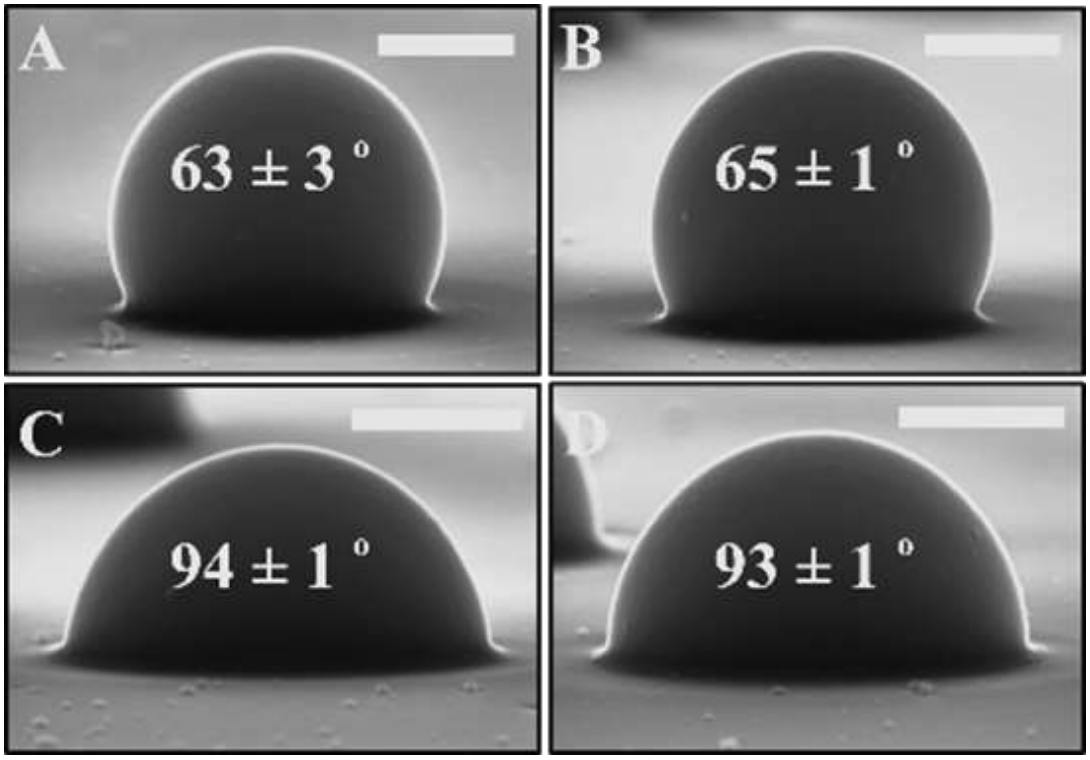

Figure 7.2. SEM micrograph of sulphate latex particles of an average diameter of 2.6 ± 0.1 μm imaged with a GTT for determining their three-phase contact angle θ_o at: (A) air-water interface, the particle suspensions dispersed in ethanol were injected from the air phase; (B) air-water interface, the particles were injected from the water phase; (C) hexadecane-water interface, particle suspensions dispersed in ethanol were injected from the hexadecane phase; and (D) hexadecane-water interface, particles were injected from the water phase. The value of θ_o was averaged out of 10 different particles protruding from the PDMS substrate obtained by templating the particles at the liquid interface. The scale bar is 1 μm on all images. The average area per sulphate group on the particles surface is 3.84 nm^2/SO_4, and the number of charged groups per particle is approximately 6×10^6.

Table 7.1. Contact angle of the sulphate latex particles measured at the air-water and oil-water interfaces and its theoretical relation (in Chapter 6) with the contact angles of porous supra-particles packed in hexagonal packing, θ_h and square packing and θ_s on the supra–particle surface.

Adsorption from the aqueous phase to the						**Adsorption from the oil or air phase to the**					
air–water interface			**hexadecane–water interface**			**air–water interface**			**hexadecane–water interface**		
θ_o/deg.	**θ_s/deg.**	**θ_h/deg.**	**θ_o/deg.**	**θ_s/deg.**	**θ_h/deg.**	**θ_o/deg.**	**θ_s/deg.**	**θ_h/deg.**	**θ_o/deg.**	**θ_s/deg.**	**θ_h/deg.**
60	**37**	**39**	**90**	**78**	**85**	**60**	**40**		**90**	**102**	**95**
61	**38**	**41**	**91**	**79**	**86**	**61**	**43**	**2**	**91**	**104**	**97**
62	**39**	**42**	**92**	**81**	**88**	**62**	**46**	**17**	**92**	**106**	**99**
63	**40**	**43**	**93**	**83**	**90**	**63**	**49**	**23**	**93**	**107**	**101**
64	**41**	**44**	**94**	**84**	**92**	**64**	**51**	**29**	**94**	**109**	**102**
65	**42**	**46**	**95**	**86**	**94**	**65**	**54**	**33**	**95**	**110**	**104**
66	**44**	**47**	**96**	**88**	**96**	**66**	**56**	**37**	**96**	**112**	**106**
67	**45**	**48**	**97**	**89**	**98**	**67**	**59**	**41**	**97**	**113**	**107**

According to Figure 7.1, the contact angle of individual particles adsorbed from the water phase to the air-water interface is 65º ± 1º and 93º ± 1º to the oil-water interface. In contrast, the contact angle of the particles adsorbed from the air phase to the air-water interface is 63º ± 3º, while the particles' contact angle adsorbed from the hexadecane phase to the hexadecane-water interface is 94º ± 1º. These data provide a general idea of the adsorption of the composite porous supra-particles, which are indicated in Chapter 6. As shown in Table **7.1**, the theory (in Chapter 6) predicts that the contact angle of the porous supra-particles impregnated with water at the air-water interface would be range from 41º–44º for a square packing and 44º–47º for a hexagonal packing of the latex particles, whereas the porous supra-particles impregnated with water adsorbed to the oil-water interface could range from 88º–92º for a hexagonal packing and 81º–84º for a square packing of the latex particles. In theory, for porous supra-particles with pores that are filled with air, the supra-particle contact angle ranges from 0º to 37º for building block particles arranged in a hexagonal packing on their surface, whereas for an arrangement of square packing, it ranges from 40º to 56º. In contrast, for supra-particle pores impregnated with hexadecane regarding its adsorption from the hexadecane phase to the hexadecane-water interface, the theory predicts that the contact angle of the porous supra-particles at an oil-water interface ranges from 101º–104º for a hexagonal packing and 107º–110º for a square packing. It should be expected that the porous supra-particle contact angle would depend on the

latex particle arrangement at the supra-particle interface and the liquid front penetration inside the pores.

7.3 Measurement of the supra-particle contact angles at liquid-fluid interfaces using a Drop Shape Analysis (DSA)

The purpose of this experiment was to find the contact angle of porous supra-particles at the oil-water and air-water interfaces, as described in section (2.2.6). The images obtained by the drop shape analysis of the particles allowed for visualising the particle position and the profiles of the liquid interfaces. The sequence images helped in tracing the particle adsorption into the droplet or bubbles and in detecting their final position. The images sequence rate for these particles to reach final attachment to a water droplet was between 2–15 min, depending on the pushing and the particles' adsorption energy. The porous supra-particles at the air-water and the hexadecane-water interface saturated with a water surface showed a stable behaviour with the change of porous particle size. Several different parameters were taken into account that could affect the porous particles wetting behaviour at the liquid interface. These parameters are the curvature of the interface, the latex particle arrangement at the supra-particle interface, the liquid front penetration inside the pores and the supra-particle size. Porous supra-particles were prepared using a 40 wt% latex particle suspension and the drop-drying method on a super-hydrophobic substrate to yield particles of 1.7 mm, 1.9 mm and 2.2 mm, respectively. The particles were thermally annealed at the polymer glass transition temperature, 106 ^{o}C, to ensure their stability when in contact with an oil or water phase. Hexadecane was used as an oil phase due to its low volatility. Two types of aqueous phases were used for these experiments: Milli-Q water and 0.1 M NaCl(aq). The particle contact angle was measured at the maximum penetration of the particle at different protrusion heights with respect to the liquid interface while inserting the particles into a droplet or a bubble.

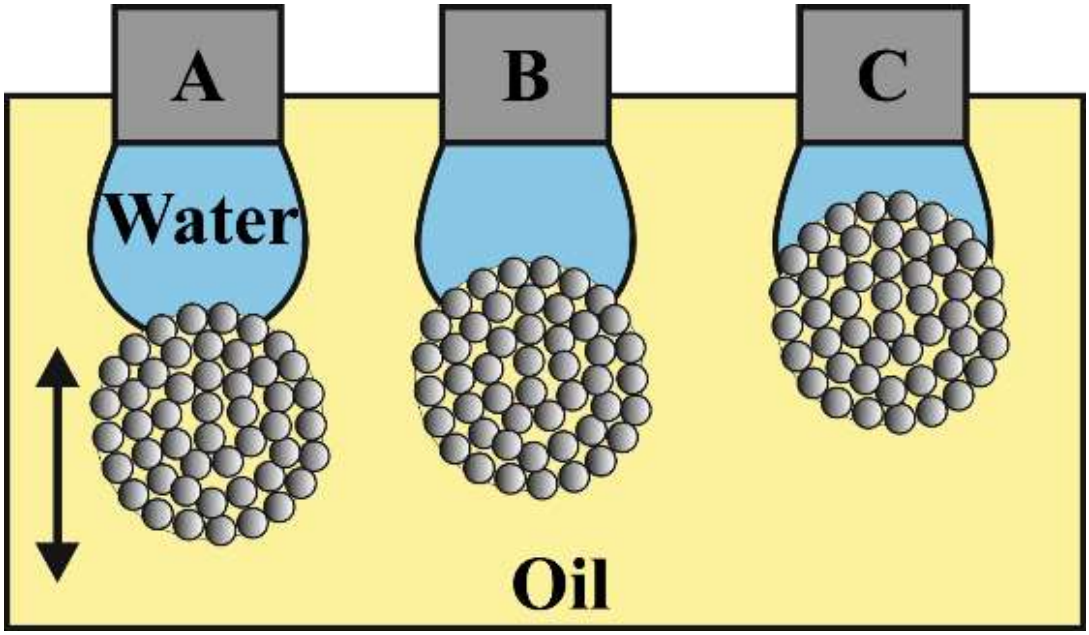

Figure 7.3. Schematic representation of a water droplet attached to porous supra-particles at the oil-water interface. (A) The initial attachment of porous particles to a water droplet, (B) after pushing the porous particles into the water droplet and (C) the maximum attachment of porous particles to the water droplet.

The protrusion heights represent the droplet height from the edge of the DSA syringe needle to the porous supra-particles equatorial line, as illustrated in Figure 7.3. In the following section, the effect of dry and impregnated porous supra-particles with water, 0.1 M NaCl(aq) and hexadecane at the air-water and oil-water interfaces is described.

7.4 Pendant drop method to determine the contact angle of porous particles

The porous supra-particles were made from 40 wt% latex particle suspensions and fused together at 106 ºC using an oil bath for 2 h, as described in Chapter 5. Particles of different sizes were obtained, and the contact angle measurements were done once they were attached directly to the fluid droplet. Once they were attached to the liquid surface, the initial contact angle was recorded, and when the particle was pushed to the maximum depth into the bubble (or liquid droplet), the final contact angle was recorded. These measurements were done in an attempt to determine the value of the particle equilibrium contact angle. The porous supra-particles' position at the interface was evaluated and measured as illustrated in Figure **7.4**. As the attachment of the porous particle to a liquid interface is influenced by the radius of the curvature of the liquid interface ($R_{droplet}$ or R_{bubble}), its effect on the attachment of particles impregnated

with different fluid phases was examined before they were attached to a curved liquid interface. The contact angle was calculated by considering a flat interface (green line) and curved interface (yellow line) to find the flounce of the radius curvature of the fluid in the contact angle between the two methods (see Figure **7.4**). The green line represents the case of a flat liquid surface contact angle (FCA), and the yellow line corresponds to the curved contact angle (CCA). The images were obtained from a side camera on a DSA mk10 and analysed using macro script on (Image Pro Plus V.6). The contact angle was determined by Eqs. (2.8) and (2.9). The particle contact angle was measured at these four positions to find the effect of the curved liquid interface on the measured particle contact angle. The contact angle values reported are an average of at least 3 measurements obtained from several DSA image sequences of different particles over at least 3–5 different samples.

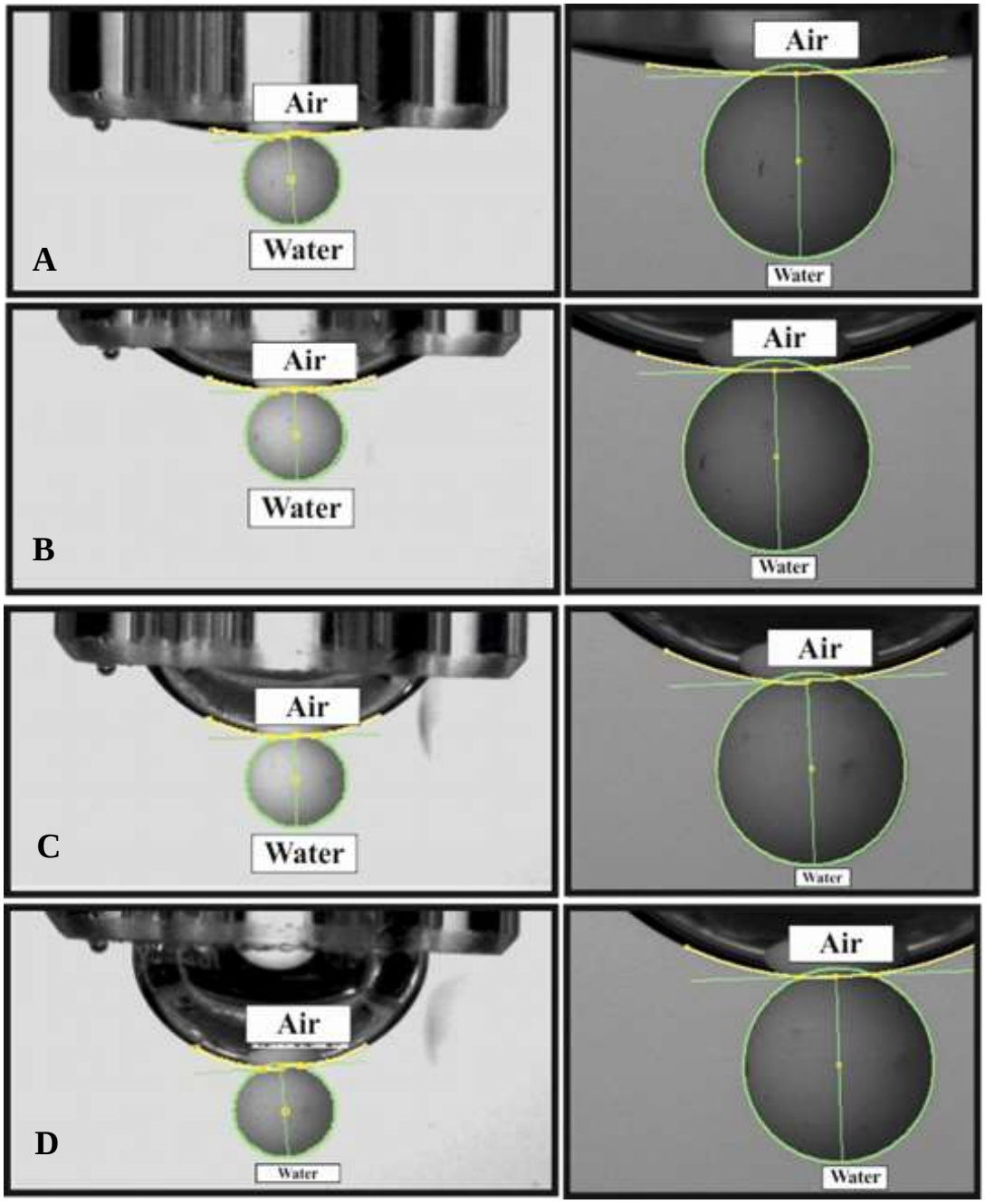

Figure 7.4. Optical photograph of the porous supra-particles attached to an air bubble produced on the syringe needle of a DSA 10 setup. The porous particle was impregnated with water before being attached to the air-water surface. The porous supra-particles were produced by the evaporation method from 40 wt% latex suspensions.

7.4.1 Contact angles of dry porous supra-particles at the a/w interface.

The three-phase contact angle of dry porous supra-particles at air-water interfaces was investigated at two positions: (i) when the particle is adsorbed at a practically flat air-

water surface (Figure **7.4**, a), which represents the practically flat radius of the curvature of the liquid interfaces and (ii) when attached to a larger bubble with a high arch (Figure **7.4**, d), which represents the largest radius of the curvature of the liquid interfaces.

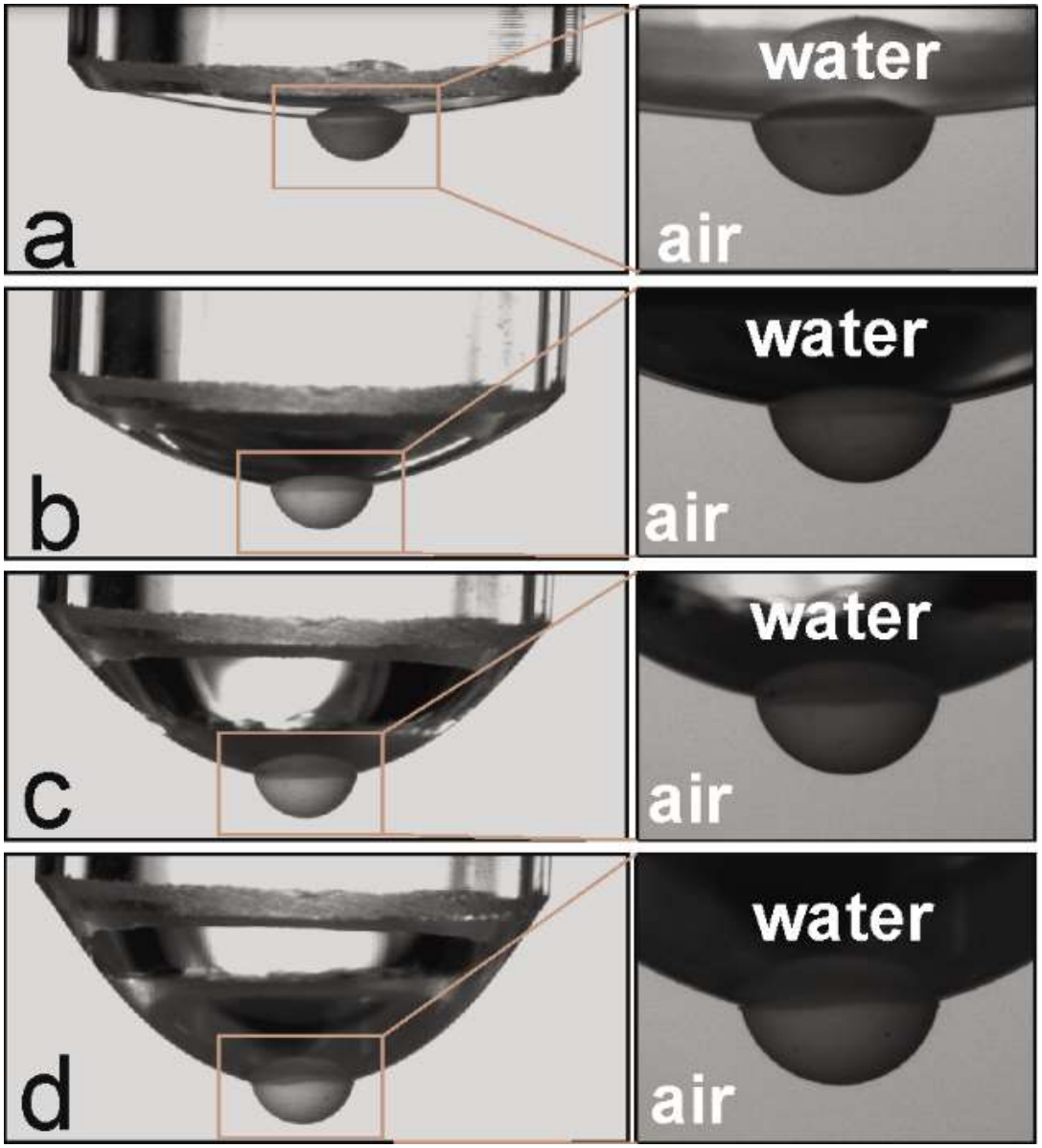

Figure 7.5. Photograph of the porous supra-particles contact angle at (a, b, c and d) an air-water surface for dry porous supra-particles.

It has been noted that when brought near the air-water interface, the dry particles adsorbed spontaneously into the interface and adjusted to their initial contact angle. The adsorption of the particles can be altered when the particles are only attached to the liquid interface (which is described as an initial contact angle) and then a force is applied (see Figure 7.3) by pushing the particles into the droplet using the cuvette base.

As can be seen in Figure **7.6**, there are different adjustments or attachment positions for the supra-particles that were calculated at different stages of immersion (as in Figure **7.5** a–d for a water drop).

A hysteresis was observed in the particle contact angle when comparing the particles' contact angle values on a flat liquid surface with those at a curved liquid surface (see Figure **7.6**). This hysteresis could be a result of the surface roughness of the porous supra-particles. For example, the initial contact angles of the supra-particles (2.2 mm) at the curved liquid interface was observed when the particles spontaneously attached to the practically flat curvature of a water droplet, 134° ± 3° (CCA, Figure **7.5**,a), to reach 141° ± 1° (CCA, Figure **7.5**,b) when the water droplet changed to the largest curvature. The calculated contact angle of the dry porous supra-particles attached to a flat interface is around 149° ± 1^{o} (FCA) for 2.2 mm particles; however, the experimental data indicate that the attachment position of the particle at the liquid interface depends on the initial pressing force applied to the particle at the a/w interface. The average contact angle of dry porous supra-particles with different diameters (1.7mm, 2.0 mm and 2.2 mm) adsorbed to an air-water interface at the lowest droplet of curvatures (see insets in Figure **7.7** s). The initial contact angle of 1.7 mm particles for CCA was 132 ^{o} ± 12^{o} and 136^{o} ± 8^{o} for FCA. Larger supra-particles had similar trends but showed larger contact angles for 2.0 mm and 2.2 mm particles, and the CCA was 141 ^{o} ±4 ^{o}, 139 ^{o} ±5 ^{o}, and the FCA was 145 ^{o} ±2 ^{o}, 147 ±4 ^{o}, respectively. The error bars were an average of 3 calculations for each image in Figure **7.5** a–d using the Image Pro Plus macro program.

It can also be noted that the porous supra-particles become more hydrophilic ($\theta \leq 90^{o}$) when applying force to the particles to change their adsorption into a/w interfaces. The final contact angle of dry porous supra-particles adsorbed to a/w interfaces for 1.7 mm particles was 69 ^{o} ± 5 ^{o} for CCA and 75 ^{o} ± 5 ^{o} for FCA, whereas the contact angle of larger particles showed higher contact angles for 2.0 mm and 2.2 mm, which were 79 ^{o} ± 1 ^{o}, 80 ^{o} ± 5 ^{o} for CCA and 85 ^{o} ± 2 ^{o}, 89 ^{o} ± 7 ^{o} for FCA, respectively (more data are presented in the Appendix, Table 8.1 and 8.2). These contact angle values are an average of 3–5 supra-particles that attached in the same procedure described previously. The measured contact angle variation in this case may be caused by the pinning of the three-phase contact line on the supra-particle surface and its building

blocks, which results in a large energy barrier for its adjustment to an equilibrium position.

In Chapter 6, the prediction for the contact angle of dry porous supra-particles at the air-water interface was based on the contact angle of its building block latex particles for square packing and 48° ± 5° and 24° ± 12° for hexagonal packing at the supra-particles' surface (Table **7.1**). The calculation of the contact angle did not match the contact angle obtained for a curved or flat interface; however, the average final experimental contact angle, which is presented in Figure **7.7** for supra-particles at different sizes, did not match the theoretical contact angle predicted, as they varied within a 20-degree difference. The attachment position of the rough porous supra-particles varies with the protrusion and indicates a very large contact angle hysteresis [181]. These results attribute this large difference between the theoretical and the experimental result to the surface roughness, which is a possible cause for the pinning of the contact line of the supra-particles. This pinning leads to trapping the porous supra-particles in a meta-stable state with a very high activation energy. Table 8.1 in the Appendix presents the measured contact angles of particles at different droplet volumes and their initial and final contact angles at the air-water interface.

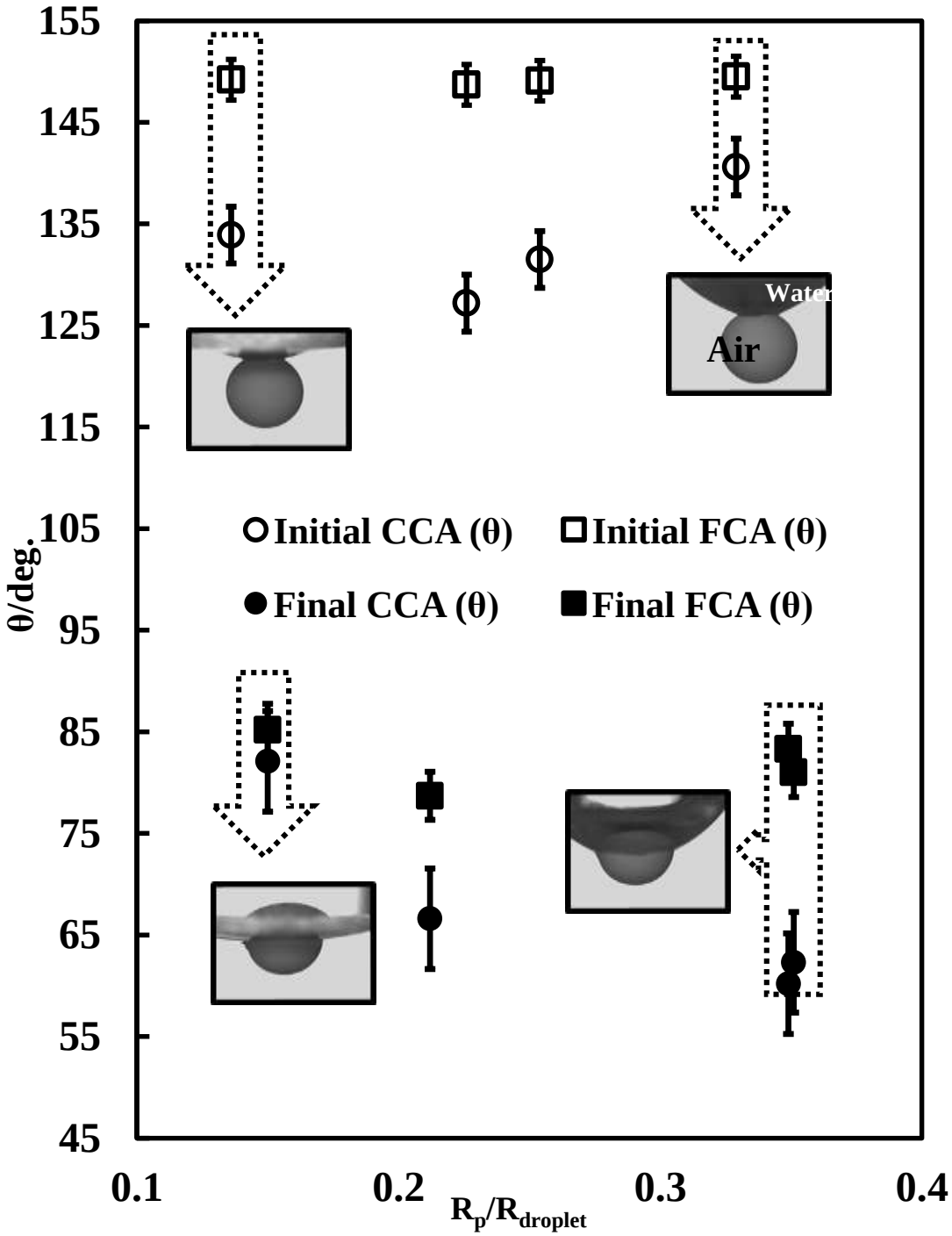

Figure 7.6. Contact angle of dry porous particles (2.2 mm) at the a/w interface as a function of the ratio between the radius of particles (R_p) and the radius of water as a fluid ($R_{droplet}$): (□) initial contact angles for a flat liquid surface (FCA), (○) initial contact angles for a curved liquid surface (CCA), (■) final contact angle for a flat liquid surface (FCA), (●) final contact angle for a curved liquid surface (CCA). The error bars denote the average of contact angle values for three-repeated calculations of the 2.2 mm particles at different stages using macro script in Image Pro Plus 6.

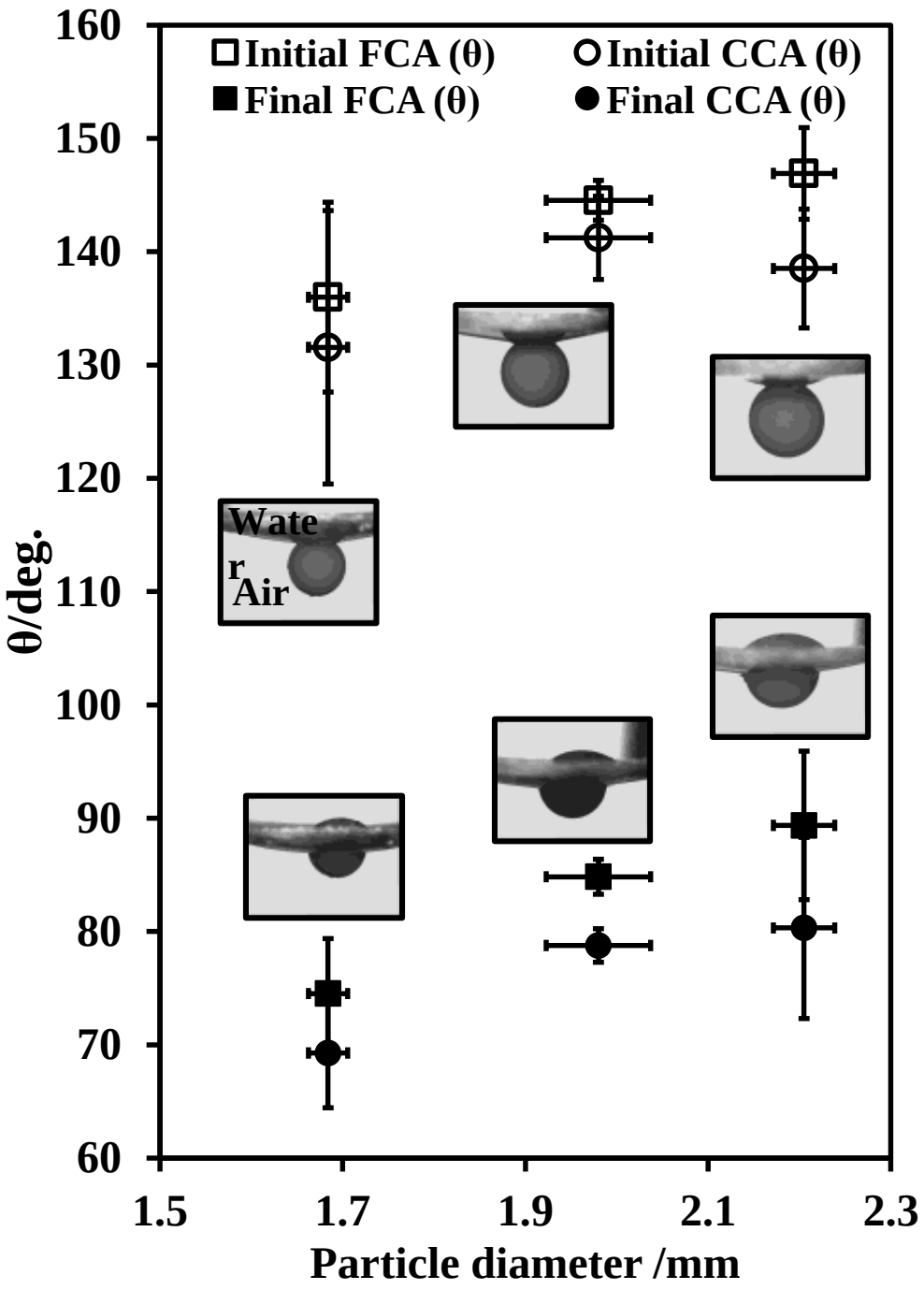

Figure 7.7. Average contact angle of dry, porous supra-particles adsorbed to a water droplet at an air-water interface as a function of the supra-particle diameter: (□) initial contact angle for a flat liquid surface (FCA), (○) initial contact angle for a curved liquid surface (CCA), (■) final contact angle for a flat liquid surface (FCA) and (●) final contact angle for a curved liquid surface (CCA). The difference in the contact angle between the initial contact angle and the final contact angle is 60^{o}. The error bars denote the average of contact angle values for three to five particles of the same diameter.

7.4.2 Contact angles of dry porous supra-particles at the air-NaCl(aq) solution interface.

It is known that the presence of electrolytes is important when preparing Pickering foams stabilised by polystyrene latex particles [182]. Here, a 0.1 M NaCl(aq) solution was used as an aqueous phase to attach dry porous supra-particles at an air-NaCl(aq) solution interface. The supra-particle contact angle adsorbed to a/w interface was investigated at two positions when adsorbed to a practically flat interface (lowest curvature) or to a larger droplet with a highest possible radius of curvature of the liquid interfaces, as shown in Figure **7.8**. A large difference between these two cases was observed at the instant of the initial contact angle of dry porous supra-particles (1.7 mm in diameter) to a practically flat surface (FCA) of (a/w), which was 116° ± 1°, and it was 109° ± 1° for CCA; however, the initial contact angle for a large droplet with a high arch to an a/w interface (FCA) was 123° ± 1° and was is 101° ± 2° for CCA.

The final contact angle after applying force by pushing the particles to reach equilibrium positions to flat and curved a/w interfaces was also investigated, as shown in Figure **7.8**. The final FCA for 1.7 mm particles adsorbed to a flat a/w interface was 62° ± 1° and was 52° ± 1° for CCA, while for larger droplets, the highest arch of an a/w interface for FCA was 72° ± 1° and was 50° ± 1° for CCA. The error bar was obtained from three repeated calculations using the macro program in Image Pro Plus. It can be seen from Table **7.1** that there is a good agreement with the theoretical value expected for dry supra-particles with a square packing of building block particles on their surface.

The effect of the supra-particle diameter on the contact angle when the particles are attached to a practically flat droplet of NaCl(aq) solution after pushing the particles into the droplet through the liquid surface is shown in Figure 7.7. The initial contact angle for supra-particles obtained for the flat liquid surface (see insets) was hydrophobic, and the final contact angle was hydrophilic. Furthermore, the initial contact angle of dry porous supra-particles (1.7 mm in diameter) adsorbed to a NaCl(aq) droplet was 121° ± 8° for FCA and 116° ± 9° for CCA, while the final contact angle after applying force to the particles into the water droplet for FCA was 63° ± 2° and 54° ± 5° for CCA. The assumption in Chapter 6 was that the contact angle of the dry porous supra-particles adsorbed to a/w interfaces would be in the

range between 40º-56º for a square packing, while it would be in the range between 0º-37º for a hexagonal packing. These experimental contact angles seem to broadly agree with the theoretical prediction for porous supra-particles at the air-water interface from the air phases, which is 48° ± 5°, as presented in Table 7.1.

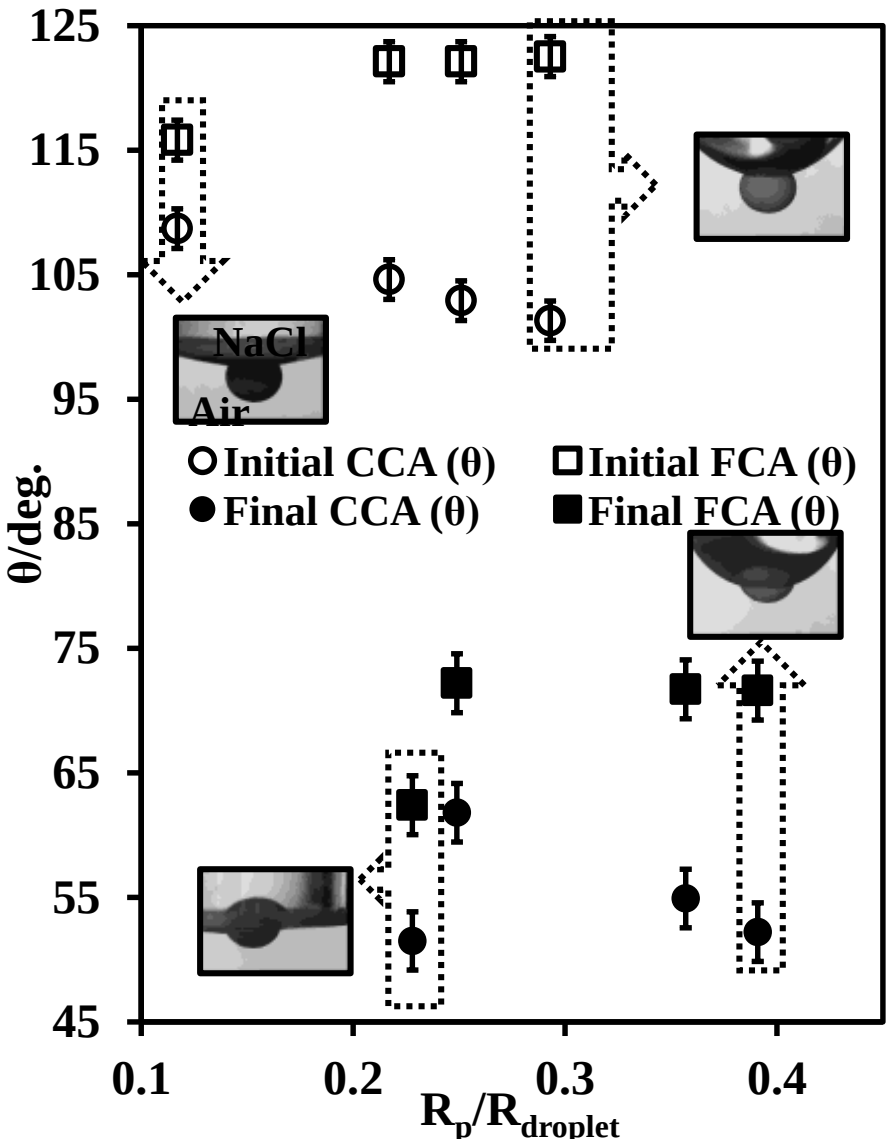

Figure 7.8. Contact angle of dry porous particles (1.7 mm) at an air-NaCl (aq) solution as a function of the ratio between the radius of the particles (R_p) and the curvature radius of the a/w water surface ($R_{droplet}$): (□) initial contact angles for a flat liquid surface (FCA), (○) initial contact angles for a curved liquid surface (CCA), (■) final contact angle for a flat liquid surface (FCA) and (●) final contact angle for a curved liquid surface (CCA). The error bars denote the average of contact angle values for three repeated calculations of the 1.7 mm particles at different stages using macro script in Image Pro Plus 6.

The initial contact angle of 2.0 mm and 2.2 mm porous supra-particles was also hydrophobic but with a high hysteresis, as the FCA values were 111 ° ± 21° and 121° ± 11°, whereas the CCA values were 105 ° ± 19° and 116° ± 10°, respectively. This large hysteresis in the initial contact angle may be due to the spontaneous adsorption of these particles to a/w interfaces. The porous supra-particles become hydrophilic when force is applied to push them into the NaCl(aq) droplet to reach the equilibrium contact angle; however, the 2.0 mm and 2.2 mm porous supra-particles did not match the predicted values obtained from Chapter 6 (see Table **7.1**). It was also found that when the supra-particles pushed (see Figure 7.3) into the final contact angle configuration, the measured contact angle increased with the increase of the particle size, especially for a curved liquid surface (See Appendix Table 8.3 and 8.4), which can be attributed to the weight of the particles. The errors bars were calculated as an average of 3–5 different particles adsorbed to a NaCl(aq) droplet.

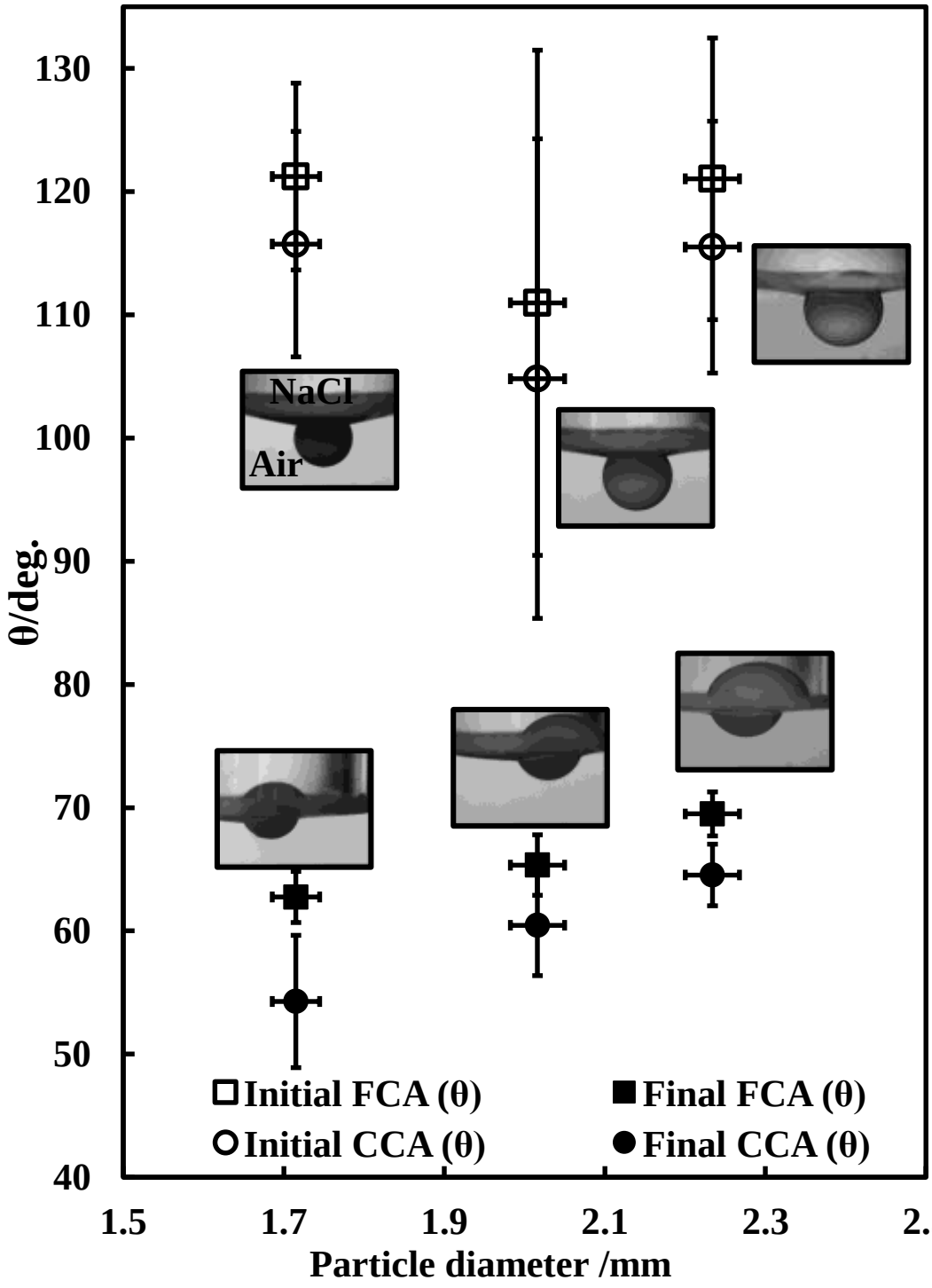

Figure 7.9. Average contact angle of three sizes of dry porous supra-particles adsorbed to a NaCl (aq) solution droplet in air versus the particle diameter: (□) initial contact angles for a flat liquid surface (FCA), (○) initial contact angles for a curved liquid surface (CCA), (■) the final contact angle for a flat liquid surface (FCA), (●) final contact angle for a curved liquid surface (CCA). The error bars denote the average of contact angle values for five particles of the same size.

7.4.3 Contact angles of water-infused porous supra-particles at the a/w surface

In this study, supra-particles, which were pre-filled with water, were used to study how they adsorb at the at air-water interfaces from the water phase. This is done by attaching the particles to air bubbles formed on a syringe needle in water and measuring their contact angles, as illustrated in Figure **7.4**. The dry porous supra-particles were impregnated initially with ethanol for 10 minutes and then incubated in the aqueous phase overnight. The contact angles of these pre-wetted porous supra-particles were found to correspond to hydrophilic ($\theta \leq 90^o$) particles as expected, and their hydrophilicity increased with the particle size. Due to the effect of the particles' sizes, the surface roughness and weight bent the interfaces due to the gravitational force by pulling the particles into the water bulk. Figure **7.10** shows the contact angle of wetted porous supra-particles at the air-water interfaces after the particles initial attachment to the air-water interface as well as when they reached final immersion.

The initial contact angle of 1.75 mm porous supra-particles was measured for different bubble sizes, and the data were recorded for the initial contact angle of the particle at the practically flat liquid surface (Figure 7.4, A) and at the curved liquid surface (Figure 7.4, D). The initial particles contact angle for a flat liquid surface CCA was 26° ±1°, and for FCA, it was 24° ±1°, while the final contact angle was 53° ± 1° and 46° ±1° for CCA and FCA, respectively; however, for a bubble of maximum size, the particles contact angle was also investigated. The initial CCA was determined to be 29° ± 1°, and the FCA was 24° ± 1°, whereas the final CCA and FCA were 57° ± 1° and 43° ± 1°, respectively. The theoretical contact angle of the pre-filled particles with water adsorbed to a/w interfaces would show a contact angle in the range between 41°-44° for square packed particles and 44°-47° for hexagonal packed particles. The final particle contact angles of flat liquid surfaces for curved contact angles, CCA, and flat contact angles, FCA, are presented in Figure 7.8 and roughly agrees with the theoretically estimated contact angle for porous supra-particles adsorbed from the water phase, as shown in Table 7.1. The average contact angle of these particles was obtained from three repetitions of calculations at each stage using macro program in Image pro plus.

The initial contact angle of 1.7 mm particles for a practically flat a/w surface was measured to be 32° ± 7° for CCA, and the final CCA was 73° ± 12°. The same trend

can be seen with 2.0 mm and 2.2 mm particles; their initial attachment corresponds to the contact angles of 23 ° ± 2° and 21° ± 1°, respectively to reach a 69° ± 3° and 57° ± 6° final contact angle, respectively. On the other hand, the initial contact angle of particles for flat liquid surfaces has a similar value of that for the curved liquid surface, which shows a low hysteresis for the initial adsorption of the water-filled porous supra-particles adsorption at the a/w surface. For the final adjustment of the supra-particles at the a/w interfaces, their contact angles only had about a 10° difference between FCA and CCA, respectively (see Tables 8.5 and 8.6 in the Appendix).

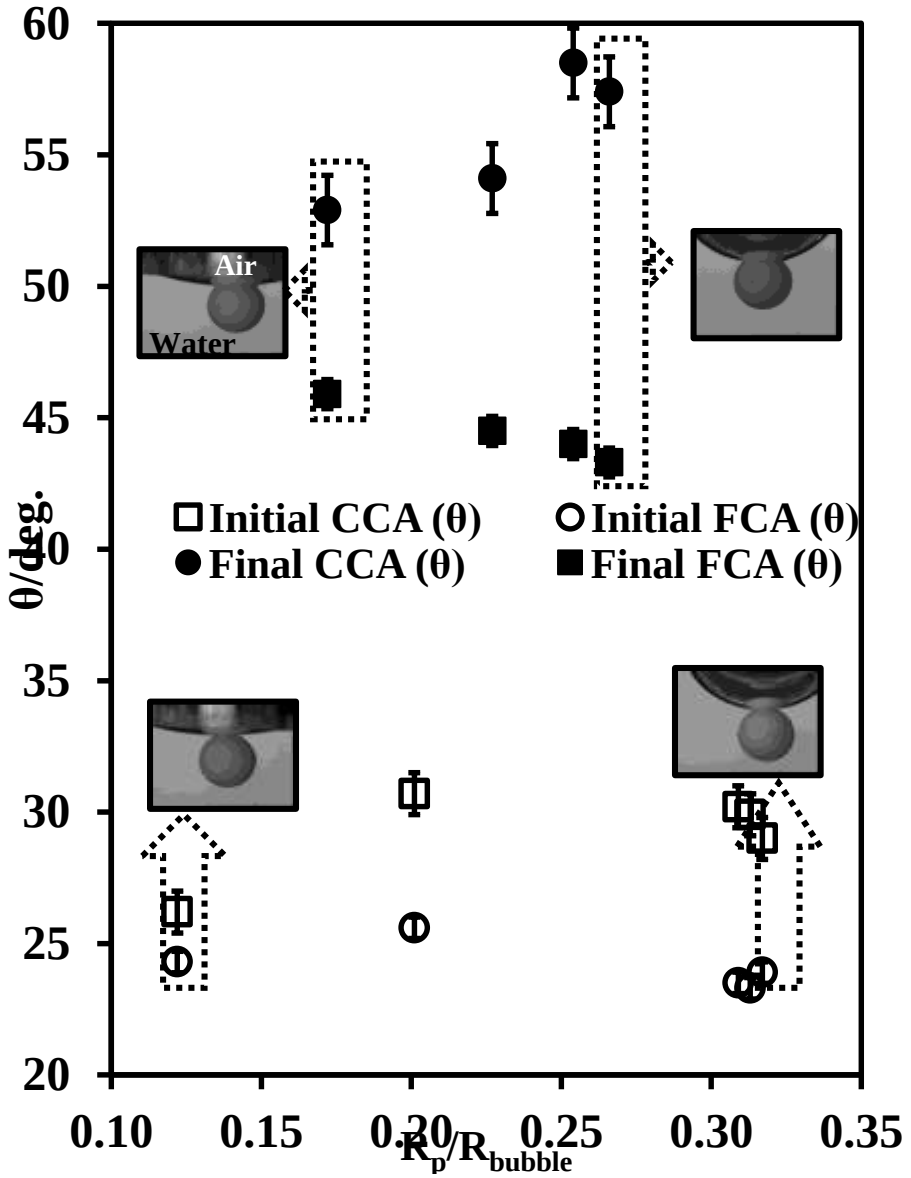

Figure 7.10. Contact angle of water-filled porous particles (1.75 mm) at a/w depending on the ratio between the radius of particles (R_p) and the radius of the air bubble (R_{bubble}): (□) initial contact angle for a flat liquid surface (FCA), (○) initial

contact angle for a curved liquid surface(CCA), (■) final contact angle for a flat liquid surface (FCA), (●) final contact angle for a curved liquid surface (CCA). The error bars denote the average of contact angle values for three repeated calculations of the 1.75 mm particles at different stages using macro script in Image Pro Plus 6.

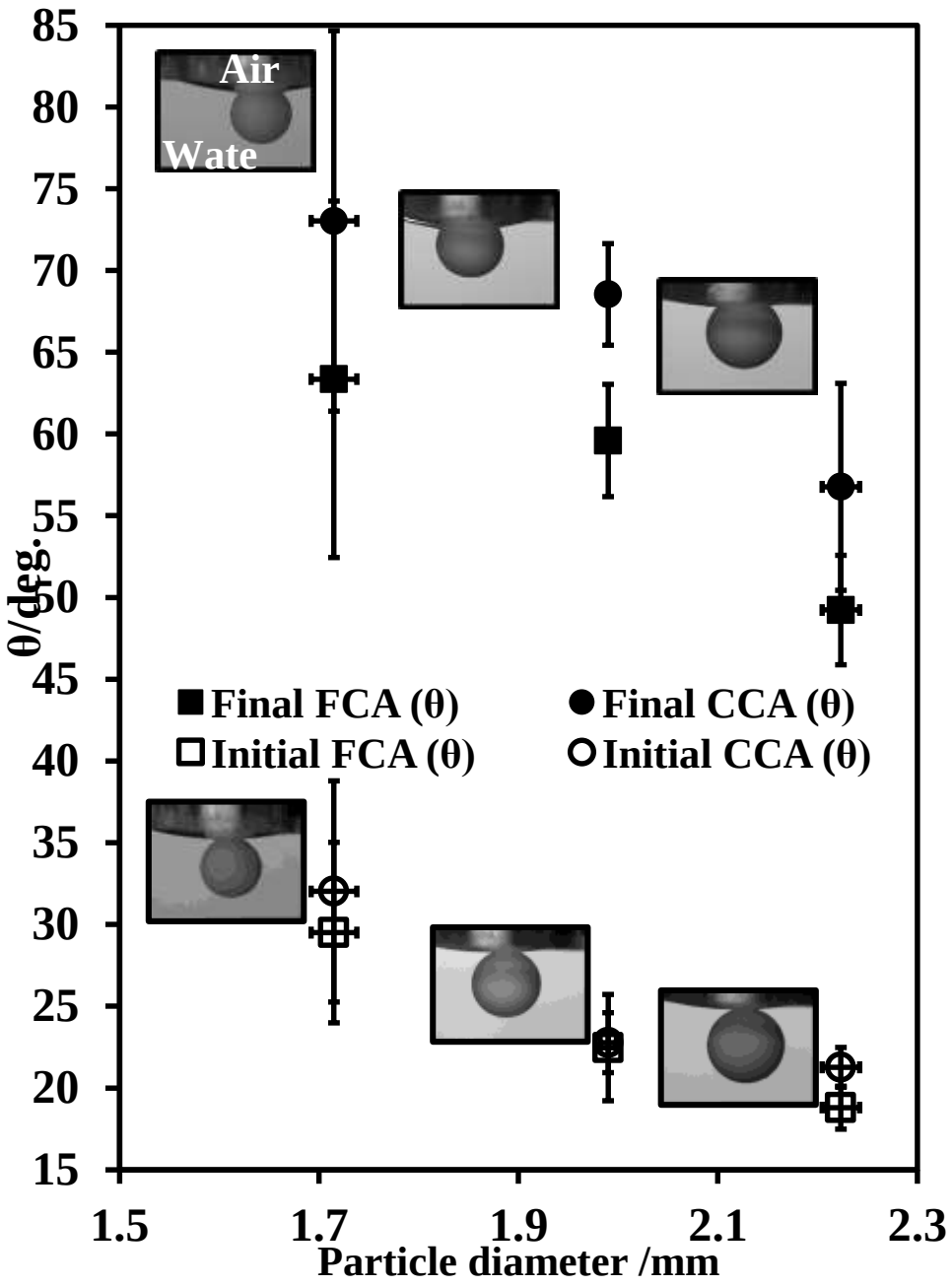

Figure 7.11. Average contact angle of water-infused porous supra-particles adsorbed to a water droplet at an air-water interface versus the supra-particle diameter: (□) initial contact angles for a flat liquid surface (FCA), (○) initial contact angles for a curve liquid surface (CCA), (■) final contact angle for a flat liquid surface (FCA), (●) final contact angle for a curved liquid surface (CCA).

7.4.4 Contact angles of water-infused porous supra-particles at the air-NaCl(aq) solution surface.

The contact angles of porous supra-particles impregnated with a NaCl(aq) solution were investigated. The dry porous particles were initially impregnated with ethanol for 10 min and then with a NaCl(aq) solution overnight. Figure **7.12** shows that the particles' initial attachment had a lower hysteresis in the particle contact angle, which is about 20º ± 3° compared with the curved contact angle, which reached up to 40º ± 2°. The initial contact angle corresponds to a hydrophilic particle (θ≤90º) as expected, but when the particle was pushed towards the liquid surface, the final contact angles increased and corresponded to a hydrophobic particle (θ≥90º). For example, the final contact angle for 1.7 mm supra-particles adsorbed to a practically flat a/NaCl(aq) solution interface and had a value of 80 º ± 1° for FCA, but for CCA, it reached up to 104 º ± 1°, which makes the particles more hydrophobic even when the particles are pre-filled with a 0.1 M aqueous solution of NaCl. The effect of adding sodium chloride to the aqueous phase can be attributed to reduced electrostatic repulsion between the particle surface and the liquid interface. Also, the final CCA shows that particles tend to behave as a hydrophobic, whereas the final FCA shows that the particles maintain their contact angle < 90° (see Appendix Tables 8.7 and 8.8). These results do not match the theoretical contact angle of pre-filled supra-particles with water adsorbed to a/w interfaces, which would show a contact angle in the range between 41º-44º for square packed particles and 44º-47º for hexagonal packed particles (see Table 7.1).

Porous supra-particles impregnated with a NaCl(aq) solution were attached from the water phase to air bubbles, and the initial and final contact angles were measured. Figure **7.13** shows that the initial contact angles of the pre-wetted porous supra-particles (1.7 mm in diameter) at the flat a/w interface for CCA and FCA were 32° ± 9º and 30° ± 6º, respectively, while the final CCA after pushing the particles into the air bubble was 80° ± 23º, and the FCA was around 71° ± 19º. The wetting behaviour changed with the increase of particle size, as larger particles became more hydrophilic. The reasons for the effect of the particle size on its contact angle is unclear but is likely strongly influenced by the contact angle hysteresis. The use of force by pushing the particles into a curved a/NaCl(aq) solution interface (Figure **7.12**) resulted in a contact angle of 122º ±1º for CCA and 104º ± 1º for FCA; however, when air was sucked from the bubble to practically flat interfaces, it resulted in expelled particles into the

NaCl(aq) phase, which resulted in a contact angle hysteresis as they reached 89 º ± 1º and 79 º ± 1º for CCA and FCA, respectively. Because of the surface roughness of these particles, these results indicate a pinning of the contact line, which impedes free movement and reaching the equilibrium contact angle.

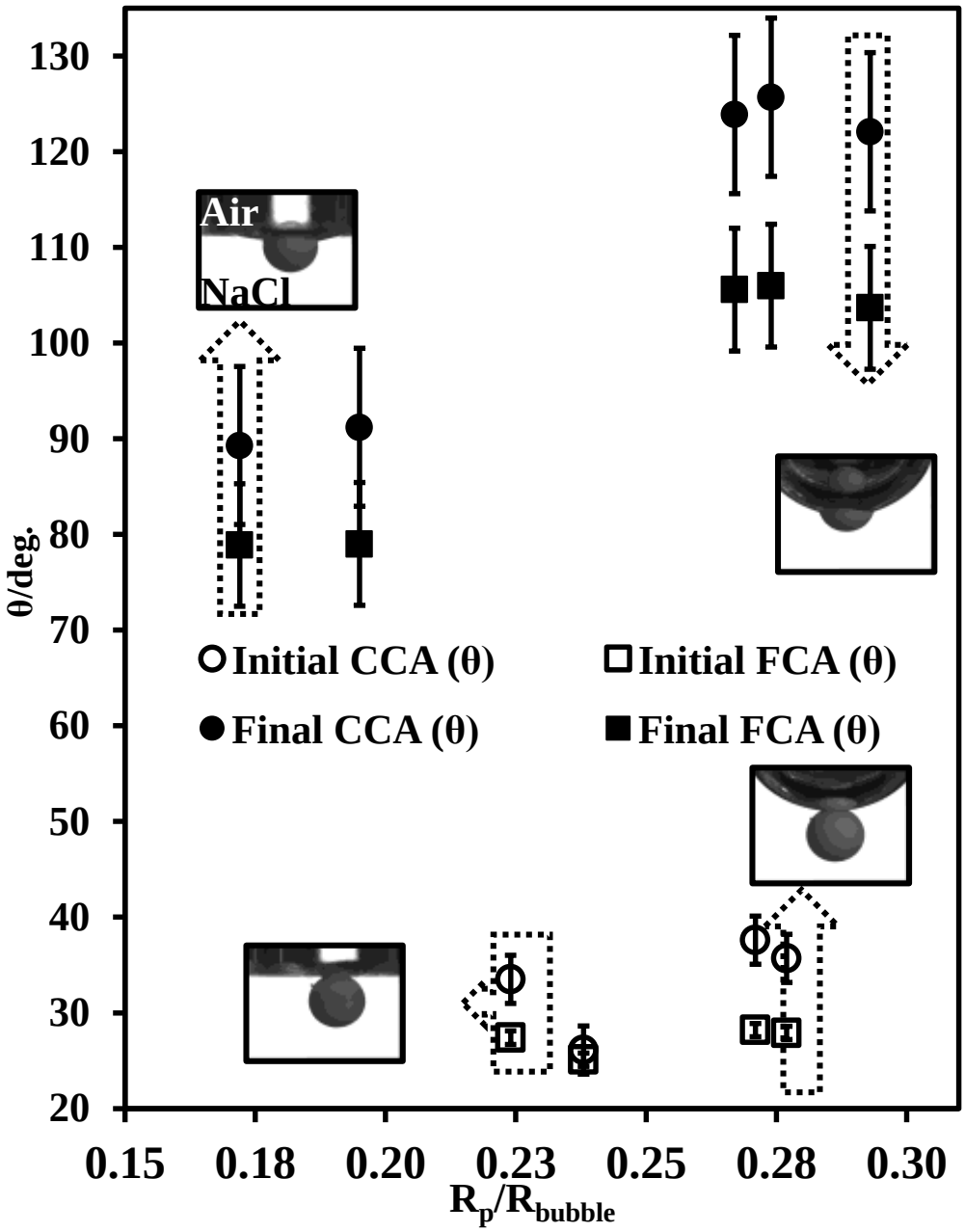

Figure 7.12. Contact angle of a dry porous particle (1.67 mm) attached to an air bubble in a NaCl (aq) solution as a function of the ratio of the particle radius (R_p) and the bubble curvature radius (R_{bubble}): (□) initial contact angle for a flat liquid surface (FCA), (○) initial contact angle for a curved liquid surface(CCA), (■) final contact angle for a flat liquid surface (FCA), (●) final contact angle for a curved liquid surface (CCA). The error bars denote the average of contact angle values for three repeated

calculations of the 1.67 mm particles at different stages using macro script in Image Pro Plus 6.

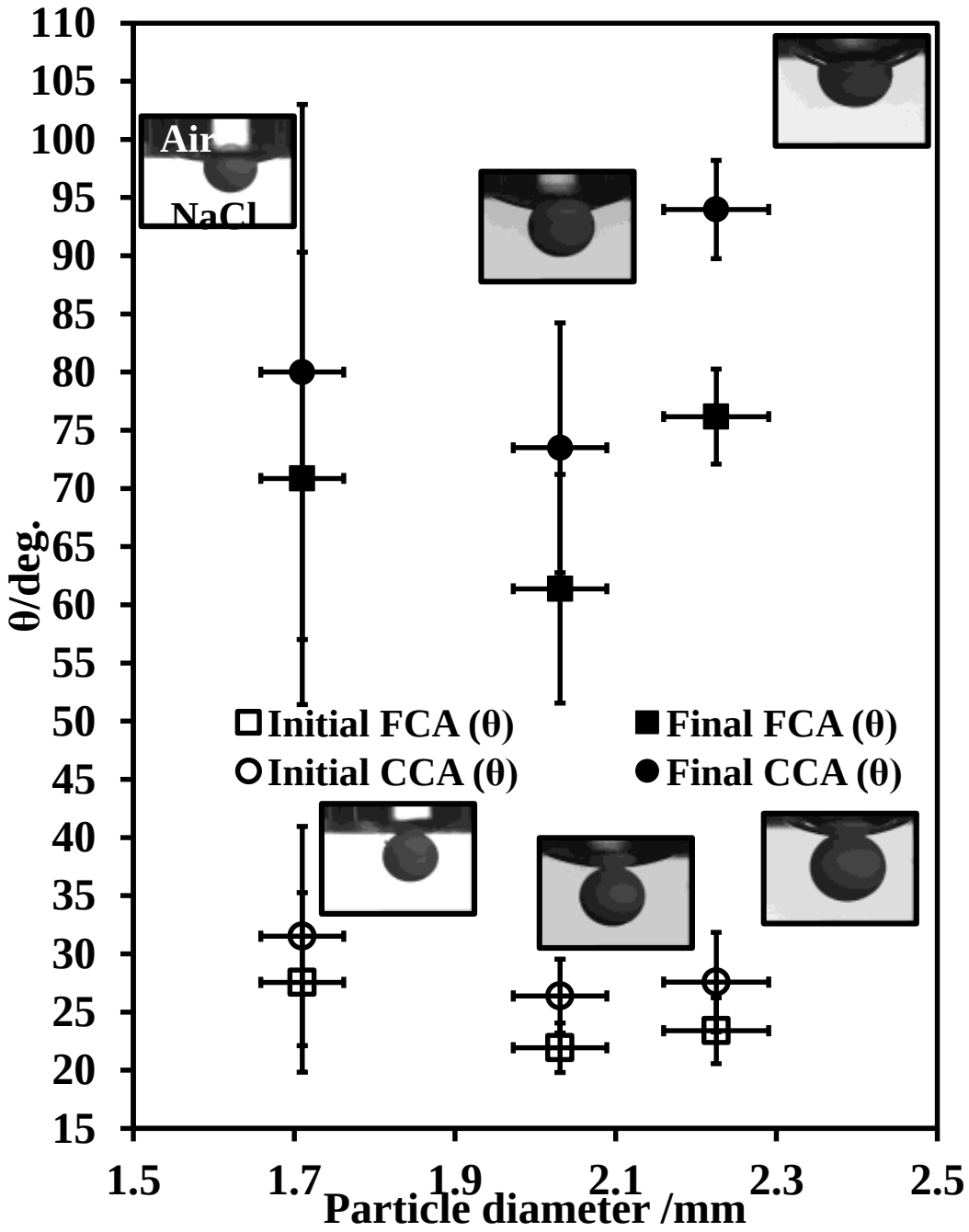

Figure 7.13. Average contact angle of water-infused porous supra-particles adsorbed to an air bubble in a 0.1 M NaCl(aq) solution: (□) initial contact angle for a flat liquid surface (FCA), (○) initial contact angle for a curved liquid surface(CCA), (■) final contact angle for a flat liquid surface (FCA), (●) final contact angle for a curve liquid surface (CCA).

7.4.5 Contact angles of water-infused porous supra-particles at the hexadecane-water interface

Infusing porous supra-particles with water has a strong influence on their adsorption at the oil-water interface compared to air-water interfaces. The 1.8 mm porous supra-particles were the only particles attached to the oil phase from the water phase, while larger particles did not adsorb to the o-w interface. Table 7.2 summarizes the contact angle achieved by different porous supra-particles (1.8 mm in diameter) pre-filled with water and then attached to a hexadecane-water interface. The initial contact angle for CCA ranged from 11° ± 1° to 20° ± 1°, which is similar to the initial FCA ranging from 12°± 1° to 18°± 1°; however, the final contact angle varied between 0° to 106° for CCA and from 0° to 94° for FCA (more contact angle data can be found in the appendix, Tables 8.9 and 8.10). Owing to the surface roughness, the results indicate a significant pinning of the contact line, which impedes free movement and reaching the equilibrium contact angle. These results are not in agreement with the contact angle estimated in the theoretical model (Chapter 6) for porous supra-particles filled with water adsorbed to an o-w interface, as shown in Table **7.1**; however, it was also noted that some of the porous supra-particles would not adsorb at the hexadecane-water interface spontaneously and were expelled away in a lateral direction from the oil droplet upon pushing them into the oil phase. The repletion of these particles is due to the possible presence of an adsorption barrier, which leads to differences in the theoretical model and the experiment [140, 157].

Table 7.2. Measured contact angle of porous supra-particles pre-wetted with water at the hexadecane-water interface in two situations: (i) when the particles are only attached to the oil droplet and (ii) when they are inserted into the oil droplet, both from the aqueous phase. The contact angles were measured at two stages: when the oil droplet was flattened by withdrawing oil from the syringe (FCA) and also for oil droplets of a fixed curvature (CCA).

Particle diameter (mm)	CCA θ/°		FCA θ/°	
	Initial	Final	Initial	Final
1.83	11	28	12	26
1.81	20	106	18	94
1.83	17	48	14	47
1.84	16	0	15	0

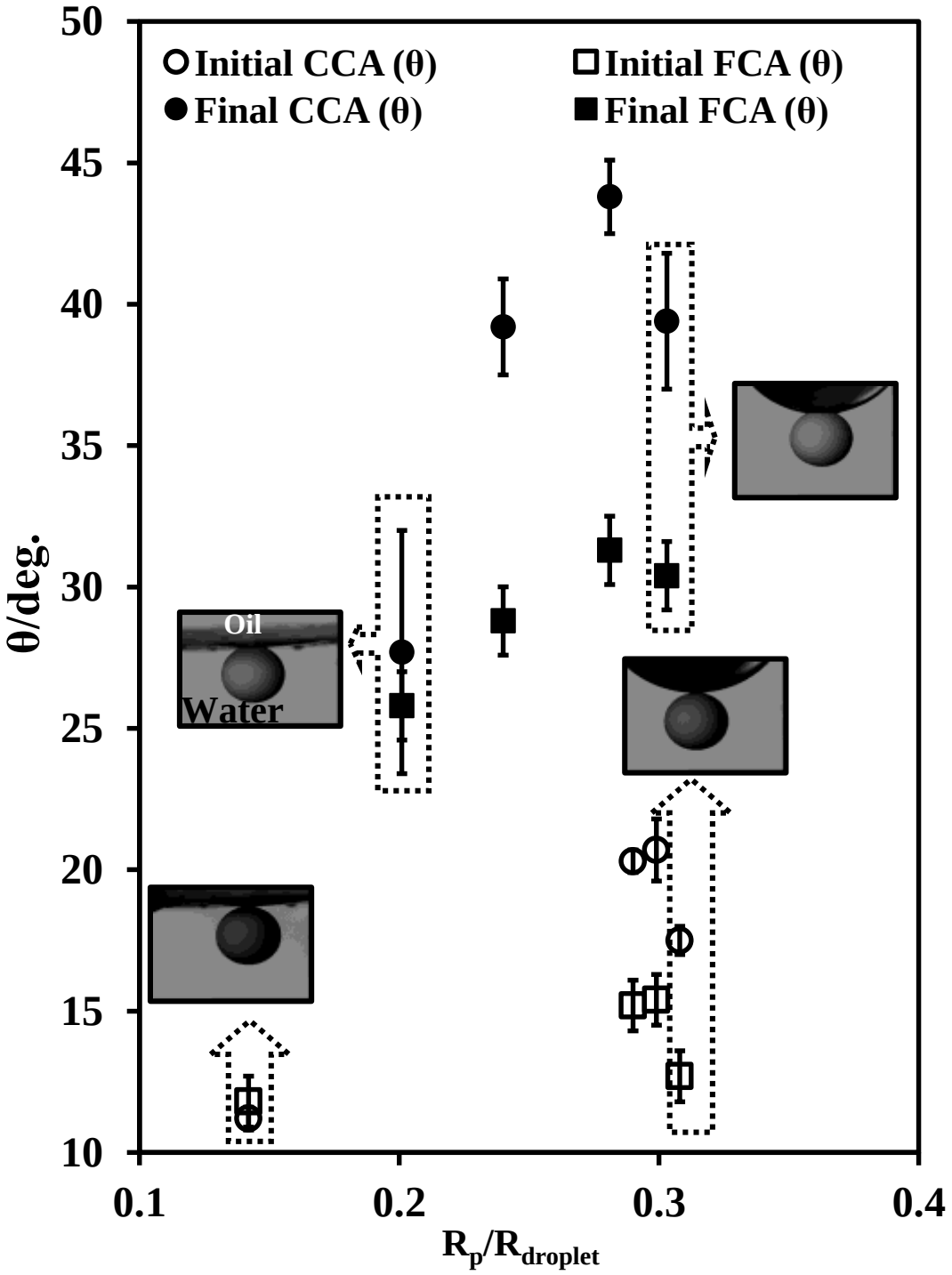

Figure 7.14. Contact angle of water-infused porous supra-particles (of diameter 1.83 mm) attached to a hexadecane drop in water as a function of the ratio between the particle radius (R_p) and the radius of the hexadecane droplet ($R_{droplet}$). The particles were approached to the oil droplet from the aqueous phase: (□) initial contact angle for a flat liquid surface (FCA), (○) initial contact angle for a curved liquid surface (CCA), (■) final contact angle for a flat liquid surface (FCA), (●) final contact angle for a curved liquid surface (CCA).

7.4.6 Contact angles of porous supra-particles infused with a NaCl(aq) solution at the hexadecane-NaCl(aq) solution interface.

It is well-recognised that the presence of a significant concentration of electrolytes in the aqueous phase facilitates the adsorption of negatively charged particles at liquid interfaces due to the screening of the electrostatic repulsion between the particle and the liquid surface [153]. To achieve a stable contact angle, 0.1 M $NaCl_{(aq)}$ was used to reduce the repulsion and maintain the interfacial tension close to that of the original oil-water interfacial tension [153]. The electrolyte influences the particles to adsorb similarly at the oil-NaCl(aq) solution interface easier than when using Milli-Q water [183]. Figure 7.13 shows the effect of the oil droplet size on supra-particle contact angle values depending on the calculation of the measurement of the surface diameter. The wettability of pores filled with the electrolyte solution causes a dramatic change in the particle wetting behaviour compared with the case of Milli-Q water. The final contact angle of the supra-particle adsorbed to curved interfaces was measured at $101^o \pm 1^o$ and $120^o \pm 1^o$ for FCA and CCA, respectively. These values are larger than the expected values presented in Table 7.1; however, the latex particle contact angles in the presence of a 0.1 M NaCl (aq) solution are expected to be different from their values obtained with the GTT for Milli–Q water for both the air-water and the oil-water interface. Regretfully, particle contact angle measurements with GTT for such a high concentration of salt were not possible, as the concentrated electrolyte interfered with ability of gellan gum to form strong gels. For this reason, it would not be a direct basis for comparison with the theoretical prediction, as the data for the latex particles' contact angle θ_o are not available for these cases.

The initial contact angle shows a low contact-angle hysteresis between the CCA and FCA values; however, after pushing the supra-particles through the oil-water interface, the contact angle hysteresis of the supra-particles between CCA and FCA increased to approximately 20° differences (see Appendix, Table 8.11 and 8.12). The FCA values exhibited a stable contact angle and did not vary with the change of the oil droplet size. The contact angle of supra-particles of varying sizes at the practically flat oil-NaCl(aq) solution interface are shown in Figure **7.16**. For 1.9 mm supra-particles, the initial contact angles were 52° ± 10° and 49 ° ± 8° for CCA and FCA, respectively. Furthermore, the final contact angles for the same particles were 116° ± 6° (CCA) and 107° ± 3° (FCA). The reason for the contact angle hysteresis could be the effect of the

pinning of the three-phase contact line due to the significant surface roughness on the supra-particles. In comparison with the supra-particles filled with water, this shows less hysteresis in the contact angle but does not agree with the estimated values in Table 7.1 due to reasons already explained above.

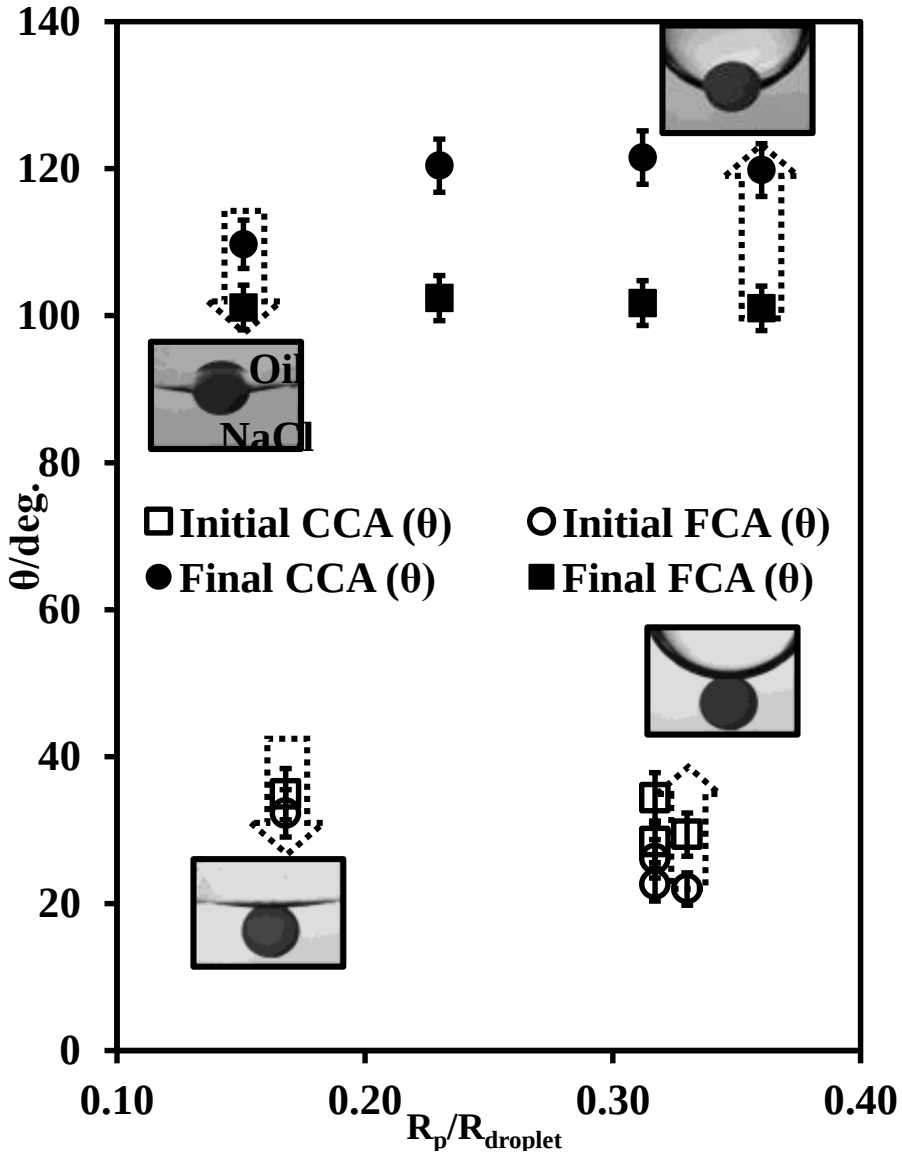

Figure 7.15. Contact angle of porous supra-particles (1.83 mm in diameter, pre-filled with 0.1 M NaCl (aq) solution) at the hexadecane-NaCl (aq) solution interface as a function of the ratio between the particle radius (R_p) and the oil droplet radius ($R_{droplet}$): (□) initial contact angle for a flat liquid surface (FCA), (○) initial contact angle for a curved liquid surface (CCA), (■) final contact angle for a flat liquid surface (FCA), (●) final contact angle for a curved liquid surface (CCA). The error bars denote the

average of contact angle values for three repeated calculations of the 1.83 mm particles at different stages using macro script in Image Pro Plus 6.

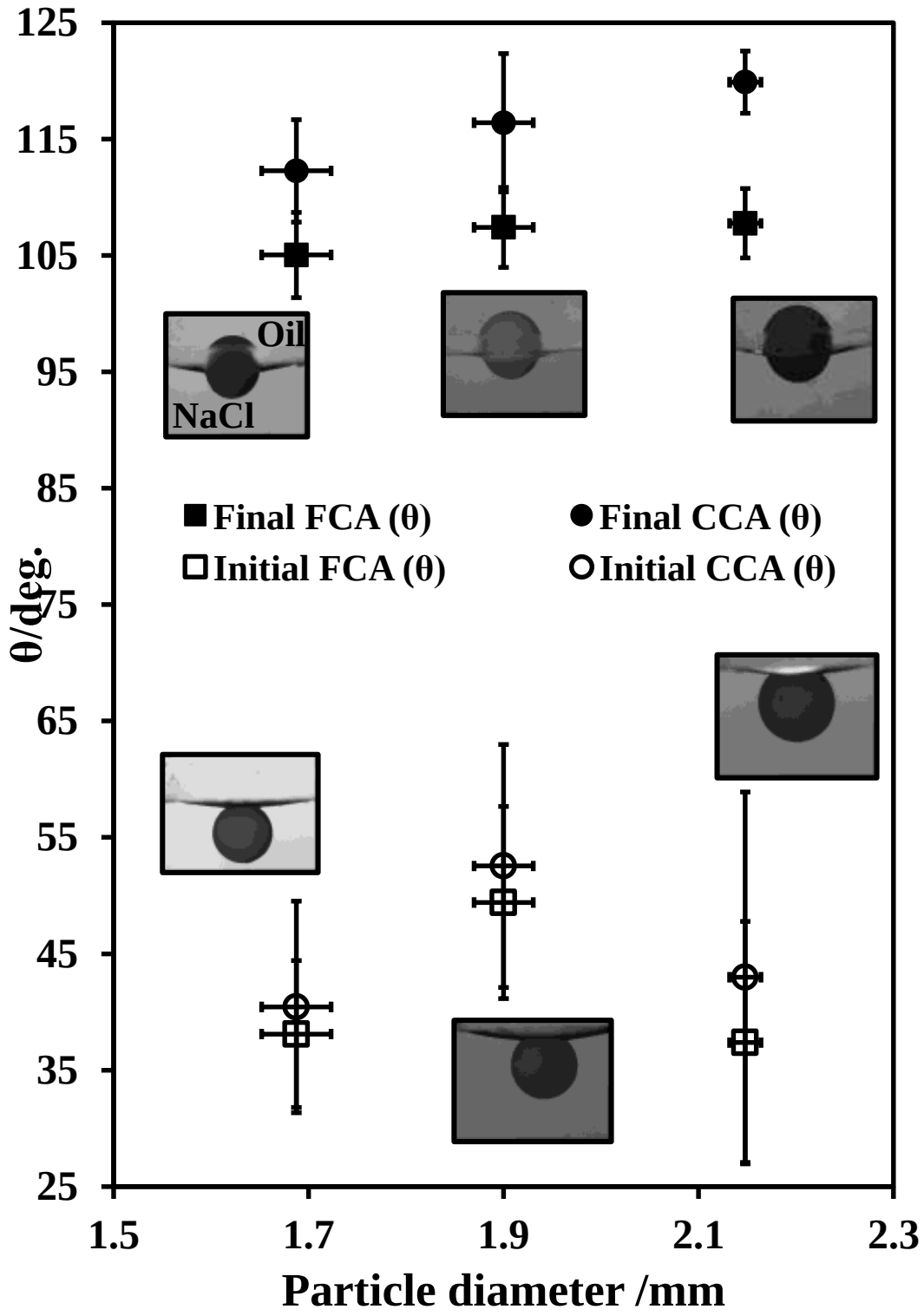

Figure 7.16. Average contact angle of porous supra-particles (infused with 0.1 M NaCl (aq) solution) adsorbed to the interface of hexadecane droplets in a NaCl(aq) solution. The particles were attached from the aqueous phase: (□) initial contact angle

for a flat liquid surface (FCA), (○) initial contact angle for a curved liquid surface (CCA), (■) final contact angle for a flat liquid surface (FCA), (●) final contact angle for a curved liquid surface (CCA).

7.4.7 Contact angle of hexadecane-infused porous supra-particles attached at the hexadecane-water interface.

Making the supra-particles super-hydrophobic was successfully done when their pores were impregnated with hexadecane and adsorbed at the hexadecane-water interface from the oil phase. Experimental data for the contact angles of porous supra-particles filled with hexadecane at different water droplet sizes is presented in Figure 7.17. The initial and the final contact angles for a flat surface were not dependent on the particle size and corresponded to 150°± 2°, respectively; however, it was found that for the curved liquid surface, the initial contact angle decreased with an increasing oil droplet size, while the values of the final contact angle fluctuated between 130° and 115°. Furthermore, the final contact angle at the curved liquid interface reached the equilibrium contact angle after pushing the supra-particles into a water droplet. After being pushed into the water droplet (by pressing), the supra-particle contact angle was 115°, and upon increasing the droplet radius, the contact angle was 128°.

The initial contact angles for porous supra-particles pre-filled with oil adsorbed to a flat hexadecane-water interface for different particle sizes were very high, 153° ± 14° for CCA and 157° ± 10° for FCA, respectively, and the final contact angles were 135° ± 15° for CCA and 140° ± 14° for FCA, respectively (see Figure **7.18**). The main reason for this is that the constituting latex particles are hydrophobic at the oil-water interface (θ_o= 94 ± 1^o), and the supra-particle surface, which has a significant surface roughness, yields a much higher contact angle than its building blocks.

The model predicted values for porous particles pre-filled with oil at the oil-water interface are in the range of 99°–104° for a hexagonal packing and 106°–110° for a square packing of latex particles at the porous particles surface (Table 7.1). The contact angle achieved for all particles impregnated with hexadecane were beyond these values, which can be seen in the Appendix Table 8.13 and 8.14.

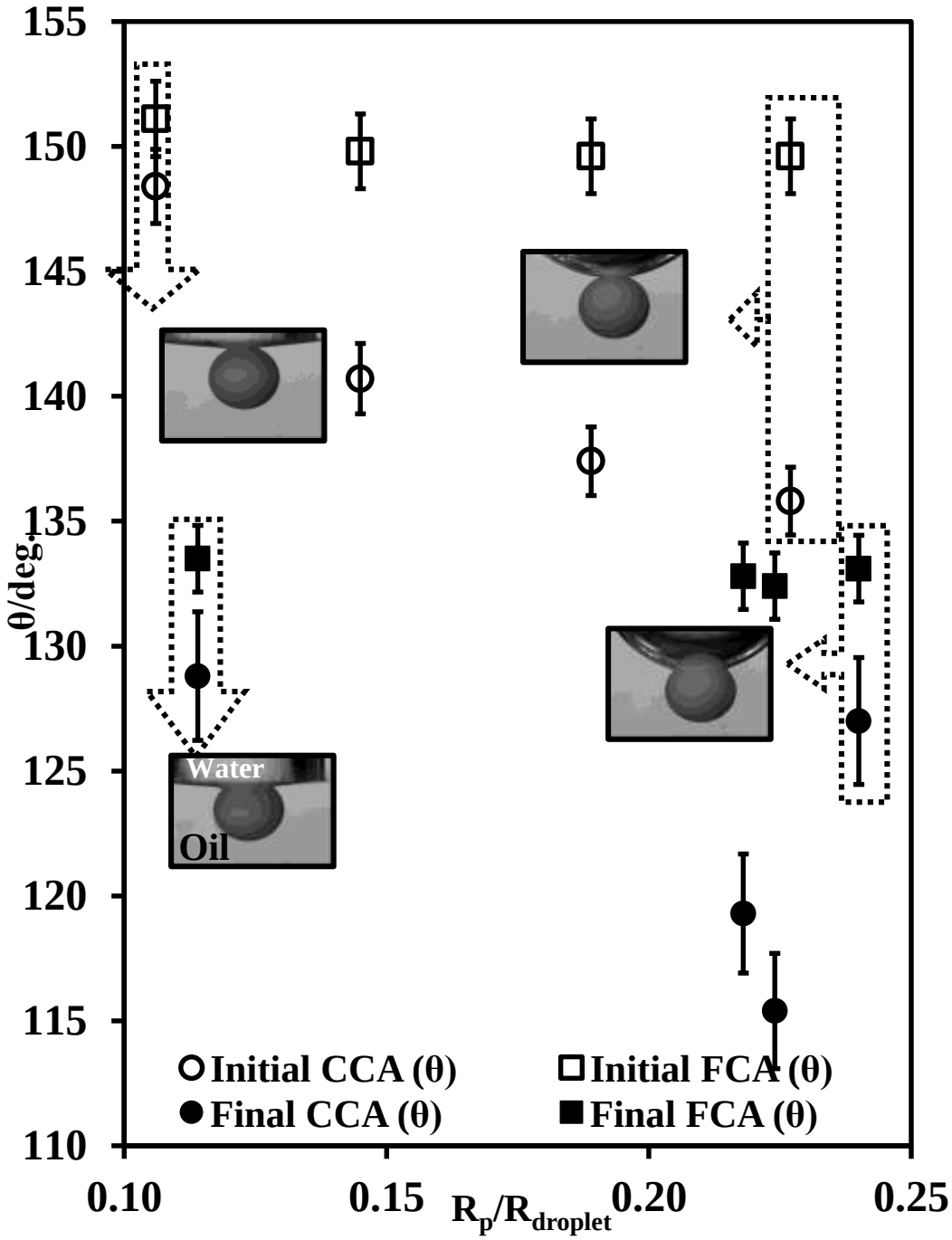

Figure 7.17. Contact angle of hexadecane pre-filled porous supra-particles (diameter of 1.83 mm) at the hexadecane-water interface as a function of the ratio of the particles (R_p) and the water drop radius ($R_{droplet}$): (□) initial contact angle for a flat liquid surface (FCA), (○) initial contact angle for a curved liquid surface (CCA), (■)final contact angle for a flat liquid surface (FCA), (●) final contact angle for a curved liquid surface (CCA). The error bars denote the average of contact angle values for three repeated calculations of the 1.83 mm particles at different stages using macro script in Image Pro Plus 6.

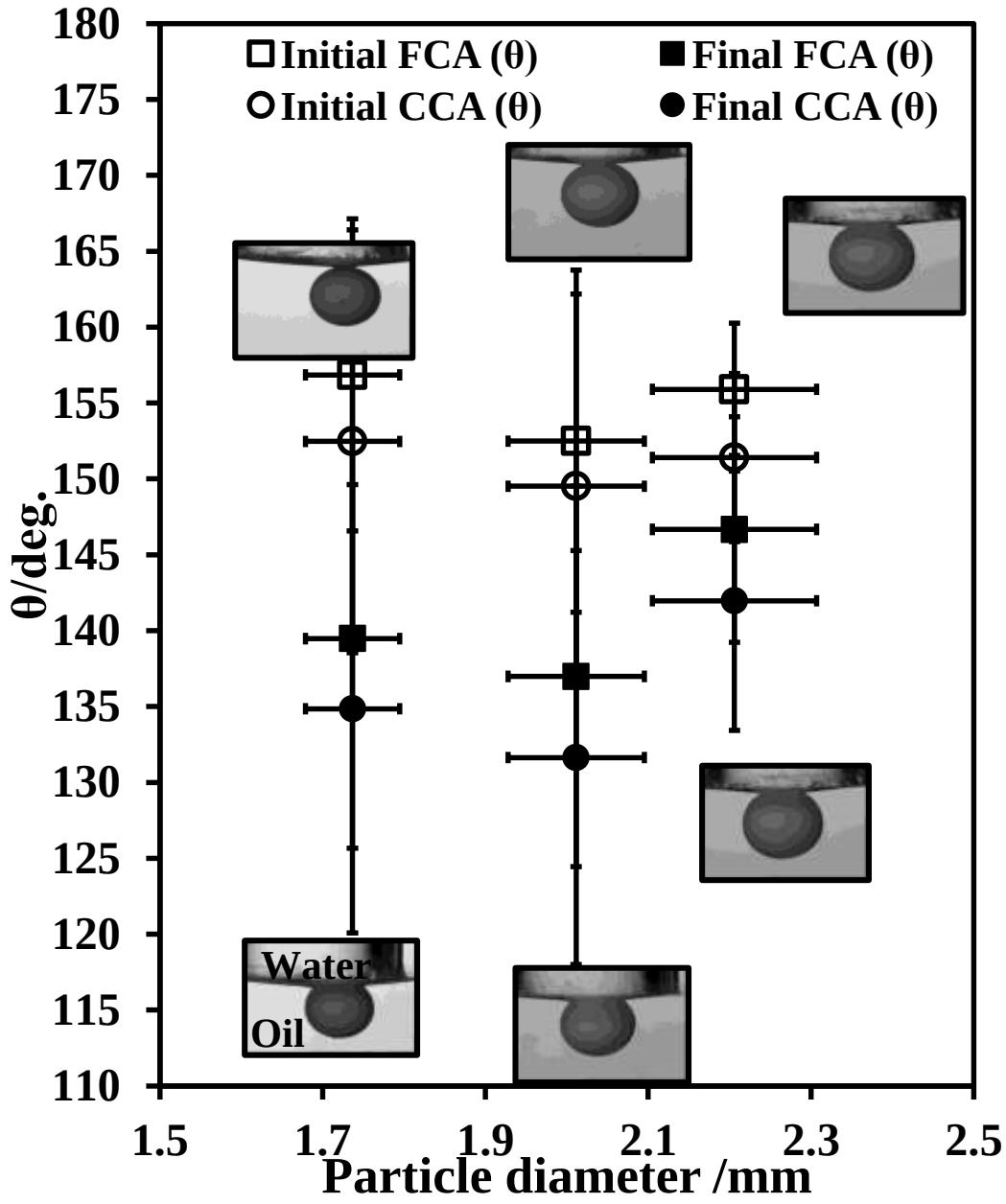

Figure 7.18. Average contact angle of hexadecane-infused porous supra-particles attached to a water droplet in water. The particles are approached to the oil-water interface through the oil-phase: (□) initial contact angle for a flat liquid surface (FCA), (○) initial contact angle for a curved liquid surface (CCA), (■) final contact angle for a flat liquid surface (FCA), (●) final contact angle for a curved liquid surface (CCA).

7.4.8 Contact angles of hexadecane-infused porous supra-particles at the hexadecane-NaCl(aq) solution interface.

In this section, the effect of using a 0.1 M NaCl(aq) solution as an aqueous phase on the adsorption of porous supra-particles impregnated with hexadecane at the

hexadecane-NaCl(aq) solution interface will be investigated. The results are in contrast with those in the previous section in which Milli-Q water was used. The contact angle of a 1.75 mm particle was investigated at different volumes of the NaCl(aq) solution droplet using two different calculations: flat surface (FCA) and curved surface (CCA). The initial and the final contact angles showed a steady contact angle with the change in the droplet volume for FCA; however, the CCA had a fluctuating result for both the initial and final contact angles. These initial contact angles increased with a decreasing aqueous drop diameter from 135° ± 2° to 139° ± 2° for CCA. For the final CCA, the contact angle ranged from 97° ± 3° to 98° ± 1°; however, when the aqueous drop diameter decreased, the initial contact angle (FCA) of the same particles maintained their contact angle at around 147° ± 1°, while the final FCA was 115° ± 2° (see Figure **7.19**).

The average initial contact angles for 1.7 mm (Figure **7.20**) porous supra-particles adsorbed to a practically flat interface were 130° ± 8° and 135° ± 9° for CCA and FCA, respectively, while the final contact angles were 100° ± 3° (CCA) and 110° ± 3° (FCA). These contact angles increased with an increase of the particle diameter from 130° ± 8° (1.7 mm) to 138° ± 7° (2.2 mm) for the initial CCA. For the final CCA, the contact angle ranged from 100° ± 3° to 120° ± 11° for 1.7 mm and 2.2 mm, respectively. This also indicates a very significant surface roughness effect, which leads to contact angle hysteresis; however, the supra-particle final contact angle of CCA agreed with the theoretical approach when the latex particles were arranged in square packing, ranging from 107°-110°, and when the particles were arranged in hexagonal packing, the range was 101-104° (more data are presented in Appendix Table 8.15 and 8.16).

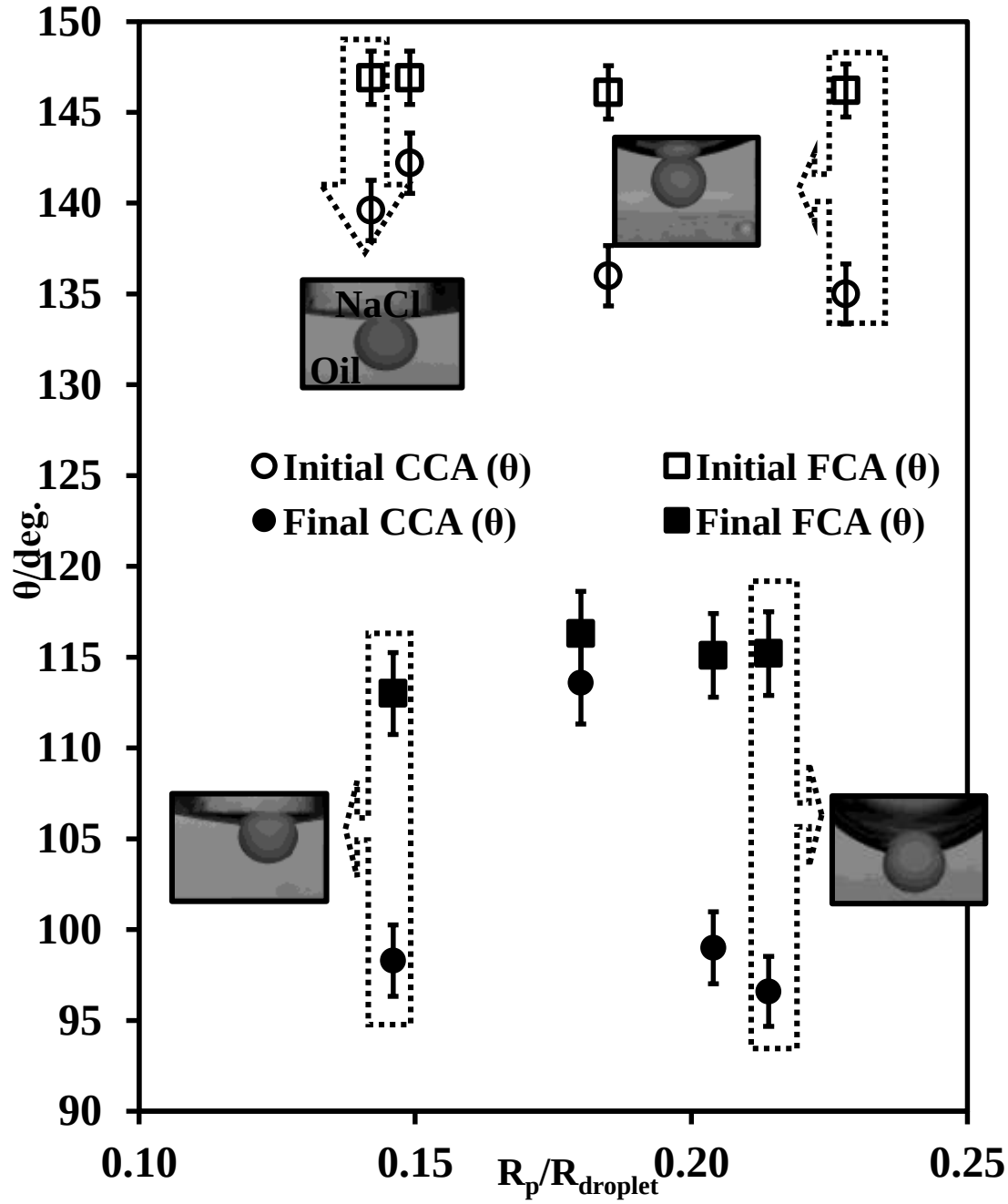

Figure 7.19. Contact angle of hexadecane-infused porous supra-particles (diameter of 1.83 mm) at the hexadecane-NaCl(aq) solution interface as a function of the ratio of the particle radius (R_p) and the aqueous drop radius ($R_{droplet}$): (□) initial contact angle for a flat liquid surface (FCA), (○) initial contact angle for a curved liquid surface (CCA), (■) final contact angle for a flat liquid surface (FCA), (●) final contact angle for a curved liquid surface (CCA). The error bars denote the average of contact angle values for three repeated calculations of the 1.7 mm particles at different stages using macro script in Image Pro Plus 6.

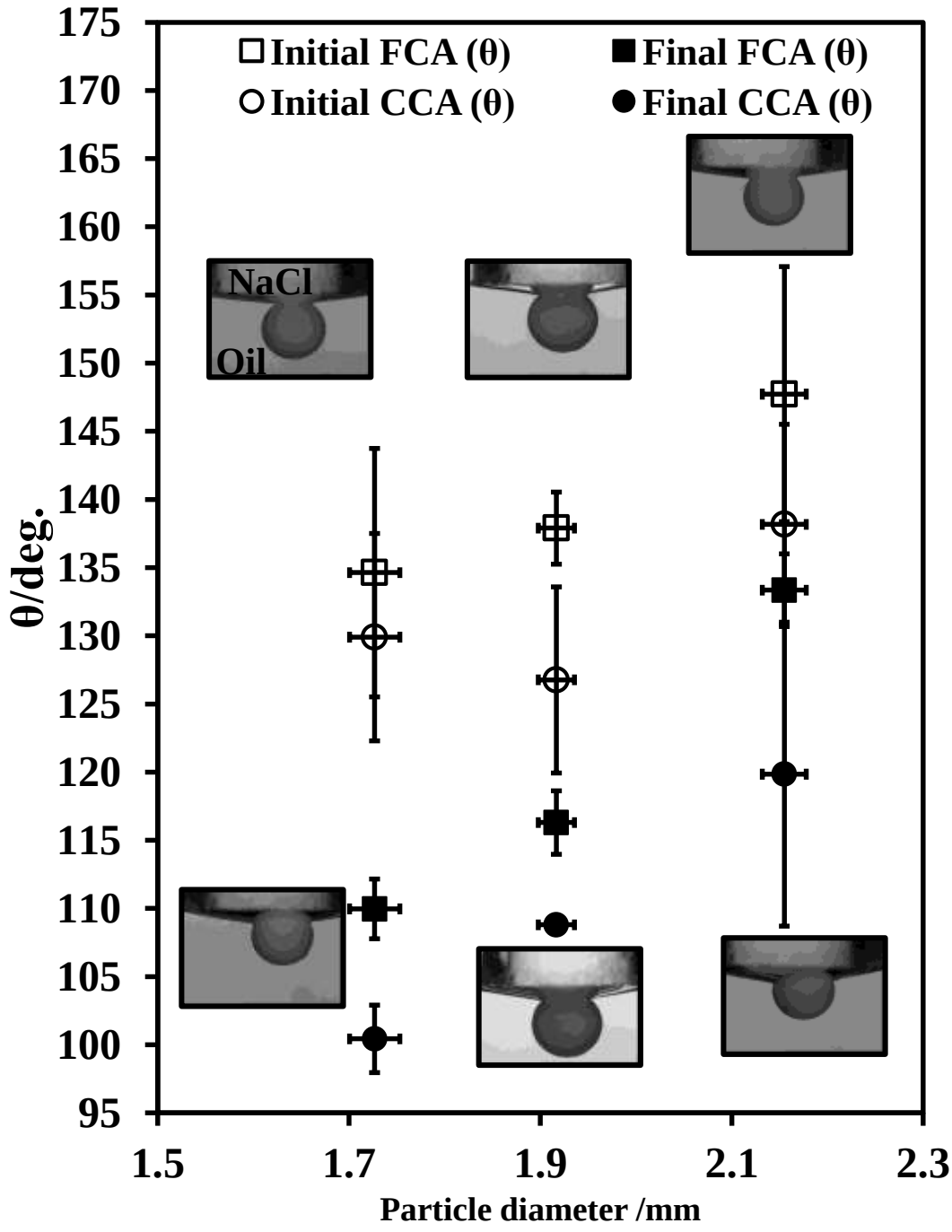

Figure 7.20. Average contact angle of hexadecane-infused porous supra-particles attached to a drop of a 0.1 M NaCl(aq) solution in hexadecane. The particle was approached to the liquid interface through the oil-phase: (□) initial contact angle for a flat liquid surface (FCA), (○) initial contact angle for a curve liquid surface (CCA), (■) final contact angle for a flat liquid surface (FCA), (●) final contact angle for a curved liquid surface (CCA).

Table 7.3. Summary of the experimental values for porous supra-particles' contact angle impregnated with hexadecane or air at the hexadecane-water and the air-water interfaces related to the theoretical values predicted in Chapter 6.

Interface type	θ_o/deg.	θ_s/deg.	θ_h/deg.	fluid	Particle diameter (mm)	R_p/R_{fluid}	CCA (θ)	±	FCA (θ)	±	
o/w	94	107-110	101-104	oil	1.81	0.233	155	1	163	0	initial
						0.140	163	0	166	0	
						0.247	119	1	134	0	final
						0.116	129	0	134	0	
a/w	63	40-56	2-37	dry	1.69	0.253	138	1	152	0	initial
						0.147	134	0	139	0	
						0.359	58	1	75	0	final
						0.116	66	4	70	1	
o/NaCl(aq)	94	107-110	101-104	oil	1.69	0.296	120	1	132	0	initial
						0.151	129	3	132	1	
						0.145	99	0	107	0	final
						0.233	108	4	123	1	
a/NaCl(aq)	63	40-56	2-37	dry	1.68	0.365	100	2	121	0	initial
						0.120	106	1	112	0	
						0.214	34	1	61	0	final
						0.171	53	1	62	0	

Table 7.4. Summary of the experimental values for porous supra-particles contact angle impregnated with water at the hexadecane-water and the air-water interfaces related to the theoretical values predicted in Chapter 6.

Interface type	θo/deg.	θs/deg.	θh/deg.	fluid	Particle diameter (mm)	Rp/Rfluid	CCA (θ)	±	FCA (θ)	±	
o/w	94	81-84	88-92	water	1.81	0.274	21	1	16	1	initial
						0.160	20	0	16	0	
						0.237	116	4	93	0	final
						0.204	106	1	94	0	
a/w	65	41-44	44-47		1.69	0.309	47	1	37	0	initial
						0.130	43	1	38	1	
						0.303	89	3	72	0	final
						0.143	81	0	73	0	
o/NaCl(aq)	94	81-84	88-92	NaCl(aq)	1.68	0.334	41	3	32	0	initial
						0.261	29	1	32	1	
						0.300	124	1	104	0	final
						0.163	107	3	102	0	
a/NaCl(aq)	65	41-44	44-47		1.65	0.307	27	1	23	1	initial
						0.140	29	1	26	0	
						0.211	96	4	92	1	final
						0.272	101	2	85	0	

As discussed in the previous section, the effects of the pinning of the three-phase contact line on the supra-particle surface can result in a very large contact angle hysteresis, which makes it very hard to determine the supra-particle equilibrium contact angle. The particle contact line pinning leads to trapping it in meta-stable states with a very high "activation energy" of shifting from meta-stable states to the particle equilibrium position, which corresponds to the global minimum of the system's free

energy. Significant mechanical energy is needed to move the particle position between these states. This is the reason that an alternative method of measurement for the supra-particle contact angle was considered, which is presented in the next section.

7.5 Sonication method for determining the contact angle of porous supra-particles at the air-water and oil-water interfaces.

The aim of this method was to find the equilibrium contact angle of porous particles attached to a/w or o/w interfaces by using vibrational energy generated from an ultrasonic bath or ultrasonic probe. The set-up is described in section 2.2.6.4. Here, the results are shown concerning the supra-particle contact angle for different amplitudes or times of vibration to reach equilibrium adsorption. Sonication was used to overcome the energy barrier, which exists between the particles and the liquid interfaces [184].

7.5.1 Contact angle of dry porous supra-particles sonicated at the air-water interface.

Dry porous supra-particles were placed onto the a/w surface and vibrated in this configuration using an ultrasonic probe in water (3 mm in diameter, Vibra-Cell from Sonics and Materials) at different amplitudes ranging from 0% to 100% for 10 minutes constantly. The observed contact angles are summarized in Figure 7.21. The dry porous particles tended to be more hydrophilic, as predicted. This method allowed for moving the particle from its initial metastable state, as its adsorption position adjusts towards the equilibrium state because of the vibration.

Dry porous particles' contact angle after vibration at different amplitudes represents the change in the contact angle with the increase in sonication power. The value of the experimentally determined equilibrium contact angle by this method agrees with the theoretical results obtained in Chapter 6, which predict that the contact angle of dry supra-particles at the a/w interface for $\theta_o = 63^o \pm 3°$ of the small "building block" particles will provide an equilibrium contact angle for the porous particles at $\theta = 2^o$-37° in a hexagonal arrangement and $\theta = 40^o$-56° in a square arrangement (Table 7.5). Given the accuracy of the GTT measurements for the latex particle contact angle, there is remarkably good agreement between the theory and the experiment.

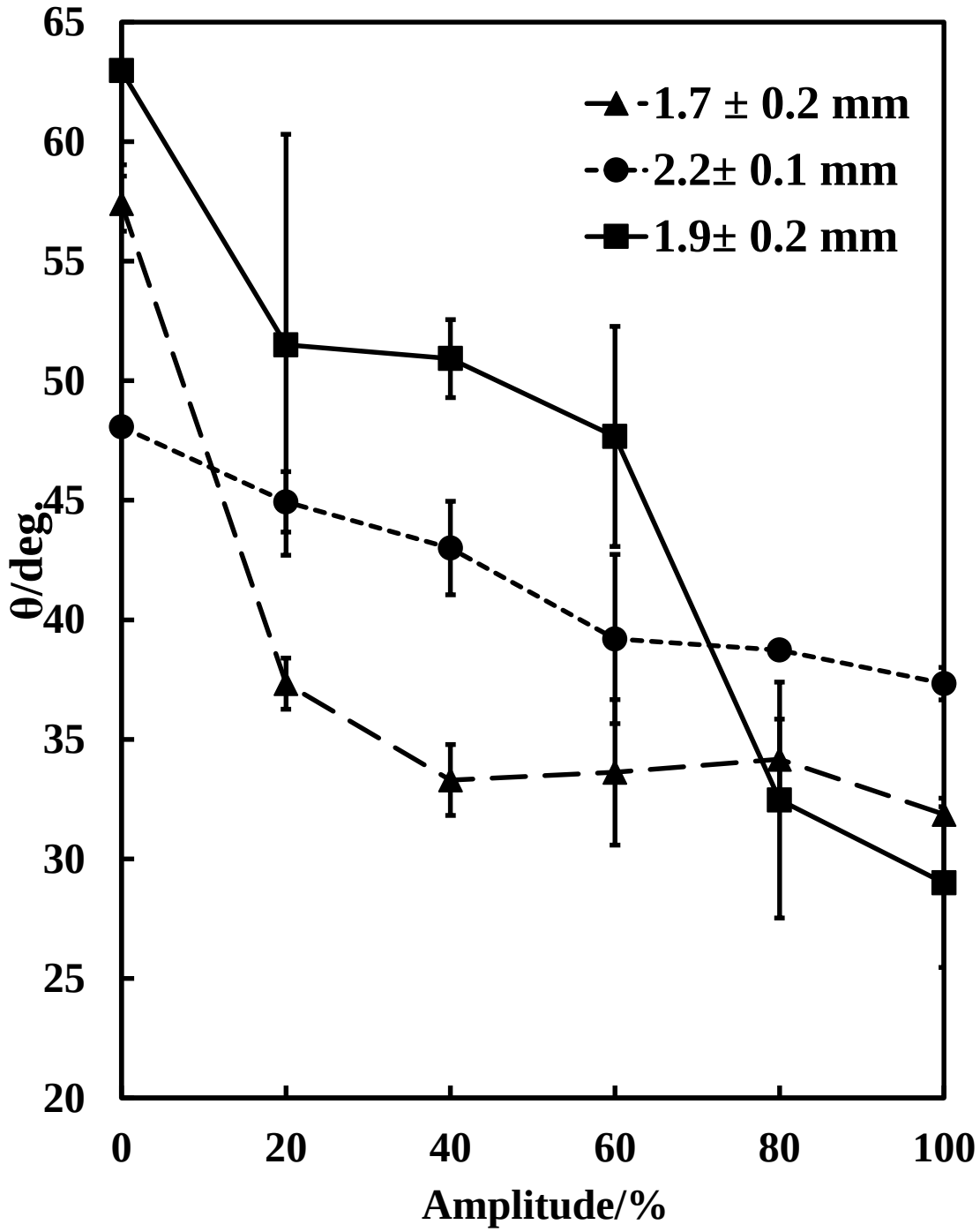

Figure 7.21. Contact angle of dry porous particles at the a/w interface after applying ultrasonication at different amplitudes, which reflects the drift of the contact angle from the initial metastable state towards an equilibrium position. The contact angle is reduced from a higher contact angle to the lowest possible after sonicating the system with the attached porous supra-particles.

In Figure **7.22** shows the change of the particles contact angle after sonication at different amplitudes, representing the effect of an increase in vibration power. This

contact angle is close to the theoretical results (Chapter 6), which predict that the contact angle of dry particles at an a/w interface $\theta_o = 63^o \pm 3°$ of the small constituting particles will provide an equilibrium contact angle for the porous supra-particles of $\theta = 30 \pm 3°$ (see Figure **6.9** and Figure **6.10**). Taking into account the very steep dependence of θ on θ_o in the vicinity of the critical contact angle of 61^o, this theoretical model for the supra-particle adsorption is in quite good agreement with the experimental data.

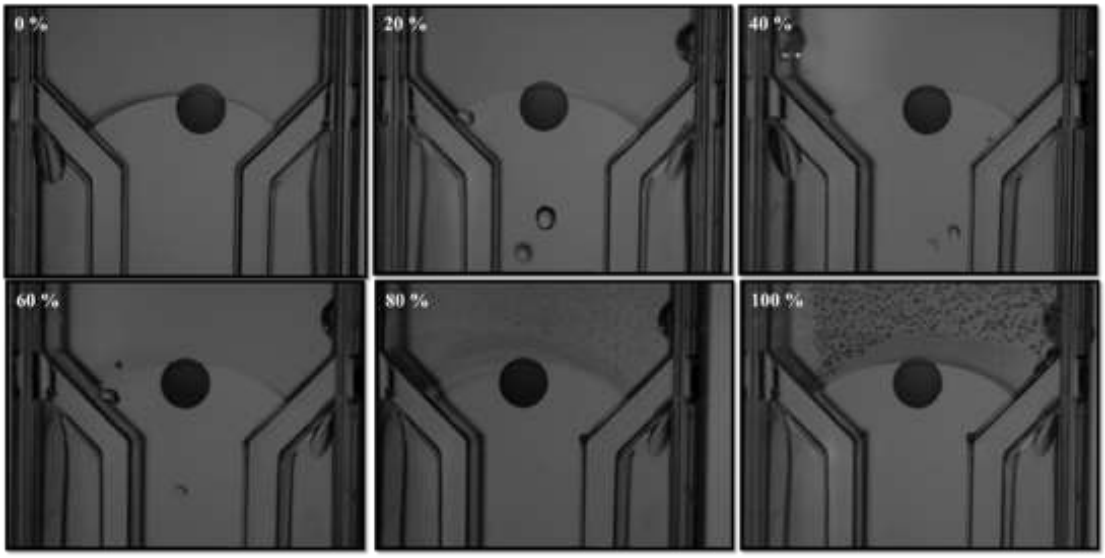

Figure 7.22. Side images of initially dry porous particles attached to the air-water interface after ultrasonication at different amplitudes. The supra-particle diameter is 1.7 ± 0.2 mm.

7.5.2 Contact angle of water-infused particles sonicated at the air-water interface.

Dry porous particles were initially washed with ethanol to extract all air from the pores. These particles were washed with the aqueous media (water or 0.1 M NaCl(aq)) to replace the ethanol overnight. The particles in the aqueous media were drawn to form a small layer for attaching the particles to the cuvette slide. The thicknesses of the layer varied because of human error (see e.g. Figure 7.25 below)[32]. Then, ultrasonication was employed for differing durations (1–30 minutes) using an ultrasonic bath (Ultrawave) or ultrasonic probe (Viber–Cell). Then, the cell was slowly toped up with water to raise the attached particles gradually and to prevent an accidental detachment from the liquid interface.

The initial contact angle of the supra-particles sonicated with the ultrasonic probe started at 30° and ended at 57°, which agreed with the contact angle of particles arranged in square packing at the air-water interface as described in Chapter 6; however, the contact angle obtained by using an ultrasonic bath had a similar trend, as the particles increased their contact angle during the sonication time but did not match the theoretical model predictions (Table 7.5). In theory, the contact angle of porous supra-particles adsorbed from water to an a/w interface would be in the range of 41-44 and 44-47 for building block particles packed on the surfaces in square or hexagonal packing, respectively. The effective force pulling the particles into the air phase could be a capillary force, which acts along the tangent to an a/w interface at the three-phase contact line (see Figure **7.23**) [35].

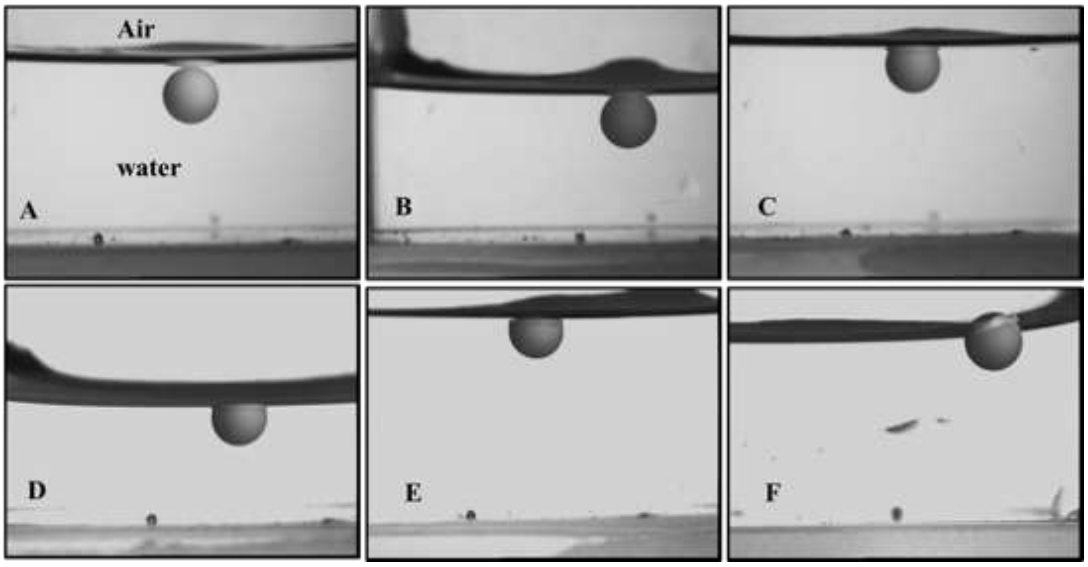

Figure 7.23. Side camera images from DSA 10 for water-wet porous supra-particles adsorbed at the a/w interface for different durations of sonication in an ultrasonic bath after: (A) 3 min, (B) 6 min, (C) 9 min, (D) 15 min, (E) 20 min and (F) 30 min (floated). The particles were attached to the air-water interface after initial sucking and the subsequent insertion of water. The water sucking step corresponds to the a/w surface pressing the particles towards the bottom of the cuvette, while the water addition step lifts the particles and the a/w interface into a viewing position.

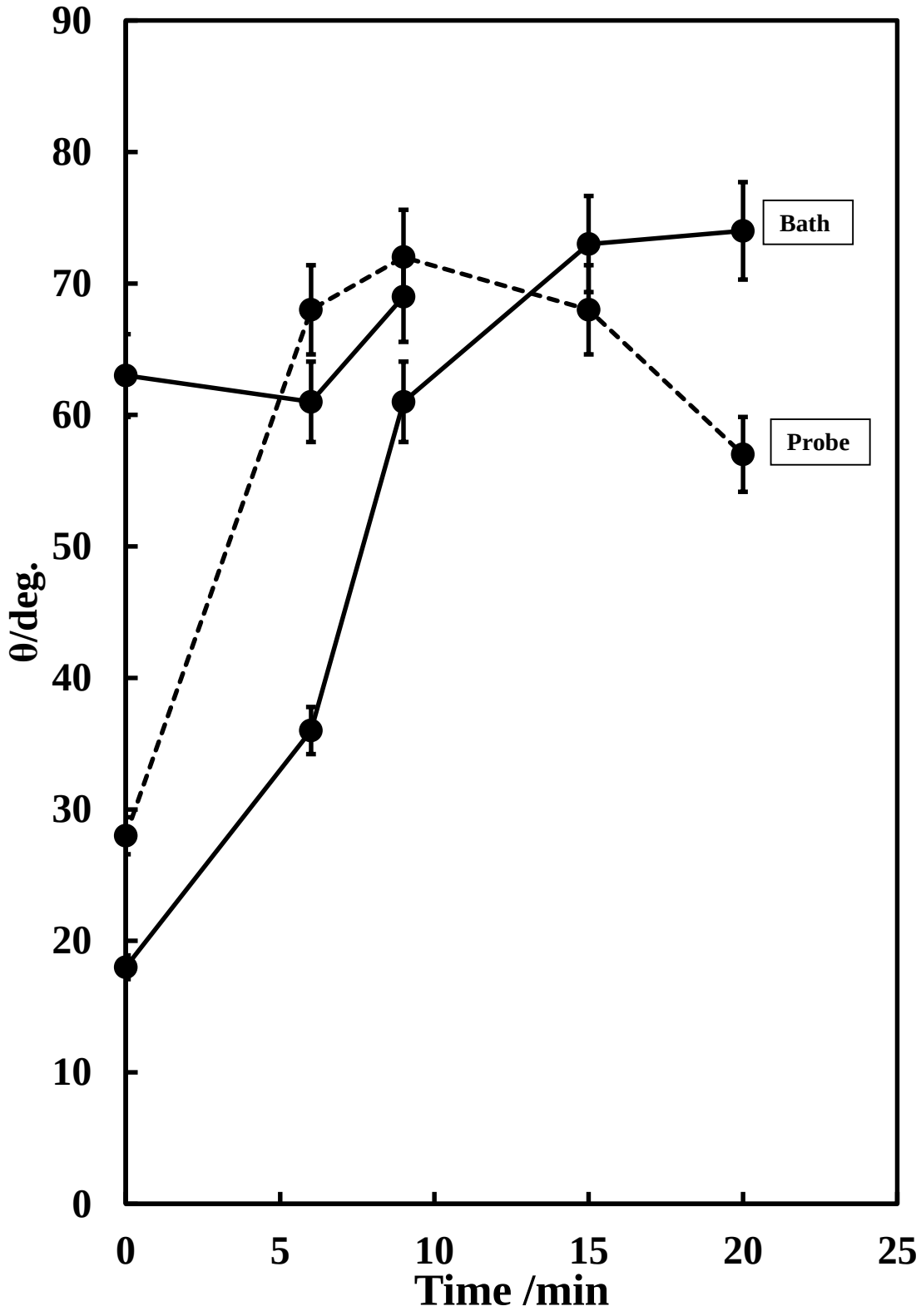

Figure 7.24. The supra-particle contact angle at the air-water interface as a function of the duration of sonication. The solid line corresponds to supra-particles treated using an ultrasonic bath and the dashed line using an ultrasonic probe as they were attached at the air-water interface.

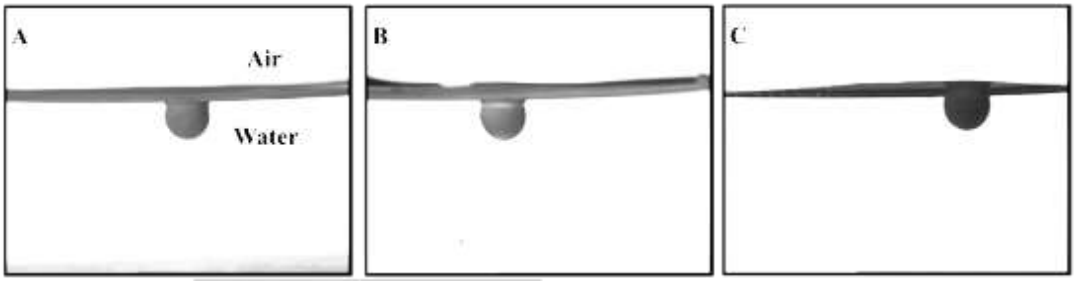

Figure 7.25. Side camera images from DSA 10 for water-wet supra-particles attached at the a/w interfaces for different sonication times in the ultrasonic bath after: (A) 3 min, (B) 6 min and (C) 9 min. The particles were initially attached at the a/w surface using a spatula.

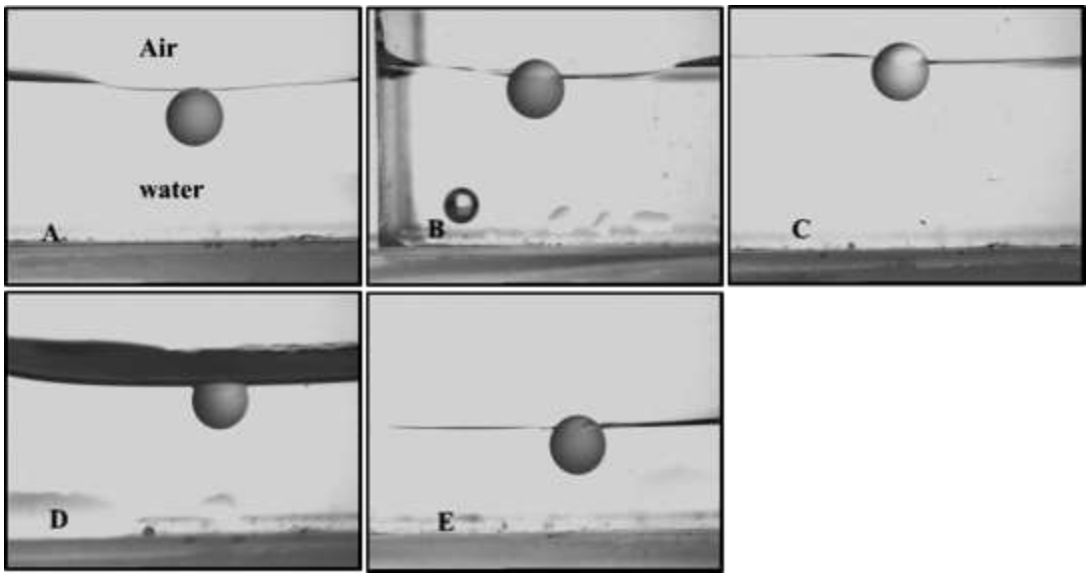

Figure 7.26. Side camera images from DSA 10 for supra-particles (1.9 mm in diameter) attached at the a/w interface. The supra-particles were infused with 0.1 M NaCl and subjected to different durations of sonication by an ultrasonic probe (40 %, 2 second pulse) at the air-NaCl(aq) solution surface: (A) 3 min, (B) 6 min, (C) 9 min, (D) 15 min and (E) 20 min.

In this section, the sonication method for determining the equilibrium contact angle for water-wet and oil-wet on porous oil-water interfaces are explained. The aim of this method was to find the equilibrium contact angle of porous particles attached to an o/w interface by using vibrational energy generated from an ultrasonic bath. The results shown here involve the supra-particle contact angle for different times of vibration to reach an equilibrium adsorption.

7.5.3 Contact angle of porous supra-particles impregnated with water at the hexadecane-water interface.

Water-infused supra-particles were attached to the hexadecane-water interface using a spatula to raise the particle to the liquid interface. The supra-particles were impregnated with Milli-Q water. The cuvette was first filled with water, and then the oil phase was added on top of it. Then, the pre-wet particles were attached to the interface through the water phase. Different images were taken before and after sonication. Ultrasoncation was applied for different durations (1–20 minutes) using an ultrasonic bath (Ultrawave); however, some of the supra-particles began to partially disintegrate (see Figure **7.27**) when they were sonicated for a long duration. A supra-particle of 1.7 mm in diameter was sonicated at the oil-water interface for differing durations to reach its global equilibrium position and contact angle. Figure 7.28 shows that the porous supra-particles maintained their contact angle at 33°; however, the third particle (see Figure **7.27**) began to increase from 12° to 71°, probably due to partial disintegration. In comparison with the theoretical model (81^o-84^o for square packing and 88^o-92^o for hexagonal packing), the expected global equilibrium contact angle was 10 to 20 degrees smaller than the experimentally obtained value (see Table 7.5).

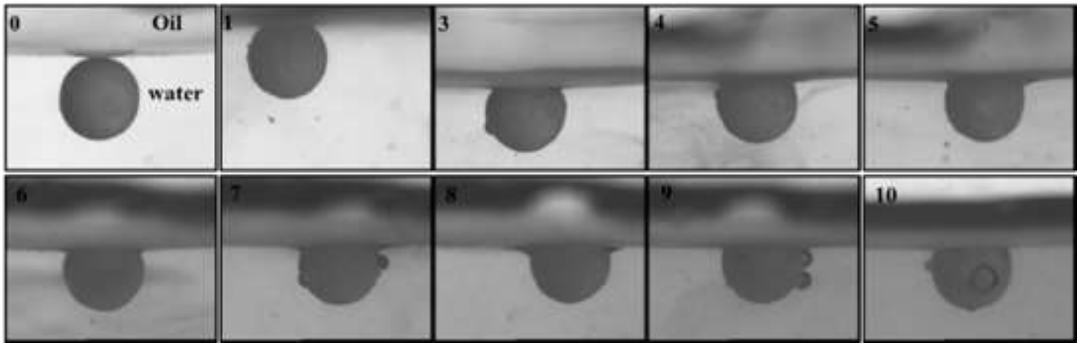

Figure 7.27. Porous supra-particles of diameters of 1.7 ± 0.2 mm initially impregnated with water and sonicated for different durations using an ultrasonic bath after being attached to the hexadecane-water interface. The number denotes the vibration time in minutes. The bubbles were observed due to the vibration generated by the ultrasound bath.

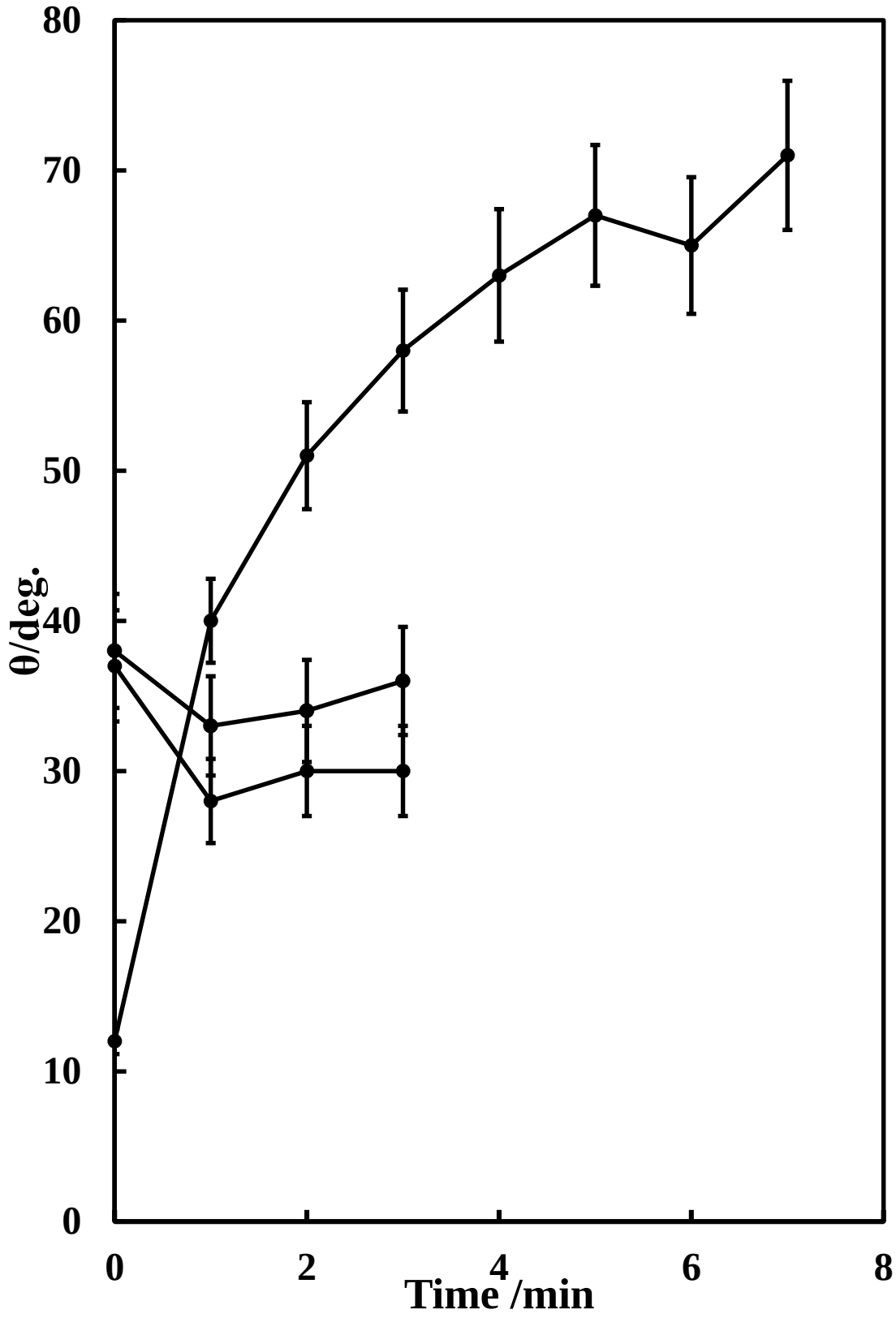

Figure 7.28. The three-phase contact angle of supra-particles with a diameter of 1.7 ± 0.2 mm pre-filled with water and attached to the hexadecane-water interfaces using a spatula. The particle contact angle is plotted versus the sonication time.

7.5.4 Contact angle of porous supra-particles impregnated with hexadecane at the hexadecane-water interface.

The dry supra-particles were first impregnated with the oil (hexadecane purified three times through aluminium chromatographic column). After that, the cuvette was filled with water, oil was added on top and then the oil-infused supra-particles were attached to the hexadecane-water interface by dropping them through the hexadecane phase with a spatula. Different images were taken before and after ultrasonication for different durations (1–30 minutes) using an ultrasonic bath (Ultrawave). Some of the particles began to lose their integrity when intensively sonicated, as can be seen from the images provided. Then, the particles were sonicated for different durations to reach their equilibrium position at the o/w interface. Figure 7.28 shows that two particles were hydrophobic at the contact angles 150° and 110°, respectively; however, as sonication was applied, the particle contact angle began to gradually decrease and had the potential to change the particle to hydrophilic with a contact angle ranging from 110° to 71°. The particles that started with a 150° contact angle remained hydrophobic after sonication with a contact angle of around 110°. In this case, the comparison of the experimental data with the theoretical model also shows that the contact angles observed agree within the range expected by the theory (for square packing, 107^{o}-110^{o}, and for hexagonal packing, 101^{o}-104^{o}), as presented in Table 7.5.

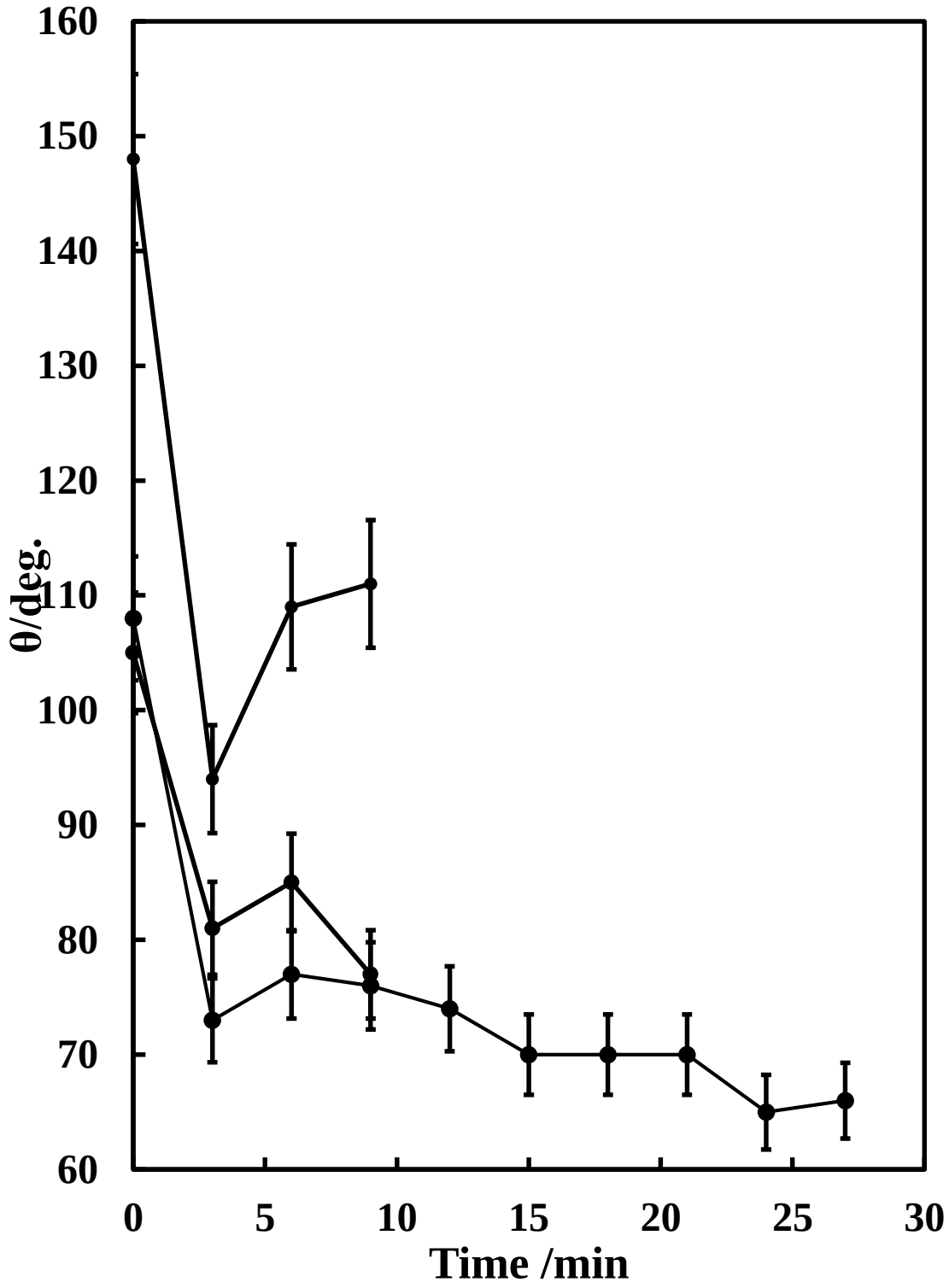

Figure 7.29. The three-phase contact angle of supra-particles with the diameter of 1.7 ± 0.2 mm pre-filled with hexadecane and attached to the hexadecane-water interfaces using a spatula. The supra-particle contact angle is plotted versus the sonication time. The three graphs correspond to three different individual particles with several runs for each particle. The supra-particle contact angle reaches 70° and 110° after sonication.

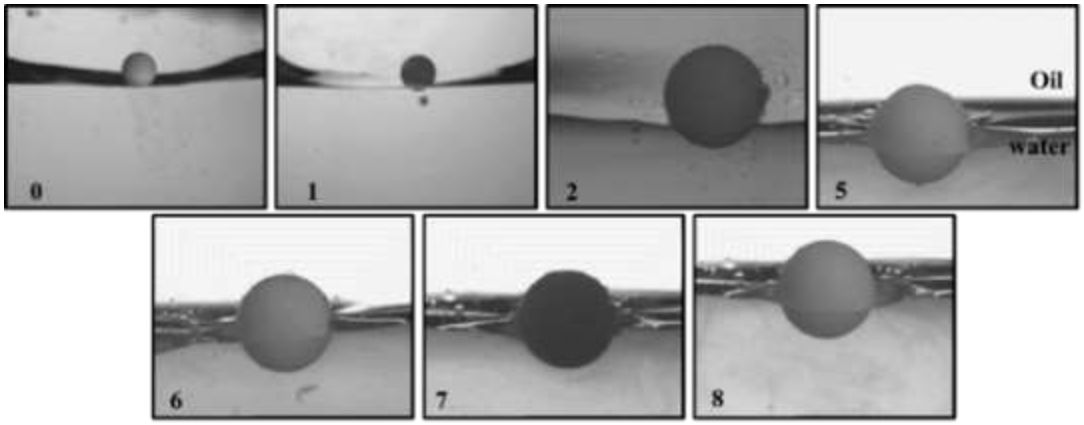

Figure 7.30. Porous supra-particles (diameter of 1.7 mm) impregnated with hexadecane at the hexadecane-water interface. The contact angle quickly reached 80° and then levelled off further after sonication.

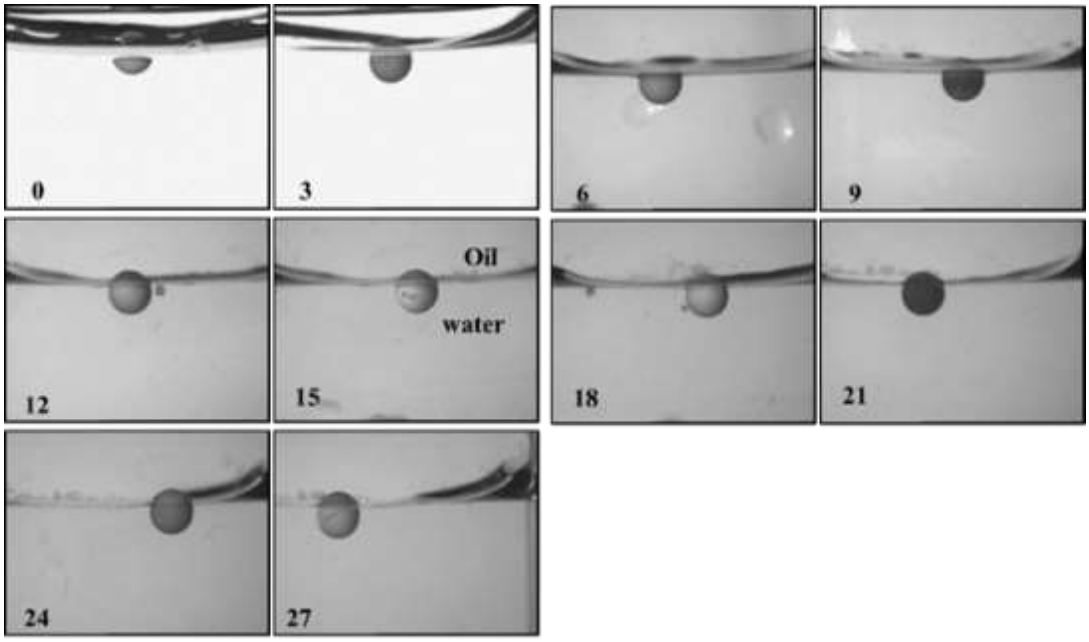

Figure 7.31. Side camera images from DSA 10 for oil-wet particles attached at the o/w interfaces at different sonication durations in ultrasonic bath time: 0–27 min. The number on the images corresponds to the sonication time in minutes. The oil is hexadecane.

Table 7.5. Summary of the experimental values for porous supra-particles' contact angle impregnated with air, water or hexadecane at the air-water and hexadecane-water interfaces related to the theoretical values predicted in Chapter 6.

Interface type	Fluid	θ_o/deg.	θ_s/deg.	θ_h/deg.	Particle diameter (mm)	CA (θ/deg.)	
						initial	final
A-W	Air	63 ± 3	40-56	2-37	1.7	57 ± 1	32 ± 1
A-W	Water	65 ± 1	41-44	44-47	1.7	28 ± 2	57 ± 3
O-W	Hexadecane	93 ± 1	81-84	88-92	1.7	105 ± 3	77 ± 4
O-W	water	94 ± 1	107-110	101-104	1.7	12 ± 3	71 ± 5

7.6 Magnetic resonance imaging for porous supra-particles at fluid-liquid interfaces.

7.6.1 Magnetic resonance imaging for dry and wet composite porous supra-particles at the air-water interface.

The aim was to visualise the air-water front penetration inside the particles when the dry or wet supra-particles were attached to the air-water interface. The black region on the MRI images shows that the porous particle with pores means that there is no water present inside the pores of the particle. The liquid water phase appears on the MRI images as a higher contrast colour than the water trapped inside the particle pores, as the shade is affected by an amount of hydrogen atoms aligning in one direction because of the effect of the magnetic field. The contact line diameter is difficult to determine with high enough precision and to observe directly because of the capillary rise of the liquid and the capillary tube. Contact angle values were approximated by drawing a circle around the particles and presuming that the grey colour near the air-water interface is the contact line diameter. The results agreed with the measurements of the contact angle for the dry particles attached to the water droplet using a pendent-drop method (see section 7.2). For water-wet supra-particles, the contact angles determined from the MRI images were smaller than those from the pendant-drop method as expected, but this agreed with the theoretical model approach for porous supra-particles adsorbed at the air-water interface.

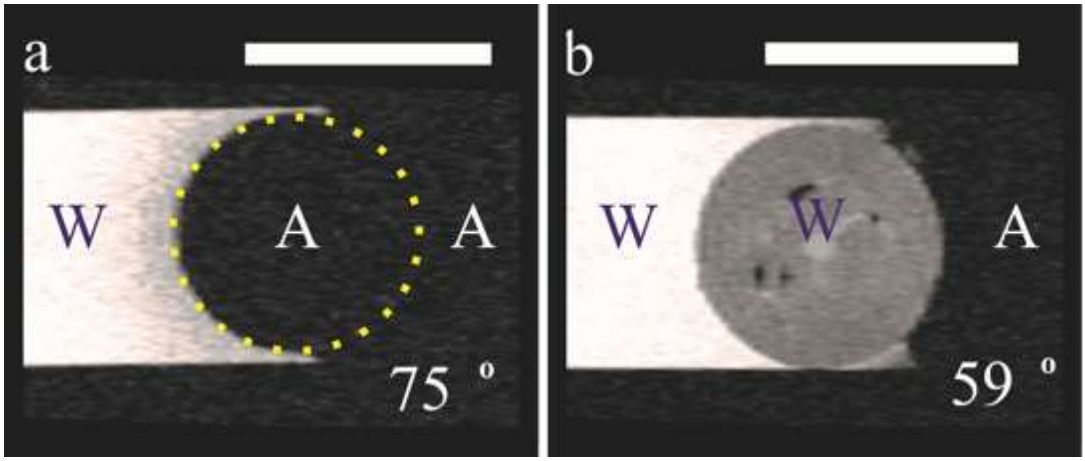

Figure 7.32. MRI images of composite porous supra-particles made from 40% 2.6 μm sulphate latex particles suspension by the evaporation and thermal annealing method. The image shows the position of the air-water surface on the porous particle surface. (a) Air imbedded inside the particle pores, as the air shows a dark region; (b) water penetrated into the porous particles at the air-water surface is seen in grey colour. The particles show different resolutions when infused with water, as the interior of the particle becomes grey, the liquid water corresponds to white and the air is represented by a black colour. The scale bar in all images is 1 mm.

7.6.2 Magnetic resonance imaging for water wet porous supra-particles attached at an oil-water interface

The brightness of the produced MRI images is due to the hydrogen atoms' alignment with the magnet. When adding oil (i.e. hexadecane), the contrast and resolution change because of the amount of hydrogen in the oil. On the MRI images for a particle infused by water at the air-water surface and oil-water interfaces, the colour of the liquid water phase is white, the water is represented by a grey colour inside the particle pores and black corresponds to the air region. When adding oil to the particle-water interface, the whole particle turns a dark grey colour because of the higher contrast in the oil, which decreases the contrast of water outside and inside the porous particle. Contrast agents, such as gadolinium chloride, were used to increase the contrast of the aqueous phase by increasing the number of protons that are aligned with the magnetic field. It can be seen from Figure 7.33 that the contrast agent has an effect on the particles image at the a/w interface. From Figure 7.33, the amount of water present at the interior of

the particles indicated by the white region shows that the structure is amorphous and not organised, whereas the structure at the surface is darker and more organised.

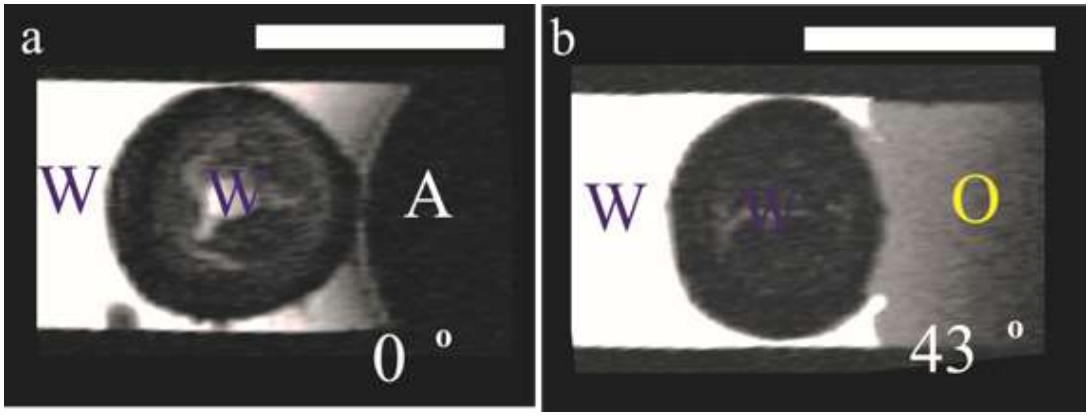

Figure 7.33. MRI images for particles pre-infused with water at (a) the air-water and (b) oil-water interface. In this image, the water contained gadolinium chloride (10^{-3} M) as a contrast agent, and the oil is hexadecane. The contrast agent increased the water brightness but turns the inside colour into black when added to the oil in (b). The scale bar in all images is 1 mm.

7.6.3 Magnetic resonance imaging for oil-wet porous supra-particles at air-oil and oil-water interfaces.

In this experiment, the porous supra-particle was inserted into the capillary tube and suspended at the oil-air and oil-water interfaces. When the particle was inside the capillary (1 mm diameter), a micro syringe needle (from SGE) was used to gently push the particle towards the liquid interface.

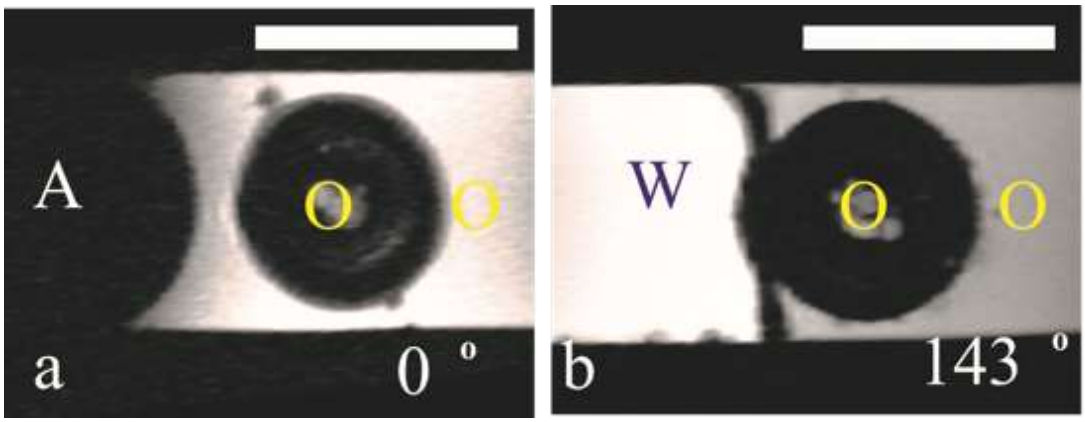

Figure 7.34. MRI images for particles filled with oil (hexadecane) at (a) air-oil and (b) oil-water interfaces. The imbibition of water is quite difficult to identify in these

images, as the interior of the particle does not change much. The scale bar in all images is 1 mm.

It can be concluded from these experiments that the supra-particle attachment at the air-water or the oil-water interface occurs only on the particle surface layer without a deep penetration of the liquid interface front deeply into the porous particle interior. If the porous particle is initially dry, it remains dry upon attachment at the air-water interface. If the porous particle is wet, it remains water-wet after attachment at both the air-water and oil-water interface. MRI images also support the opposite statement that if the supra-particle is oil-wet, it remains oil-wet after attachment to the oil-water interface.

7.7 Conclusions

The wettability of the model porous supra-particles was investigated at different liquid-fluid interfaces by studying the contact angle for the dry and wet porous supra-particles, as these particles are hydrophilic at air water interfaces and hydrophobic at oil-water interfaces. Two different methods for measuring the supra-particle attachment position at the liquid interface were used in an attempt to evaluate the particle equilibrium contact angle. Large contact angle hysteresis was observed with the pending drop method for the evaluation of the supra-particle attachment position at the air-water and oil-water interfaces for a range of cases, which involved dry, water-infused and oil-infused particles. The supra-particles remained trapped in a series of metastable states when attached to the liquid surface. The hysteresis is a result of the pinning of the supra-particle contact line on the "building block" latex particles, which prevents free adjustment towards the equilibrium position. A sonication method was developed, which allows the supra-particle position to be adjusted at the liquid interface with its contact angle drifting towards equilibrium.

The contact angles of the small latex particles were determined experimentally by using the GTT and the theoretical model from Chapter 6 to calculate the expected supra-particle contact angles at air-water and oil-water interfaces for particle infusion with air, water or oil. The latex particle building blocks showed contact angles of about 65^{o} at the air-water interface and 94^{o} at the hexadecane-water interface. For dry supra-particles attached to the air-water interface as well as water-wet particles, a reasonably good quantitative agreement was found between the experimental data and the

theoretical predictions from Chapter 6 for the supra-particle contact angle. The contact angle for wet particles had a mixture of contact angle values, which is likely because of the arrangement of smooth particles at the outer surface of supra-particles. Porous supra-particles were prepared using a 40% solution, and different sizes and different volumes from the suspension were obtained. The hydrophobicity of the particles when wet with water or dry had a similar contact angle, which means the liquid front penetration does not influence the contact angle. When the contact angle is measured at the air-water and hexadecane-water interface, the result is significant hysteresis because the particle roughness is not the same for all particles used in these experiments. Another reason could be attributed to force applied by pushing the particles to penetrate into the droplet or bubble that cause the particles to detach from the droplet or bubble. The particles contact angles are hydrophilic when they are filled with water and become hydrophobic when they are filled with hexadecane. The variations in the contact angle at the o/w interface is due to the roughness of the supra-particles or the ability of the NaCl(aq) droplet to displace the oil from the surface of the particle. Magnetic resonance imaging was used as a method for the localisation of the air-water and oil-water interfaces in the pores of dry and pre-wet supra-particles. The MRI results indicate that the liquid interface does not penetrate through the supra-particle interior pores. The particle attachment at the air-water and oil-water interfaces occurs through the adsorption of the surface layer of colloid particles on the composite supra-particle surface. These results indicate that the mechanism of attachment of densely packed particles aggregates at liquid surfaces.

Chapter 8: Summary of conclusions, main results and future work

8.1 Conclusions

The adsorption of colloid particles at liquid interfaces plays a critical role in many industrial applications, such as particles–stabilised emulsions and foams. The wettability of particulate materials, like dry powders and the attachment the individual particles at liquid interface depends not on the particles surface chemistry but also on their shape, surface anisotropic character, aggregation, porosity and the structuring of particles into larger aggregates. Until very recently all these factors have been largely ignores in particle wettability studies at liquid interfaces, partially due to the lack of suitable methods for investigation of these effects, geometrical and theoretical complexity of the capillarity problems involving compound and structured particle at liquid interfaces. In the present thesis, novel experimental methods were developed to partially address these problems by investigation of the adsorption of complex particles at liquid surfaces and putting together new theoretical models of their wetting behaviour.

In Chapter 1 present a detailed literature overview on wetting and spreading as well as introduce the methods for studying wettability of surfaces and colloid particles at liquid interfaces recently developed. In Chapter 2 described the materials and the methods used in several techniques which explored for studying the adsorption behaviour of a range of particle. Also, discuss the classic Gel Trapping Technique (GTT), which is one of the central methods used in this thesis for determining the particle contact angle at air–water and oil–water interfaces. Moreover new techniques was proposed for preparation of model supra–particles that produced from monodisperse latex particles with controlled size and overall porosity. Two original methods for measuring the supra–particle contact angle and the determination of their equilibrium position at the liquid–fluid interface was also developed and presented in this thesis.

In Chapter 3, the adsorption and orientation of several types of anisotropic particles and porous particles at air–water or oil–water interfaces by applying the Gel Trapping Technique were studied. This method replaces the aqueous phase by hydrogel solution which is then gelled to arrests the position of the adsorbed particles at the water–fluid interface. The replicated hydrogel surface with the attached particles is then moulded

with PDMS and imaged using scanning electron microscopy to reveal the particle contact angle at the original surface. Needle–like aragonite microcrystals and rhombohedral calcite microcrystals were successfully trapped on the PDMS mould at the decane–water and air–water interfaces. It was found that the aragonite microcrystal particles prefer to orientate along the liquid interface, although at high particle concentrations at an air–water interface they can also orientate in an upright position with respect to the liquid interface. The adsorption of calcite microcrystals at an air–water interface, shows that they preferred to orientate the face the rhombohedral crystal on the plain of the interface. The results did not show any fixed position to justify the calcite crystal preferred orientation angle at the liquid interface. Also ethyl cellulose microfibers adsorption were investigated at both the air–water and the decane–water interfaces. A high aggregation of ethyl cellulose microfibers were observed at the fluid interface, and the end of the fibres tend to be in the non–polar phase, caused by alterations of fibre surface roughness. The orientation and the attachment of anisotropic particles were observed; nevertheless, the complexity of the anisotropic particles' shapes did not allow direct evaluation of the particles' contact angle. Also the adsorption of polydisperse and highly porous hydrophilic and hydrophobic silica microparticles were studied at the decane–water and the air–water interface. The hydrophilic porous particles mostly were preferentially exposed to the aqueous phase at both air–water and oil–water interface. The experimental results marked that the hydrophobic porous silica particles were mostly immersed inside the oil phase. These results from this chapter are important and can provide an important insights about the orientation and attachment of anisotropic particles at fluid surfaces in various formulations based on shape–anisotropic particles for stabilising emulsions and foams.

The particles functional surface groups can also affect their wetting behaviour at liquid–fluid interfaces Chapter 4 presented the second project of this thesis, which focused on studying the adsorption of carboxylic modified latex (CML) particles with different surface densities of carboxylic groups and particle size at liquid–fluid interfaces. Here, also gel trapping techniques was used to determine and investigate the three–phase contact angle of CML particles at oil–water and air–water interfaces. The SEM images showed that the contact angle of the CML microparticles actually varies with the particle size due to the different surface density of of COOH groups.

Moreover, the influences of COOH group ionisations were calculated at the particles' surfaces and the electric double layer free energy on particles' wettability. The results of the calculations showed that the COOH dissociation effect was too low to explain the variation of the CML microparticles contact angle at the at liquid–fluid interface. Furthermore, the impact of the initial phase was experimentally investigated, where the particles were injected at the fluid interface. The results show that the initial liquid phase does not change the particles' wettability considerably within the experimental error. However, the effect of the hysteresis of the CML microparticles contact angle at the dodecane–water and the air–water interfaces are affected by syneresis of the gellan gum hydrogel and produced the same contact angles. Also, the effect of the presence of a salt in the aqueous phase on the wetting behaviour of the CML microparticles were experimentally and theoretically examined and found that it is insignificant in the case of moderate salt concentrations. The emulsion formation presented that CML microparticles with a high surface density of a COOH groups stabilised oil–in–water emulsions as their contact angle was less than 90°. However, for the CML microparticles of low COOH group density, the particle contact angle was higher than 90° at the oil–water interface and they stabilised water–in–oil emulsions. An alternative explanation about the preferred type of Pickering emulsion based on the bridging ability of the stabilising particles for the emulsion droplets were suggested. In Chapter 5 of this thesis a simple method was developed for fabrication of millimetre–sized model porous supra–particles using smaller monodisperse particles as building blocks. Such porous composite particles were aimed to use for testing the effect of the initial fluid phase on the porous supra–particles' wettability at the liquid–fluid interface as well as the porous particle surface morphology. Finally, the effect of the infusion of porous supra–particles with different fluid phases on their contact angles at oil–water and air–water interfaces were investigated experimentally. Nevertheless, Chapter 5 introduces various approaches to forming porous composite supra–particles shapes, depending on the technique used. Those approaches include: (i) evaporation of latex particles' suspension on hot super hydrophobic surfaces using shaker or hand rolling followed by thermal annealing, or (ii) using PDMS moulds with spherical cavities to filter out latex suspensions and produce porous particles. Partially fusing the individual latex particles together from rigid supra–particles was achieved by annealing them near to the polystyrene glass–transition temperature, although glassy and transparent porous supra particles were formed above the polystyrene glass

temperatures. The fabricated composite porous supra–particles morphology had a rough surface, and a porous and amorphous structure. The advantages of this method are in controlling the shape and size of spherical porous supra–particles by varying the initial particle concentration, evaporation temperatures and volume of the sulphate latex particles suspension. It was found that a spherical supra–particle shape is successfully formed by concentration, 40–70 wt%; however, below 30 wt%, it did not form particles of a spherical shape. On the other hand, less porous and denser supra–particles were obtained from a 50–70wt% suspension concentration. Latex suspensions of 40 wt% (and lower) initial particle concentration yielded supra–particles of higher porosity.

In Chapter 6 a theoretical model was developed of the adsorption of porous supra–particles at a fluid–liquid interface. The model considers the wetting behaviour of an agglomerated cluster of particles, typical for powdered materials. the adsorption energy of a composite spherical porous supra–particle built up from smaller spherical particles to the oil–water interface were calculated. Two typical cases were considered in this model: (i) a water–filled porous supra–particle adsorbed at the oil–water interface from the water phase, and, (ii) an oil–filled supra–particle adsorbed at the oil–water interface from the oil–phase. The main assumption for this theory was that only the first layer of small colloid particles on the supra particles surfaces is attached to the liquid interface. The predictions of this theoretical model are also valid for adsorption of liquid infusused colloidosomes to an oil–water interface in the same way as for the porous supra–particles. Two packing structures were also considered for the smaller particles on the surface of the porous supra–particles (or colloidosmes), i.e. square packing and hexagonal packing. For both packing structures, the connection between the three–phase contact angle of small “building block” particles and the contact angle of the liquid infused porous supra–particles were derived. The predictions of the method showed that the porous supra–particles would have different contact angle depending on the initial liquid phase by which the particles were immersed before they attached to the oil–water interface. The theoretical model predicts that the macroscopic contact angle and the attachment position of the porous supra–particles at the liquid interface does not depend on their size in first approximation. However, the theory predicts that the contact angle strongly depend on the type of fluid infused in the supra–particles and the fluid phase from which the

particle approaches the liquid interface. In contrast, the equilibrium three–phase contact angle of the non–porous smooth colloidal particles at the liquid–fluid interfaces is independent of the original initial fluid phase from where the adsorption takes place. An expression was also derived for the adsorption energy of the porous supra–particles at the oil–water interface for pores initially infused with water or oil. It was observed that the contact angle of porous supra particles infused with water at the oil–water interface has a physical solution only for values of the building block particle contact angle smaller or equal to approximately 119^o or 126^o for hexagonal packing or square packing respectively. The contact angle of porous supra–particles infused with oil has physical solutions' values only for the building block particle contact angle larger or equal to approximately 61^o or 54^o for hexagonal packing and square packing respectively. The theory predicts that supra–particles of hexagonal packing of building blocks on their surface has high adsorption energy in compared with the same size of supra–particles with square packing of the building block particles on their surface. This theory is also valid for porous supra–particles (or colloidosomes) adsorption to air–water interfaces.

For Chapter 7, the model for porous supra-particles created in Chapter 5 was used to test the theoretical predictions that informed the model presented in Chapter 6. The GTT was used to measure the contact angle of the small latex particles at both the air-water and oil-water interfaces. Furthermore, the actual macroscopic contact angle of the composite supra-particles made of the same latex particles at the same liquid interface were measured. Porous supra-particles were investigated at different fluid-liquid interfaces by studying the stability in the contact angle for the dry and pre-wet supra-particles. The contact angles for these particles adsorbed from air was $63^o \pm 3^o$ and $65^o \pm 3^o$ from water, whereas the contact angle for adsorption from hexadecane was $93^o \pm 1^o$ and $94^o \pm 1^o$ from water. The effect of the energy barrier between the particles and the fluid interface on porous supra-particles was observed during the experiments using a pendant drop method. To overcome this factor, the 0.1 M of NaCl(aq) solution was used to allow particles to adsorb at the interfaces. These contact angles were calculated at two different positions when the particles were at practically flat interfaces and when the particles reached a high arch with a larger droplet. At those positions, two calculations were taken into account, the curved contact angle (CCA) and the flat contact angle (FCA), to determine the effect of curvature on contact angle calculations. The theoretical contact angle values for these particles to attach to

the interface was dependent on the building block particle arrangement on the surface of the porous supra-particles. The contact angle for adsorbed particles from air interface should be in the range 40^o-56^o or 2^o-37^o, while 41^o-44^o was adsorbed from water and 44^o-47^o was at the air-water interfaces; however, the contact angle for particles adsorbed from the oil phase should be 107^o-110^o or 101^o-104^o, whereas it should be 81^o-84^o or 88^o-92^o from the water phase to the oil-water interface.

Porous supra-particles of different sizes were prepared using a 40 wt% suspension to form different sizes. The contact angle for pre-wet supra-particles at the air-water surface showed variations, which can be explained by different packings of latex particles on their surfaces. Compared to the theoretical contact angles, the wettability of particles adsorbed from air to the air-water interface showed some agreement with the contact angle of particles with sizes of 1.7 mm. The expected contact angle should become hydrophilic, but it reached a higher contact angle due to the energy barrier preventing the particles from reaching the equilibrium position. It was difficult to overcome the energy barrier by only using the power of the syringe to push the particles against the glass surface.

Significant hysteresis was found in the supra-particle contact angle, which traps the particles in a range of metastable states and makes it difficult to reach global equilibrium. The variation in the contact angles at the oil-water interface is due to the surface roughness of the supra-particles and the pinning of the porous supra-particle contact line on the surface of the building block particles. Notably, for both phases at a/w and o/w, the contact angle increased with the particles sizes, which showed larger hysteresis. The reasons could be due to the increment of the weight of the particles and the increment of the surface roughness compared to the small particles. The contact angle increased with the increments of salt, which breaks the energy barrier.

A sonication method was also developed for particles attached to a liquid interface, which allows them to adjust their attachment positions at the liquid interface close to equilibrium. The results from our experiments show that when adsorbing at the hexadecane-water interface, the supra-particles behaved as hydrophilic when they were pre-filled with water and hydrophobic when they were pre-filled with hexadecane. The sonication methods showed a more reasonable contact angle at Milli-Q water, which could not be done using the pendant drop method. This could be due

to the energy input of ultra-sonication, which can provide enough power to overcome the energy barrier that exists between the particles and the fluid interfaces.

The sonication method produced results that are in line with the theoretically predicted contact angles for supra-particles based on the values of the contact angles of their building blocks measured with the GTT. As presented in the second part of Chapter 7, the wetting of porous particles attached to an air-water interface for particles adsorbed from air and for particles adsorbed from water have agreement with the theoretical model. At hexadecane-water interfaces, the particles that were filled with hexadecane presented an agreement with the theoretical values, while water-filled particles followed the expected trend but remained below 90^{o}, which did not match the theoretical contact angle. The reasons could be because the flounce of the water infused in the pores tended to make the particles more into water phase.

Also, the presence of concentrated electrolytes in the aqueous phase showed that the wettability of the composite supra-particles changes due to reducing the electrostatic repulsion that exists between the particles and the fluid interfaces. Magnetic resonance imaging (MRI) was used to localise the position of the liquid interface inside the adsorbed porous supra-particles. In this study, the penetration of liquid into porous supra-particles was investigated with an adequate resolution and a satisfactory contrast. It was found that the MRI results confirm the assumption that the liquid interface attaches to the supra-particle surface only at the surface layer of small building block particles.

8.2 Future work

Gel trapping techniques provide suitable information for different particles' shapes and chemical functionality at liquid interfaces. They also can be used to investigate the adsorption of magnetic particles, patchy particles, positively charged particles and Janus particles at fluid interfaces.

The hand rolling of porous supra–particles suspensions can be developed to be automated using hollow spherical supra hydrophobic balls, which allow the latex particle suspensions to roll instead without spilling the particles' droplets. Also, it can be employed in fabrication anisotropic assemblies with different properties, such as magnetic and optical ones. These porous supra–particles can also be used to develop advanced laser techniques in terms of reflection laser lights inside the pores, providing a three–dimensional structure.

Additionally, this method can be used for preparing porous supra–particles with different impregnated fluids and studying their behaviour at different liquid interfaces. A mixture of two different particles, based on size, shape or chemical structure, can be used and their attachment to fluid interfaces studied.

A computational investigation of porous particles impregnated with different fluids is needed to evaluate the effect of liquid front penetration at fluid interfaces. Beside that, it also be useful to study the effect of adsorption of dry porous supra-particles to water droplet based on Washburn method.

The hypothesis can be upgraded to finding the effect of lateral interaction between multiple porous supra–particles impregnated with the same fluid or with mixture fluids at fluid interfaces.

8.3 Appendix

Table 8.1. Experimental data for the contact angles of dry porous supra–particles adsorbed at the air–water interface. $H_{initial}$ is the initial particle protrusion.

Particle diameter (mm)	R_p/R_{fluid}	CA $_{CURVE}$ (θ)	±	CA $_{FLAT}$ (θ)	±	$H_{initial}$/(mm)
1.67	0.211	128.1	0.3	140.7	0.2	1.56
	0.202	131.8	1.3	142.1	0.1	
	0.199	135.8	1.8	135.1	0.4	
	0.154	136.5	2.1	144.2	0.3	
	0.242	67.7	1.3	80.4	0.2	0.12
	0.236	63.5	1.7	79.3	0.2	
	0.168	71.5	0.8	80.1	0.1	
	0.087	75.9	1.0	79.1	0.2	
	0.249	61.8	2.3	72.3	0.1	0.04
	0.193	50	0.7	66.6	0.3	
	0.138	63.4	2.5	70.9	0.7	
	0.112	67.6	2.9	69.3	0.2	
1.69	0.253	137.9	0.7	152	0.1	1.53
	0.147	133.8	0.4	139.3	0.2	
	0.359	58	1.4	74.5	0.3	0.07
	0.116	66.4	3.8	70.4	1.4	
1.65	0.263	113.9	1.6	129.5	0.4	1.43
	0.152	114.6	0.4	121.9	0.1	
	0.169	60.3	5.9	81.9	0.7	0.25
	0.156	71.4	0.4	80.2	0.5	
1.71	0.368	116.0	0.1	131.8	0.4	1.48
	0.196	123.0	0.0	131.3	1.0	
	0.279	61.1	1.0	77.3	0.2	0.15
	0.075	77.5	0.6	80.5	0.2	
1.7	0.216	131.2	0.4	144.4	0.1	1.49
	0.143	149.9	10.6	143.2	4.3	
	0.183	52.2	0.9	71.2	0.1	0.361
	0.158	63.5	1.4	72.2	0.8	
2.01	0.256	131.2	2.0	146.6	0.5	1.77
	0.216	133.5	2.3	147.3	0.6	
	0.141	135.5	2.4	147.1	0.5	
	0.136	141.3	0.4	147	0.2	
	0.401	58.9	0.2	82.3	0.0	0.59
	0.207	58.7	2.5	77.0	0.2	
	0.166	77.0	3.0	84.0	0.2	

	0.139	**61.9**	**1.4**	**76.1**	**0.2**	
	0.456	**75.7**	**13.7**	**77.8**	**0.2**	
	0.23	**59.1**	**0.8**	**81.1**	**0.3**	**0.28**
	0.188	**56.7**	**0.9**	**77.6**	**0.0**	
	0.137	**77.1**	**1.5**	**82.7**	**0.2**	
	0.257	**125.9**	**1.7**	**144.7**	**0.3**	**1.93**
2.03	**0.342**	**145.7**	**8.1**	**143.1**	**7.7**	
	0.300	**66.9**	**1.8**	**85.7**	**0.1**	**0.20**
	0.099	**80.7**	**0.2**	**86.3**	**0.2**	
	0.237	**127.8**	**0.5**	**146.8**	**0.2**	**1.74**
1.9	**0.197**	**136.7**	**0.2**	**143.5**	**0.3**	
	0.355	**62.6**	**4.5**	**83.8**	**0.3**	**0.66**
	0.122	**78.5**	**0.4**	**85.5**	**0.3**	
	0.329	**140.6**	**0.6**	**149.5**	**0.3**	
	0.254	**131.5**	**2.7**	**149.1**	**0.7**	**2.11**
	0.226	**127.2**	**2.0**	**148.7**	**0.3**	
2.21	**0.136**	**133.9**	**2.5**	**149.2**	**0.6**	
	0.351	**62.3**	**1.7**	**81.0**	**0.2**	
	0.349	**60.2**	**1.0**	**83.3**	**0.2**	
	0.212	**66.6**	**0.2**	**78.7**	**0.1**	**0.07**
	0.15	**82.1**	**2.8**	**85.2**	**0.3**	
	0.237	**130.8**	**0.9**	**150.5**	**0.3**	**2.10**
2.27	**0.244**	**145.8**	**0.6**	**152.2**	**0.3**	
	0.304	**77.4**	**2.6**	**101.1**	**0.1**	**0.57**
	0.286	**77.2**	**1.1**	**89.2**	**0.1**	
	0.224	**121.2**	**0.5**	**143**	**0.2**	**2.02**
2.21	**0.178**	**140.6**	**1.0**	**145.8**	**0.6**	
	0.143	**74.8**	**0.2**	**82.9**	**0.1**	**0.90**
	0.259	**73.9**	**0.5**	**98.7**	**0.2**	
	0.255	**127.6**	**1.1**	**150.1**	**0.0**	**2.03**
2.17	**0.231**	**143.7**	**0.6**	**150.3**	**0.3**	
	0.323	**69.9**	**4.5**	**93.4**	**0.1**	**0.46**
	0.253	**94.8**	**0.3**	**95.9**	**2.9**	
	0.294	**114.2**	**1.1**	**139.9**	**0.3**	**1.99**
2.17	**0.302**	**131.3**	**0.8**	**140.8**	**0.2**	
	0.324	**54.9**	**3.6**	**84.0**	**0.2**	**0.45**
	0.220	**83.9**	**2.8**	**88.3**	**0.4**	
	0.233	**125.9**	**0.5**	**145.1**	**0.2**	**1.77**
2.2	**0.209**	**135.8**	**0.2**	**143.1**	**0.2**	
	0.238	**57.5**	**1.2**	**80.0**	**0.2**	**0.40**
	0.155	**70.0**	**0.4**	**78.9**	**0.2**	

Table 8.2. Summary of the contact angles of dry porous supra–particles adsorbed at the air–water interface (from the above table) compared to the theoretical model.

Interface type	Fluid	θ_o/deg.	θ_s/deg.	θ_h/deg.	Particle diameter (mm)	CCA (θ/deg.)		FCA (θ/deg.)	
			40	**2**		**initial**	**final**	**initial**	**final**
A-W	**Air**	**63 ± 3**	**49**	**23**	**1.7**	**132 ± 12**	**69 ± 5**	**136 ± 8**	**75 ± 5**
			51	**29**	**2.0**	**141 ± 4**	**79 ± 1**	**145 ± 2**	**85 ± 2**
			56	**37**	**2.2**	**139 ± 5**	**80 ± 8**	**147 ± 4**	**89 ± 7**

Table 8.3. Experimental data for the contact angles of dry porous supra–particles adsorbed at the air–water interface where the aqueous phase is 0.1 M NaCl solution.

Particle diameter (mm)	R_p/R_{fluid}	CA $_{curve}$ (θ)	±	CA $_{FLAT}$ (θ)	±	$H_{initial}$/(mm)
1.7	0.293	101.3	2.2	122.5	0.5	1.58
	0.251	102.9	0.9	122.1	0.3	
	0.217	104.6	0.6	122.1	0.2	
	0.117	108.7	0.3	115.8	0.2	
	0.313	49.9	0.6	71.3	0.1	0.26
	0.273	54.1	0.6	73.0	0.1	
	0.194	58.3	1.1	72.8	0.1	
	0.115	67.0	0.4	72.9	0	
	0.391	52.2	1.2	71.6	0	0.12
	0.357	54.9	1.2	71.7	0.2	
	0.249	61.8	2.9	72.2	0.1	
	0.228	51.5	0.7	62.4	0.1	
1.68	0.365	100.1	2.3	120.6	0.4	1.68
	0.120	106	0.9	112	0.4	
	0.214	34.3	1.3	61.1	0.3	0.28
	0.171	53.0	1.1	61.7	0.3	
1.72	0.234	119.3	1.0	139.1	0.2	1.52
	0.162	119.2	0.4	126.6	0.1	
	0.206	34.6	1.4	60.5	0.4	0.18
	0.224	49.3	0.2	60.7	0.2	
1.76	0.243	123.0	0.5	141.1	0.1	1.42
	0.165	129.1	4.8	130.5	0.4	
	0.321	46.5	1.6	66.9	0.4	0.23
	0.136	63.3	2.6	66.2	0.3	
2.05	0.242	111.0	0.3	135.7	0.1	1.91
	0.215	115.1	2.4	136.1	0.4	
	0.117	117.1	0.3	122.7	0.2	
	0.112	117.6	0.5	136.5	0.2	
	0.266	43.0	3.4	67.7	0.2	0.39
	0.260	53.9	0.3	68.6	0.1	
	0.234	46.5	2.8	67.9	0.4	
	0.198	63.8	3.6	68.1	0.2	
2.04	0.292	107.5	3.6	131.9	0.2	1.90
	0.220	116.6	2.4	116.9	0.8	
	0.340	43.5	2.7	65.8	0.3	0.34
	0.110	59.2	0.2	64.9	0.1	
1.98	0.299	99.2	0.4	122.3	0.1	1.92
	0.165	108.6	2.2	113.7	0.2	
	0.340	46.9	1.7	68.2	0.1	0.62
	0.134	66.0	3.6	68.2	1.0	
2.04	0.301	102.6	5.0	127.3	0.2	1.87
	0.201	114.9	8.6	114.2	0.1	
	0.398	42.2	1.7	63.6	0.3	0.16
	0.171	59.0	3.4	62.2	0.3	
1.97	0.453	57.9	6.0	75.8	0.5	0.85
	0.129	66.4	1.5	73.6	0.5	
	0.302	46.4	1.7	64.5	0.4	0.44
	0.223	54.3	1.1	63.3	0.2	

	0.579	128.8	1.9	145.7	0.5	
	0.275	122.3	3.6	146.0	0.6	1.98
	0.270	124.2	0.7	135.2	0.2	
2.23	0.402	47.4	3.3	72.4	0.0	
	0.382	50.6	2.9	72.6	0.2	0.50
	0.316	58.3	2.7	72.9	0.3	
	0.123	64.2	0.3	70.8	0.2	
2.29	0.257	104.8	1.8	134.7	0.2	1.93
	0.252	108.7	8.6	109.8	0.3	
	0.377	43.1	0.5	68.0	0.2	0.54
	0.105	60.9	0.5	66.4	0.3	
2.25	0.270	92.3	2.7	123.3	0.0	2.00
	0.168	99.3	0.4	108.1	0.1	
	0.406	46.1	0.6	70.3	0.2	0.49
	0.199	67.7	3.9	70.6	0.1	
2.20	0.253	113.1	1.1	139.8	0.3	2.09
	0.493	118.4	0.5	118.7	3.5	
	0.361	43.9	1.3	70.5	0.5	0.56
	0.178	66.9	0.2	71.1	1.2	
2.20	0.374	113.8	1.5	137.4	0.1	2.13
	0.156	126.9	0.3	133.4	0.1	
	0.431	43.8	3.1	70.7	0.1	0.64
	0.108	63.0	0.9	68.6	0.4	

Table 8.4. Summary of the the contact angles of dry porous supra–particles adsorbed at the air–water interface where the aqueous phase is 0.1 M NaCl solution (from the above table) compared to the theoretical model.

Interface type	Fluid	θo/deg.	θs/deg.	θh/deg.	Particle diameter (mm)	CCA (θ/deg.)		FCA (θ/deg.)	
			40	2		initial	final	initial	final
A-NaCl	Air	63 ± 3	49	23	1.7	116 ± 9	54± 5	121 ± 8	63 ± 2
			51	29	2.0	105 ± 19	60 ± 4	111 ± 21	65 ± 2
			56	37	2.2	116 ± 10	65 ± 3	121 ± 11	70 ± 2

Table 8.5. Experimental data for the contact angles of water–infused porous supra–particles adsorbed at the air–water interface.

Particle diameter (mm)	R_p/R_{fluid}	CA CURVE (θ)	±	CA FLAT (θ)	±	$H_{initial}$/(mm)
1.75	0.317	29.0	1.0	23.9	0.7	1.53
	0.313	29.9	0.4	23.3	0.3	
	0.309	30.2	2.8	23.5	0.1	
	0.201	30.7	0.3	25.6	0.0	
	0.122	26.2	0.6	24.3	0.9	
	0.266	57.4	0.6	43.3	0.2	0.80
	0.254	58.5	1.4	44	0.2	
	0.227	54.1	1.9	44.5	0.1	
	0.172	52.9	0.0	45.9	0.6	
1.7	0.304	33.5	2.4	26.4	0.1	1.50
	0.163	26.5	1.7	25.6	0.3	
	0.181	62.0	5.3	59.7	0.3	0.67
	0.240	79.7	4.9	62.4	0.1	
1.69	0.309	46.5	0.9	36.6	0.2	1.41
	0.130	42.9	1.1	38.4	0.5	
	0.303	89.2	2.7	71.8	0.2	0.67
	0.143	80.6	0.4	73	0.1	
1.72	0.287	29.1	0.8	21.8	0.3	1.43
	0.114	24.5	1.2	22.5	1.1	
1.72	0.293	36.1	1.3	28.3	0.6	1.72
	0.155	32.5	0.9	29.7	0.5	
	0.271	95.9	2.7	75.8	0.2	1.57
	0.174	78.9	1.3	72.1	0.1	
1.98	0.345	28.6	3.2	21.5	0.3	1.83
	0.337	23.7	3.0	19.5	0.1	
	0.336	29.3	2.7	21.8	0.5	
	0.106	22.8	1.4	21.3	0.5	
	0.337	71.8	1.6	59.2	0.1	1.08
	0.345	80.3	4.9	61.3	0.1	
	0.335	79.5	4.7	60.9	0.2	
	0.163	68.4	0.2	60.0	0.0	
2.05	0.347	28.7	2.0	21.7	0.2	1.86
	0.346	29.7	1.9	22.2	0.3	
	0.281	28.0	2.4	21.7	0.0	
	0.156	23.7	2.5	21.8	0.4	
1.99	0.442	28.7	2.5	23.5	1.1	1.85
	0.179	25.0	6.8	26.9	7.2	
	0.308	73.8	2.0	55.4	0.3	1.28
	0.210	64.8	0.5	55.2	0.1	
2.00	0.406	23.4	5.8	19.3	1.4	1.91
	0.121	20.5	1.6	19.2	0.5	
	0.367	82.6	4.0	63.4	0.1	0.91
	0.168	72.4	0.4	63.6	0.1	
2.25	0.330	30.8	0.4	21.3	0.3	2.15
	0.325	29.4	0.7	20.8	0.2	
	0.311	28.3	2.2	21.2	0.4	

	0.180	**21.7**	**2.5**	**19.0**	**0.7**	
	0.394	**66.0**	**0.7**	**49.2**	**0.1**	**1.00**
	0.379	**65.4**	**1.1**	**49.2**	**0.3**	
	0.346	**63.6**	**0.3**	**49.1**	**0.1**	
	0.177	**59.2**	**0.7**	**50.0**	**0.3**	
2.21	**0.301**	**31.9**	**1.4**	**21.8**	**0.2**	**2.05**
	0.152	**19.6**	**0.8**	**17.1**	**0.3**	
	0.275	**69.2**	**3.7**	**48.3**	**0.1**	**1.33**
	0.100	**48.1**	**2.9**	**44.8**	**1.0**	
2.21	**0.367**	**31.5**	**1.8**	**22.5**	**0.3**	**2.08**
	0.190	**22.5**	**1.4**	**20.3**	**0.5**	
	0.244	**83.5**	**0.2**	**57.4**	**0.1**	**0.66**
	0.220	**63.0**	**0.3**	**52.9**	**0.0**	

Table 8.6. Summary of the contact angles of water–infused porous supra–particles adsorbed at the air–water interface (from the above table) compared to the theoretical model.

Interface type	**Fluid**	**θo/deg.**	**θs/deg.**	**θh/deg.**	**Particle diameter (mm)**	**CCA (θ/deg.)**		**FCA (θ/deg.)**	
						initial	**final**	**initial**	**final**
A-W	**Water**	**65 ± 1**	**41**	**44**	**1.7**	**32 ± 7**	**73 ± 12**	**30 ± 6**	**63 ± 11**
			42	**46**	**2.0**	**23 ± 2**	**69 ± 3**	**22 ± 3**	**60 ± 3**
			44	**47**	**2.2**	**21 ± 1**	**57 ± 6**	**19 ± 1**	**49 ± 3**

Table 8.7. Experimental data for the contact angles of porous supra–particles infused with 0.1 M NaCl(aq) solution adsorbed at the air–NaCl(aq) solution interface.

Particle diameter (mm)	R_p/R_{fluid}	CA CURVE (θ)	±	CA FLAT (θ)	±	$H_{initial}$/(mm)
1.67	0.277	35.7	1.3	27.9	0.5	1.63
	0.271	37.6	0.3	28.2	0.2	
	0.238	26.1	3.4	25.1	0.4	
	0.224	33.5	0.4	27.4	0.3	
	0.267	103.3	2.0	83.0	0.1	0.69
	0.258	102.7	2.3	82.9	0.0	
	0.230	90.2	2.2	81.1	0.1	
	0.208	100.5	0.9	82.0	0.1	
	0.293	122.1	0.7	103.7	0.0	0.24
	0.274	125.7	0.3	106.0	0.1	
	0.267	123.9	0.3	105.6	0.2	
	0.195	91.2	5.1	79.0	0.1	
	0.172	89.3	0.3	78.9	0.1	
1.72	0.285	26.3	3.0	20.4	0.1	1.60
	0.183	16.8	3.1	16.2	0.1	
	0.242	55.3	0.6	41.0	0.3	1.27
	0.212	38.1	3.7	36.3	1.3	
1.71	0.228	59.9	3.5	44.5	0.2	1.47
	0.155	46.1	1.2	40.4	0.4	
	0.242	112.5	4.4	93.4	0.2	0.28
	0.192	97.8	2.6	90.1	0.1	
1.65	0.307	27.2	1.0	22.6	0.6	1.65
	0.140	28.5	0.5	25.8	0.0	
	0.211	95.5	4.2	91.5	0.8	1.46
	0.272	101.1	2.2	85.3	0.1	
1.8	0.307	27.8	4.9	23.9	0.6	1.71
	0.179	32.7	0.7	27.9	0.2	
	0.317	73.2	0.4	61.5	0.1	0.86
	0.148	73.7	1.3	63.7	0.1	
2.063	0.362	18.0	3.0	18.1	1.0	2.00
	0.330	32.6	0.6	23.1	0.2	
	0.329	30.5	2.5	22.3	0.3	
	0.316	30.5	1.4	22.9	0.3	
	0.354	67.3	0.5	55	0.1	1.10
	0.308	88.7	3.8	66.5	0.0	
	0.240	85.9	3.9	66.1	0.1	
	0.175	66.6	4.2	56.2	0.2	
1.93	0.341	24.6	2.3	20.2	0.3	1.86
	0.214	27.1	0.4	23.7	0.1	
	0.253	101.3	3.3	83.3	0.1	0.63
	0.205	92	1.2	78.2	0.2	
2.06	0.281	26.9	1.3	20.4	0.3	2.02
	0.221	21.6	2.1	18.3	0.1	
	0.241	87.2	1.8	68.7	0.1	0.80
	0.219	69.0	0.8	57.7	0.4	
2.07	0.238	26.3	1.2	22.8	0.6	2.01
	0.355	31.4	1.3	24.4	0.1	
	0.246	72.7	5.3	56.5	0.1	0.46
	0.205	66.4	1.1	53.4	0.1	

2.29	**0.432**	**28.1**	**0.6**	**18.1**	**5.2**	
	0.429	**21.4**	**6.6**	**17.9**	**1.7**	**2.12**
	0.399	**20.8**	**0.7**	**14.7**	**0.4**	
	0.256	**21.6**	**3.0**	**19.1**	**1.1**	
	0.408	**103.0**	**2.8**	**79.4**	**0.1**	**0.98**
	0.379	**106.7**	**2.4**	**80.7**	**0.4**	
	0.302	**98.9**	**3.1**	**79.7**	**0.1**	
	0.301	**97.5**	**0.9**	**80.9**	**0.1**	
2.17	**0.320**	**29.9**	**0.4**	**23.5**	**0.3**	**2.12**
	0.250	**27.4**	**0.5**	**23.1**	**0.4**	
	0.332	**85.5**	**1.0**	**70.8**	**0.1**	**0.90**
	0.326	**88.8**	**2.2**	**71.5**	**0.2**	
2.15	**0.341**	**28.4**	**1.0**	**22.7**	**0.2**	**2.06**
	0.237	**27.6**	**1.6**	**24.5**	**0.2**	
	0.308	**86.3**	**2.4**	**72.4**	**0.1**	**0.88**
	0.232	**90.9**	**0.7**	**72.8**	**0.2**	
2.29	**0.328**	**33.2**	**2.9**	**25.7**	**0.2**	**2.28**
	0.303	**33.7**	**1.8**	**26.9**	**0.3**	
	0.312	**98.5**	**1.8**	**78.2**	**0.1**	**0.67**
	0.293	**98.7**	**3.7**	**79.5**	**0.2**	

Table 8.8. Summary of the contact angles of porous supra–particles infused with 0.1 M NaCl(aq) solution adsorbed at the air–NaCl(aq) solution interface (from the above table) compared to the theoretical model.

Interface type	**Fluid**	**θo/deg.**	**θs/deg.**	**θh/deg.**	**Particle diameter (mm)**	**CCA (θ/deg.)**		**FCA (θ/deg.)**	
						initial	**final**	**initial**	**final**
A-NaCl(aq)	**NaCl(aq)**	**65 ± 1**	**41**	**44**	**1.7**	**32 ± 9**	**80 ± 23**	**28 ± 8**	**71 ± 19**
			42	**46**	**2.0**	**26 ± 3**	**74 ± 11**	**22 ± 2**	**61 ± 10**
			44	**47**	**2.2**	**28 ± 4**	**94 ± 4**	**23 ± 3**	**76 ± 4**

Table 8.9. Experimental data for the contact angles of water–infused porous supra–particles adsorbed at the hexadecane–water interface.

Particle diameter (mm)	R_p/R_{fluid}	CA CURVE (θ)	±	CA FLAT (θ)	±	$H_{initial}$/(mm)
1.83	0.308	17.5	0.5	12.7	0.5	1.78
	0.299	20.7	1.1	15.4	0.4	
	0.290	20.3	0.4	15.2	0.2	
	0.142	11.2	0.4	11.8	0.4	
	0.303	39.4	2.4	30.4	0.4	1.51
	0.281	43.8	1.3	31.3	0.2	
	0.240	39.2	1.7	28.8	0.2	
	0.201	27.7	4.3	25.8	0.6	
1.81	0.274	20.7	0.7	16.2	0.5	1.73
	0.160	19.9	0.0	17.5	0.0	
	0.237	116.1	3.9	93	0.4	0.24
	0.204	105.6	0.9	93.9	0.3	
1.84	0.271	18.2	1.6	12.7	1.1	1.84
	0.317	16.2	4.7	15.3	1.9	
1.83	0.339	16.9	1.3	14.0	1.4	1.67
	0.405	45.6	1.1	38.3	0.9	
	0.116	47.6	7.0	46.5	0.3	1.49

Table 8.10. Summary of the contact angles of water–infused porous supra–particles adsorbed at the hexadecane–water interface (from the above table) compared to the theoretical model.

Interface type	Fluid	θo/deg.	θs/deg.	θh/deg.	Particle diameter (mm)	CCA (θ/deg.)		FCA (θ/deg.)	
						initial	final	initial	final
O-W	Water	93 ± 1	81 83 84	88 90 92	1.8	16 ± 3	45 ± 39	15 ± 2	42 ± 34

Table 8.11. Experimental data for the contact angles of porous supra–particles infused with 0.1 M NaCl(aq), adsorbed at the hexadecane– NaCl (aq) interface.

Particle diameter (mm)	R_p/R_{fluid}	CA CURVE (θ)	±	CA FLAT (θ)	±	$H_{initial}$/(mm)
1.74	0.330	29.4	2.1	22.0	0.2	1.645
	0.317	28.4	0.8	22.6	0.0	
	0.317	34.4	1.4	26.1	0.7	
	0.168	34.9	1.9	32.3	0.5	
	0.360	119.8	0.4	101.0	0.5	0.626
	0.312	121.5	0.7	101.7	0.1	
	0.230	120.4	0.6	102.4	0.1	
	0.151	109.7	0.3	101.1	0.1	
1.69	0.293	54.7	0.3	40.8	0.2	1.543
	0.145	45.3	1.4	42.3	0.7	
	0.283	133.1	3.0	110.2	0.2	0.212
	0.164	117.9	0.6	109.0	0.2	
1.68	0.334	41.0	2.6	31.6	0.4	1.578
	0.261	29.0	1.4	31.6	0.8	
	0.300	124.3	0.6	103.7	0.1	0.23
	0.163	106.6	3.1	101.7	0.1	
1.64	0.283	56.9	0.5	43.1	0.1	1.442
	0.154	52.5	0.0	46.2	0.3	
	0.292	126.1	1.4	106.9	0.1	0.39
	0.191	114.9	3.6	108.4	0.2	
1.94	0.339	54.3	0.3	41.0	0.0	1.77
	0.319	50.0	0.2	38.1	0.2	
	0.306	43.3	0.4	35.2	0.1	
	0.165	45.2	2.6	42.9	0.3	
1.94	0.663	122.1	9.2	108.2	1.8	0.39
	0.382	118.7	3.3	108.6	0.7	
	0.305	128.4	3.4	108.6	0.2	
	0.168	121.4	0.7	112.5	0.4	
1.92	0.368	58.9	0.9	44.2	0.2	1.78
	0.130	46.9	0.9	44.7	0.5	
	0.487	123.6	2.2	105.7	0.3	0.58
	0.103	113.8	0.6	108.2	0.2	
1.91	0.370	52.0	2.0	39.5	0.2	1.54
	0.144	40.6	2.6	40.7	0.9	
	0.368	122.8	0.8	103.8	0.1	0.45
	0.153	117.4	0.5	109.0	0.2	
1.86	0.377	39.8	0.4	30.4	0.2	1.80
	0.124	66.9	0.2	60.6	0.1	
	0.333	122.5	1.0	101.5	0.3	0.62
	0.114	106.4	3.1	102.6	0.5	
1.87	0.391	66.1	5.7	53.5	0.1	1.75
	0.102	63.1	0.1	58.1	0.0	
	0.380	123	2.9	104.8	0.3	0.48
	0.413	141	2.9	120	2.3	
2.16	0.242	40.6	1.1	33.1	0.5	1.92
	0.328	47.5	0.6	35.7	0.2	
	0.373	51.4	0.3	37.7	0.1	
	0.150	44.7	1.3	40.2	0.1	
	0.424	124.9	0.4	104.4	0.1	0.67

	0.550	124.3	1.7	103.9	0.1	
	0.534	124.1	1.0	104.2	0.2	
2.16	0.458	54.3	2.2	40.7	0.1	2.15
	0.189	44.6	2.3	42.1	0.3	
	0.492	131.5	4.4	110.5	0.4	0.52
	0.188	115.7	2.1	107.9	0.3	
2.12	0.445	70.4	5.2	52.7	0.3	2.07
	0.449	132.1	1.7	110.5	0.2	0.41
	0.142	119.5	0.8	111.9	0.5	
2.14	0.425	36.5	1.0	26.4	0.0	2.01
	0.126	31.9	0.3	28.5	0.1	
	0.499	128.9	4.7	106.6	0.6	0.66
	0.186	120.2	0.6	110.1	0.3	
2.16	0.377	36.6	1.8	25.6	0.5	2.02
	0.194	23.3	1.0	23.3	0.4	
	0.351	126	4.0	103.1	0.3	0.40
	0.272	120	2.9	104.7	0.6	

Table 8.12. Summary of the contact angles of porous supra–particles infused with 0.1 M NaCl(aq), adsorbed at the hexadecane– NaCl (aq) interface (from the above table) compared to the theoretical model.

Interface type	Fluid	θo/deg.	θs/deg.	θh/deg.	Particle diameter (mm)	CCA (θ/deg.)		FCA (θ/deg.)	
						initial	final	initial	final
O-NaCl(aq)	NaCl(aq)	93 ± 1	81	88	1.7	40 ± 9	112 ± 4	38 ± 6	105 ± 4
			83	90	1.9	53 ± 10	116 ± 6	49 ± 8	107 ± 3
			84	92	2.1	43 ± 16	120 ± 3	37 ± 10	108 ± 3

Table 8.13. Experimental data for the contact angles of hexadecane–infused porous supra–particles adsorbed at the hexadecane–water interface.

Particle diameter (mm)	R_p/R_{fluid}	CA $_{CURVE}$ (θ)	±	CA $_{FLAT}$ (θ)	±	$H_{initial}$/(mm)
1.68	0.249	146.8	1.2	154.9	0.3	1.43
	0.204	147.9	1.6	155.5	0.1	
	0.168	150.9	1.9	156.3	0.2	
	0.109	153.2	0.5	155.9	0.0	
	0.275	131.2	0.7	141.0	0.4	0.15
	0.159	142.3	2.1	146.0	0.8	
	0.153	126.6	2.5	141.1	0.6	
	0.151	136.2	1.4	140.8	0.5	
	0.146	138.8	1.2	143.7	0.5	
1.68	0.153	124.5	0.6	139.0	0.5	0.02
	0.149	125.8	0.6	131.6	0.7	
	0.132	136.3	0.0	141.0	0.2	
	0.117	123.2	1.1	136.0	0.5	
1.81	0.233	154.8	0.6	163.4	0.1	1.56
	0.140	163.4	0.4	165.7	0.1	
	0.247	119.0	0.5	134.0	0.2	0.75
	0.116	128.9	0.2	133.7	0.3	
1.8	0.244	153.2	0.4	161.6	0.0	1.70
	0.175	157.3	1.5	160.6	0.8	
	0.203	105.9	2.9	124.8	0.3	0.43
	0.117	115.6	0.6	121.4	0.4	
1.77	0.305	155.1	1.9	163.7	0.0	1.62
	0.166	165.3	3.2	167.1	2.4	
	0.291	150.3	2.6	160.0	0.1	0.85
	0.146	156.1	0.4	159.1	0.0	
1.68	0.188	146.8	0.3	155.7	0.0	1.58
	0.139	152.4	1.5	155.8	0.8	
1.82	0.194	148.2	0.4	158.0	0.1	1.65
	0.162	158.2	1.0	161.0	0.6	
	0.243	147.8	0.4	156.6	0.0	1.09
	0.133	158.9	2.8	161.7	2.3	
2.05	0.227	135.8	0.5	149.6	0.1	
	0.189	137.4	0.5	149.6	0.4	1.79
	0.145	140.7	0.5	149.8	0.2	
	0.106	148.4	0.9	151.1	0.6	
	0.240	127.0	4.3	133.1	0.4	
	0.224	115.4	0.4	132.4	0.1	
	0.218	119.3	1.8	132.8	0.1	0.92
	0.114	128.8	0.9	133.5	0.3	
2.05	0.241	112.9	4.9	128.7	0.1	
	0.174	112.7	0.4	127.4	0.0	
	0.147	118.2	0.9	127.4	0.1	0.20
	0.119	120.9	0.2	126.6	0.2	
1.98	0.297	148.0	3.0	157.5	0.2	1.78
	0.103	162.6	5.1	163.6	3.7	
	0.293	112.3	2.0	132.0	0.1	0.77
	0.107	129.9	0.3	134.3	0.3	
2.08	0.390	143.5	0.3	156.0	0.2	1.93
	0.269	148.2	0.4	156.5	0.0	

	0.151	**128.4**	**0.6**	**134.4**	**0.4**	**0.54**
	0.414	**124.8**	**2.4**	**140.1**	**0.0**	
2.07	**0.419**	**142.2**	**3.6**	**154.0**	**0.4**	**2.07**
	0.171	**156.5**	**0.9**	**154.0**	**1.0**	
2.03	**0.376**	**101.4**	**6.2**	**122.9**	**0.1**	**0.98**
	0.133	**114.0**	**0.7**	**120.3**	**0.4**	
	0.289	**136.5**	**1.1**	**150.9**	**0.3**	**1.75**
	0.118	**151.8**	**0.6**	**154.6**	**0.4**	
2.3	**0.118**	**133.4**	**6.4**	**132.0**	**0.1**	**0.38**
	0.367	**115.1**	**1.1**	**134.5**	**0.2**	
	0.392	**135.4**	**3.4**	**152.3**	**0.3**	
	0.368	**134.2**	**3.0**	**151.6**	**1.2**	
	0.284	**136.9**	**2.3**	**151.4**	**1.2**	**1.88**
	0.195	**157.0**	**7.5**	**155.5**	**0.1**	
	0.165	**143.0**	**2.3**	**153.0**	**0.2**	
2.15	**0.339**	**148.8**	**0.5**	**160.1**	**0.3**	**1.51**
	0.203	**158.7**	**1.6**	**161.9**	**0.7**	
2.23	**0.446**	**132.1**	**0.2**	**146.1**	**0.2**	**1.20**
	0.165	**142.6**	**3.3**	**146.4**	**1.8**	
2.31	**0.430**	**143.0**	**1.1**	**155.8**	**0.2**	**1.92**
	0.141	**155.1**	**2.1**	**158.7**	**0.6**	
2.04	**0.522**	**134.7**	**3.3**	**147.6**	**3.3**	**2.08**
	0.168	**152.6**	**1.3**	**156.5**	**0.4**	
	0.476	**141.7**	**3.3**	**153.7**	**0.1**	**0.85**
	0.169	**152.1**	**2.0**	**155.9**	**0.8**	
	0.375	**133.0**	**3.0**	**147.1**	**0.2**	**1.73**
	0.149	**147.6**	**2.8**	**149.4**	**0.7**	
	0.169	**131.2**	**0.5**	**137.7**	**0.2**	**0.91**
	0.432	**124.5**	**1.2**	**139.4**	**0.1**	

Table 8.14. Summary of the contact angles of hexadecane–infused porous supra–particles adsorbed at the hexadecane–water interface (from the above table) compared to the theoretical model.

Interface type	**Fluid**	**θo/deg.**	**θs/deg.**	**θh/deg.**	**Particle diameter (mm)**	**CCA (θ/deg.)**		**FCA (θ/deg.)**	
						initial	**final**	**initial**	**final**
O-W	**Hexadecane**	**94 ± 1**	**107**	**101**	**1.7**	**152 ± 14**	**135 ± 15**	**157 ± 10**	**139± 14**
			109	**102**	**2.0**	**150 ± 13**	**132 ± 14**	**152 ± 11**	**137 ± 13**
			110	**104**	**2.2**	**151 ± 6**	**142 ± 9**	**156 ± 4**	**147 ± 7**

Table 8.15. Experimental data for the contact angles of hexadecane infused porous supra–particles adsorbed at the hexadecane–NaCl(aq) solution interface .

Particle diameter (mm)	R_p/R_{fluid}	CA CURVE (θ)	±	CA FLAT (θ)	±	$H_{initial}$/(mm)
1.75	0.228	135.0	1.8	146.2	0.7	1.45
	0.185	136.0	1.1	146.1	0.1	
	0.149	142.2	1.0	146.9	0.6	
	0.142	139.6	1.5	146.9	0.4	
	0.214	96.6	3.0	115.2	0.2	1.08
	0.204	99.0	3.5	115.1	0.1	
	0.180	113.6	5.2	116.3	0.7	
	0.146	98.3	0.5	113.0	0.3	
1.74	0.261	108.8	2.2	125.3	0.4	1.22
	0.126	121.0	3.7	125.1	0.4	
	0.276	91.3	1.4	109.9	0.6	0.67
	0.143	103.9	1.3	110.0	0.4	
1.65	0.222	142.1	1.7	152.0	0.4	1.19
	0.163	149.2	0.8	153.3	0.5	
1.69	0.296	119.5	1.3	131.9	0.1	1.12
	0.151	129.1	3.0	131.9	0.5	
	0.145	99.1	0.4	106.9	0	0.47
	0.233	107.8	3.6	123.1	0.5	
1.93	0.201	119.4	0.3	137.5	0.1	1.50
	0.183	131.4	0.3	138.2	0.3	
	0.174	120.4	0.2	137.6	0.1	
	0.130	122.5	0.5	137.3	0	
1.93	0.306	126.4	10.3	136.4	0.4	1.19
	0.289	119.8	2.8	135.4	0.5	
	0.268	118.7	3.0	135.4	0.0	
	0.161	121.4	2.8	135.0	0.3	
1.89	0.254	130.8	1.6	142.5	0.2	1.45
	0.140	136.4	0.5	141.4	0.3	
	0.243	98.6	1.1	115.5	0.3	0.62
	0.143	108.8	0.2	116.3	0.2	
2.14	0.248	135.8	0.4	150.6	0.1	1.83
	0.205	136.0	0.1	149.4	0.2	
	0.194	146.6	0.4	151.9	0.3	
	0.116	137.8	0.1	150.4	0.2	
2.13	0.230	141.9	0.7	156.1	0.1	1.94
	0.270	118.5	3.3	136.6	0.2	1.17
	0.180	131.0	0.1	137.7	0.1	
2.16	0.284	138.4	1.6	152.5	0.5	1.64
	0.232	146.4	0.4	152.5	0.1	
2.19	0.278	111.1	1.10	132.2	0.1	1.52
	0.133	126.6	0.40	131.9	0.1	
	0.239	120.5	3.00	126.8	0.5	1.10
	0.292	108.7	4.80	129	0.1	

Table 8.16. Summary of the contact angles of hexadecane infused porous supra–particles adsorbed at the hexadecane–NaCl(aq) solution interface (from the above table) compared to the theoretical model.

Interface type	Fluid	θo/deg.	θs/deg.	θh/deg.	Particle diameter (mm)	CCA (θ/deg.)		FCA (θ/deg.)	
						initial	final	initial	final
O-NaCl(aq)	Hexadecane	94 ± 1	107	101	1.7	130 ± 8	100 ± 2	135 ± 9	110 ± 2
			109	102	2.0	127 ± 7	109 ± 1	138 ± 3	116 ± 1
			110	104	2.2	138 ± 7	120 ± 11	148 ± 9	133 ± 4

References

1. Bormashenko Edward, Y., *Wetting of Real Surfaces*. 2013.
2. Davies, J. T.; Rideal, E. K., *Interfacial phenomena*. Academic Press: 1963.
3. Tadros, T. F.; Vincent, B. P., *Encyclopedia of Emulsion Technology: Basic Theory*. Marcel Dekker New York, 1983.
4. Paunov, V. N., Novel Method for Determining the Three-Phase Contact Angle of Colloid Particles Adsorbed at Air−Water and Oil−Water Interfaces. *Langmuir* **2003,** *19* (19), 7970.
5. Adamson, A. W., *Physical Chemistry of Surfaces*. Wiley: New York, 1990.
6. Horozov, T.; Arnaudov, L., A Novel Fast Technique for Measuring Dynamic Surface and Interfacial Tension of Surfactant Solutions at Constant Interfacial Area. *J Colloid Interface Sci* **1999,** *219* (1), 99.
7. Drelich, J., MEASUREMENT OF INTERFACIAL TENSION IN FLUID-FLUID SYSTEMS. **2002**, 3152.
8. Young, T., An Essay on the Cohesion of Fluids. *Philosophical Transactions of the Royal Society of London* **1805,** *95* (0), 65.
9. Shaw, D. J., *Introduction to colloid and surface chemistry*. Butterworth-Heinemann: 1992.
10. Cosgrove, T., *Colloid Science: Principles, Methods and Applications*. John Wiley & Sons: 2010.
11. Dupré, A., Theorie Mecanique de la Chaleur, chapter IX, Actions Moleculaires (Suite). *Gauthier-Villars, Paris* **1869**.
12. Awaja, F.; Gilbert, M.; Kelly, G.; Fox, B.; Pigram, P. J., Adhesion of polymers. *Prog Polym Sci* **2009,** *34* (9), 948.
13. Schroder, M. E., Work of Adhesion of a Sessile Drop to a Clean Surface. *J Colloid Interface Sci* **1999,** *213* (2), 602.
14. Colloidal particles at liquid interfaces: An introduction. In *Colloidal Particles at Liquid Interfaces*, Binks, B. P.; Horozov, T. S., 2006; pp 1.
15. Blake, M. S.; Johnston, K. H.; Russell-Jones, G. J.; Gotschlich, E. C., A rapid, sensitive method for detection of alkaline phosphatase-conjugated anti-antibody on Western blots. *Anal Biochem* **1984,** *136* (1), 175.
16. Li, X.-M.; Reinhoudt, D.; Crego-Calama, M., What do we need for a superhydrophobic surface? A review on the recent progress in the preparation of superhydrophobic surfaces. *Chemical Society Reviews* **2007,** *36* (8), 1350.
17. Shirtcliffe, N. J.; McHale, G.; Atherton, S.; Newton, M. I., An introduction to superhydrophobicity. *Adv Colloid Interface Sci* **2010,** *161* (1-2), 124.
18. Latthe, S. S.; Gurav, A. B.; Maruti, C. S.; Vhatkar, R. S., Recent Progress in Preparation of Superhydrophobic Surfaces: A Review. *Journal of Surface Engineered Materials and Advanced Technology* **2012,** *2* (2), 76.
19. Horozov, T. S.; Braz, D. A.; Fletcher, P. D.; Binks, B. P.; Clint, J. H., Novel film-calliper method of measuring the contact angle of colloidal particles at liquid interfaces. *Langmuir* **2008,** *24* (5), 1678.
20. Gao, N.; Yan, Y., Characterisation of surface wettability based on nanoparticles. *Nanoscale* **2012,** *4* (7), 2202.
21. Extrand, C. W.; Kumagai, Y., An Experimental Study of Contact Angle Hysteresis. *J Colloid Interface Sci* **1997,** *191* (2), 378.
22. Kandlikar, S. G.; Steinke, M. E., Contact angles and interface behavior during rapid evaporation of liquid on a heated surface. *Int J Heat Mass Tran* **2002,** *45* (18), 3771.

23. Pieranski, P., Two-Dimensional Interfacial Colloidal Crystals. *Phys Rev Lett* **1980,** *45* (7), 569.
24. Maestro, A.; Bonales, L. J.; Ritacco, H.; Rubio, R. G.; Ortega, F., Effect of the spreading solvent on the three-phase contact angle of microparticles attached at fluid interfaces. *Phys Chem Chem Phys* **2010,** *12* (42), 14115.
25. Isa, L.; Lucas, F.; Wepf, R.; Reimhult, E., Measuring single-nanoparticle wetting properties by freeze-fracture shadow-casting cryo-scanning electron microscopy. *Nature communications* **2011,** *2*, 438.
26. Schmitt, V.; Destribats, M.; Backov, R., Colloidal particles as liquid dispersion stabilizer: Pickering emulsions and materials thereof. *Cr Phys* **2014,** *15* (8-9), 761.
27. Johnson, A. J. Membrane permeation from solutions, particle dispersions and particle-stabilised emulsions. University of Hull, Hull, United Kingdom, 2013.
28. de Folter, J. W. J.; van Ruijven, M. W. M.; Velikov, K. P., Oil-in-water Pickering emulsions stabilized by colloidal particles from the water-insoluble protein zein. *Soft Matter* **2012,** *8* (25), 6807.
29. Dickinson, E., Food colloids research: historical perspective and outlook. *Adv Colloid Interface Sci* **2011,** *165* (1), 7.
30. Kruglyakov, P. M.; Nushtayeva, A. V., Phase inversion in emulsions stabilised by solid particles. *Adv Colloid Interface Sci* **2004,** *108-109*, 151.
31. Extrand, C. W., Water contact angles and hysteresis of polyamide surfaces. *J Colloid Interface Sci* **2002,** *248* (1), 136.
32. Extrand, C. W.; Moon, S. I., Using the Flotation of a Single Sphere to Measure and Model Capillary Forces. *Langmuir* **2009,** *25* (11), 6239.
33. Liu, X.; Wang, X.; Liang, Y.; Zhou, F., Floating behavior of hydrophobic glass spheres. *Journal of Colloid and Interface Science* **2009,** *336* (2), 743.
34. Dupas, J.; Forny, L.; Ramaioli, M., Powder wettability at a static air–water interface. *Journal of Colloid and Interface Science* **2015,** *448*, 51.
35. Nguyen, A. V., New method and equations for determining attachment tenacity and particle size limit in flotation. *International Journal of Mineral Processing* **2003,** *68* (1–4), 167.
36. Danov, K. D.; Kralchevsky, P. A.; Boneva, M. P., Electrodipping Force Acting on Solid Particles at a Fluid Interface. *Langmuir* **2004,** *20* (15), 6139.
37. Velev, O. D.; Denkov, N. D.; Paunov, V. N.; Kralchevsky, P. A.; Nagayama, K., Capillary image forces: II. Experiment. *Journal of colloid and interface science* **1994,** *167* (1), 66.
38. Botto, L.; Lewandowski, E. P.; Cavallaro, M.; Stebe, K. J., Capillary interactions between anisotropic particles. *Soft Matter* **2012,** *8* (39), 9957.
39. Lewandowski, E. P.; Bernate, J. A.; Searson, P. C.; Stebe, K. J., Rotation and alignment of anisotropic particles on nonplanar interfaces. *Langmuir* **2008,** *24* (17), 9302.
40. Lewandowski, E. P.; Cavallaro, M., Jr.; Botto, L.; Bernate, J. C.; Garbin, V.; Stebe, K. J., Orientation and self-assembly of cylindrical particles by anisotropic capillary interactions. *Langmuir* **2010,** *26* (19), 15142.
41. Lewandowski, E. P.; Searson, P. C.; Stebe, K. J., Orientation of a Nanocylinder at a Fluid Interface. *J. Phys. Chem. B* **2006,** *110*, 4283.
42. Lazghab, M.; Saleh, K.; Pezron, I.; Guigon, P.; Komunjer, L., Wettability assessment of finely divided solids. *Powder Technol* **2005,** *157* (1-3), 79.
43. Kossen, N. W. F.; Heertjes, P. M., The determination of the contact angle for systems with a powder. *Chemical Engineering Science* **1965,** *20* (6), 593.
44. Washburn, E. W., The Dynamics of Capillary Flow. *Physical Review* **1921,** *17* (3), 273.

45. Washburn, E. W., Note on a Method of Determining the Distribution of Pore Sizes in a Porous Material. *Proceedings of the National Academy of Sciences of the United States of America* **1921,** *7* (4), 115.
46. Siebold, A.; Nardin, M.; Schultz, J.; Walliser, A.; Oppliger, M., Effect of dynamic contact angle on capillary rise phenomena. *Colloid Surface A* **2000,** *161* (1), 81.
47. Siebold, A.; Walliser, A.; Nardin, M.; Oppliger, M.; Schultz, J., Capillary Rise for Thermodynamic Characterization of Solid Particle Surface. *J Colloid Interface Sci* **1997,** *186* (1), 60.
48. Maestro, A.; Guzman, E.; Ortega, F.; Rubio, R. G., Contact angle of micro- and nanoparticles at fluid interfaces. *Curr Opin Colloid In* **2014,** *19* (4), 355.
49. Sedlacik, M.; Pavlinek, V., A tensiometric study of magnetorheological suspensions' stability. *Rsc Adv* **2014,** *4* (102), 58377.
50. Bartell, F. E.; Osterhof, H. J., Determination of the Wettability of a Solid by a Liquid. *Industrial & Engineering Chemistry* **1927,** *19* (11), 1277.
51. Morrison, I. D.; Ross, S., *Colloidal Dispersions: Suspensions, Emulsions, and Foams*. Wiley: 2002.
52. Kralchevsky, P. A.; Paunov, V. N.; Denkov, N. D.; Nagayama, K., Capillary image forces: I. Theory. *Journal of colloid and interface science* **1994,** *167* (1), 47.
53. Petkov, J. T.; Denkov, N. D.; Danov, K. D.; Velev, O. D.; Aust, R.; Durst, F., Measurement of the Drag Coefficient of Spherical-Particles Attached to Fluid Interfaces. *Journal of Colloid and Interface Science* **1995,** *172* (1), 147.
54. Weon, B. M.; Lee, J. S.; Kim, J. T.; Pyo, J.; Je, J. H., Colloidal wettability probed with X-ray microscopy. *Curr Opin Colloid In* **2012,** *17* (6), 388.
55. Arnaudov, L. N.; Cayre, O. J.; Cohen Stuart, M. A.; Stoyanov, S. D.; Paunov, V. N., Measuring the three-phase contact angle of nanoparticles at fluid interfaces. *Phys Chem Chem Phys* **2010,** *12* (2), 328.
56. Gasperini, L.; Mano, J. F.; Reis, R. L., Natural polymers for the microencapsulation of cells. *J R Soc Interface* **2014,** *11* (100), 20140817.
57. Hui, Y. H., *Handbook of food science, technology, and engineering*. Taylor & Francis: Boca Raton, 2006.
58. Wang, Q.; Cui, S. W., Understanding the physical properties of food polysaccharides. *Food carbohydrates: chemistry, physical properties and applications. Taylor and Francis, New York* **2005**, 161.
59. Cayre, O. J.; Paunov, V. N., Contact angles of colloid silica and gold particles at air-water and oil-water interfaces determined with the gel trapping technique. *Langmuir* **2004,** *20* (22), 9594.
60. Cayre, O. J.; Paunov, V. N., Fabrication of microlens arrays by gel trapping of self-assembled particle monolayers at the decane-water interface. *J Mater Chem* **2004,** *14* (22), 3300.
61. Paunov, V. N.; Cayre, O. J.; Noble, P. F.; Stoyanov, S. D.; Velikov, K. P.; Golding, M., Emulsions stabilised by food colloid particles: role of particle adsorption and wettability at the liquid interface. *J Colloid Interface Sci* **2007,** *312* (2), 381.
62. Al-Shehri, H.; Horozov, T. S.; Paunov, V. N., Adsorption of carboxylic modified latex particles at liquid interfaces studied by the gel trapping technique. *Soft Matter* **2014,** *10* (34), 6433.
63. Sharp, E. L.; Al-Shehri, H.; Horozov, T. S.; Stoyanov, S. D.; Paunov, V. N., Adsorption of shape-anisotropic and porous particles at the air-water and the decane-water interface studied by the gel trapping technique. *Rsc Adv* **2014,** *4* (5), 2205.

64. Santini, E.; Kragel, J.; Ravera, F.; Liggieri, L.; Miller, R., Study of the monolayer structure and wettability properties of silica nanoparticles and CTAB using the Langmuir trough technique. *Colloid Surface A* **2011,** *382* (1-3), 186.
65. Fujii, S.; Murakami, R., Smart Particles as Foam and Liquid Marble Stabilizers. *Kona Powder Part J* **2008,** *26* (26), 153.
66. Reed, K. M.; Borovicka, J.; Horozov, T. S.; Paunov, V. N.; Thompson, K. L.; Walsh, A.; Armes, S. P., Adsorption of sterically stabilized latex particles at liquid surfaces: effects of steric stabilizer surface coverage, particle size, and chain length on particle wettability. *Langmuir* **2012,** *28* (18), 7291.
67. Gharabaghi, M.; Aghazadeh, S., A review of the role of wetting and spreading phenomena on the flotation practice. *Curr Opin Colloid In* **2014,** *19* (4), 266.
68. Klobes, P.; Meyer, K.; Munro, R. G.; Science, M.; Laboratory, E.; Standards, N. I. o.; Technology, *Porosity and Specific Surface Area Measurements for Solid Materials*. U.S. Department of Commerce, Technology Administration, National Institute of Standards and Technology: 2006.
69. Sing, K. S. W.; Everett, D. H.; Haul, R. A. W.; Moscou, L.; Pierotti, R. A.; Rouquerol, J.; Siemieniewska, T., Reporting Physisorption Data for Gas Solid Systems with Special Reference to the Determination of Surface-Area and Porosity (Recommendations 1984). *Pure Appl Chem* **1985,** *57* (4), 603.
70. Haber, J., Manual on Catalyst Characterization. *Pure Appl Chem* **1991,** *63* (9), 1227.
71. Everett, D., Definitions, terminology and symbols in colloid and surface chemistry. *Pure Appl. Chem* **1972,** *31*, 577.
72. Nichols, G.; Byard, S.; Bloxham, M. J.; Botterill, J.; Dawson, N. J.; Dennis, A.; Diart, V.; North, N. C.; Sherwood, J. D., A review of the terms agglomerate and aggregate with a recommendation for nomenclature used in powder and particle characterization. *Journal of pharmaceutical sciences* **2002,** *91* (10), 2103.
73. Chang, S. S.; Clair, B.; Ruelle, J.; Beauchene, J.; Di Renzo, F.; Quignard, F.; Zhao, G. J.; Yamamoto, H.; Gril, J., Mesoporosity as a new parameter for understanding tension stress generation in trees. *Journal of experimental botany* **2009,** *60* (11), 3023.
74. Rouquerol, J., *Characterization of Porous Solids III: Proceedings of the IUPAC Symposium (COPS III), Marseille, France, May 9-12, 1993*. Elsevier Science Limited: 1994; Vol. 87.
75. Fletcher, P. D. I.; Haswell, S. J.; He, P.; Kelly, S. M.; Mansfield, A., Permeability of silica monoliths containing micro- and nano-pores. *J Porous Mat* **2011,** *18* (4), 501.
76. Cong, J. J.; Chen, Y. Z.; Luo, J.; Liu, X. Y., Fabrication of graphene/polyaniline composite multilayer films by electrostatic layer-by-layer assembly. *J Solid State Chem* **2014,** *218*, 171.
77. Bruckschen, B.; Seitz, H.; Buzug, T.; Tille, C.; Leukers, B.; Irsen, S., Comparing different porosity measurement methods for characterisation of 3D printed bone replacement scaffolds. *Biomedizinische Technik* **2005,** *50*, 1609.
78. Gokmen, M. T.; Du Prez, F. E., Porous polymer particles-A comprehensive guide to synthesis, characterization, functionalization and applications. *Prog Polym Sci* **2012,** *37* (3), 365.
79. Velev, O. D.; Lenhoff, A. M.; Kaler, E. W., A class of microstructured particles through colloidal crystallization. *Science* **2000,** *287* (5461), 2240.
80. Paunov, V. N.; Cayre, O. J., Supraparticles and "Janus" particles fabricated by replication of particle monolayers at liquid surfaces using a gel trapping technique. *Adv Mater* **2004,** *16* (9-10), 788.

81. Dinsmore, A. D.; Hsu, M. F.; Nikolaides, M. G.; Marquez, M.; Bausch, A. R.; Weitz, D. A., Colloidosomes: selectively permeable capsules composed of colloidal particles. *Science* **2002,** *298* (5595), 1006.
82. Yuan, C. H.; Zeng, B. R.; Yu, S. R.; Mao, J.; Chen, X. L.; Luo, W.; Xu, Y. T.; Chang, F. C.; Dai, L. Z., An airflow-controlled solvent evaporation route to hollow microspheres and colloidosomes. *Rsc Adv* **2014,** *4* (10), 4796.
83. Rossier-Miranda, F. J.; Schroen, K.; Boom, R., Microcapsule production by an hybrid colloidosome-layer-by-layer technique. *Food Hydrocolloid* **2012,** *27* (1), 119.
84. Kim, S. H.; Lim, J. M.; Lee, S. K.; Heo, C. J.; Yang, S. M., Biofunctional colloids and their assemblies. *Soft Matter* **2010,** *6* (6), 1092.
85. Watanabe, T.; Ono, T.; Kimura, Y., Continuous fabrication of monodisperse polylactide microspheres by droplet-to-particle technology using microfluidic emulsification and emulsion-solvent diffusion. *Soft Matter* **2011,** *7* (21), 9894.
86. Abraham, S.; Park, Y. H.; Lee, J. K.; Ha, C. S.; Kim, I., Microfluidic synthesis of reversibly swelling porous polymeric microcapsules with controlled morphology. *Adv Mater* **2008,** *20* (11), 2177.
87. He, X. D.; Ge, X. W.; Liu, H. R.; Wang, M. Z.; Zhang, Z. C., Synthesis of cagelike polymer microspheres with hollow core/porous shell structures by self-assembly of latex particles at the emulsion droplet interface. *Chem Mater* **2005,** *17* (24), 5891.
88. Sander, J. S.; Studart, A. R., Multiwalled functional colloidosomes made small and in large quantities via bulk emulsification. *Soft Matter* **2014,** *10* (1), 60.
89. Hyuk Im, S.; Jeong, U.; Xia, Y., Polymer hollow particles with controllable holes in their surfaces. *Nat Mater* **2005,** *4* (9), 671.
90. Jeong, U.; Im, S. H.; Camargo, P. H.; Kim, J. H.; Xia, Y., Microscale fish bowls: a new class of latex particles with hollow interiors and engineered porous structures in their surfaces. *Langmuir* **2007,** *23* (22), 10968.
91. Zhao, Y.; Zhao, X.; Sun, C.; Li, J.; Zhu, R.; Gu, Z., Encoded silica colloidal crystal beads as supports for potential multiplex immunoassay. *Analytical chemistry* **2008,** *80* (5), 1598.
92. Kim, S. H.; Lee, S. Y.; Yi, G. R.; Pine, D. J.; Yang, S. M., Microwave-assisted self-organization of colloidal particles in confining aqueous droplets. *J Am Chem Soc* **2006,** *128* (33), 10897.
93. Yi, G. R.; Manoharan, V. N.; Klein, S.; Brzezinska, K. R.; Pine, D. J.; Lange, F. F.; Yang, S. M., Monodisperse micrometer-scale spherical assemblies of polymer particles. *Adv Mater* **2002,** *14* (16), 1137.
94. Yi, G. R.; Jeon, S. J.; Thorsen, T.; Manoharan, V. N.; Quake, S. R.; Pine, D. J.; Yang, S. M., Generation of uniform photonic balls by template-assisted colloidal crystallization. *Synthetic Met* **2003,** *139* (3), 803.
95. Rastogi, V.; Melle, S.; Calderon, O. G.; Garcia, A. A.; Marquez, M.; Velev, O. D., Synthesis of Light-Diffracting Assemblies from Microspheres and Nanoparticles in Droplets on a Superhydrophobic Surface. *Adv Mater* **2008,** *20* (22), 4263.
96. Cho, Y. S.; Kim, S. H.; Yi, G. R.; Yang, S. M., Self-organization of colloidal nanospheres inside emulsion droplets: Higher-order clusters, supraparticles, and supraballs. *Colloid Surface A* **2009,** *345* (1-3), 237.
97. Klein, S. M.; Manoharan, V. N.; Pine, D. J.; Lange, F. F., Synthesis of spherical polymer and titania photonic crystallites. *Langmuir* **2005,** *21* (15), 6669.
98. Velev, O. D.; Furusawa, K.; Nagayama, K., Assembly of latex particles by using emulsion droplets as templates .1. Microstructured hollow spheres. *Langmuir* **1996,** *12* (10), 2374.

99. Velev, O. D.; Furusawa, K.; Nagayama, K., Assembly of latex particles by using emulsion droplets as templates .2. Ball-like and composite aggregates. *Langmuir* **1996,** *12* (10), 2385.
100. Kuncicky, D. M.; Bose, K.; Costa, K. D.; Velev, O. D., Sessile droplet templating of miniature porous hemispheres from colloid crystals. *Chem Mater* **2007,** *19* (2), 141.
101. Park, J.; Moon, J.; Shin, H.; Wang, D.; Park, M., Direct-write fabrication of colloidal photonic crystal microarrays by ink-jet printing. *J Colloid Interface Sci* **2006,** *298* (2), 713.
102. Rastogi, V.; Garcia, A. A.; Marquez, M.; Velev, O. D., Anisotropic particle synthesis inside droplet templates on superhydrophobic surfaces. *Macromolecular rapid communications* **2010,** *31* (2), 190.
103. Perazzo, A.; Preziosi, V.; Guido, S., Phase inversion emulsification: Current understanding and applications. *Adv Colloid Interface Sci* **2015,** *222* (0), 581.
104. Chapter 1 Emulsions - Recent Advances in Understanding. In *Modern Aspects of Emulsion Science*, Binks, B. P., The Royal Society of Chemistry: 1998; pp 1.
105. Solids-stabilized emulsions: A review. In *Colloidal Particles at Liquid Interfaces*, Lopetinsky, R. J. G.; Masliyah, J. H.; Xu, Z., 2006; pp 186.
106. Chapter 4 Emulsion Flocculation and Creaming. In *Modern Aspects of Emulsion Science*, Robins, M. M.; Hibberd, D. J., The Royal Society of Chemistry: 1998; pp 115.
107. Chapter 7 Coalescence in Emulsions. In *Modern Aspects of Emulsion Science*, Kabalnov, A. S., The Royal Society of Chemistry: 1998; pp 205.
108. Chapter 8 - Theory of emulsion flocculation. In *Interface Science and Technology*, Petsev, D. N., Petsev, D. N., Ed. Elsevier: 2004; Vol. Volume 4, pp 313.
109. Binks, B. P.; Lumsdon, S. O., Influence of particle wettability on the type and stability of surfactant-free emulsions. *Langmuir* **2000,** *16* (23), 8622.
110. Wang, L.; Sondi, I. I.; Matijevic, E., Preparation of Uniform Needle-Like Aragonite Particles by Homogeneous Precipitation. *J Colloid Interface Sci* **1999,** *218* (2), 545.
111. Chibowski, E.; Holysz, L.; Szczes, A., Adhesion of in situ precipitated calcium carbonate in the presence and absence of magnetic field in quiescent conditions on different solid surfaces. *Water Res* **2003,** *37* (19), 4685.
112. Ogino, T.; Suzuki, T.; Sawada, K., The Formation and Transformation Mechanism of Calcium-Carbonate in Water. *Geochim Cosmochim Ac* **1987,** *51* (10), 2757.
113. Campbell, A. L.; Holt, B. L.; Stoyanov, S. D.; Paunov, V. N., Scalable fabrication of anisotropic micro-rods from food-grade materials using an in shear flow dispersion-solvent attrition technique. *J Mater Chem* **2008,** *18* (34), 4074.
114. Chassin, P.; Jounay, C.; Quiquampoix, H., Measurement of the Surface Free-Energy of Calcium-Montmorillonite. *Clay Miner* **1986,** *21* (5), 899.
115. Jouany, C., Surface Free-Energy Components of Clay-Synthetic Humic-Acid Complexes from Contact-Angle Measurements. *Clay Clay Miner* **1991,** *39* (1), 43.
116. Gellan gum. In *Thickening and Gelling Agents for Food*, Gibson, W.; Sanderson, G. R., Imeson, A., Ed. Springer US: 1997; pp 119.
117. Jansson, P. E.; Lindberg, B.; Sandford, P. A., Structural Studies of Gellan Gum, an Extracellular Polysaccharide Elaborated by Pseudomonas-Elodea. *Carbohyd Res* **1983,** *124* (1), 135.
118. Nakajima, K.; Ikehara, T.; Nishi, T., Observation of gellan gum by scanning tunneling microscopy. *Carbohyd Polym* **1996,** *30* (2-3), 77.

119. Klang, V.; Valenta, C.; Matsko, N. B., Electron microscopy of pharmaceutical systems. *Micron* **2013,** *44* (0), 45.
120. Binks, B. P.; Boa, A. N.; Kibble, M. A.; Mackenzie, G.; Rocher, A., Sporopollenin capsules at fluid interfaces: particle-stabilised emulsions and liquid marbles. *Soft Matter* **2011,** *7* (8), 4017.
121. Dickinson, E., Food emulsions and foams: Stabilization by particles. *Curr Opin Colloid In* **2010,** *15* (1-2), 40.
122. Kalashnikova, I.; Bizot, H.; Cathala, B.; Capron, I., New Pickering emulsions stabilized by bacterial cellulose nanocrystals. *Langmuir* **2011,** *27* (12), 7471.
123. Graeme, G.; Karsten, B.; Markus, P.; Michael, K.; Hans-Jürgen, B.; Karlheinz, G., Contact angles and wetting behaviour of single micron-sized particles. *Journal of Physics: Condensed Matter* **2005,** *17* (9), S445.
124. Li, Z.; Giese, R. F.; Vanoss, C. J.; Yvon, J.; Cases, J., The Surface Thermodynamic Properties of Talc Treated with Octadecylamine. *Journal of Colloid and Interface Science* **1993,** *156* (2), 279.
125. Subrahmanyam, T. V.; Monte, M. B. M.; Middea, A.; Valdiviezo, E.; Lins, F. F., Contact angles of quartz by capillary penetration of liquids and captive bubble techniques. *Miner Eng* **1999,** *12* (11), 1347.
126. Jouany, C.; Chassin, P., Determination of the Surface-Energy of Clay Organic-Complexes by Contact-Angle Measurements. *Colloid Surface* **1987,** *27* (4), 289.
127. Ecke, S.; Preuss, M.; Butt, H. J., Microsphere tensiometry to measure advancing and receding contact angles on individual particles. *J Adhes Sci Technol* **1999,** *13* (10), 1181.
128. Clint, J. H.; Taylor, S. E., Particle-Size and Interparticle Forces of Overbased Detergents - a Langmuir Trough Study. *Colloid Surface* **1992,** *65* (1), 61.
129. Hadjiiski, A.; Dimova, R.; Denkov, N. D.; Ivanov, I. B.; Borwankar, R., Film trapping technique: Precise method for three-phase contact angle determination of solid and fluid particles of micrometer size. *Langmuir* **1996,** *12* (26), 6665.
130. Hadjiiski, A.; Tcholakova, S.; Ivanov, I. B.; Gurkov, T. D.; Leonard, E. F., Gentle Film Trapping Technique with Application to Drop Entry Measurements. *Langmuir* **2002,** *18* (1), 127.
131. Hadjiiski, A.; Dimova, R.; Denkov, N. D.; Ivanov, I. B., Film Trapping Technique : Precise Method for Three-Phase Contact Angle Determination of Solid and Fluid Particles of Micrometer Size. **2001,** *7463* (18), 6665.
132. The Gel Trapping Technique: A Novel Method for Characterizing the Wettability of Microparticles and the Replication of Particle Monolayers. In *Nanostructured and Advanced Materials for Applications in Sensor, Optoelectronic and Photovoltaic Technology*, Paunov, V. N.; Cayre, O. J., Vaseashta, A.; Dimova-Malinovska, D.; Marshall, J. M., Eds. Springer Netherlands: 2005; Vol. 204, pp 363.
133. Noble, P. F.; Cayre, O. J.; Alargova, R. G.; Velev, O. D.; Paunov, V. N., Fabrication of "hairy" colloidosomes with shells of polymeric microrods. *J Am Chem Soc* **2004,** *126* (26), 8092.
134. Aveyard, R.; Binks, B. P.; Clint, J. H., Emulsions stabilised solely by colloidal particles. *Adv Colloid Interfac* **2003,** *100*, 503.
135. Chibowski, E.; Holysz, L., Use of the Washburn Equation for Surface Free-Energy Determination. *Langmuir* **1992,** *8* (2), 710.
136. Lehle, H.; Noruzifar, E.; Oettel, M., Ellipsoidal particles at fluid interfaces. *Eur. Phys. J. E* **2008,** *26*, 151.
137. Newton, B. J.; Brakke, K. A.; Buzza, D. M., Influence of magnetic field on the orientation of anisotropic magnetic particles at liquid interfaces. *Phys Chem Chem Phys* **2014,** *16* (47), 26051.

138. Paunov, V. N.; Kralchevsky, P. A.; Denkov, N. D.; Nagayama, K., Lateral Capillary Forces between Floating Submillimeter Particles. *Journal of Colloid and Interface Science* **1993,** *157* (1), 100.
139. Ballard, N.; Bon, S. A., Equilibrium orientations of non-spherical and chemically anisotropic particles at liquid-liquid interfaces and the effect on emulsion stability. *J Colloid Interface Sci* **2015,** *448* (0), 533.
140. Deshmukh, O. S.; van den Ende, D.; Stuart, M. C.; Mugele, F.; Duits, M. H. G., Hard and soft colloids at fluid interfaces: Adsorption, interactions, assembly & rheology. *Adv Colloid Interfac* **2015,** *222*, 215.
141. Wenzel, R. N., Resistance of Solid Surfaces to Wetting by Water. *Industrial & Engineering Chemistry* **1936,** *28* (8), 988.
142. Erbil, H., *Solid and liquid interfaces*. Blackwell Publishing, Oxford: 2006.
143. Alargova, R. G.; Paunov, V. N.; Velev, O. D., Formation of polymer microrods in shear flow by emulsification--solvent attrition mechanism. *Langmuir* **2006,** *22* (2), 765.
144. Wege, H. A.; Kim, S.; Paunov, V. N.; Zhong, Q.; Velev, O. D., Long-term stabilization of foams and emulsions with in-situ formed microparticles from hydrophobic cellulose. *Langmuir* **2008,** *24* (17), 9245.
145. Campbell, A. L.; Stoyanov, S. D.; Paunov, V. N., Fabrication of functional anisotropic food-grade micro-rods with micro-particle inclusions with potential application for enhanced stability of food foams. *Soft Matter* **2009,** *5* (5), 1019.
146. Furst, E. M., Directing colloidal assembly at fluid interfaces. *Proceedings of the National Academy of Sciences of the United States of America* **2011,** *108* (52), 20853.
147. Leal-Calderon, F.; Schmitt, V.; Bibette, J., *Emulsion Science: Basic Principles*. Springer: 2007.
148. Murray, B. S.; Ettelaie, R., Foam stability: proteins and nanoparticles. *Curr Opin Colloid In* **2004,** *9* (5), 314.
149. Du, Z. P.; Bilbao-Montoya, M. P.; Binks, B. P.; Dickinson, E.; Ettelaie, R.; Murray, B. S., Outstanding stability of particle-stabilized bubbles. *Langmuir* **2003,** *19* (8), 3106.
150. Ashby, N. P.; Binks, B. P.; Paunov, V. N., Bridging interaction between a water drop stabilised by solid particles and a planar oil/water interface. *Chem Commun (Camb)* **2004,** (4), 436.
151. Kirchmajer, D. M.; Steinhoff, B.; Warren, H.; Clark, R.; Panhuis, M. I. H., Enhanced gelation properties of purified gellan gum. *Carbohyd Res* **2014,** *388*, 125.
152. Berg, J. C., *An Introduction to Interfaces & Colloids: The Bridge to Nanoscience*. World Scientific: 2010.
153. Paunov, V. N.; Binks, B. P.; Ashby, N. P., Adsorption of charged colloid particles to charged liquid surfaces. *Langmuir* **2002,** *18* (18), 6946.
154. Horozov, T. S., Foams and foam films stabilised by solid particles. *Current Opinion in Colloid and Interface Science* **2008,** *13* (3), 134.
155. Horozov, T. S.; Aveyard, R.; Clint, J. H.; Neumann, B., Particle zips: Vertical emulsion films with particle monolayers at their surfaces. *Langmuir* **2005,** *21* (6), 2330.
156. Horozov, T. S.; Binks, B. P., Particle-stabilized emulsions: A bilayer or a bridging monolayer? *Angewandte Chemie - International Edition* **2006,** *45* (5), 773.
157. Kralchevsky, P. A.; Ivanov, I. B.; Ananthapadmanabhan, K. P.; Lips, A., On the thermodynamics of particle-stabilized emulsions: curvature effects and catastrophic phase inversion. *Langmuir* **2005,** *21* (1), 50.

158. Davies, G. B.; Kruger, T.; Coveney, P. V.; Harting, J.; Bresme, F., Interface deformations affect the orientation transition of magnetic ellipsoidal particles adsorbed at fluid-fluid interfaces. *Soft Matter* **2014,** *10* (35), 6742.
159. CHAPTER 2 Interactions and Conformations of Particles at Fluid-Fluid Interfaces. In *Particle-Stabilized Emulsions and Colloids: Formation and Applications*, Park, B. J.; Lee, D.; Furst, E. M., The Royal Society of Chemistry: 2015; pp 8.
160. Ramsden, W., Separation of solids in the surface-layers of solutions and 'suspensions' - Preliminary account. *Proc. R. Soc. (London)* **1903,** *72*, 156.
161. Pickering, S. U., CXCVI.?Emulsions. *Journal of the Chemical Society, Transactions* **1907,** *91* (0), 2001.
162. Aveyard, R.; Clint, J. H.; Horozov, T. S., Aspects of the stabilisation of emulsions by solid particles: Effects of line tension and monolayer curvature energy. *Phys Chem Chem Phys* **2003,** *5* (11), 2398.
163. Binks, B. P.; Fletcher, P. D. I., Particles adsorbed at the oil-water interface: A theoretical comparison between spheres of uniform wettability and "Janus" particles. *Langmuir* **2001,** *17* (16), 4708.
164. Jiang, S.; Granick, S., Janus balance of amphiphilic colloidal particles. *J Chem Phys* **2007,** *127* (16), 161102.
165. Aveyard, R., Can Janus particles give thermodynamically stable Pickering emulsions? *Soft Matter* **2012,** *8* (19), 5233.
166. Park, B. J.; Lee, D., Equilibrium Orientation of Nonspherical Janus Particles at Fluid · Fluid Interfaces. *ACS Nano* **2012,** *6* (1), 782.
167. Rezvantalab, H.; Shojaei-Zadeh, S., Capillary interactions between spherical Janus particles at liquid-fluid interfaces. *Soft Matter* **2013,** *9* (13), 3640.
168. Kumar, A.; Park, B. J.; Tu, F. Q.; Lee, D., Amphiphilic Janus particles at fluid interfaces. *Soft Matter* **2013,** *9* (29), 6604.
169. Park, B. J.; Choi, C. H.; Kang, S. M.; Tettey, K. E.; Lee, C. S.; Lee, D., Geometrically and chemically anisotropic particles at an oil-water interface. *Soft Matter* **2013,** *9* (12), 3383.
170. Hu, M.; Mi, B., Enabling graphene oxide nanosheets as water separation membranes. *Environmental science & technology* **2013,** *47* (8), 3715.
171. Dasgupta, S.; Katava, M.; Faraj, M.; Auth, T.; Gompper, G., Capillary assembly of microscale ellipsoidal, cuboidal, and spherical particles at interfaces. *Langmuir* **2014,** *30* (40), 11873.
172. Morris, G.; Hadler, K.; Cilliers, J., Particles in thin liquid films and at interfaces. *Curr Opin Colloid In* **2015,** *20* (2), 98.
173. Morris, G.; Neethling, S. J.; Cilliers, J. J., A model for investigating the behaviour of non-spherical particles at interfaces. *Journal of Colloid and Interface Science* **2011,** *354* (1), 380.
174. Morgan, A. R.; Ballard, N.; Rochford, L. A.; Nurumbetov, G.; Skelhon, T. S.; Bon, S. A. F., Understanding the multiple orientations of isolated superellipsoidal hematite particles at the oil–water interface. *Soft Matter* **2013,** *9* (2), 487.
175. Ailin, D. Particle Assisted Wetting. Dissertation, Chemnitz University of Technology, Saxony, Germany, 2007.
176. Braz, D. A. Particle-stabilised foams and foam films. University of Hull, HULL, 2009.
177. Binks, B. P.; Murakami, R., Phase inversion of particle-stabilized materials from foams to dry water. *Nat Mater* **2006,** *5* (11), 865.
178. Murakami, R.; Bismarck, A., Particle-Stabilized Materials: Dry Oils and (Polymerized) Non-Aqueous Foams. *Adv Funct Mater* **2010,** *20* (5), 732.

179. Tian, J.; Arbatan, T.; Li, X.; Shen, W., Liquid marble for gas sensing. *Chem Commun (Camb)* **2010,** *46* (26), 4734.
180. Chin, J. M.; Reithofer, M. R.; Tan, T. T.; Menon, A. G.; Chen, E. Y.; Chow, C. A.; Hor, A. T.; Xu, J., Supergluing MOF liquid marbles. *Chem Commun (Camb)* **2013,** *49* (5), 493.
181. de Gennes, P., Wetting: statics and dynamics. *Reviews of Modern Physics* **1985,** *57* (3), 827.
182. Binks, B. P.; Duncumb, B.; Murakami, R., Effect of pH and salt concentration on the phase inversion of particle-stabilized foams. *Langmuir* **2007,** *23* (18), 9143.
183. Du, K.; Glogowski, E.; Emrick, T.; Russell, T. P.; Dinsmore, A. D., Adsorption Energy of Nano- and Microparticles at Liquid-Liquid Interfaces. *Langmuir* **2010,** *26* (15), 12518.
184. Stocco, A.; Drenckhan, W.; Rio, E.; Langevin, D.; Binks, B. P., Particle-stabilised foams: an interfacial study. *Soft Matter* **2009,** *5* (11), 2215.